Delft University of Technology

Photochromic Properties of Rare-Earth Oxyhydrides

Nafezarefi, Fahimeh

DOI
10.4233/uuid:eb54d12f-079a-41a4-8d75-1a0fdf2af412

Publication date
2020

Citation (APA)
Nafezarefi, F. (2020). *Photochromic Properties of Rare-Earth Oxyhydrides*. [Dissertation (TU Delft), Delft University of Technology]. https://doi.org/10.4233/uuid:eb54d12f-079a-41a4-8d75-1a0fdf2af412

Important note
To cite this publication, please use the final published version (if applicable).
Please check the document version above.

Copyright
Other than for strictly personal use, it is not permitted to download, forward or distribute the text or part of it, without the consent of the author(s) and/or copyright holder(s), unless the work is under an open content license such as Creative Commons.

Takedown policy
Please contact us and provide details if you believe this document breaches copyrights.
We will remove access to the work immediately and investigate your claim.

This work is downloaded from Delft University of Technology.
For technical reasons the number of authors shown on this cover page is limited to a maximum of 10.

Photochromic Properties of Rare-Earth Oxyhydrides

Photochromic Properties of Rare-Earth Oxyhydrides

Dissertation

for the purpose of obtaining the degree of doctor
at Delft University of Technology,
by the authority of the Rector Magnificus prof.dr.ir. T.H.J.J. van der Hagen,
chair of the Board for Doctorates to be defended publicly on
Friday 7 February 2020 at 15:00 o'clock

by

Fahimeh NAFEZAREFI
Master of Science in Advanced Materials Science
Technical University of Munich, University of Augsburg &
Ludwig Maximilian University of Munich, Germany
- joint Master's degree -
born in Tehran, Iran

This dissertation has been approved by the promotor.

Composition of the doctoral committee:

Rector Magnificus,	chairperson
Prof. dr. B. Dam	Delft University of Technology, promotor

Independent members:

Prof. dr. ir. J.E. ten Elshof	University of Twente
Prof. dr. F.M. Mulder	Delft University of Technology
Prof. dr. A.P.M. Kentgens	Radboud University Nijmegen
Dr. S. Karazhanov	Institute for Energy Technology, Norway
Dr. A. Borgschulte	Swiss Federal Laboratories for Materials Science and Technology (EMPA), Switzerland
Prof. dr. A. Schmidt-Ott	Delft University of Technology, reserve member

Other member:

Dr. S. Cornelius	Dresden, Germany

Front cover artwork by: Maryam Sheykhinejad, Tehran
e: m.sheykhinejad@yahoo.com

Printed by: GVO drukkers & vormgevers B. V.

Copyright © 2020 by F. Nafezarefi

ISBN 978-94-6332-602-5

An electronic version of this dissertation is available at http://repository.tudelft.nl/

The doctoral research has been carried out in the Materials for Energy Conversion and Storage (MECS) group, Department of Chemical Engineering, Faculty of Applied Sciences, Delft University of Technology. This work is part of the Open Technology research program with project number 13282, which is (partly) financed by the Netherlands Organisation for Scientific Research (NWO).

Contents

1 Motivation **1**
1.1 Saving energy with smart windows 1
1.2 Outline of this thesis 4
References 6

2 Introduction to rare-earth metals **7**
2.1 Introduction 8
2.2 Rare-earth metal hydrides 11
2.3 Rare-earth metal oxides 17
2.4 Rare-earth metal hydroxides and oxyhdroxides 19
2.5 Rare-earth metal oxyhydrides 19
2.6 Production and environmental impact 21
2.7 Conclusion 23
References 24

3 Introduction to photochromic glasses **27**
3.1 Introduction 28
3.2 Silver halide doped glasses, a classical example 29
3.2.1 Photochromic effect 30
3.2.2 Photo-induced absorption spectra 31
3.2.3 Optical bleaching 34
3.3 Photochromic glasses without silver 40
3.4 Kinetic of the bleaching process 40
3.5 Summary 43
References 45

4 Photochromism in rare-earth metal oxyhydrides general behavior (Y, Er, Dy, Gd) **49**
4.1 Introduction 50
4.2 Experimental 51
4.3 Critical pressure: dihydride to oxyhydride transition 53
4.4 Photochromic effect and change of absorption coefficient 62
4.5 Absence of photochromic effect in YH_3 thin films 66
4.6 Energy threshold 69

4.7 Reproducibility of the photochromic effect and the so-called memory effect 73
4.8 Optical bleaching 74
4.9 Applicability of these materials 76
4.10 Conclusion 78
References 79

5 Effect of the addition of zirconium on the photochromic properties of yttrium oxyhydride 83
5.1 Introduction 84
5.2 Experimental 85
5.3 Results 86
5.3.1 The nature of zirconium in yttrium oxyhydride 86
5.3.2 Effect of the addition of zirconium on yttrium oxyhydride: structural, optical and photochromic properties 93
5.4 Discussion 102
5.5 Conclusion 104
References 105

6 Photochromic Neodymium oxyhydride thin films 107
6.1 Introduction 108
6.2 Experimental methods 109
6.3 Results 110
6.3.1 As-deposited neodymium based thin films 110
6.3.2 Effect of protection layer (ALD) 119
6.3.3 Comparison of photochromic properties of NdO_xH_y and YO_xH_y thin films 126
6.3.4 Stability of ALD coated NdO_xH_y films 128
6.4 Application 128
6.5 Discussion 129
6.6 Conclusion 130
References 132
Appendix 134

7 Electronic nature of yttrium dihydride, oxyhydride and oxide thin films 143
7.1 Introduction 144
7.2 Experimental methods 144
7.2.1 Correction for charging effects 146

7.3 Results 149
7.4 Discussion 158
7.5 Conclusion 159
7.2 References 160

Summary **163**
Samenvatting **167**
Acknowledgments **171**
Curriculum Vitae **175**
List of publications **177**

1

Motivation

1.1 Saving energy with smart windows

Energy is an essential factor for the sustainable development of our industrialized world which highly depends on fossil energy sources. Considering the environmental impacts and the increasing pollution and exploitation of fossil energy resources, the implementation of new energy concepts is essential for our future industrialized society.[1] The sustainability challenges concerning energy saving and environment protection are huge and will require major changes in the way that energy is supplied and consumed.[2] Also the building sector with its high energy consumption needs effective actions to reduce its CO_2 emissions. Buildings account for approximately 40% of the energy consumption and 36% of the CO_2 emissions (in the EU).[3] For residential buildings the majority of the consumed energy is used for internal heating and cooling systems. Approximately 60% of the energy consumed in buildings is lost through windows.[4] By better use of the functionality of a window and making, for instance, so-called smart windows, innovative and energy-efficient buildings can be developed. Smart window technology can offer an efficiency upgrade and promise to contribute to a cost-effective building technology.[5] Smart windows would need to acquire the ability to control the amount of heat and intensity of light that enters the building.[6] Especially reducing the need of cooling would make a contribution to the reduction in the energy usage of buildings.

One well-known class of smart windows are the chromogenic windows.[6] Chromogenic materials are able to change their optical appearance reversibly. There are different types of chromogenic materials including photochromic, thermochromic, gasochromic and electrochromic materials.[7] Electrochromic materials show adjustable optical properties obtained by applying an electrical potential which gives the user the direct control over the desired appearance. One of the most studied electrochromic materials is tungsten oxide (WO_3).[7] Gasochromic materials, on the other hand, change their optical properties under exposure to a certain gas atmosphere. Examples of such materials are SnO_2, MoO_3, and V_2O_5 that show a change of optical properties by interaction with hydrogen gas.[7] Thermochromic materials show a change in optical and electrical transport properties- often in conjunction with a change in crystal structure- as a result of heating and/or cooling.[7] The structural change affects the transmittance of ultraviolet and/or infrared radiation. The most commonly used and studied metal oxide materials with thermochromic properties are vanadium oxide and titanium oxide.[7] Finally, photochromic materials exhibit a reversible transformation between two optical states, namely bleached, transparent state and darkened state upon exposure to electromagnetic radiation (usually UV light).[7]

Illumination of a photochromic material with light of sufficient energy results in the formation of a darkened state. This leads to a reduction in transmittance and an increase in absorbance (Figure 1.1).[8] As soon as we stop the excitation, the material returns to its original state.[8]

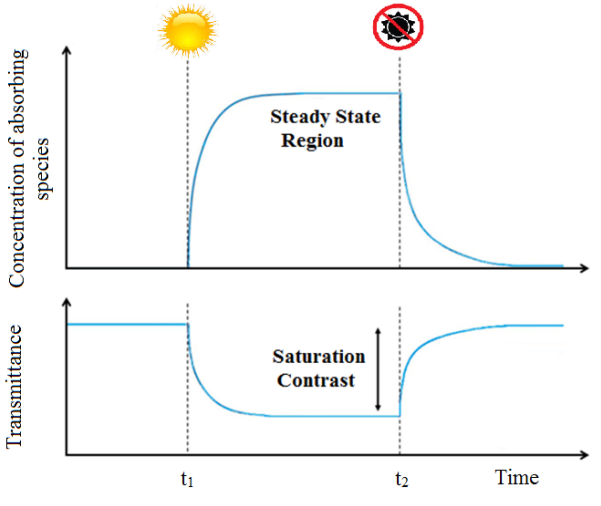

Figure 1.1. Response of a photochromic system when exposed to radiation (picture modified from reference [8]).

The emphasis of the research presented in this thesis is on photochromic materials for smart windows. Photochromic smart windows consist of window glass coated with a thin-film material that changes its property when exposed to sunlight. In this way, less light is transmitted into the building on a sunny day under intense sunlight which reduces the need for artificial lighting and air conditioning. Undeniably, the largest group of photochromic materials discovered are based on organic compounds.[9-11] However, they show fatigue upon extended exposure to sunlight due to limited stability vs. oxygen, humidity, and heat, as well as ultra-violet (UV).[9] On the other hand, inorganic photochromic materials are intrinsically more stable and they offer wider range of spectral sensitivity. An early application of these materials can be found in silver halide doped glasses where the photochromic effect is based on the reversible formation of plasmonic nanoparticles.[12, 13]

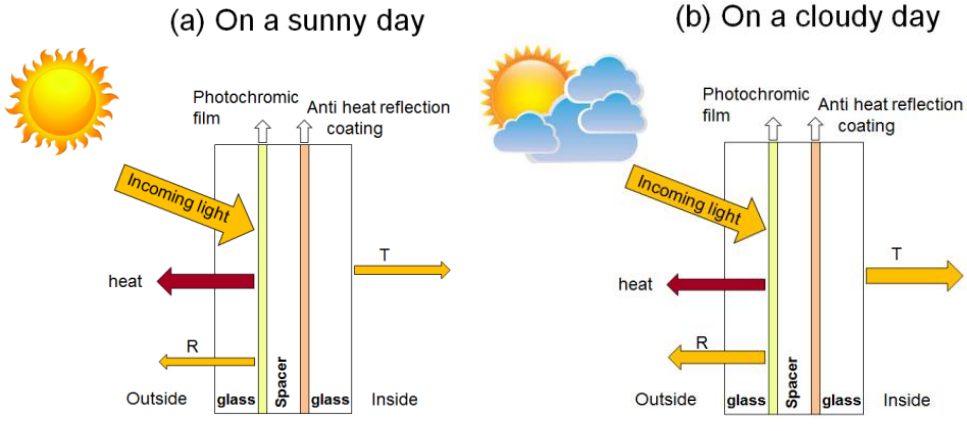

Figure 1.2. Operational principles of a double glazed smart window with use of photochromic thin film (a) On a cloudy day (b) On a sunny day. Sunlight result in a darkening of the photochromic film and consequently less amount of light enters the building. The absorption of the film increases upon darkening and in order to block the reflected heat back into building, an anti-heat reflection coating is required.

Figure 1.1 shows the working principle of a smart double glazed photochromic window. On a sunny day, the UV light present in the sunlight spectrum will darken the window. The UV light is blocked, the transmittance and reflectance drops, the absorption will increase. Consequently, less light enters the building. In order to avoid the heat radiating from the darkened window entering the building, an anti-heat reflection coating is required. As a result the temperature inside the building will not fluctuate and less energy is needed for air conditioning and reduce the need for

artificial lighting. On a cloudy day, there is less UV light available. Therefore, a larger fraction of the incident sunlight will enter the building in comparison to a sunny day.

A remarkable photochromic effect was observed in yttium-oxy-hydride (YO_xH_y) thin films at ambient conditions which were synthesised by reactive sputtering.[14] This semiconducting material show a strong photochromic response upon illumination with photons above its band gap (Eg ≈ 2.6 eV).[14,15] Window glass blocks most of UV radiation while allowing transmission of visible light into the interior.[16] Since YO_xH_y has a band gap of around 2.6 eV, the photo-darkening can take place using not only UV but also blue light. Such a property makes this material promising for application in smart windows where photo-darkening may take place behind the glass window. The main aim of this thesis is to investigate the behaviour of this new class of photochromic materials, in order to provide the stepping stones for a better insight in the properties of these materials and thereby improve their properties. In the course of our investigation based on chemical composition analysis by a combination of Rutherford backscattering, the rare-earth oxyhydrides are found in a wide composition range along the REH_3-RE_2O_3 line in a ternary RE−O−H composition-phase diagram.[17] In this ternary phase diagram the rare-earth oxyhydrides are described by the general formula of REO_xH_{3-2x} where $0.5 \leq x \leq 1.5$.[17] Nevertheless, for the sake of simplicity in this thesis, the rare-earth oxyhydrides are mostly describe by the general formula of REO_xH_y.

1.2 Outline of this thesis

This thesis is structured as follows:

Chapter 2 provides a literature overview of rare-earth metals, hydrides, oxides, hydroxides, oxyhydroxides and oxyhydrides. It describes their chemistry, physics and characteristic properties.

Chapter 3 provides an overview of the properties of a well-known inorganic photochromic material, namely silver halide crystals trapped in a glass matrix. This material provides a basic insight in photochromism which helps us to explore this effect in YO_xH_y.

In **Chapter 4**, we clarify that the transparent and photochromic YO_xH_y thin film is in fact formed by air oxidation of as-deposited, metallic $YH_{1.9+\delta}$ thin films. These films are made by direct current reactive magnetron sputtering of an yttrium target in an Ar/H_2 reactive gas mixture. Similary, dihydride films of Er, Dy and Gd turn into

photochromic oxyhydride films on air exposure. We find that the photon energy required to obtain a photochromic effect is given by the optical band gap of the material. The photochromic contrast of the rare-earth oxyhydrides extend over a very wide spectral range (from the optical band gap to way beyond 2 micron), which implies that they modulate both visible as well as near-infrared light. We predict the oxyhydrides of the remaining rare-earths (incl. Sc)[17] to be also photochromic.

In **Chapter 5,** we set to investigate the role of point defect mobility. Inspired by the photochromic effect in silver halide doped silicate glasses, we proposed that the mobility of point defects is an essential ingredient in photochromic YO_yH_x. To verify this hypothesis we probed the effect of lattice contraction in YO_yH_x as induced by the addition of zirconium. We find that upon adding Zr to YO_xH_y, the fcc lattice is compressed, while the bleaching speed is decreased. We conclude that these changes are due to a change in the properties of the YO_xH_y matrix as we did not detect any photochromism in films where Zr is the only cation. The interpretation of these findings is however not straightforward, since we cannot exclude Zr to enter the YO_yH_x lattice.

In **Chapter 6** we report on the photochromic properties of neodynium oxyhydride (NdO_xH_y). We establish that the photochromic response strongly depends on the deposition conditions. We demonstrate the possibility of making rare-earth oxyhydride films with tunable photochromic properties by means of the deposition conditions, which affects the microstructure and composition of the films.

In **Chapter 7** With the use X-ray photoelectron spectroscopy (XPS) depth profiling with Ar etching we investigate the electronic structure differences between yttrium oxide, yttrium dihydride and yttrium oxyhydride thin films. We find that in yttrium oxide thin films, yttrium ions are in their highest oxidation state (Y^{3+}). Yttrium dihydride films demonstrate two distinct contributions of Y^{+2} and Y^{+3}(in minority) Yttrium oxyhydride film demonstrates the presence of Y^{+3} as a major component with a small presence of Y^{+2} which increases slightly upon illumination. This hints towards the formation and growth of metallic YH_2 nano-clusters in the YO_xH_y matrix upon illumination.

The thesis is concluded by a short summary.

References

[1] A. Heshmati, S. Abolhosseini, and J. Altmann, "Alternative Renewable Energy Production Technologies," in *The Development of Renewable Energy Sources and its Significance for the Environment*, ed Singapore: Springer Singapore, 2015, pp. 31-64.

[2] A. Allouhi, Y. El Fouih, T. Kousksou, A. Jamil, Y. Zeraouli, and Y. Mourad, "Energy consumption and efficiency in buildings: current status and future trends," *Journal of Cleaner Production,* vol. 109, pp. 118-130, 2015.

[3] "European Commission, "Energy performance of buildings", available from: https://ec.europa.eu/energy/en/topics/energy-efficiency/energy-performance-of-buildings, retrieved on 22-07-2019."

[4] A. Gustavsen, B. Jelle, D. Arasteh, and C. Kohler, *State-of-the-Art Highly Insulating Window Frames - Research and Market Review*, 2007.

[5] Y. Wang, E. L. Runnerstrom, and D. J. Milliron, "Switchable Materials for Smart Windows," *Annual Review of Chemical and Biomolecular Engineering,* vol. 7, pp. 283-304, 2016.

[6] D. M. Addington and D. L. Schodek, "Smart materials and new technologies : for the architecture and design professions," ed. Amsterdam ;: Architectural Press, 2005.

[7] A. P. Daniela Nunes, Lidia Santos, Pedro Barquinha, Luis Pereira, Elvira Fortunato, Rodrigo Martins,, "Chromogenic applications," in *Metal Oxide Nanostructures*, A. P. Daniela Nunes, Lidia Santos, Pedro Barquinha, Luis Pereira, Elvira Fortunato, Rodrigo Martins, Ed., ed: Elsevier, 2019, pp. 103-147.

[8] G. H. Brown, "Introduction," in *Photochromism: Techniques of chemistry, vol. III*, G. H. Brown, Ed., ed New York Wiley-Interscience, 1971.

[9] R. Pardo, M. Zayat, and D. Levy, "Photochromic organic-inorganic hybrid materials," *Chem Soc Rev,* vol. 40, pp. 672-87, Feb 2011.

[10] K. Sasaki and T. Nagamura, "Ultrafast all-optical switch using complex refractive index changes of thin films containing photochromic dye," *Applied physics letters,* vol. 71, pp. 434-436, 1997.

[11] H. Tian and S. Yang, "Recent progresses on diarylethene based photochromic switches," *Chem Soc Rev,* vol. 33, pp. 85-97, Feb 20 2004.

[12] R. J. Araujo, "Photochromism in glasses containing silver halides," *Contemporary Physics,* vol. 21, pp. 77-84, 1980/01/01 1980.

[13] G. P. Smith, "Photochromic glasses: properties and applications," *Journal of Materials Science,* vol. 2, pp. 139-152, 1967.

[14] T. Mongstad, C. Platzer-Bjorkman, J. P. Maehlen, L. P. A. Mooij, Y. Pivak, B. Dam*, et al.*, "A new thin film photochromic material: Oxygen-containing yttrium hydride," *Solar Energy Materials and Solar Cells,* vol. 95, pp. 3596-3599, Dec 2011.

[15] T. Mongstad, C. Platzer-Bjorkman, S. Z. Karazhanov, A. Holt, J. P. Maehlen, and B. C. Hauback, "Transparent yttrium hydride thin films prepared by reactive sputtering," *Journal of Alloys and Compounds,* vol. 509, pp. S812-S816, Sep 2011.

[16] I. Duarte, A. Rotter, A. Malvestiti, and M. Silva, "The role of glass as a barrier against the transmission of ultraviolet radiation: an experimental study," *Photodermatology, Photoimmunology & Photomedicine,* vol. 25, pp. 181-184, 2009.

[17] S. Cornelius, G. Colombi, F. Nafezarefi, H. Schreuders, R. Heller, F. Munnik*, et al.*, "Oxyhydride nature of rare-earth-based photochromic thin films," *The journal of physical chemistry letters,* vol. 10, pp. 1342-1348, 2019.

2

Introduction to rare-earth metals

This chapter provides an introduction to rare-earth metals, and their hydrides, oxides, hydroxides, oxyhydroxides and oxyhydrides summarizing their structural and physical properties. Rare-earth elements are used in several high technology industrial products. New applications are expected to continue to be discovered and developed. Therefore the strong demand for these elements is anticipated to grow. China is likely to remain the world's main rare-earth supplier because of large resources, competitive prices, low-cost wages, and minimal environmental and permitting requirements. If the world community wishes to establish a green energy environment, there is a strong need for a global agreement and international policies on the rare-earth materials.

This chapter is partially based on:
E. F. E. ten Have, Investigation of the photochromic properties of dysprosium oxyhydride, Delft university of Technology, MSc thesis, 2016.[1]

2.1 Introduction

The term "rare earth metals" is usually applied to the group of 17, strongly related, heavy elements that comprise of scandium (Sc), yttrium (Y) and the lanthanide group.[2] Sc and Y are included in this group as they have ionic radii similar to lighter f-block elements and their chemical behaviour and properties are very similar to lanthanides.[2] In Figure 2.1, they are outlined in the periodic system of the elements. Despite what their name suggests rare-earth elements are abundant in the earth's crust.[3] For example, Yttrium is the 27th most abundant element found on earth.[4] The name yttrium, was given because the black mineral was first discovered in the village of Ytterby in Sweden.[2] The rare-earth elements were first isolated in the 18th and 19th century as oxides from rare minerals. An oxide of an element was known as the "terre" of that element in French or "Erde" of that element in German, which were major scientific languages in 19th century.[2] The translation to English is earth. That is why they are called rare earth elements.[2]

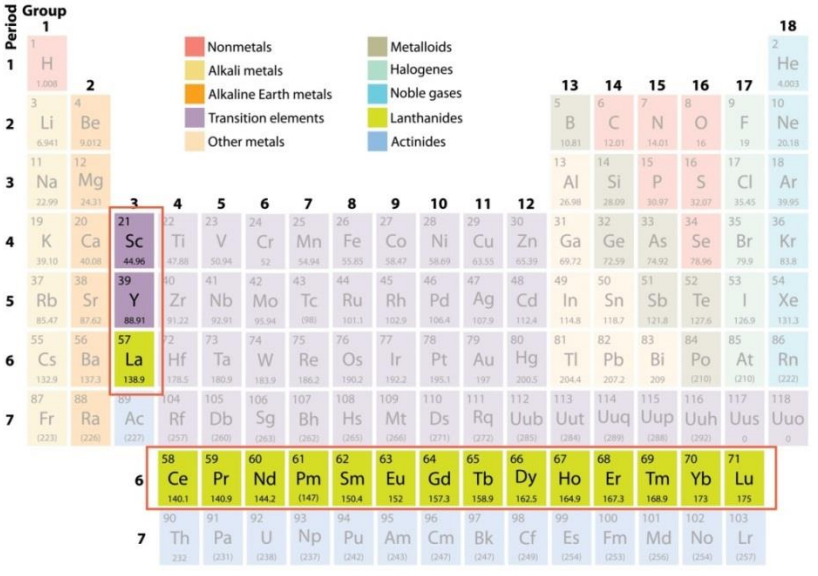

Figure 2.1. The periodic system of the elements. Scandium, yttrium and lanthanides are outlined together forming the rare-earth metals group (picture reused from the reference [5]).

Figure 2.2 shows the abundance of various metal elements in comparison to rare earth metals. Separation of individual rare-earth elements was initially a difficult challenge for chemists because of their chemical and physical similarities and high reactivity.[6] It was not until 20th century that efficient separation processes were developed.[6] The

rare-earth elements are classified into two categories: the light rare-earth elements also known as the cerium group which starts from lanthanum till europium, and the heavy rare-earth elements consisting of the elements from gadolinium till lutetium.[3]

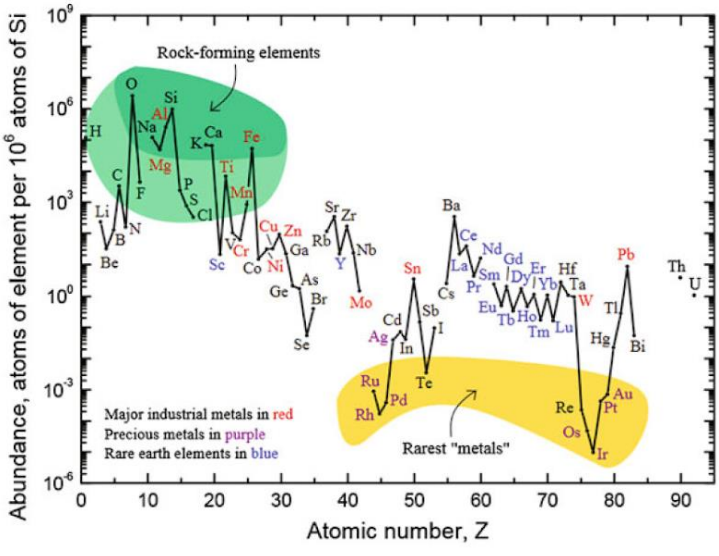

Figure 2.2. The abundance of the elements given in atom fraction as a function of the atomic number (picture reused from the reference [2]).

The characteristic nature of rare-earth elements is due to their electronic structure. There is no 4f electron in scandium, yttrium and Lanthanum. They have the valance electron configuration of ns^2 $(n-1)d^1$. The 14 elements from Cerium to Lutetium have valence electronic configuration represented by of $6s^2 5d^1$ $4f^{n-1}$ or $6s^2$ $4f^n$.[7] The explanation for two typical electronic configurations is that in neutral atoms, the 5d and 4f electrons have similar energies.[7]

The elements in the first row of the f-block exhibit a decrease in atomic radius from lanthanum, Z=57 to lutetium, Z=71. The term lanthanide contraction is used for this phenomenon caused by imperfect shielding of 4f electrons.[8] As the atomic number increases, the attraction between the nucleus and outmost orbital electron increases gradually. This causes neighboring lanthanides to have similar but not identical properties.[8] Figure 2.3a shows a clear trend of change in ionic radius with increasing the atomic number of the rare-earth elements. The differences in ionic radius, atomic volume and lattice parameters of the unit cell for a selection of rare-earth metals relevant in our work are listed in Table 2.1. The table shows that most rare-earth metals have a hexagonal close packed (hcp) crystal structure at room temperature.[9]

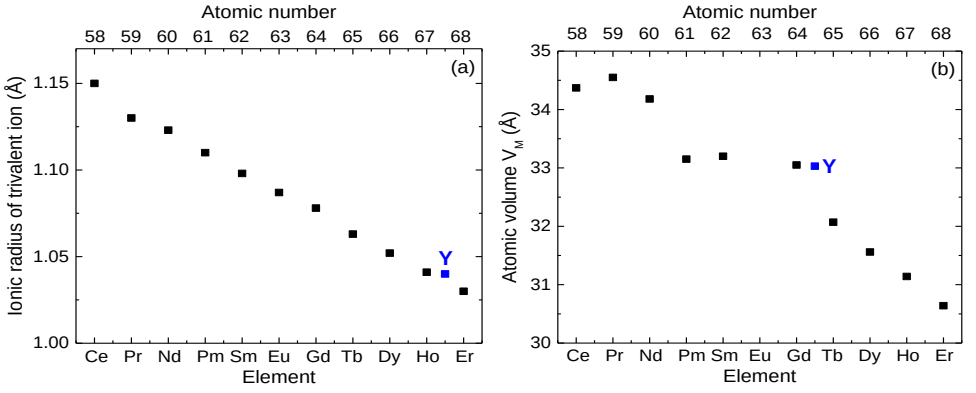

Figure 2.3. (a) Ionic radius of the rare earth elements versus atomic number. In terms of ionic radius, yttrium falls under the group of heavy rare earth elements.[10] (b) The calculated atomic volume of rare earth metals as a function of atomic number.[11,12]

Table 2.1. Differences in ionic radius, atomic volume and lattice parameters of the unit cell of the rare earth metals.

Element	**Atomic number**	**Crystal Ionic radius of trivalent ion (Å)** [10]	**Crystal structure at RT** [11,12]	**Crystal parameter at RT** [11,12]		**V_A (Å^3/metal atom)** [11,12]
				a (Å)	**c (Å)**	
Y	39	1.040	hcp	3.6482	5.7318	33.03
Ce	58	1.15	fcc	5.6167	-	34.37
Pr	59	1.13	wurtzite	3.6721	11.8326	34.55
Nd	60	1.123	wurtzite	3.6582	11.7966	34.18
Pm	61	1.11	wurtzite	3.65	11.65	33.15
Sm	62	1.098	rhombohedral	3.6229	26.207	33.11
Eu	63	1.087	bcc	4.5827	-	48.12
Gd	64	1.078	hcp	3.6336	5.7810	33.05
Tb	65	1.063	hcp	3.6055	5.6966	32.07
Dy	66	1.052	hcp	3.5915	5.6501	31.56
Ho	67	1.041	hcp	3.5778	5.6178	31.14
Er	68	1.030	hcp	3.5592	5.5850	30.64

Praseodymium and neodymium have a wurtzite structure. The wurtzite has a hexagonal packing structure with stacking sequence of ABAC instead of a simple AB sequence of the hcp structure.[9] Cerium is the only rare-earth metal that forms a face-centred cubic structure.[9] The atomic volume of each rare-earth is calculated from the number of metal atoms per unit cell and the unit cell volume. The change of unit cell

volume on hydrogenation is not as smooth the ionic radius, probably due to different stackings achieved in the various crystal structures (Figure 2.3b).

2.2 Rare-earth metal hydrides

Because of their similarities, the rare-earth metals are expected to have similar hydrogenation characteristics.[9] All rare-earth metals form dihydrides that have a fluorite-type structure and can easily take up more hydrogen to form trihydrides,[9] except for europium and ytterbium that only form orthorhombic dihydrides. The phase diagram of the rare-earth-hydrogen systems shows of various phases depending on the hydrogen concentration. A schematic phase diagram for rare-earth hydrogen system is displayed in Figure 2.4.

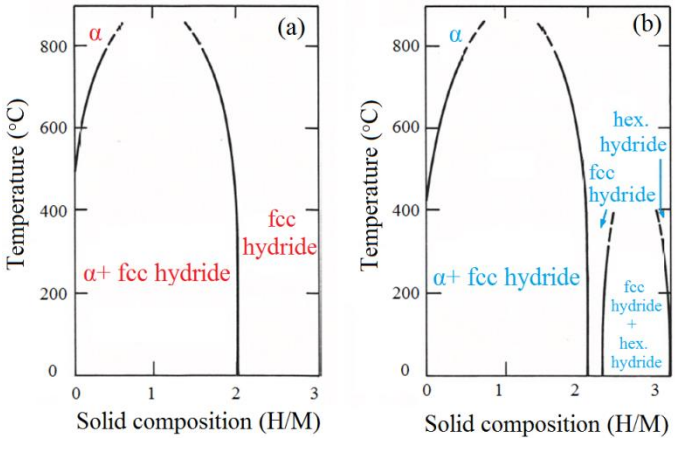

Figure 2.4. Schematic phase diagram of the rare-earth-hydrogen system (a) light rare-earth elements La, Ce, Pr and Nd (b) heavy rare-earth elements Sm, Gd, Dy, Er, Tb, Ho, Tm and Lu.[9]

A distinction can be made between light rare-earth (Figure 2.4a) and the heavy rare-earth elements (Figure 2.4b). Various phases are formed and the actual positions of the phase boundaries depend on the particular metal-hydrogen system involved and temperature.[9] At low concentrations, a metallic, solid solution α-phase is formed. At higher H/RE ratios, a metallic β-phase with the fcc structure is formed where hydrogen atoms situated in the tetrahedral sites. This ideal structure corresponds to MH_2. However, small deviations from stoichiometry are observed due to hydrogen vacancies or interstitial hydrogen atoms in the octahedral site.[13] The light rare-earth metals form a trihydride without having to change their structure, by filling the octahedral sites with hydrogen.[9] However, heavy rare-earth metals form an insulating

trihydride γ-phase with an hcp structure, where hydrogen occupies the octahedral and tetrahedral sites. This transformation occurs before the composition MH_3 is reached.[9] Room temperature solubility ranges of the rare-earth hydrides are summarized in Table 2.2. More details about each phase is explained in the following sections.

Table 2.2. Estimated solubility ranges for rare-earth hydrides.[13]

Group I	Group II		Group III
Fluorite	Fluorite	Hexagonal	Orthorhombic
$LaH_{1.95-3}$	$YH_{1.9-2.23}$	$YH_{2.77-3}$	$EuH_{1.86-2}$
$CeH_{1.8-3}$	$SmH_{1.92-2.55}$	$SmH_{2.59-3}$	$YbH_{1.80-2}$
$PrH_{1.9-3}$	$GdH_{1.8-2.3}$	$GdH_{2.85-3}$	
$NdH_{1.9-3}$	$TbH_{1.9-2.15}$	$TbH_{2.81-3}$	
	$DyH_{1.95-2.08}$	$DyH_{2.86-3}$	
	$ErH_{1.86-2.13}$	$ErH_{2.97-3}$	
	$TmH_{1.99-2.41}$	$TmH_{2.76-3}$	
	$LuH_{1.85-2.23}$	$LuH_{2.78-3}$	

a-phase

The α-phase is a solid solution where the hydrogen atoms are distributed in tetrahedral sites of the metal lattice and behave as impurity scattering centers.[14] In Table 2.3, the lattice parameters in the α-phase for various hydrogen concentrations, x, at various temperatures are listed together with their atomic volume. Table 2.4 shows available data for the expansion coefficient in the two lattice directions.[14]

Table 2.3. The crystallographic parameters, existence range and atomic volume of the of α-phase rare-earth metals.[14] Note that the missing data was not available in literature.

Phase	Rare-Earth Element	x (REH_x)	Tempe-rature (K)	Lattice parameter		V_A (Å^3/metal atom)
				a (Å)	c (Å)	
α-phase hexagonal close packed	Y	0.12-0.22	300	3.6542-3.6637	5.7654-5.794	33.34-33.67
	Dy	0.2	675	3.6269	5.7255	32.61
	Ho	0.2	645	3.6087	5.6985	32.13
	Er	0.27	775	3.6035	5.7	32.05
	Ce	0-1.8				34.37
α-phase other structures	Pr	0-1.9				34.54
	Nd	0-1.9				34.18

Table 2.4. Expansion upon insertion of hydrogen and enthalpy of solution of hydrogen for some rare earth hydrides.[14] Note that the missing data was not available in literature.

Phase	Rare-Earth Element	Expansion coefficient upon insertion of H (static)	
		$\Delta a/(a\Delta x)$ (10^{-4}/at%)	**$\Delta c/(c\Delta x)$ (10^{-4}/at%)**
	Y	1.37-1.93	4.59-4.76
α-phase hexagonal close packed	Dy	4.15	3.21
	Er	3.63	3.87
	Gd		

β-phase

Upon further hydrogenation, a phase transition occurs and the β-phase rare-earth hydride is formed.[14] This REH_2 phase ideally comprises of an fcc lattice with two hydrogen per unit cell occupying the tetrahedral sites. This transformation from hcp to fcc is accompanied by a shift in the stacking of atomic planes along the hcp c-axis.[14] Table 2.5 shows the lattice parameter and calculated atomic volume of β-phase for the ranges of atomic ratio H/RE. The presence of hydrogen has significant effects on the band structure of the metal. The introduced hydrogens induce states below the d (or f) band.[15] Taking Y as an example, the 1*s* hydrogen bands hybridize with the Y 4*d*5*s* band leading to two bands below the Fermi level, each containing two electrons. The remaining electron in the conduction band is responsible for the metallic character of the REH_2 compounds. When hydrogen starts to move into the yttrium film first the resistivity slightly increases due to impurity scattering but then it decreases considerably until the β-phase is reached. In this phase the resistivity is minimal which shows that YH_2 is a better conductor than pure yttrium. The main reason for the increased electrical conductivity is the reduced electron phonon coupling.[16]

Table 2.5. Expansion upon insertion of hydrogen and enthalpy of solution of hydrogen for some rare-earth hydrides. Note that x does not quantify the existence range of the β-phase but only reflects the data for which lattice parameters are known.[14] Note that the missing data was not available in literature.

Phase	Rare-Earth Element	x (REH_x)	Lattice parameter a (Å)	Expansion coefficient $\Delta a/(a\Delta x)$ (10^{-4}/at%)	V_A (Å^3/metal atom)
	Y	2-2.1	5.2082- 5.2056	-0.5	35.32-35.27
β-phase at RT	Ce	2-2.9	5.581- 5.5364	-1.8	43.46-42.43
	Pr	2-2.47	5.518- 5.483	-1.35	42.0-41.21
	Nd	2-2.47	5.4689- 5.430	-1.4	40.89-40.03
	Gd	2-2.25	5.3022- 5.2926		37.06-37.06
	Dy	2-2.27	5.206- 5.1988	-0.5	35.27-35.13
	Ho	2	5.165	-0.5	34.45
	Er	2	5.129		33.73

γ-phase

Increasing the hydrogen content above the limit of the β–phase, which occurs at x=2.1 for Y, leads to a growing volume fraction of the hexagonal γ–phase for most rare-earth metals (except Sc, La, Pr, Nd). This phase is semi-conducting and accordingly the thin RE-films show a reversible switchable mirror effect.[17] The unit cell and atomic volume of the γ–phase for a range of rare-earth metals in our studies is presented in Table 2.6.

Table 2.6. The lattice parameter and calculated atomic volume for the given atomic ratios H/Re (x) in the γ-phase of the rare-earth hydrides. Note that x does not quantify the existence range of the γ-phase and only the data for which lattice parameters are known.[14]

Phase	Rare-Earth Element	x (REH_x)	Lattice parameter		V_A (Å^3/metal atom)
			a (Å)	c (Å)	
γ-phase Hexagonal close packed	Y	3	3.675	6.657	38.93
	Gd	2.91-3	3.73-3.76	6.71-6.705	40.42-41.05
	Dy	>2.9	3.7	6.658	39.47
	Ho	>2.9	3.642	6.56	37.68
	Er	>2.9	3.621	6.526	37.05

Expansion in atomic volume

Upon hydrogen insertion the atomic volume expands to accommodate this change in lattice content. The change in atomic volume ($\Delta V_{A,\,0\rightarrow 2}$) going from rare-earth metal to metal dihydride (when x=2) can be calculated from the equations below.

$$\Delta V_{A,0\rightarrow 2} = \frac{[(V_A(x{=}2) - V_A(x{=}0)]}{V_A(x{=}0)} \tag{2-1}$$

Similarly, the change in atomic volume ($\Delta V_{A,\,0\rightarrow 3}$) going from rare-earth metal to metal trihydride (when x=3) can be calculated from:

$$\Delta V_{A,0\rightarrow 3} = \frac{[(V_A(x{=}3) - V_A(x{=}0)]}{V_A(x{=}0)} \tag{2-2}$$

Figure 2.5 shows the expansion in atomic volume calculated from equation 2-1, 2-2. The atomic volume expansion when going from metal to metal dihydride decreases when the atomic number of rare-earth element increases. The expansion in atomic volume is increased upon insertion of hydrogen to obtain the trihydride. The calculated volume expansion difference going from dihydride to trihydride is around 10%. This is in agreement with experimental findings reported by Kerssemakers et. al.[18] The expansion is out of plane along the fcc [111] direction in the dihydride or equivalently in [0001] direction in the hexagonal trihydride.[18] The change in distance between atoms going from metal to dihydride and trihydride can be observed in Figure 2.6.

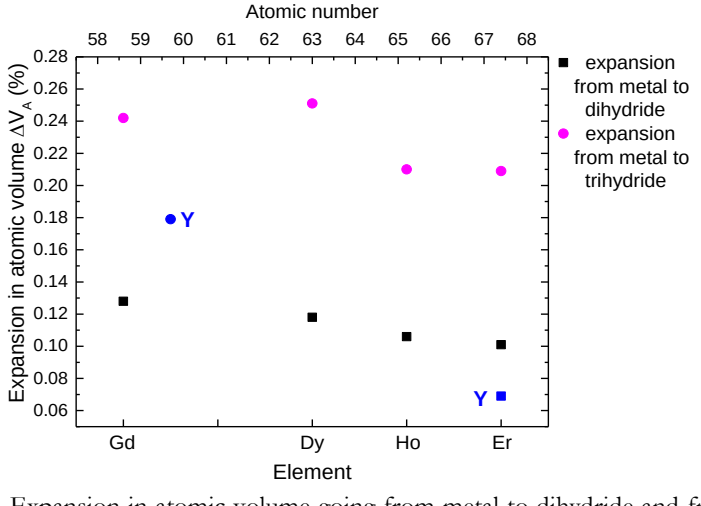

Figure 2.5. Expansion in atomic volume going from metal to dihydride and from metal to trihydtide using the equation 1, 2 and 3.

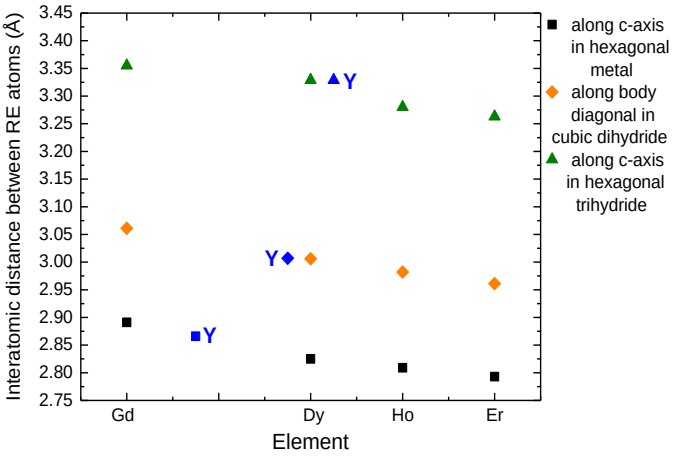

Figure 2.6. Comparison of interatomic distance between rare-earth atoms along the c-axis in hcp metal structure, along the body diagonal of cubic dihydride structure and along the c-axis of the hcp trihydride structure.

Thermodynamics

The rare-earths (including Y and Sc) have a strong affinity for hydrogen. They easily react with hydrogen to form dihydrides and when the hydrogen pressure is high enough they form a trihydride.[13] The thermodynamic properties of the rare-earth hydrides are usually obtained from the measurement of the hydrogen pressure in equilibrium with the metal hydride as a function of temperature.[13] The formation enthalpy of these hydrides (ΔH_f) determines the amount of heat which is released during hydrogen absorption and consequently is to be supplied again in case of desorption. The more thermodynamically stable the hydride, the larger ΔH_f, and the higher temperature is needed in order to desorb hydrogen (reverse reaction) and vice versa. From the definition of the equilibrium constant we know that $-RT \ln K = \Delta G°$, where $\Delta G°$ is the change in standard Gibbs free energy upon hydrogenation.[13] Inserting the $\Delta G° = \Delta H° - T\Delta S°$ into the equation considering $K = {}^{1}/_{P_{H2}}$ yields equation 2-4.

$$\ln P_{H_2} = (\Delta H_f/RT) - (\Delta S_f/R) \qquad (2\text{-}4)$$

Where ΔH_f and ΔS_f are the enthalpy and entropy of formation of the dihydride respectively.[13] The enthalpy of formation for trihydride can be obtained from adding the enthalpy of dihydride formation and the enthalpy of dihydride to trihydride transformation.[13,14] The exceptions are Ce, Pr and Nd where the enthalpy of trihydride formation can be calculated the same way as the enthalpy of the dihydride

formation because they have no cubic to hexagonal transformation. The enthalpy of formation of the dihydride and trihydride phase for some rare-earth metals are plotted in Figure 2.7.

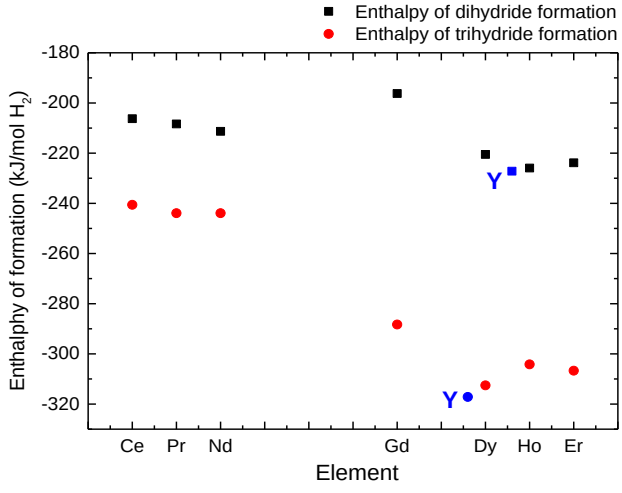

Figure 2.7. Enthalpy of formation rare-earth dihydride and trihydride.[13,14]

2.3 Rare-earth metal oxides

The composition of the rare-earth oxides depends on the temperature, oxygen activity and whether it is in equilibrium or in a metastable equilibrium.[19] Most rare-earth metals form stable sesquioxides with the exception of Ce, Pr and Tb. While for the sesquioxides the trivalent ground-state configuration is found to be the most favourable, Ce, Pr and Tb have the tetravalent configuration in their dioxide form.[20] Ce metal oxidizes completely to CeO_2 in the presence of air. Pr occurs naturally as Pr_6O_{11} and forms a stoichiometric fluorite structure PrO_2 under positive oxygen pressure.[20] The rare-earth sesquioxide crystallize in three forms, A-type(hexagonal), B-type(monoclinic) and C-type(cubic) structures.[20] At low temperatures, the phase formed for almost all the rare-earth sesquioxides is the C-type structure. [21] The C-type sesquioxides has space group $1a\bar{3}$ and is isostructural to the mineral bixbyite $(Fe,Mn)_2O_3$.[19,21] It can be imagined as distorted fluorite cell with two vacancies paired along the body diagonal of the anion cube (Figure 2.8). The unit cell is eight times that of a fluorite unit cell due to a doubling of the fluorite lattice constant.[19,21] 64 rare-earth cations are found in each unit cell. The metal atoms are arranged in a distorted fcc sub-lattice with only ¾ of the tetrahedral sites occupied by anions.[21] All metals have an octahedral anion coordination.[19] Table 2.7 lists the rare-earth crystal structures and lattice parameters together with their atomic volume. In Figure 2.9 the

enthalpy of formation of rare-earth oxides are plotted. Yttrium shows the lowest enthalpy of formation among all rare-earth oxides.

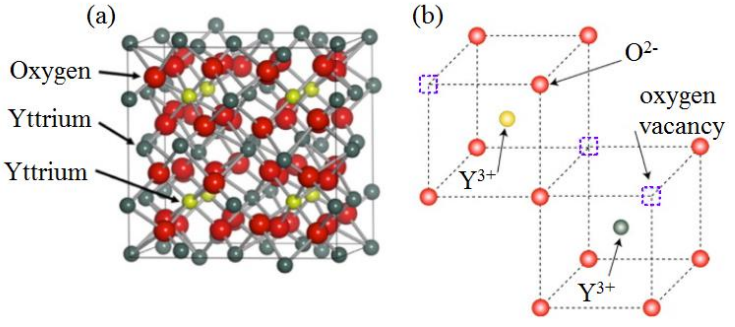

Figure 2.8. Schematic representation of the cubic bixibyite oxide structure (a) the bixbyite unit cell of Y_2O_3 (b) Two non-equivalent Y-sites surrounded by neightbouring O atoms (the actual position of the O atoms is slightly shifted from the corners of the cubes). The small squares are structural oxygen vacancies.[22]

Table 2.7. Lattice parameter and the atomic volume of C-type rare-earth oxides (RE_2O_3).[19,23]

Compound	Lattice parameter a (Å) [19, 23]	V_A (Å³/metal atom)
Y_2O_3	10.6	18.61
Nd_2O_3	11.08	21.25
Gd_2O_3	10.8122	19.75
Dy_2O_3	10.6647	18.95
Ho_2O_3	10.6065	18.64
Er_2O_3	10.5473	18.33

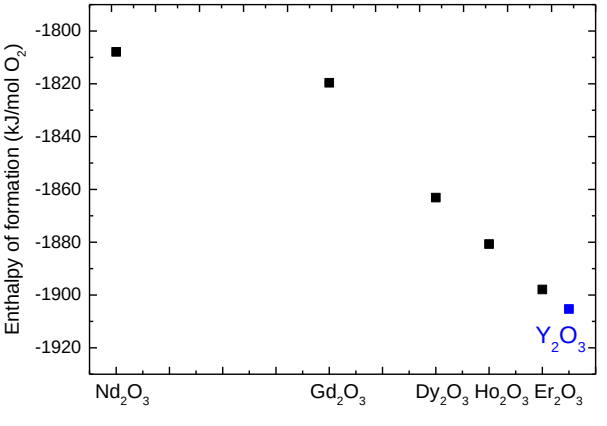

Figure 2.9. The rare earth oxide enthalpies of formation.[12]

2.4 Rare-earth hydroxides and oxyhydroxides

Two well characterized phases have been reported as a result of reaction of rare-earth sesquioxides with water: rare-earth hydroxide $RE(OH)_3$ or the rare-earth oxyhydroxide REO(OH). All the rare-earth hydroxides show a hexagonal UCl3-type structure with space group $P6_3/m$.[21] Formation of the hydroxide phase is less probable going from light to heavy rare earth elements. When establishing the phase diagram for the binary Ln_2O_3-H_2O system, also the oxyhydroxide phase was identified. The oxyhydroxide phase, was an intermediate phase found in the decomposition of hydroxides under hydrothermal conditions.[21]

2.5 Rare-earth oxyhydrides

Recently, yttrium oxy-hydride was identified as the oxygen-containing yttrium hydride in which Mongstad et al. discovered photochromism.[24,25] Our follow up study showed that the transparent photochromic YO_xH_y is in fact formed by air oxidation of as-deposited β-YH_2 films.[26] In order to understand and evaluate the properties of the newly discovered material, Cornelius et al.[27] established a ternary RE-O-H composition phase diagram (Figure 2.10). This was done by a combination of Rutherford backscattering (RBS) and elastic recoil detection (ERD). The rare-earth oxyhydrides exist in a wide composition range described by the formula $RE^{3+}O_x^{2-}H_{3x-2}^{-}$ where $0.5 \leq x \leq 1.5$ along the MH_3-M_2O_3 line indicated by the grey area in Figure 2.10 (the exact composition boundaries are still unknown).[27] The rare-earth oxyhydrides can be clearly distinguished from the rare-earth hydroxides described by the formula $RE^{3+}O_x^{2-}H_{2x-3}^{+}$ where $1.5 \leq x \leq 3$ along the H_2O-M_2O_3 line and do not show any photochromic properties.[27] A generalized structural model proposed for rare-earth oxyhydride is based on the fcc ($Fm\bar{3}m$) structure in which the 4 lattice sites are occupied by RE cations. The various compositions are obtained by a change in the occupation of the tetrahedral and octahedral interstices.

Remarkably, the RE-oxyhydrides were identified in powders several decades ago.[28] In 2016, Kobayashi et. al. reported the hydride ion (H^-) conductivity in the $La_{2-x-y}Sr_{x+y}Li_{1-x}HO_{3-y}$ system[29] suggesting that oxyhydrides may in general be promising materials for energy storage and conversion applications.[29] Recently RE-oxyhydrides received renewed attention as solid state H⁻electrolytes as hydride (H^-) conductivity is shown in LnHO oxyhydrides, in which anionic ordering is observed depending on the lanthanide size.[30] The enlarged hydride pathway as a result of the anion ordering is a

key parameter for the hydride conduction based on the indirect interstitial mechanism.[30]

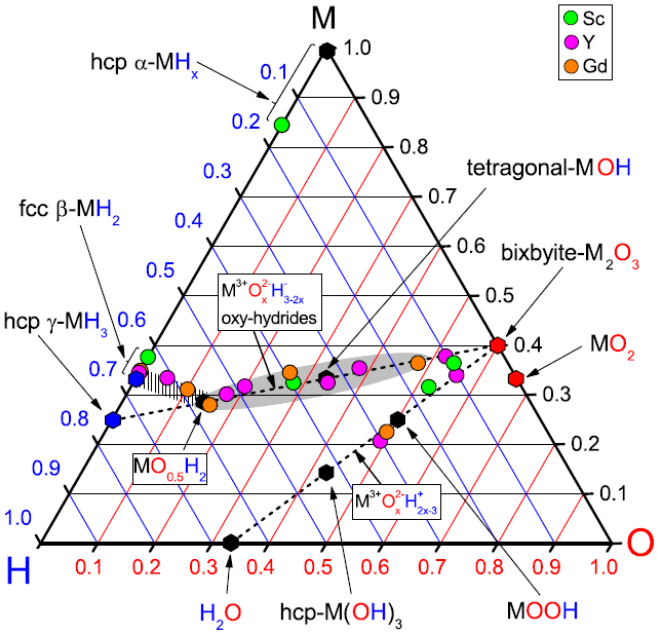

Figure 2.10. Ternary M-O-H chemical composition and phase diagram where M = Sc, Y, Gd. Compositions with the same charge state of both cations and anions are indicated with the black dashed lines. The coloured circles show the chemical compositions of MO_xH_y thin films obtained from ion beam analysis. The uncertainty in the composition is given by the diameter of the data points which corresponds to ± 1 atom %. The highlighted grey area indicates the composition region in which photochromism is observed.[27]

2.6 Production and environmental impact

As discussed earlier, the term 'rare-earths' is misleading, as it does not refer to their abundance in the earth's crust, but to the inconspicuous appearance of the minerals from which they were originally isolated.[31] Despite the amount and wide variety of resources around the globe, China became the world's dominant producer of rare earth metals starting in the 90s offering low prices, making others throughout the world unable to compete.[32] The global production of rare-earth elements over a period of 1983 to 2003 is depicted in Figure 2.11.[6] Currently China with one-third of world's rare-earth reserves, is still the world leader in rare-earth elements exploration and production.[33]

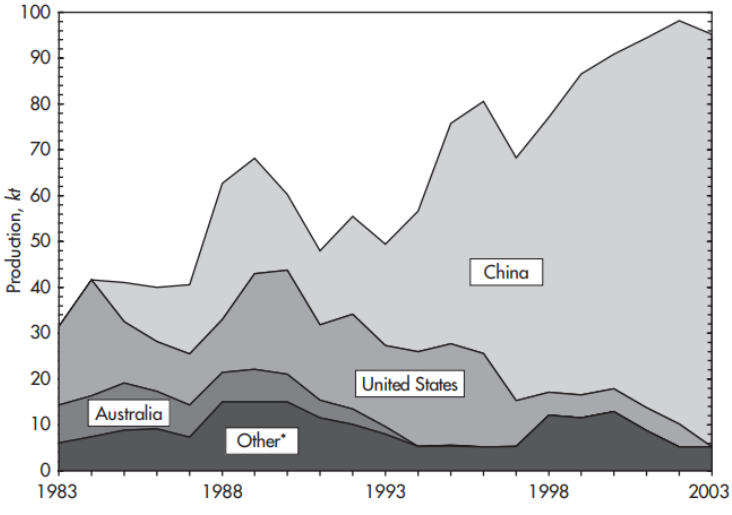

Figure 2.11. Global production of rare-earth elements from 1983 to 2003. **Other*** include India, Brazil, Kyrgyzstan, Sri Lanka, Russia, Malaysia, and Thailand.[6]

Rare-earth metals are vital to some of the world's growing industries. During the last three decades, there has been an explosion in the applications of rare-earth elements and their alloys in several technology devices such as: wind turbines, solar panels, magnetic resonance imaging (MRI), LED lighting, hybrid automobiles, rechargeable batteries.[31,33] For example, Neodymium is a material extensively used in wind turbines, as well as in hybrid cars; cerium is the material used in catalytic converters in cars; lanthanum can be used in high developed rechargeable batteries.[34] Therefore rare-earth metals are essential in green technologies that lead to reducing carbon emission and decarbonization of global economy envisioned in the Paris Climate Agreement, agreed to by 192 countries in 2015.[34] The expected increase in the

demand for renewable energy, makes the rare-earth materials critical for many high technology renewable technologies. The demand for rare-earths is likely to increase between 7–8% annually.[32]

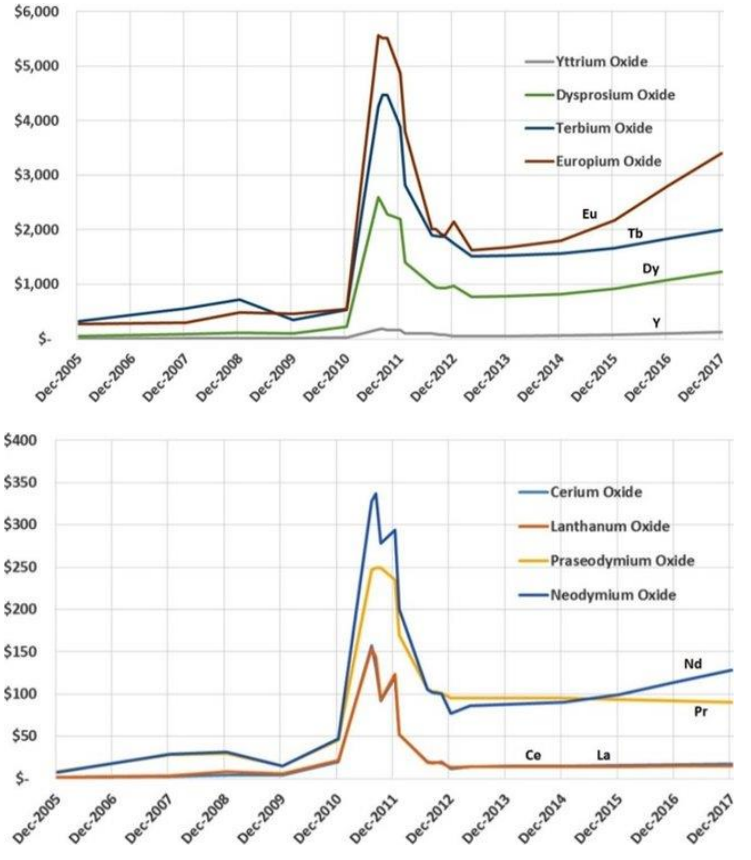

Figure 2.12. Rare-earth oxide prices per kg.[35]

There are large differences in market prices of rare-earth elements and the prices depend on the type of rare-earth and the degree of purity determined by the specifications in the applications.[35] Figure 2.12 shows the price range of different rare-earth element from 2015 to 2017.[35] Since China is the world's leading producer and exporter of rare-earth elements the prices of rare earth elements are largely dependent on Chinese national policies.[32] Between 2009 and 2011, there was a sharp increase in price due to tightening supply policies of China.[32] Historically, the prices of rare-earth elements steadily increased because of China's rising domestic demand and escalating export controls.[32]

Regulating the prices of rare-earth metals is very important, as they are needed for many renewable energy devices. If the world community wishes to establish a green energy environment, there is a strong need for a global agreement and international policies on rare-earth materials taking into account that only a handful of countries are really in control of these materials.[34] Recycling and waste management of rare-earth elements is also very important and can contribute to minimize the negative environmental impacts caused by rare-earth production.[32] However, this is not simple as in economic terms the profitability of the recycled rare-earth depends on its price in the market.[36] For example recycling yttrium was profitable because of the high price of yttrium between 2012-2013. However, between 2014 and 2016 recycling yttrium was not cost effective. This shows policymakers must encourage recovery and recycling solutions with appropriate policies.[36]

The rare-earth environmental impact needs to be studied at greater depth. The possibility of these elements finding their way into different environmental pathways to the ground and surface waters, will probably have some contribution to the environmental pollution and human health.[33] The insufficient environmental regulations and controls in the mining and production activities led to significant environmental and health impacts in countries such as China, US, India, Malaysia and Brazil.[33] Therefore, there is a great need for developing a sustainable exploitation schemes to prevent further environmental impact. Instead of opening new mines, recycling of these elements has to be considered and paid attention to.[33]

2.7 Conclusion

To summarize, this chapter provides and introduction to rare-earth metals, hydrides, oxides hydroxides, oxyhydroxides and oxyhydrides. The binary rare-earth oxyhydrides offer an interesting combination of hydride and oxide characteristics. To understand their physical properties we need to bridge a wide range of disciplines ranging from physics to solid state chemistry and material science. The increasing demand of rare-earth elements which are necessary components of many high-tech products across a wide range of applications can change the shape of global policies.

References

[1] E. F. E. ten Have, "Investigation of the photochromic properties of dysprosium oxyhydride," MSc thesis, Delft university of Technology, 2016.

[2] J. H. L. Voncken, "The Rare Earth Elements: an Introduction," 1st ed. 2016. ed. Cham: Springer International Publishing, 2016.

[3] A. R. Jha, *Rare Earth Materials: Properties and Applications*: CRC Press, 2014.

[4] R. E. Krebs, *The history and use of our earth's chemical elements : a reference guide*, 2nd ed. ed. Westport: Greenwood, 2006.

[5] *Rare Earth Resources Ltd, "Rare Earth Elements", available from: http://www.rareelementresources.com/rare-earth-elements#.Vlxidisi-Io, retrieved on 22-07-2019*.

[6] S. B. Castor and J. B. Hedrick, "Rare earth elements," *Industrial minerals volume, 7th edition: Society for mining, metallurgy, and exploration, Littleton, Colorado,* pp. 769-792, 2006.

[7] I. McGill, "Rare earth elements," *Ullmann's encyclopedia of industrial chemistry,* 2000.

[8] S. A. Cotton, *Lanthanide and actinide chemistry*. Chichester, England ;: Wiley, 2006.

[9] W. M. Mueller, J. P. Blackledge, G. G. Libowitz, and U. S. A. E. Commission, *Metal hydrides*. New York: Academic Press, 1968.

[10] R. D. Shannon, "Revised Effective Ionic-Radii and Systematic Studies of Interatomic Distances in Halides and Chalcogenides," *Acta Crystallographica Section A,* vol. 32, pp. 751-767, 1976.

[11] H. W. King, "Crystal structures of the elements at 25°C," *Bulletin of Alloy Phase Diagrams,* vol. 2, pp. 401-402, 1981/12/01 1981.

[12] D. R. Lide, *CRC handbook of chemistry and physics*: CRC press, 2004.

[13] G. G. Libowitz and A. J. Maeland, "Hydrides," in *Hand book on the Physics and Chemistry of Rare Earths*, K. A. Gschneider and J. L. Eyring, Eds., ed Amsterdam Elsvier 1979, pp. 299-336.

[14] P. Vajda, "Hydrogen in rare-earth metals, including RH_{2+x} Phases," *Handbook on the Physics and Chemistry of Rare Earths,* vol. 20, pp. 207-291, 1995.

[15] G. G. Libowitz, "Metallic hydrides; fundamental properties and applications," *Journal of Physics and Chemistry of Solids,* vol. 55, pp. 1461-1470, 1994.

[16] J. N. Daou, A. Lucasson, P. Vajda, and J. P. Burger, "Observation of the optical and acoustic electron-phonon coupling in Sc, Y and Lu dihydrides and dideuterides by electrical resistivity," *Journal of Physics F: Metal Physics,* vol. 14, pp. 2983-2993, 1984.

[17] J. N. Huiberts, R. Griessen, A. T. M. van Gogh, N. J. Koeman, J. P. Dekker, and P. H. L. Notten, "Yttrium and lanthanum hydride films with switchable optical properties," *Journal of Alloys and Compounds,* vol. 253-254, pp. 44-50, 1997.

[18] J. W. J. Kerssemakers, S. J. van der Molen, R. Günther, B. Dam, and R. Griessen, "Local switching in epitaxial YH_x switchable mirrors," *Physical Review B,* vol. 65, p. 075417, 02/01/ 2002.

[19] E. Schweda, "Rare earth oxides," in *Key Engineering Materials*, 1992, pp. 187-216.

[20] L. Petit, A. Svane, Z. Szotek, and W. M. Temmerman, "First-principles study of rare-earth oxides," *Physical Review B,* vol. 72, 2005.

[21] G. Adachi, N. Imanaka, and Z. C. Kang, "Binary rare earth oxides," ed. Dordrecht ;: Kluwer Academic Publishers, 2004.

[22] R. J. Gaboriaud, F. Paumier, and B. Lacroix, "Disorder-order phase transformation in a fluorite-related oxide thin film: In-situ X-ray diffraction and modelling of the residual stress effects," *Thin Solid Films,* vol. 601, pp. 84-88, 2016.

[23] C. E. Curtis, "Properties of Yttrium Oxide Ceramics," *Journal of the American Ceramic Society,* vol. 40, pp. 274-278, 1957.

[24] T. Mongstad, C. Platzer-Bjorkman, S. Z. Karazhanov, A. Holt, J. P. Maehlen, and B. C. Hauback, "Transparent yttrium hydride thin films prepared by reactive sputtering," *Journal of Alloys and Compounds,* vol. 509, pp. S812-S816, Sep 2011.

[25] T. Mongstad, C. Platzer-Bjorkman, J. P. Maehlen, L. P. A. Mooij, Y. Pivak, B. Dam*, et al.*, "A new thin film photochromic material: Oxygen-containing yttrium hydride," *Solar Energy Materials and Solar Cells,* vol. 95, pp. 3596-3599, Dec 2011.

[26] F. Nafezarefi, H. Schreuders, B. Dam, and S. Cornelius, "Photochromism of rare-earth metal-oxy-hydrides," *Applied Physics Letters,* vol. 111, p. 103903, 2017.

[27] S. Cornelius, G. Colombi, F. Nafezarefi, H. Schreuders, R. Heller, F. Munnik*, et al.*, "Oxyhydride Nature of Rare-Earth-Based Photochromic Thin Films," *The Journal of Physical Chemistry Letters,* vol. 10, pp. 1342-1348, 2019.

[28] B. Malaman and J. F. Brice, "Etude structurale de l'hydruro-oxyde LaHO par diffraction des rayons X et par diffraction des neutrons," *Journal of Solid State Chemistry,* vol. 53, pp. 44-54, 1984.

[29] G. Kobayashi, Y. Hinuma, S. Matsuoka, A. Watanabe, M. Iqbal, M. Hirayama*, et al.*, "Pure H^- conduction in oxyhydrides," *Science (New York, N.Y.),* vol. 351, pp. 1314-7, 2016.

[30] H. Ubukata, T. Broux, F. Takeiri, K. Shitara, H. Yamashita, A. Kuwabara*, et al.*, "Hydride Conductivity in an Anion-ordered Fluorite Structure LnHO with an Enlarged Bottleneck," *Chemistry of Materials,* 2019.

[31] G. Charalampides, K. Vatalis, V. Karayannis, A. Baklavaridis, E. th Innovative Manufacturing, and I. Energy Conference, "Environmental Defects and Economic Impact on Global Market of Rare Earth Metals," *IOP Conference Series: Materials Science and Engineering,* vol. 161, 2016.

[32] N. A. Mancheri, B. Sprecher, G. Bailey, J. Ge, and A. Tukker, "Effect of Chinese policies on rare earth supply chain resilience," *Resources, Conservation & Recycling,* vol. 142, pp. 101-112, 2019.

[33] V. Balaram. (2019, Rare earth elements: A review of applications, occurrence, exploration, analysis, recycling, and environmental impact. *Geoscience Frontiers 10(4),* 1285-1303.

[34] E. Apergis and N. Apergis, "The role of rare earth prices in renewable energy consumption: The actual driver for a renewable energy world," *Energy Economics,* vol. 62, pp. 33-42, 2017.

[35] G. Barakos, H. Mischo, and J. Gutzmer, *Status Quo and Future Evaluations of Global Rare Earth Mining (with Respect to Special Rare Earth Element-industry Criteria)*, 2015.

[36] M. Favot and A. Massarutto, "Rare-earth elements in the circular economy: The case of yttrium," *Journal of Environmental Management,* vol. 240, pp. 504-510, 2019.

3

Introduction to photochromic glasses

Photochromic glasses are one of the most widespread types of optical glasses. When light of a short wavelength interacts with photochromic materials, they darken. A well-known example of inorganic photochromic materials is the silver halide dopped copper glass. When illuminated, a chemical reaction takes place and silver ions are converted into elemental silver. A similar reaction occurs when a photographic film is exposed to light. However, as opposed to the photographic film, in glasses the reaction is reversible. In this chapter, I describe the basic parameters of photochromic glasses, how the absorption spectra can be explained and the results of the experimental and theoretical study of the kinetics of the photochromic reaction.

3.1 Introduction

Photochromism is defined as a photo-induced, reversible transformation of a material between two states that possess distinguishable absorption spectra.[1] The induced absorption is typically caused by ultraviolet (UV) light and is observed by the human eye as a change of color. Initially, the material is transparent and in a thermodynamically stable state with low light absorption.[1] Upon exposure to electromagnetic radiation with photons above certain threshold energy, a forward reaction, the so-called (photo-)darkening occurs where the material is in a thermodynamically less stable state with high light absorption. The photochromic reaction is reversible and the reverse reaction is called bleaching. As shown in Figure 3.1, when the exciting radiation is turned on at time t_1, the concentration of absorbing species increases and the transmittance of the material drops.[1] This process continues until the system reaches a steady state. In the steady state, the darkening and thermal bleaching processes are active simultaneously.[1]

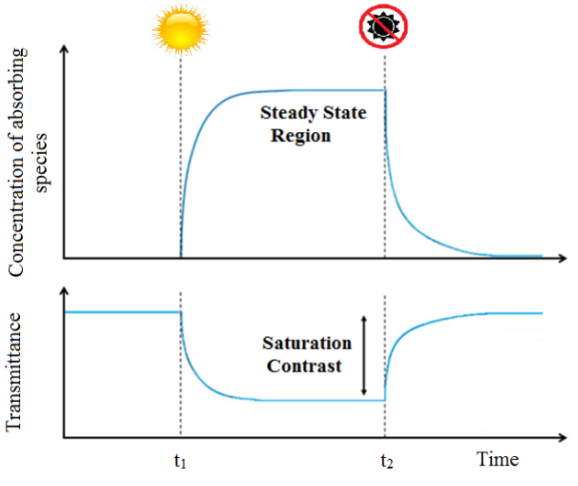

Figure 3.1. Response of a photochromic system when the exciting radiation is turned on at time t_1, during exposure to radiation and when it is cut off at time t_2 (picture modified from reference [1]).

An equilibrium is established at a certain concentration of absorbing species which is characterized by the saturation value of optical contrast.[1] Upon removal of the exciting radiation at time t_2, the concentration of absorbing species decreases and the material reverts from darkened state to the bleached state. Its rate depends on the kinetics of the backward bleaching reaction.[1,2] It is important to note that the exciting radiation must exceed the minimum energy for the photochromic reaction to proceed so that the absorbing species can form. The reverse reaction may occur via optical

bleaching, thermal bleaching or both. Thermal bleaching is a thermal relaxation of the material. Optical bleaching, on the other hand, is caused by exposing the material to light of longer wavelengths, than those used for the darkening process, i.e. in the energy range of the absorption band.[1,2] The photochromic effect may occur in both organic and inorganic materials. Organic photochromic materials are mostly activated by UV light and involve light-induced isomerization or a geometrical change of molecules.[2] Inorganic photochromic materials, on the other hand, offer a wider range of spectral sensitivity in comparison to their organic counterparts. This ranges from infrared to X-rays, with UV being the most common.[2]

3.2 Silver halide doped glasses, a classical example

A well-known example of inorganic photochromic materials is silver halide crystals trapped in a glass matrix. The first case of these photochromic eye glasses was developed by Corning Inc. in the 1960s.[3] Typically, these self-darkening glasses are composed of alkali metal borosilicate glass and silver halide crystals with a small amount of copper. The glass attains its photochromic nature after it is brought to a molten state wherein the silver, copper, and halide ions are dispersed. After that, the glass is cast into a homogeneous blank. In the next step, the glass is heat-treated at a constant temperature and then rapidly cooled down. The heat treatment is essential for the manufacturing of the photochromic glasses because it leads to the formation and growth of silver halide crystals, which provide the glass with its photochromic properties.[4] X-ray diffraction analysis [5] and Differential Scanning Calorimetry [6] are used to verify the presence of silver halide microcrystalline phase in photochromic glasses. The composition and heat-treatment are very important parameters that influence the formation of defects and enhance the diffusion of species which determine the photochromic properties of the final product.[3] The presence of copper ions contributes to the optical properties of the final product. In these photochromic glasses, the total concentration of silver ranges from 0.2% to 0.7% (in weight percent) and halogen in the range of 0.2% to 0.4% (in weight percent) in terms of the total concentration of the glass.[7] The quantity of added copper oxide is typically in the range of 0.016% to 0.20% (in weight percent).[8] These photochromic glasses contain around 4×10^{15} crystallites/cm^3 with a size of 5-10 nm and an average spacing of about 10-100 nm.[9] Irradiation of these AgCl crystals by light with photon energies larger than the band gap generates mobile electron-hole pairs and the formation of silver specks, which cause the reversible photo-darkening.[8] Depending on the choice of utilized halogen, the threshold wavelength at which the glass darkens is altered. If a heavier halogen is implemented, the glass can become more sensitive to smaller

wavelengths, as the energy required to excite the electron-hole pairs becomes larger with the size of the halogen.[10]

3.2.1 Photochromic effect

Photochromism in inorganic materials, in general, involves localized defects and impurities. In silver chloride doped glasses, the copper additive is in a monovalent state (cuprous ions). This copper is incorporated into the AgCl-crystals and occupies a silver ion site, thus forming a substitutional point defect. Silver chloride itself is not an ideal crystalline solid and contains several other types of defects in its unit cell. For example, there are vacant lattice sites called Frenkel defects, where the cation or anion is displaced to the interstitial position. The photochromic behavior in silver chloride glasses depends on the interaction of these defects with light.[4] These defects give rise to additional allowed levels within the forbidden band gap.[10] Figure 3.2 shows the energy band diagram together with a schematic drawing of the lattice at the beginning of the irradiation process. Light of sufficiently high energy (UV or blue) to overcome the band gap of the silver chloride generates an electron in the conduction band and a hole in the valance band.[3] The electrons can be trapped by interstitial silver ions (Frenkel defects) and become neutralized. On the other hand, the holes can be captured by Cu^{+} ions and form Cu^{2+} ions (Figure 3.2). In this way, the recombination of electrons and holes is blocked, and the formation of Cl_2 is prevented.[3] The neutral Ag interstitials are mobile, and the coagulation of these silver atoms results in the creation of a speck of silver at the interface with the glass matrix. These silver clusters absorb the light and make the glass dark.[3] This is because the light, which corresponds to a plasmon oscillation frequency of the nanoparticle generates a plasmon absorption resonance.[11,12]

If all Cu^{+} ions form Cu^{2+} ions, further growth of silver clusters becomes less likely, and recombination becomes more effective. The system reaches a steady state, and the transmittance does not drop any further since the system reaches a point where there are as many absorption centers formed as there are destroyed. When the irradiation ceases, there are two possible recombination paths which can lead to bleaching. Firstly, an electron can be thermally emitted from the silver speck into the conduction band and recombine with the trapped hole in a Cu^{2+} ion. A second possibility is the emission of holes from Cu^{2+} ions into the valance band where it can diffuse to the glass interface and recombine with an electron from the silver speck. When silver ions are formed, they diffuse back and incorporate into the silver halide lattice.[3, 8] The presence of copper is essential to ensure that no Cl_2 is formed which would make the process irreversible. The mechanism proposed for photochromic glasses is similar to

photography emulsions, which is an irreversible process because the hole is trapped by halide ion to form halide molecules and the silver ion is reduced to metallic silver atoms by a developing agent. Halide molecules react with the gelatin and cannot be regenerated again. The photochromic glass shows reversibility due to the presence of Cu^{+} ions which act as a deep hole trap.[13] Electron spin resonance (ESR) measurements have been used to prove the formation of Cu^{2+} upon darkening.[14,15]

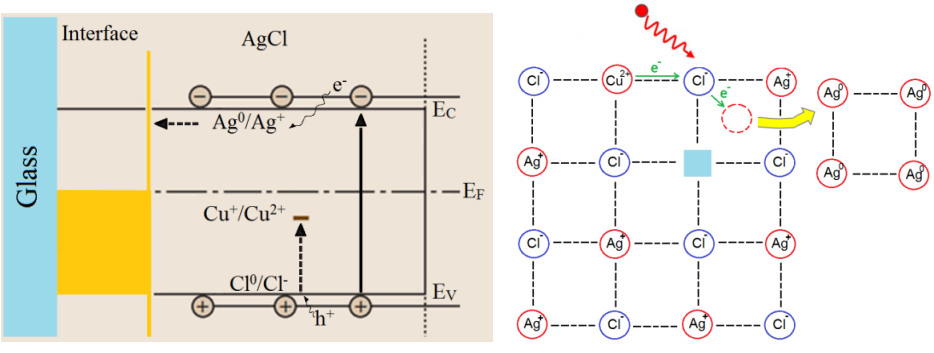

Figure 3.2. Schematic drawing of the energy band diagram (left) and the crystal structure (right). Irradiation leads to the transfer of an electron from chloride to silver and formation of silver clusters (picture modified from reference [3, 16]).

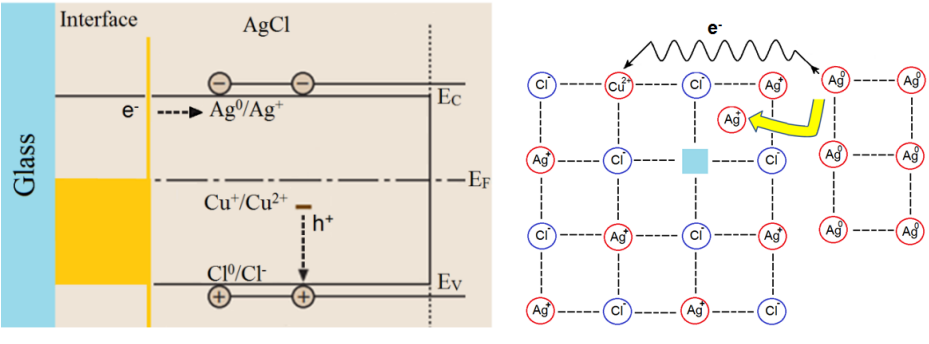

Figure 3.3. Schematic drawing of the energy band diagram (left) and the crystal structure (right) when irradiation is ceased (picture modified from reference [3,16]).

3.2.2 Photo-induced absorption spectra

Solar irradiation makes the photochromic glass dark. Figure 3.4 shows the change of transmittance of a commercially available photochromic glass when exposed to certain amounts of sunlight.[17] This change is mostly in the visible part of the spectrum with a peak approximately around 500 nm wavelength. The average radius of silver halides crystallites was estimated to be in the range of $2.5 < r < 15$ nanometers according to

Smith's experimental work.[18] Assuming this size range for *spherical metallic silver*, the photo-induced absorption spectra with a maximum at 550 nm cannot be explained. If we assume spherical silver colloids are formed, a bell shape absorption band in the visible range with a maximum at about 395 nm is expected for particles with a diameter of 10 nm.[19]

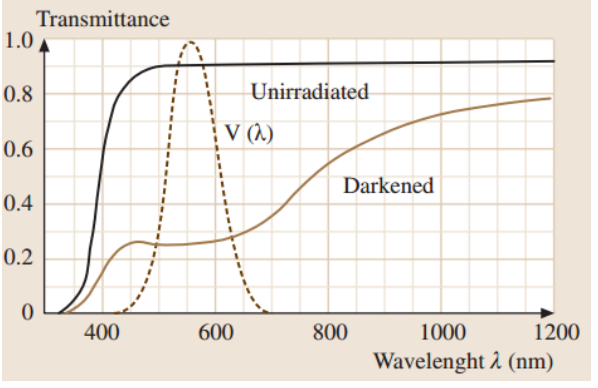

Figure 3.4. Spectral transmittance of 2mm commercial photochromic glass as a function of wavelength before and after exposure to 15 min solar irradiation at 20 °C. The dashed curve indicated the spectral sensitivity of the human eye (reused from reference [17]).

As shown in Figure 3.5a we need 40 nm Ag spheres to explain the absorption at 550 nm.[18] But such an assumption is incorrect because the silver clusters cannot exceed the AgCl-crystallite size (estimated to be 40 nm). Likewise, the migration of these clusters from one region to another is prohibited by the glass matrix.[20] Even under the assumption that all silver ions in the silver halide crystals are converted to silver atoms, it is still not possible to cover the entire sphere of AgCl-crystallite with silver atoms.[20] Therefore to explain the induced absorption band, we need to consider the shape of the metallic silver specks.[12] Dotsenko and Zakharov suggested a shell model to explain the photo-induced spectrum. The proposed model assumes a AgCl/Ag core/shell structure, consisting of silver halide surrounded by metallic silver particles. Taking an outer radius in the range of 2.5 nm < r < 15 nm, the maximum absorption band shift depends on the ratio of the two radii. This was the first attempt of using Mie theory to describe the optical properties in a glass containing metallic particles.[20] Moriya attempted to calculate the photo-induced absorption spectra of photochromic glass using Gans theory which is an extended Mie theory assuming prolate and oblate ellipsoids silver particles.[21] When the particles are assumed ellipsoids, the absorption band splits into two. One band at shorter wavelengths due to the absorption of light polarized parallel to the short axis of the ellipsoid. The other band shifts to longer wavelengths due to the absorption of light polarized parallel to the long axis of the

ellipsoid.[19,22] According to Moriya, the experimental data from UV induced absorption spectra of the photochromic glass could be explained to proximity using non-spherical silver particles.[22] Interestingly, the experiments revealed that the darkening in the copper doped silver halide glasses is related to the optical absorption edge. Figure 3.6 shows the optical absorption of the glass before any exposure to light. This glass is subjected to the light of different wavelengths, and the value of optical absorption at 550 nm is taken from each measurement. Connecting the points to plot the curve make one believe that darkening involves band gap excitation.[23]

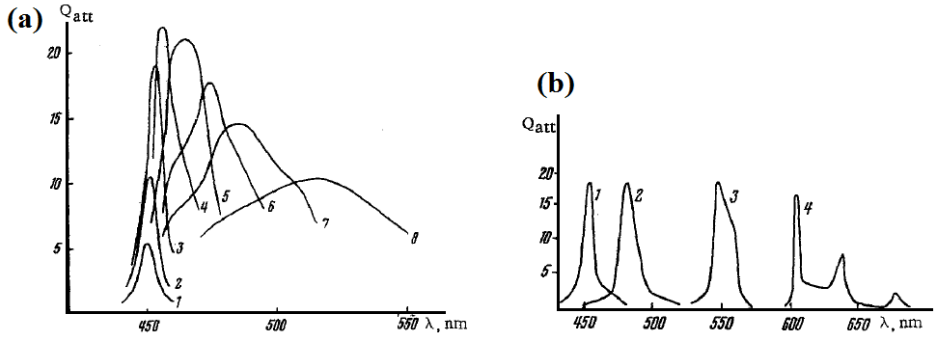

Figure 3.5. (a) light attenuation for spherical silver particles of radius 1) 2.5; 2) 5; 3) 10; 4) 15; 5) 20; 6) 25; 7) 30 and 8) 40 nm. (b) light attenuation using the double layer model with outer radius of 10 nm and q = 1) ∞; 2) 2; 3) 1.39 and 4) 1.2 where q is the ratio of outer to inner sphere (reused from reference [20]).

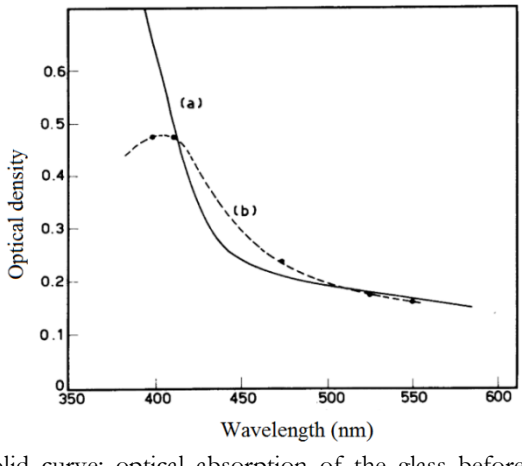

Figure 3.6. (a) Solid curve: optical absorption of the glass before exposure to light (Optical density is the logarithm of transmittance) (b) Dashed curve: optical absorption of the glass at 550 nm after the glass was exposed to light with different wavelength presented in points. (reused from reference [23]).

3.2.3 Optical bleaching

Destruction of the photographic latent image has been observed by the exposure of photographic emulsion to blue light and subsequently to the light of longer wavelength (Herschel effect).[24] Upon second exposure, light of longer wavelength causes the ejection of a photo-electron from latent image to the conduction band of silver halide crystal.[24] Based on this phenomena, it has been suggested by Borelli et. al.[13, 25] that a similar effect occurs in photochromic silver halide glasses where the material can bleach back to its original state either thermally, which can be accelerated by heating the glass, or via optical bleaching, through exposing the glass to light that interacts with silver specks and thereby reduces their size. As previously mentioned, silver specks are formed in silver halide photochromic glasses upon exposure to UV light. These silver specks are in contact with silver halide and form an interface (See Figure 3.7). At thermodynamic equilibrium, the Fermi levels in the two materials line up. Vacuum level will be continuous across the interface and band bending occurs at the interface (not shown in Figure 3.7). Borelli et. al. [13,25] suggested that a Fermi contact is formed and the Fermi level lies midway of AgCl band gap at 1.6 eV. Single electron excitation can inject an electron into the conduction band of silver halide crystal. This simple picture shows that the minimum energy required to overcome the potential barrier (the energy threshold for bleaching) is 1.6 eV. The optical absorption and thereby the ejection of electrons is enhanced in the case of plasmonic resonance.

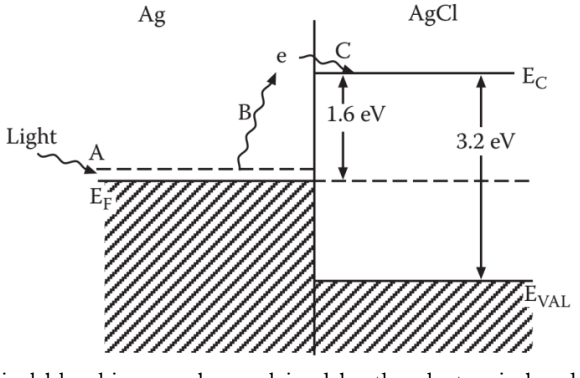

Figure 3.7. Optical bleaching can be explained by the electronic band structure at the silver-silver halide interface. An electron in the silver metal particle is optically excited to the silver chloride conduction band (reused from reference [24]).

Plasmon resonance arises from oscillations of a conduction electron in metal nanoparticles due to interaction with the electric field of light.[26] Spectral positions of surface plasmon peaks can be interpreted and related to the size and distribution of the silver specks.[12, 25] The broad absorption band therefore implies the

superimposition of different silver specks with various size and geometry. According to the authors, optical bleaching occurs with the light of wavelengths within the UV-induced absorption band.[12,13,25] Figure 3.8a shows the effect of optical bleaching caused by exposing the darkened glass to a different wavelength. A change in absorbance is observed due to optical bleaching. This figure indicates that a certain absorption band can be selectively bleached in a certain wavelength range corresponding to that of the bleaching light. For example, when 607 nm bleaching light is used, a large change in absorption is observed around 600 nm in comparison to shorter and longer wavelengths. According to the authors, this observation supports the ellipsoid model where only ellipsoids that absorb the bleaching light are destroyed resulting in the decreased absorption corresponding to that wavelength. A silver ion is photo-released from the colloidal particles whose absorption overlaps with the wavelength of the bleaching light.[12] The efficiency of optical bleaching as a function of the wavelength of light is depicted in Figure 3.8b. This plot demonstrates that the optical bleaching is present at 1.9 eV (650 nm) and its efficiency decreases quickly as the bleaching wavelength reaches the predicted minimum energy value of 1.6 eV (780 nm), which corresponds to the Ag surface plasmon oscillation.[12,25] According to the authors, bleaching with energies lower than 1.6 eV becomes less effective. For example, the efficiency of optical bleaching for energies lower than 1.55 eV (800 nm) is decreased by three orders of magnitude.[12,13,25]

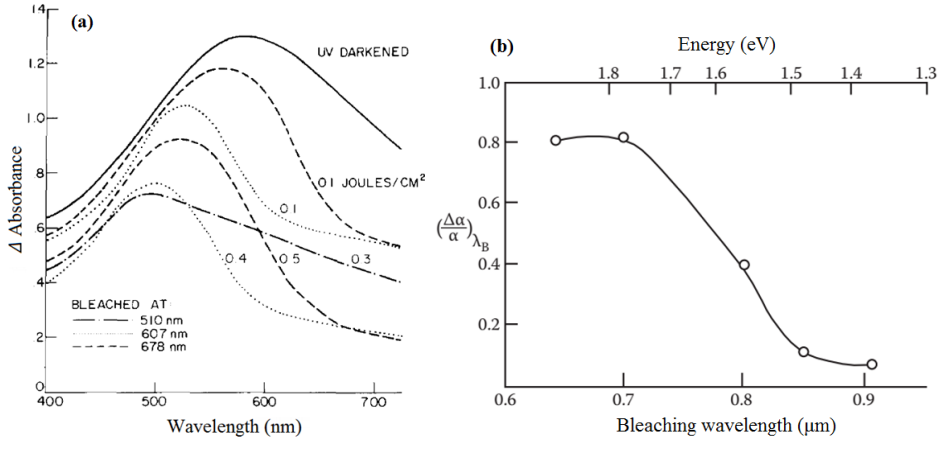

Figure 3.8. (a) Change of absorption spectrum due to the selective optical bleaching of photochromic glass. After the glass was darkened using UV light, several areas of the sample were optically bleached by varying light wavelength and exposure (reused from reference [12]). (b) Optical bleaching efficiency demonstrated by a change of absorption coefficient after bleaching as a function of energy (reused from reference [13]).

There are certain types of photochromic glasses reported by Seward, known as thermally darkenable photochromic glass (TDPC), which are prepared by precipitating copper doped silver halide crystallites in lanthanum borate base glasses.[27] In these glasses, the silver to halogen ratio varied between 1:1 to 4:1 and contains a small amount of copper in the range of 0.016 to 0.064 by weight. More detailed composition of such glasses is reported in the patent literature.[27] This type of glasses has the highest transparency when cooled to 15 ºC while exposed to bleaching light. The glass darkens as the temperature increases up to 400 C.[27] The author refers to this phenomena as induced thermal darkening. The exact reason for these peculiar properties was not explained. [27] Besides the thermal darkening characteristics, this type of glasses shows photochromic properties when exposed to UV light.[27] The difference between induced thermal darkening and the photochromic effect is depicted in Figure 3.9. In Seward's work, it is not clear if the energy threshold measurement outcome only applies for this type of glasses or in general to any silver halide photochromic glass.[27] Based on this description, we assumed this picture also applies to all silver halide photochromic glasses. The study in Seward's work revealed that the photochromic effect depends on the wavelength of the irradiation and showing that again there is a minimum energy of the photons needed to achieve the photochromic effect.[27] Figure 3.10 shows the darkening and bleaching sensitivity of such a glass. To study the darkening efficiency, the glass, which was initially in the bleached state was exposed to a 150-W xenon lamp as an activating light source with a combination of filters with different wavelengths.[27]

The corresponding change in transmittance before and after the exposure to irradiation was measured. In the optical bleaching experiments, the darkened sample was exposed to bleaching light with the use of narrow band filters. The change in transmittance after darkening and transmittance after exposure to bleaching light was recorded. The energy of the light source used in the optical bleaching experiments was six times larger in comparison to the UV light source implemented in the darkening experiment to acquire the equivalent change in optical density.[27] This demonstrates the different levels of sensitivity of the darkening and bleaching process on light source intensity.

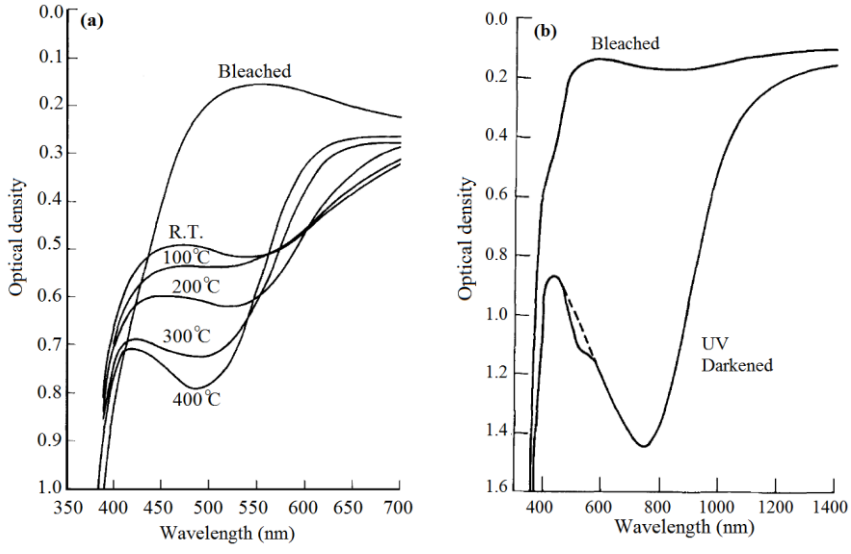

Figure 3.9. (a) Induced thermal darkening in 3 mm TDPC glass upon increase of temperature. (b) photochromic response of 2 mm TDPC glass after 30 min UV illumination at 1000 mW cm^{-2} at 370 nm (reused from reference [27]).

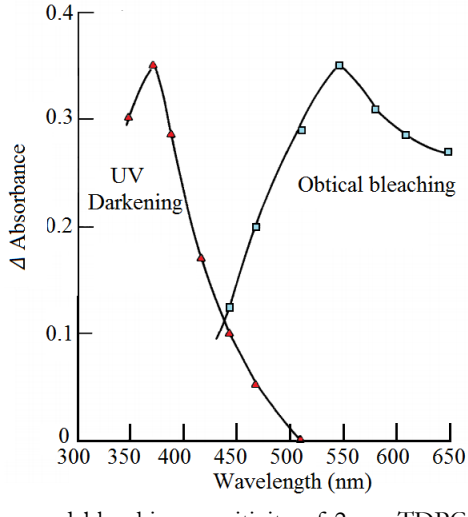

Figure 3.10. Darkening and bleaching sensitivity of 2mm TDPC glass. The change of absorbance between darkened and bleached state was measured by comparing the transmittance at 550 nm. Samples were illuminated by a150 W xenon lamp (24 mJ cm^{-2}) with different filters with pass bands of 10 nm centered at 348, 370, 385, 416, 443, 466 and 510 nm. The bleaching sensitivity curve is plotted by exposure of darkened glass to visible light with 150 mJ cm^{-2} energy. Narrow band filters centered at 443, 466, 510, 544, 577, 607 and 648 nm were used. The difference between the darkened state and partially bleached state was considered for optical bleaching experiment (reused from reference [27]).

It appears from Figure 3.10 that there is an energy threshold for both the darkening and optical bleaching processes. Copper doped silver chloride has a band gap of around 387 nm (3.2 eV). The maximum darkening sensitivity was observed at a light wavelength of 370 nm (note that the pass band was of about 10 nm). Instead of a sharp cut off at the band gap value, the darkening is observed at higher wavelengths. The change in absorption is at its maximum at a wavelength around the band gap value and starts to decrease as the wavelength increases and stops at 500 nm. The presence of defects could be a reason for that, as they can introduce localized allowed energy levels between the valence band and conduction bands. The optical bleaching starts at 450 nm, and the change of absorption begins to increase and reaches a maximum at 550 nm, followed by a decrease as the wavelength of the bleaching light is further increased.[27] The value of this maximum wavelength coincides with the photo-induced absorption spectrum. The crossover between darkening and bleaching sensitivity curves indicates the coexistence of two processes in the certain spectral range. This means that the material is also optically bleached during the darkening process when it is exposed to the light of these wavelengths.

In photochromic glasses, the silver particles that are formed after irradiation can have certain shapes: they can be elongated, ellipsoid or spherical. As a result, photo-bleaching by polarized light may be used to identify the shape of these particles as was demonstrated by the Corning research group.[25,28,29] Figure 3.11 shows their experimental work. The glass is initially in a clear state and then subjected to UV illumination. The transmission drops until the system reaches a steady state.[25] The excitation source was then switched off, and a polarized bleaching light was turned on. They have found that the transmission of the glass in a direction parallel and perpendicular to polarization direction was different, suggesting a dichroic effect is produced (Figure 3.11a).[25] The dichroic effect is further increased if the glass is exposed to polarizing light during the darkening (Figure 3.11b). The polarization effect was found to be reversible and dichroic orientation could easily be changed by altering the polarization of the bleaching light.[25]

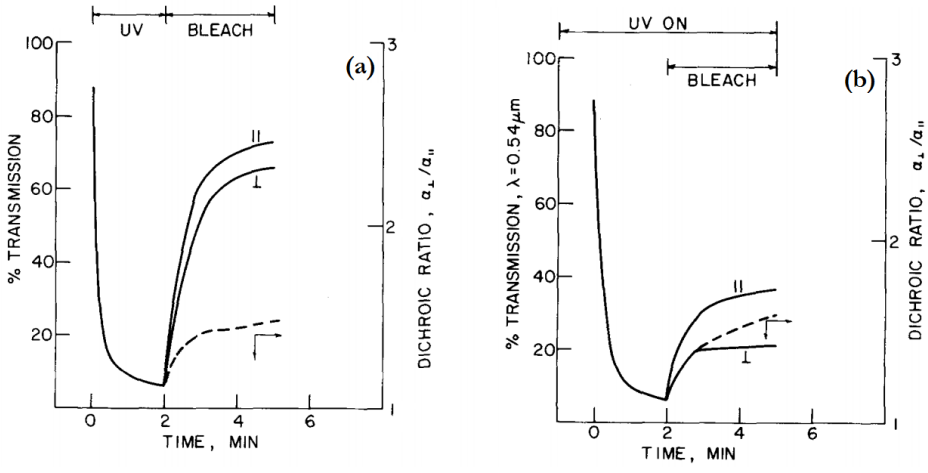

Figure 3.11. (a) Photo-induced optical anisotropy in the photochromic glass. Transmission of photochromic glass at 546 nm perpendicular and parallel to the polarization direction of the light source. At first, UV light was used for irradiation and then the glass was exposed to polarized light at 510 nm from an Ar ion laser. The dashed line is the dichroic ratio $\alpha_\perp/\alpha_{||}$ where α is the absorption coefficient. (b) When UV and polarized light is used simultaneously (reused from reference [25]).

To explain the optical response of such photochromic glass, the Corning research group suggested the following model. When the photochromic glass is exposed to a photodarkening UV light source, there is a random distribution in shape and size of silver particles, each absorbing a different wavelength. The polarizing light can reshape the fraction of the silver specks with certain geometrical orientation, by bleaching those particles whose orientation coincides with polarization direction of the bleaching light and experiences the highest level of light absorption. These are then destroyed more rapidly.[25,28] The photo-induced optical anisotropy was found to be reversible and the dichroic effect can easily be changed by the change of the polarization of the bleaching light.[25,28] Such a glass shows a memory effect, meaning that after it is bleached completely, the dichroic effect reappears again when the glass is darkened using UV light. The authors believe that a few silver clusters might remain in the glass which cannot be destroyed. They can serve as deep electron traps, and once such a glass is re-exposed to UV light, those speck starts to grow larger.[25,28]

3.3 Photochromic glasses without silver

Glasses containing copper halide or a mix of cadmium and copper halide free of silver have also been reported to show a photochromic effect.[30,31] This occurs in a specific type of glasses that allow the presence of Cu^{+2}. Because of the Cu^{+2} substitution, cation vacancies are created. A distribution of empty vacancy states below the conduction band is thereby created which makes the excitation by photons with energies less than the band gap possible.[13] The kinetics of the darkening and thermal bleaching are reported to be similar to those in photochromic glasses containing silver and can be explained by the diffusion model.[32] A core/shell model considering a metallic shell of copper with a CuCl core has been proposed to describe the photochromic effect for this type of glasses.[33] However, optical bleaching was not observed for any copper-cadmium photochromic glass.[34] This characteristic limited their application to information storage devices for selective erasure.[34] The exact reason for the lack of optical bleaching was not explained in the literature. The absence of optical bleaching brought questions to the proposed model of the photochromic effect in this type of glasses which was supposed to be similar to that in doped silver halide glasses. EPR and optical absorption measurements supported the colloidal copper model. Formation of colloidal Cu^0 claimed to be responsible for the observed darkening effect in the visible range.[35]

3.4 Kinetics of the bleaching process

Different approaches have been developed to describe the kinetics of bleaching processes in glasses containing silver halides.[8] Araujo[36,37] et al proposed a diffusion model to predict the kinetics of darkening and bleaching processes in photochromic glasses. According to this model, during the exposure of the glass to light with the appropriate photons, an electron is excited to the conduction band leaving a positively charged hole in the valence band. Once the electron is in the conduction band, it can diffuse and then be trapped by Ag^+ ions at intestinal positions to form Ag^0. Cu^+ ions, on the other hand, trap a positive hole and become Cu^{+2} ion. At this instant, the electron-hole pair cannot recombine, and silver speck continues to grow to form an Ag^0_n colloid. But what is the mechanism for the backward reaction/thermal bleaching? Some authors have suggested thermal relaxation of the holes into the valence band occurring during the bleaching process. However thermal energy is not sufficient for the charge transfer to occur due to the barriers present between the location where electrons are excited to and the location where the trap is formed. This is especially evident since the photochromic effect can take place at very low temperatures and the

glass can bleach back to its original transparent state (e.g. -40 °C).[38] Therefore, there should be another mechanism involved that transfers the electrons from the silver specks to the Cu^{+2} ions. When metal is brought into contact with a semiconductor, which in this case is silver colloids and silver halide matrix, a potential barrier arises within the semiconductor. Only electrons in the silver colloid with energies equal to Cu^{2+} ion state can tunnel.[36, 37] If we accept the recombination of charges between the electron and the hole traps are via a tunneling process, both silver colloid and Cu^{2+} ions should be close enough to allow the tunneling process to take place. Along with the electron tunneling, the positive charge on the colloid is dissipated by a silver ion reentering the crystal structure. According to the authors, the tunneling probability through a rectangular potential barrier in WKB approximation is expressed by: $P_T(z) \propto exp\left[-\frac{1}{h} + \{8m(\phi - E)\}^{\frac{1}{2}} W\right] \approx exp\,[-\alpha W]$. where E is the electron energy and m is electron mass in the barrier. ϕ is the height of the energy barrier. It has to be noted here that some of the references listed in Araujo's work are based on oral presentations, submitted abstracts to a conference or private communication with the co-workers and therefore is not listed in this chapter.[36,37]

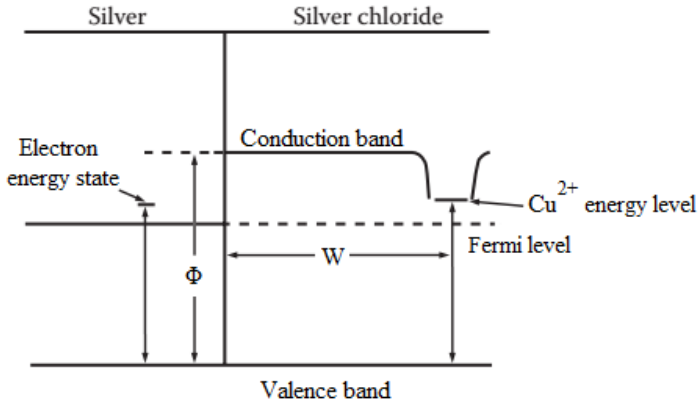

Figure 3.12 | Energy diagram for the Ag-AgCl interface (modified from reference [13]). In this picture, ϕ is the height of the energy barrier, W is the barrier width. This is a simple drawing where the semiconductor band bending at the interface is ignored.

The role of copper in AgCl based glasses has been criticised by Ferley et al. [39] They questioned the electron spin resonance (ESR) data reported by Marquardt et. al.[15,40] to prove the role of Cu^{2+} ions in the photochromic process.[39] They questioned the long term stability of previously reported systems. Ferley et al. demonstrated that their own experiments did not show a detectable increase in the concentration of Cu^{2+} ions due to illumination even if they use similar glass used in as Marquardt and colleagues'

work. Nevertheless, Ferley et al. [39] did not question the role of silver in photochromic glasses. Therefore, they proposed an alternative model based on radiation-induced defects in the microcrystal.[39] Initially, Ferley and colleagues did not find any paramagnetic defects at room temperature or 77 K even when the sample was cooled to 20 K immediately after irradiation. However, when the illuminated photochromic glass was cooled to 20 K, they observed Cl_2^-,Ti^{3+}, O^- defects by ESR while no change in EPR signal of Cu^{2+} due to illumination was detected.[39] Formation of Cl_2^- molecule ions due to X-ray radiation in borate glasses as a result of hole trapping has been confirmed by EPR studies.[41] Therefore, Ferley et. al. suggested the possibility of formation of a halogen radical which is able to capture an electron and act as hole trap centre.[39] On the other hand, silver atoms act as electron trap centres. In order for such a process to be reversible, it requires for such radicals to have low thermal stability or be in close proximity to silver atoms for recombination to occur.[39]
Ferley et al. questioning the previous model is noteworthy. Mrquardt et. al.[15,40] reported ESR data on silver halide photochromic glasses can be questioned if their system has not been well calibrated and the long term stability of the system has not been checked. Having said that, Caurant et. al [14] devoted an EPR investigation of photogenerated Cu^{2+} in photochromic glasses pointing towards the formation of divalent copper due to illumination by the presence of a noticeable signal. It is possible that the amount of Cu^{2+} that is formed due to illumination in Ferley's work was too small to be detected by ESR which requires concentrations larger than ~10^{18}-10^{19} cm^{-3}.[14]

The radiation-induced defect hypothesis was further investigated by Kraevskii et al.[42-44] He criticized the core-shell model (formation of Ag colloids around AgCl nanocrystals). He suggested the spontaneous dissociation of such a shell after cessation of irradiation at room temperature to be unlikely.[42] Instead, he proposed a different model in which the photochromic effect is explained as an interaction between defects in nanocrystals (e.g AgCl or CuCl depending on the type of glass) and the lattice defect of glass matrix at the interface upon illumination.[42] They came to this conclusion based on the analysis of the UV induced absorption spectra, where they decomposed the spectra into several bands associated with: [43,44] (1) lattice defects of the glass matrix. (2) defects of nanocrystals, the bands attributed to Cl_2^- and Cl_2^0 defects, known as chlorine centres analogous to V_K and H-defects in KCl crystals.[45] (3) exciton hole spectrum that arises and disappears together with the bands of radiation-induced defects which according to authors is indicative of the interaction between them.

In my opinion, the three models proposed so far fail to provide a compelling explanation for all the phenomena observed in photochromic glasses. Experimental and analytical work in the Kraevskii et al.[42-44] study is very interesting and mostly focuses on CuCl photochromic glasses. The AgCl photochromic glass experimental data were taken from someone else's work and fitted by the authors. Even if we believe that similar phenomena happens in both types of photochromic glasses, their explanation about the exciton hole role is not very clear and convincing to me. Although the number of studies supporting the first model is much larger, coming across studies that question the well-accepted models and pointing out their flaws, would make a reader to carefully evaluate the gathered information from the experimental body of work and reflect on their line of reasoning. In my opinion, although there is no direct observation of the species responsible for the photochromic effect has been reported to confirm the validity of suggested models, the core-shell ellipsoid model is more convincing, based on indirect experimental observations.

3.5 Summary

AgCl doped glasses exhibit photochromic properties when prepared using the proper annealing conditions. Exposure of the photochromic glass to light with sufficient energy (above the fundamental ionic crystal absorption edge) causes a reversible change in optical properties. This is due to the formation of electron-hole pairs. The electrons are trapped by interstitial silver ions to form mobile silver atoms which coalesce to form a silver speck at the interface of the silver halide/glass matrix. The plasmonic resonances in these metallic particles are responsible for the induced optical absorption. The holes, on the other hand, are ultimately trapped by Cu^{+} ions to form Cu^{+2} ions and slow down the recombination of electrons and holes. It has been suggested that metallic silver particles are formed around silver halide particles. The wide induced absorption spectra was explained using ellipsoids silver particles.

The bleaching occurs when an electron from the silver speck reverts back into the conduction band and then recombines with the trapped hole. Simultaneously, a silver ion has to leave the silver speck in order to maintain electric neutrality. The broad photo-induced absorption spectra were explained using a model involving a wide variety of silver ellipsoids with different shapes and sizes. The possibility to use polarized light to reshape the silver specks in a certain orientation further confirmed the presence of this wide range of silver speck geometries.

Optical bleaching is a photo-emission process where irradiation excites an electron from the top of the Fermi level of the silver into the conduction band of silver halide. The optical bleaching has been investigated using the light of different wavelengths. Experimental results in thermally darkenable photochromic glasses revealed a range of excitations around the band gap of silver halide doped copper. The efficiency of darkening has been found to decrease as the energy of light decreased. The experimental findings indicate that in a certain spectral range below the band gap (lower energies) of this material there is a crossover between darkening and bleaching. This means a certain wavelength can darken and bleach the glass simultaneously. We assumed this picture is true for all silver halide doped copper glasses.

Additional interesting properties related to the photochromic effect in silver halide doped copper glasses is inducing optical anisotropy with the use of polarized visible light of longer wavelengths. It was observed that after the glass is darkened if exposed to polarized light, the measured transmittance in the direction parallel and perpendicular to the polarization direction of the bleaching light will be different. According to the authors, this experiment strongly indicates that silver specks have ellipsoids shape. This means the light interacts with silver specks depending on their orientation (geometry and arrangement). Moreover, if the glass is exposed to UV light together with polarized light, favorably oriented specks grow further at the expense of unfavorable orientations. According to the authors, this experiment strongly indicates that silver specks have are ellipsoids.

The kinetics of the photochromic effect have been explained using the diffusion model. Based on this model, thermal bleaching and optical bleaching are separable processes. Electron tunneling was used by Araujo to describe the bleaching process which only takes place if the trapped electron and hole are closer than some critical distance. The well-accepted core-shell model (in AgCl or CuCl glasses) induced by illumination in the photochromic glasses and the role of copper have been questioned by Ferley and Kraevskii. They both proposed an alternative model where the photochromic effect is explained as the formation and recombination of intrinsic defects in nanocrystals and glass matrix at the interface.

Hopefully, the body of knowledge incorporated into this chapter and the references provided will stimulate future studies in this area. In particular, I hope that the reader will recognize from Section 3.2.4 that kinetics of photochromic glasses is much more complicated than just a summary of mathematical equations that claimed to perfectly matches the experimental data.

References

[1] G. H. Brown, "Introduction," in *Photochromism: Techniques of chemistry, vol. III*, G. H. Brown, Ed., ed New York Wiley-Interscience, 1971.

[2] P. Bamfield and M. G. Hutchings, "Chromic Phenomena: Technological Applications of Colour Chemistry," Third edition. ed. Croydon: National Book Network International (NBNi), 2018.

[3] H. J. Hoffmann, "Photochromic glasses," in *The Properties of Optical Glass*, H. Bach and N. Neuroth, Eds., ed Berlin: Springer, 1995, pp. 275-290.

[4] R. J. D. Tilley, *Defects in Solids*: Wiley & Sons, Inc., 2008.

[5] H. Bach and G. Gliemeroth, "Phase Separation in Phototropic Silver-Halide-Containing Glasses," *Journal of the American Ceramic Society,* vol. 54, pp. 528-529, 1971.

[6] V. A. Bershtein, A. V. Dotsenko, L. M. Egorova, V. M. Egorov, and V. A. Tsekhomsky, "Submicron crystals of a photochromic phase in glass analyzed using differential scanning calorimetry," *Soviet journal of glass physics and chemistry,* vol. 18, 1992.

[7] A. Paul, *Chemistry of Glasses*, 2nd ed. London Chapman and Hall, 1990.

[8] A. V. Dotsenko, L. B. Glebov, and V. A. Tsekhomsky, *Physics and Chemistry of Photochromic Glasses*. Boca Raton: CRC Press, 1998.

[9] G. K. Megla, "Optical Properties and Applications of Photochromic Glass," *Applied Optics,* vol. 5, pp. 945-960, 1966.

[10] R. J. Araujo, "Photochromic glasses," in *Techniques of chemistry Vol. III: Photochromism*, G. H. Brown, Ed., ed New York: Wiley-Interscience, 1971.

[11] E. Ringe, J. M. McMahon, G. C. Schatz, R. P. Van Duyne, K. Sohn, J. Huang*, et al.*, "Unraveling the effects of size, composition, and substrate on the localized surface plasmon resonance frequencies of gold and silver nanocubes: A systematic single-particle approach," *Journal of Physical Chemistry C,* vol. 114, pp. 12511-12516, 2010.

[12] I. T. P. Seward, "Coloration and Optical Anisotropy in Silver-Containing Glasses," *Journal of Non-Crystalline Solids,* vol. 40, pp. 499-513, 1980.

[13] N. F. Borrelli, *Photosensitive Glass and Glass-Ceramics*: CRC press, 2016.

[14] D. Caurant, D. Gourier, and M. Prassas, "Electron-paramagnetic-resonance study of silver halide photochromic glasses: Darkening mechanism," *Journal of Applied Physics,* vol. 71, pp. 1081-1090, 1992.

[15] C. L. Marquardt, J. F. Giuliani, and G. Gliemeroth, "A study of copper ions in silver-halide photochromic glasses," *Journal of Applied Physics,* vol. 48, p. ournal of Applied Physics, 1977.

[16] R. J. Araujo, "Photochromic Glasses," in *Encyclopedia of physical science and technology*, R. A. Meyers, Ed., 3rd ed. ed. San Diego: Academic Press, 2002, pp. 49-56.

[17] M. Brinkmann, J. Hayden, M. Letz, S. Reichel, C. Click, W. Mannstadt*, et al.*, "Optical Materials and Their Properties," in *Springer Handbook of Lasers and Optics*, F. Träger, Ed., ed New York: Springer 2007, pp. 249-372.

[18] G. P. Smith, "Photochromic glasses: Properties and applications," *Journal of Materials Science,* vol. 2, pp. 139-152, March 01 1967.

[19] M. Mennig and K. J. Berg, "Determination of size shape and concentration of spheroidal silver colloids embedded in glass by VIS-spectroscopy," *Materials Science & Engineering B,* vol. 9, pp. 421-424, 1991.

[20] A. V. Dotsenko and V. K. Zakharov, "Calculation of light attenuation spectra by coloration centers of photochromic glass based on a silver halide," *Journal of Applied Spectroscopy,* vol. 21, pp. 1654-1657, 1974.

[21] S. D. Stookey and R. J. Araujo, "Selective Polarization of Light Due to Absorption by Small Elongated Silver Particles in Glass," *Applied Optics,* vol. 7, pp. 777-779, 1968/05/01 1968.

[22] Y. MORIYA, "A Speculation on an Absorption Center Induced in the Photochromic Glass Containing Silver Halide Crystals," *Journal of the Ceramic Society of Japan,* vol. 84 pp. 252-254, 1976.

[23] F. G. Wakim, "Some Properties of Photochromic Borosilicate Glass," in *Recent Advances in Science and Technology of Materials: Volume 2*, A. Bishay, Ed., ed Boston, MA: Springer US, 1974, pp. 123-131.

[24] N. F. S. Mott and R. W. Gurney, *Electronic processes in ionic crystals*, 2d ed. ed. Oxford: Clarendon Press, 1948.

[25] N. F. Borrelli, J. B. Chodak, and G. B. Hares, "Optically Induced Anisotropy in Photochromic-Glasses," *Journal of Applied Physics,* vol. 50, pp. 5978-5987, 1979.

[26] A. A. Toropov and T. V. Shubina, *Plasmonic Effects in Metal-Semiconductor Nanostructures*: Oxford University Press 2015.

[27] T. P. Seward Iii, "Thermally darkenable photochromic glasses," *Journal of Applied Physics,* vol. 46, pp. 689-694, 1975.

[28] N. F. Borrelli and I. T. P. Seward, "Photoinduced optical anisotropy and color adaptation in silver-containing glasses," *Applied Physics Letters,* vol. 34, pp. 395-397, 1979.

[29] S. D. Stookey and R. J. Araujo, "Selective Polarization of Light Due to Absorption by Small Elongated Silver Particles in Glass," *Applied Optics,* vol. 7, pp. 777-779, 1968.

[30] R. J. Araujo, "Photochromic Glass," in *Glass I: Treatise on Materials Science and Technology*. vol. 12, M. Tomozawa and R. H. Doremus, Eds., ed, 1977, pp. 91-122.

[31] D. M. Trotter, J. W. H. Schreurs, and P. A. Tick, "Copper-cadmium halide photochromic glasses: Evidence for a colloidal darkening mechanism," *Journal of Applied Physics,* vol. 53, 1982.

[32] R. J. Araujo and N. F. Borrelli, "Diffusion-model interpretation of the darkening and fading of photochromic glasses," *Journal of Applied Physics,* vol. 47, pp. 1370-1373, 1976.

[33] A. V. Dotsenko, V. K. Zakharov, S. A. Kuchinskii, and T. E. Chebotareva, "Calculation of extinction spectra due to colloidal copper particles in copper halide photochromic glasses," *Journal of Applied Spectroscopy,* vol. 39, pp. 1288-1292, November 01 1983.

[34] R. J. Araujo, "Photochromic Glass," in *Treatise on Materials Science & Technology*. vol. 12, M. Tomozawa and R. H. Doremus, Eds., ed, 1977, pp. 91-122.

[35] V. Ghiordanescu, S. V. Nistor, and L. Dollingher, "The effect of copper ions on optical properties of silver-halide photochromic glasses," *physica status solidi (a),* vol. 59, pp. 861-865, 1980.

[36] R. J. Araujo, "Kinetics of Bleaching of Photochromic Glass," *Applied Optics,* vol. 7, pp. 781-786, 1968/05/01 1968.

[37] R. J. Araujo, N. F. Borrelli, and D. A. Nolan, "The influence of electron-hole separation on the recombination probability in photochromic glasses," *Philosophical Magazine Part B,* vol. 40, pp. 279-289, 1979.

[38] D. C. Look and W. L. Johnson, "Transmittance of photochromic glass at environmental extremes " *Applied Optics,* vol. 18, 1979.

[39] L. Ferley, T. Mattern, and G. Lehmann, "An alternative model for the photochromism of glasses," *Journal of Non-Crystalline Solids,* vol. 92, pp. 107-121, 1987.

[40] C. L. Marquardt, J. F. Giuliani, and R. T. Williams, "Darkening mechanisms in silver-halide photochromic glasses : Flash-photolysis and ESR studies," *Journal of Applied Physics,* vol. 47, pp. 4915-4925, 1976.

[41] D. L. GRISCOM, P. C. TAYLOR, and P. J. Bray, "Paramagnetic resonance of room temperature-stable V-Type Centers in irradidated alkali halide–boron oxide glasses," *Journal of Chemical Physics,* vol. 50, pp. 977-983, 1969.

[42] S. L. Kraevskii, "An Alternative Model for Photochromism of Glasses: Reversible Injection of Carriers from a Microcrystal and Its Surface States into Point Defects of Glass," *Glass Physics and Chemistry,* vol. 27, pp. 315-330, 2001.

[43] S. L. Kraevskii, V. F. Solinov, and A. M. and Zyabnev, "Spectral Hole Burning in the Exciton Line of CuCl Microcrystals in Glasses and the Nature of Photochromic Effect," *Fiz. Khim. Stekla.,* vol. 24, pp. 711-720, 1998.

[44] S. L. Kraevskii, V. F. Solinov, and A. M. Zyabnev, "Interaction between excitons of CuCl microcrystals and intrinsic color centers of matrix in photochromic glass " *Fiz. Khim. Stekla. ,* vol. 25, pp. 151-158, 1999.

[45] S. L. Kraevskii and V. F. Solinov, "Interface models for the photochromism and thermochromism of glasses with nanocrystals," *Journal of Non-Crystalline Solids,* vol. 316, pp. 372-383, 2003.

4

Photochromism in rare-earth metal oxyhydrides, general behavior (Y, Er, Dy,Gd)

Recently, thin films of yttrium oxyhydride (YO_xH_y) have been reported to show an unusual color-neutral photochromic effect which is promising for application in smart windows. Our present work demonstrates that also oxyhydrides based on Gd, Dy, and Er have photochromic properties and crystal structures similar to YO_xH_y. Compared to YO_xH_y, the optical bandgaps of the lanthanide-based oxyhydrides are smaller, while photochromic contrast and kinetics show large variation among different cations. Based on these findings, we propose that cation alloying is a viable pathway to tailor the photochromic properties of oxyhydride materials. Furthermore, we predict that the oxyhydrides of the other lanthanides are also potentially photochromic.

This chapter is partially based on:
F. Nafezarefi, H. Schreuders, B. Dam, and S. Cornelius, "Photochromism of rare-earth metal oxy-hydrides" *Applied Physics Letters,* vol. 111, 2017.

4.1. Introduction

Owing to their application in hydrogen storage, metal hydrogen systems have been the subject of extensive research over the past decades. These materials have a large mobility and solubility of hydrogen.[1] Since bulk characterizations are limited, thin film techniques have been developed that lead to intriguing findings such as switchable mirrors.[1] The yttrium hydrogen system is a prototype for these materials. Pd capping of Y thin films allows for a reversible (de)hydrogenation.[2,3] The optical changes involved in the (de)hydrogenation process was demonstrated by the switchable mirror effect in YH_x.[4] Depending on the hydrogen concentration, the yttrium hydrogen system exhibits three structural phases. Upon hydrogenation, metallic yttrium with hexagonal structure changes to the cubic dihydride phase (β-$YH_{1.9–2.1}$) and finally the hexagonal trihydride phase (γ-$YH_{2.7–3}$).[1] While the $YH_{1.9+\sigma}$ phase is a black and opaque metal, the trihydride is a transparent semiconductor with a direct optical bandgap of 2.6 eV.[5]

Photochromism is defined as a reversible transformation induced by light irradiation between two states of a material that have different optical absorption spectra.[6, 7]. A unique photochromic effect was discovered by Mongstad et al. in an oxygen-containing yttrium hydride thin films prepared by reactive sputtering after excitation by an AM1.5 solar spectrum at room temperature and ambient pressure.[8] This polycrystalline semiconductor has an optical bandgap of about 2.6 eV and an fcc crystal structure with a lattice constant of 5.35–5.40 Å.[9,10] The initially transparent material photo-darkens in a wide spectral range covering the visible (VIS) and near-infrared (NIR) with a time constant in the order of minutes.[8] Hence, yttrium oxyhydride (YO_xH_y) was proposed as a promising material for application in energy saving smart windows and other chromogenic devices.[11] Photochromism is observed in both inorganic and organic compounds. Organic photochromic materials exhibit narrow spectral absorption bands together with fast switching behavior.[12-14] However, due to limited stability vs. oxygen, humidity, and heat, as well as ultra-violet (UV) irradiation induced fatigue,[12] complex processing is often required to tailor the photochromic response and to enhance the product lifetime. In contrast, inorganic photochromic materials have the potential for higher physicochemical stability and show a wider range of spectral sensitivity and broader absorption bands, resulting in color-neutral photochromism, albeit at lower switching speed. A well-known example of inorganic photochromic materials is silver halide doped glasses where the photochromic effect is based on the reversible formation of plasmonic nanoparticles.[15,16]

While the photochromic mechanism in YO_xH_y remains to be uncovered, Mongstad et al. suggested that the fcc crystal structure and the presence of oxygen are essential for the photochromic effect.[8,17] Here, the question arises whether other rare-earth metal based oxyhydrides show similar properties. The lanthanides show physical and chemical behavior very similar to Y in terms of mostly trivalent oxidation state, ionic radius, as well as crystal structure and properties of compounds formed with oxygen and hydrogen. Indeed, we find that the oxyhydrides of Gd, Dy and Er are photochromic. This allows us to explore possible structural and chemical effects in the photochromic properties of the MO_xH_y material family. Interestingly, we observe (i) lower optical bandgaps of the rare-earth oxyhydrides compared to YO_xH_y (ii) variation in photochromic kinetics for different M, and (iii) exceptionally strong photochromism in GdO_xH_y particularly in the NIR spectral region. Furthermore, we find that there is a critical deposition pressure which allows for the ex-situ formation of the oxyhydride. The ex-situ oxidation transition in the air to the photochromic MO_xH_y state can be prevented, by keeping the reactive sputter pressure low. This allows us in fact to identify the conditions for a MH_2 film produced by in-situ reactive sputtering. The formation of transparent photochromic MO_xH_y thin films only takes places after exposure to air when the sample is deposited above a certain critical value of the reactive sputter deposition pressure.

4.2. Experimental

Thin films of yttrium and other rare-earth (Gd, Dy, Er) hydrides and oxyhydrides are prepared by reactive, direct current magnetron sputtering from 2-inch metal targets (99.9% purity) at 100W in an Ar/H_2 gas mixture (5N purity) with 12.5 vol. % of H_2 followed by post-oxidation in air. The films are sputtered on unheated UV-grade fused silica (f-SiO_2) substrates. The deposition system was kept at a base pressure below 3×10^{-6} Pa and the total pressure, "P", during deposition was varied by using a butterfly reducing valve mounted at the turbo molecular pump inlet. Structural, optical, and photochromic properties were investigated by a combination of X-ray diffraction (XRD), optical spectroscopy, and UV excitation.

A Bruker D8 Advance X-ray diffractometer equipped with a Co source (λ= 1.7890 ˚A) and a LynxEye linear detector was used to record X-ray diffraction (XRD) data in Bragg-Brentano geometry. Lattice constants were determined from the (111) and (200) diffraction peak positions obtained by fitting a double Pseudo-Voigt peak function (to account for the Co-$K\alpha_{1/2}$ doublet) to the experimental data. The resulting peak positions were also corrected for instrumental deviations in scattering angle, 2Θ,

by measuring a NIST certified SRM-1976b corundum Al_2O_3 powder standard in the same geometry. The reference patterns from the International Centre for Diffraction Data (ICDD) Powder Diffraction File (PDF) that are used for the discussion of crystal structure of directly sputtered rare-earth dihydrides and rare-earth oxy-hydridres. The complete XRD diffraction patterns of MH_2 and MO_xH_y thin films (thickness range 270 to 330nm) which were used to obtain the lattice constants.

To measure the optical band gap, the transmittance and reflectance of the films are recorded using a Perkin Elmer Lambda 900 Spectrophotometer. This device is equipped with an integrating sphere and uses two radiation sources; a deuterium lamp and a tungsten halogen lamp to cover the working wavelength range of 200 to 2500 nm. A photomultiplier is used in the UV/Vis (200-860 nm) range while a lead sulfide detector is used in the NIR (860-2500 nm) range. In this set up the sample receives one wavelength at a time and the measurements take several minutes. Due to the slow acquisition speed of the Lambda 900, it was only used for 'static' measurements, i.e. before photo-darkening or after several hours of UV illumination when the saturation contrast is reached. In order to follow the time dependence of the photochromic effect, additional 'dynamic' transmittance measurements were performed using a custom-built optical fiber-based spectrometer setup. It consists of a Quartz-Tungsten-Halogen / Deuterium white light source (DH-2000BAL, Ocean Optics) and a Si-based array spectrometer (HR4000, Ocean Optics) covering a wavelength range of 230 to 1050. In this set up only transmittance data are collected all at once, which allows fast measurements. The fast acquisition time is necessary to minimize the influence of the optical measurement on the observed photochromic properties.

For photo-darkening experiments, a low-pressure mercury lamp (Herolab GmbH) was used. The absolute UV irradiance was determined using a calibrated USB-2000+ spectrometer (Ocean Optics) with a relative uncertainty of about 10%. The measured irradiance for each experiment is given in the respective figure captions. The integrated irradiance of the standard AM1.5 solar spectrum1 is 4610 μWcm^{-2} [18] in the same wavelength range as the Herolab UV lamp. For energy threshold measurements, an Osram quartz tungsten halogen lamp type HLX 64640 was used at operating condition of 22 V and 6.4 A. The spectral irradiance of the lamp was measured by a USB2000+RAD spectrometer from Ocean Optics. In addition, an IR filter was used to cut off light with wavelengths longer than 900 nm. The IR filter was placed between the sample and the lamp and was used to avoid thermally bleaching the film. A blowing fan was placed next to the sample to dissipate any heat caused by the lamp and minimize any temperature effect.

The micro-structure of selected films was studied by scanning electron microscopy (SEM) using a FEI NovaNano SEM in immersion mode, which uses an through-lens detector for secondary electrons (TLD-SE). The working distance was around 5 mm and the acceleration voltage was set to 5 kv. For this purpose films were deposited onto Si(100) substrates and sputter coated with 10 nm Au to avoid charging effects. Cross-section imaging was observed in normal incident direction.

4.3. Critical pressure: dihydride to oxyhydride transition

In contrast to what was previously reported by Mongstad et al.[8,9] we do not always obtain transparent and photochromic films after reactive sputtering of Y in Ar/H_2 mixtures followed by exposure to air. Films prepared below a certain critical deposition pressure remain dark metallic upon exposure to air. These films are not photochromic and show a low transmission over the entire spectrum, except for a narrow region in the red part of the visible spectrum (Figure 4.1). Such a transmittance window has previously been reported for yttrium dihydride films by van Gogh et al., in particular in the hydrogen-poor part of the dihydride solubility range (i.e. $YH_{1.9}$).[5] We do not find any systematic correlation of the transmittance window peak wavelength with the cation size or lattice constant (Figure 4.2). The position (wavelength) of the dihydride window has been reported to shift with hydrogen/metal ratio [19,20] (see Figure 4.3a) as well as Y/La ratio in alloyed hydrides.[5]

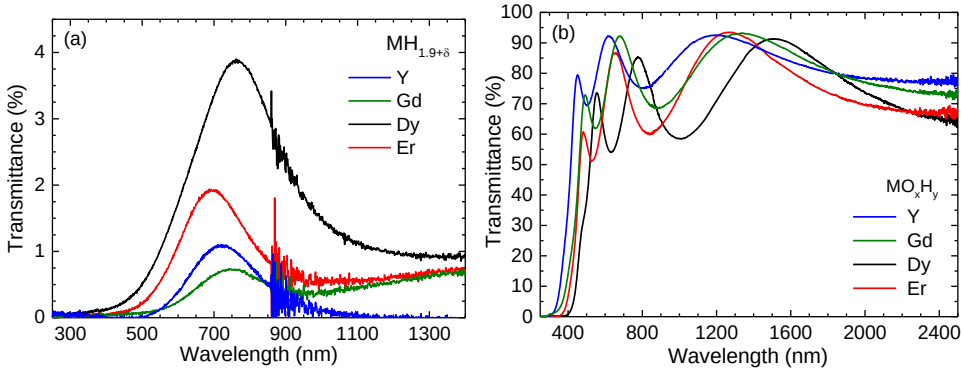

Figure 4.1. (a) Characteristic transmittance window of Y and other rare-earth dihydride thin films directly prepared by reactive magnetron sputtering below the critical deposition pressure. The difference in maximum transmittance is a result of film thickness variation between 188 nm (M=Dy) and 320 nm (M=Gd). These samples appear black metallic upon deposition and remain so when exposed to air. (b) Transmission spectra of YO_xH_y, GdO_xH_y, DyO_xH_y and ErO_xH_y films (thickness between 270 and 350 nm).

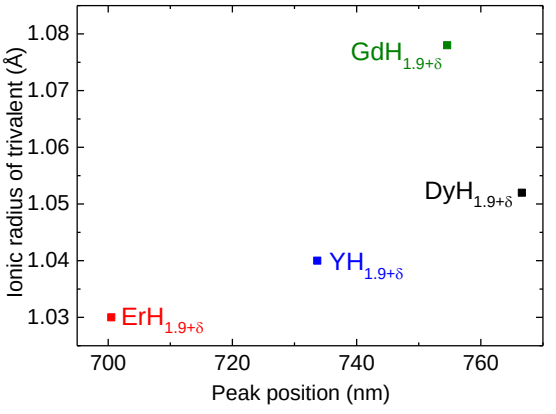

Figure 4.2. Ionic radius of the selected rare-earth metals against the peak position of rare-earth hydrides at the wavelength maximum (ionic radius values taken from reference [21]).

The window is supposed to arise from a combination of small free electron and low inter-band absorption near the plasma frequency. According to the Drude model, electrons are treated as classical particles within a free-electron approximation. Where the equation of motion for the ideal free gas electron gives the dielectric function as:[22]

$$\varepsilon(\omega) = 1 - \frac{\omega_p^2}{\omega(\omega + i\Gamma)} \tag{4-1}$$

With ω_p plasma frequency and Γ is the scattering rate. The plasma frequency is obtained from $\omega_p = \frac{N_e e^2}{\varepsilon_0 m^*}$, where m^* is the effective mass of the electron, e is the charge of the electron, N_e is the electron density per unit volume and ε_0 is the relative permittivity of vacuum.[22] Over a wide frequency range, the optical properties of metals can be explained by the Drude model. In low frequency region below plasma frequency, metals reflect light. Above the plasma frequency, metals transmit incident radiation.

If a perfect dihydride is formed, we expect the ionic radius to change the peak position to some extent. This is because the size of the atoms determines the band structure (property of the material) and it changes the electron density indirectly. In order to show the effect of ionic radius, we have calculated the plasma frequency for ideal dihydride structures. Figure 4.3b shows the calculated plasma frequency for different rare-earth dihydride. Here we can see the trend of increase in plasma

frequency (in nanometer) as the ionic radius increases. Therefore, if we have a perfect dihydride, the peak position will shift as the electron concentration is changing. As we don't have a perfect dihydride film and we don't know the hydrogen concentration in our films, the variation that we see in peak position is most likely an effect of minor changes in the hydrogen/metal ratio, or rather a free electron density, in different samples.

In any case, the observation of the characteristic transmittance window is a strong indicator for the presence of the metallic fcc-dihydride phase (MH_2). Note, that in the work by van Gogh et. al. the metallic thin films were prepared by molecular beam epitaxy and capped with Pd followed by ex-situ hydrogenation step. Our optical and structural analysis demonstrates that stable rare-earth dihydride thin films can be produced directly by reactive sputter deposition i.e., without the need for Pd capping and a separate hydrogenation step.

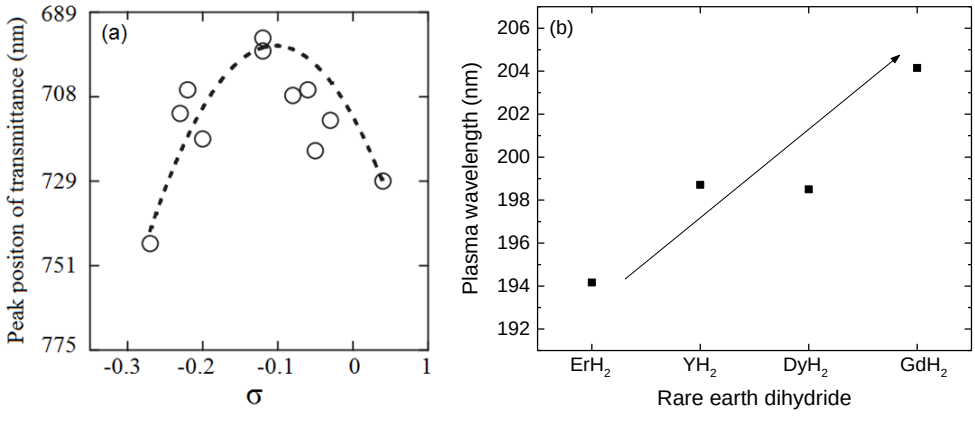

Figure 4.3. (a) Transmittance window peak position for various δ, which is the hydrogen deficient quantity in $YH_{2+\delta}$ (-0.3< δ <0.05). A dashed line is a least-square fit (reused from reference [19]). (b) Change of plasma wavelength ($1/\omega_p$) with different rare-earth dihydride.

All reactively sputtered rare-earth films initially appear black opaque inside the vacuum chamber and in the glove box (P_{O2} <1 ppm), However, depending on the reactive sputter pressure, as soon as they are exposed to air, they may instantly react and become transparent. Figure 4.1b shows the optical transmittance of the rare-earth oxyhydrides prepared above their critical pressures. They appear yellowish transparent due to the absorption of blue and violet light caused by band-to-band excitations. These transparent films have a substantial oxygen content of around 20-30 at. % based on ion-beam analysis results which are comparable to earlier reports.[23] These

transparent materials are referred to as metal oxyhydrides (MO_xH_y). The oxygen uptake of these films from the air is driven by the large difference in formation enthalpy between oxides and hydrides e.g., -1895 kJ/mol [24] for bixbyite-Y_2O_3 vs. -228 kJ/mol [25,26] for YH_2.

The air-oxidation of the MH_2 films that are grown at a higher pressure is most likely related to their higher porosity. The microstructure of sputtered thin films strongly depends on the ad-atom mobility of deposited species, which is controlled by the flux of energetic particles arriving at the film surface (mainly sputtered atoms and back-reflected Ar neutrals) as well as the substrate temperature. These effects result in the well-known structure zone model introduced by Thornton [27] and later refined by Anders [28]. This model was developed to describe the different film morphologies that develop in different pressure and substrate temperature regions as depicted in Figure 4.4. According to this model, the primary process affecting adatom mobility is the surface temperature of the growing film, T_s, and the melting point of the deposition material, T_m.[27,28] In addition, the sputtering gas pressure is taken into account. As shown in Figure 4.4, various characteristic micro-structures were predicted to form based on sputtering pressure and T_s/T_m.[27,28] At low T_s/T_m and high sputtering pressure, Zone 1 forms. The sputtered film has small and elongated grains that form a columnar structure with porous morphology This morphology is a result of low diffusion and low mobility of the atoms adsorbed by substrate surface at low substrate temperatures. Such structure appears in amorphous as well as polycrystalline films. Zone T, a transition state between Zone I and II take place at higher T_s/T_m.[27,28] In this region as a result of higher substrate temperature, the surface diffusion governs the films morphology as in zone II.[27,28] The films are smooth and dense, but still as in zone 1 preserving a fibrous texture. Zone II takes place at $T_s/T_m > 0.3$ where the surface diffusion dominates. The sputtered film in this zone consist of a coarser columnar structure. Increasing the substrate temperature, the crystalline perfection increase, the bulk diffusion dominates and coarse columnar or equiaxed crystallites form.[27,28]

According to this zone model, if we grow films at higher pressures, the average energy of sputtered atoms is reduced due to an increased number of collisions of the energetic particles with the process gas on their way from sputter target to substrate. This effectively reduces the average energy of the impinging particles as the reactive gas pressure during sputtering is increased. As a result, the adatom mobility is low and atoms are generally not displaced from the location at which they attach to the film surface. Thus, they cannot rearrange optimally to the most energetically favorable position when they arrive at the substrate. This decrease in surface mobility leads to

the formation of a film with a high density of lattice imperfections.[27,28] On the other hand, a dense microstructure should be observed for films grown at low reactive sputter pressure due to the higher kinetic energy of arriving sputtered atoms because of the reduced scattering by Ar ions.[27,28] These concepts can qualitatively explain our observation that a critical pressure, p*, exists such that films deposited at p < p* remain stable metallic dihydrides, whereas films deposited above p* transform into semiconducting oxyhydrides upon air exposure. Figure 4.5 shows the SEM cross-section images from yttrium dihydride and oxyhydride films. Both films show columnar structure where dihydride films appears more compact.

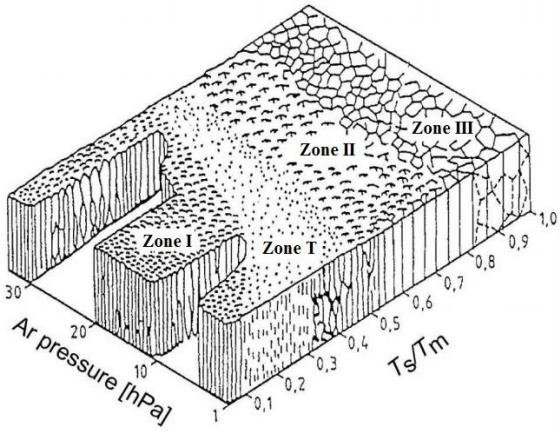

Figure 4.4. Schematic of influence of substrate temperature and argon pressure on the microstructure of sputtered films (Figure reused from reference [27]).

The structure of the films can be classified as Zone 1 or T, where surface diffusion is more pronounced but grain boundary diffusion is limited, leading to competitive grain growth of columnar domains. Oxyhydride film probably exhibits voided boundaries which facilitate oxygen diffusion into the film. Yttrium is a relatively light element in comparison to the other selected rare-earth metals. This means that at the same conditions (power, pressure, Ar/H_2 ratio), the heavier rare-earth based samples are less affected by collisions with argon ions. Hence, higher pressure is needed to obtain a similar porosity. Experimentally, we find $p^*(YO_xH_y) \simeq 0.4$ Pa whereas $p^* \simeq 0.6$ Pa for Gd, Dy, and Er oxyhydrides. This material dependence of p*, and hence MH_2 film density, is likely also attributed to a significant contribution of back-reflected Ar neutrals to the overall energy flux towards the growing films. Both the reflection probability and the average energy of the reflected Ar neutrals increase with the atomic mass of the target.[29,30] Taking into account the large mass difference between the rare-earth metals and Y, a higher gas pressure is required in the case of Gd, Dy,

and Er to achieve similar (porous) thin film micro-structure as in YH_x allowing for air-oxidation and formation of MO_xH_y.

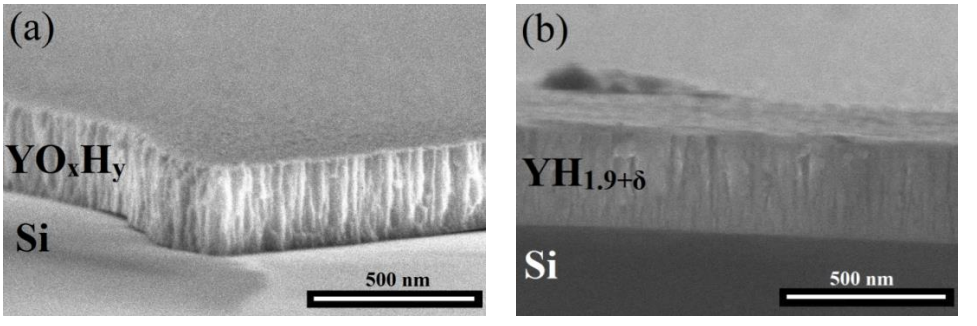

Figure 4.5. SEM cross-section images showing columnar growth morphology in 270 nm (a) yttrium oxyhydride film prepared above critical pressure (0.5 Pa) and (b) yttrium dihydride film prepare below critical pressure (0.3 Pa).

Figure 4.6a shows the XRD patterns of the rare-earth metal hydride films grown at relatively low pressures. All films deposited at pressures below their critical pressure p* (Y at 0.3 Pa and Gd, Dy, and Er at 0.5 Pa) are black metallic upon deposition and remain so when exposed to air. Their diffraction patterns are consistent with the face-centered cubic (fcc) structure of the CaF_2 prototype (space group Fm-3 m) characteristic of the metallic β-MH_2 phases. Figure 4.6b shows the summarized lattice constant values. We find a 0.8–1.2% lattice expansion of these in-situ sputtered dihydride films (full red circles) relative to the reference values taken from ICDD-PDF (open red circles). The DyH_2 and ErH_2 films show a more strong (111) preferred orientation as compared to YH_2 and GdH_2 which suggests that these two latter films are more randomly oriented. The optical and structural analysis of films prepared below the p* confirms that these films have a dihydride nature. The lattice constant value of 5.27 ± 0.01 Å of sputtered yttrium hydride is in agreement with an earlier report by Mongstad et al.[8] We observe significantly smaller lattice constants in Pd capped YH_2, DyH_2, and ErH_2 thin films prepared by sputtering of metal layers in pure Ar followed by a separate hydrogenation step at p_{H2} = 1 bar at RT (full green diamonds). These results are closer to the reference values which represent highly ordered structures obtained by hydrogenation of (bulk) metals at elevated temperatures. Since the Pd capped films were grown using the same sputter targets, substrates, pressure, and discharge power, we can rule out target impurities and energetic particle bombardment effects as the origin of the lattice expansion of the directly sputtered MH_2 films. Instead, it seems plausible that this effect is related to the interaction of H with the lattice. In contrast to hydrogenation, reactive

sputtering can be regarded as a non-equilibrium process. Therefore, a certain amount of disorder of the H sub-lattice may be present in directly sputtered MH_2 films, i.e. a fraction of H atoms occupy the octahedral lattice sites, instead of tetrahedral sites as in the ideal fcc-MH_2 structure.

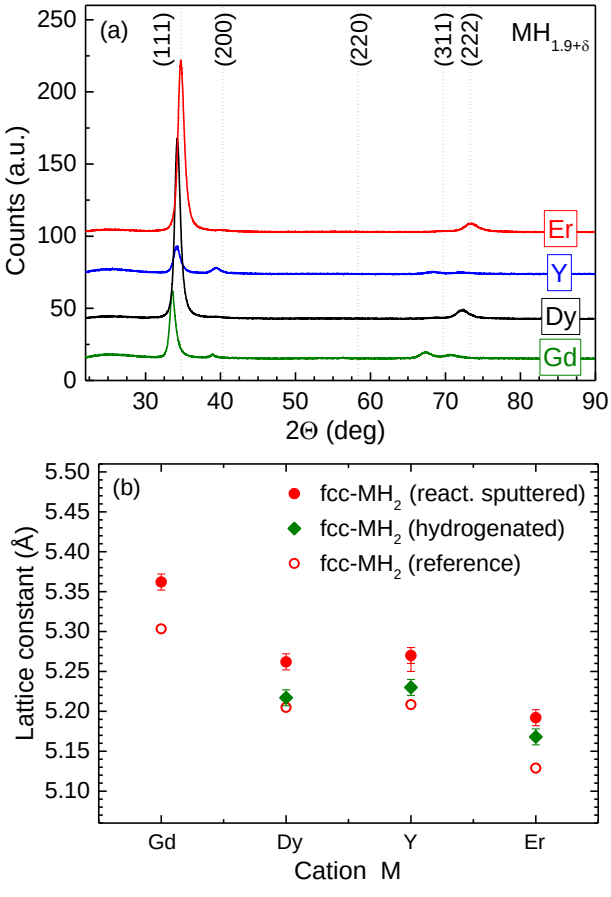

Figure 4.6. (a) shows the XRD patterns of directly sputtered rare-earth metal hydride thin films with different cations M grown below their critical pressures. The vertical lines are peak positions corresponding to fcc-ErH_2 ICDD-PDF pattern #00-06-0141 with a 1.2% expanded lattice constant of 5.19 °A to match the experimental data. The lanthanide contraction effect due to decreasing cation radius with an increasing number of 4f electrons is visible in the systematic shift of the (111) peaks towards higher scattering angles. We find that the dihydride thin films generally show strong (111) preferred orientation (b) Lattice constants of directly sputtered dihydride MH_2 thin films (full red circles), Pd caped MH_2 thin films (full green diamonds). Experimental XRD results (full symbols) from present work are compared to reference data taken from the ICDD-PDF database (open symbols).

Figure 4.7a shows the XRD pattern of air oxidized transparent photochromic oxyhydride MO_xH_y films grown at pressures above p* (Y at 0.5 Pa and Gd, Dy, and Er at 0.7 Pa). It appears that again a face-centered cubic (fcc) phase is formed., The Dy and Er oxyhydride films show an additional (200) peak suggesting a less textured nature compared to dihydride films. The lattice constant values in terms of the different cations, post-deposition oxidation and the effect of critical pressure on the thin film crystal structure are summarized in Figure 4.7b. The MO_xH_y films show a substantial lattice expansion of 1.9–2.8% relative to the corresponding MH_2 films sputtered below p*. This lattice expansion is attributed to the incorporation of oxygen after air exposure. We find a value of 5.37 ± 0.01 Å for YO_xH_y which is within the range of values reported in earlier publications.[9,10] The well-known lanthanide contraction with an increasing number of 4f-electrons is reflected in the systematic decrease of lattice constants of the fcc-MH_2 dihydrides (open red circles) as well as the cubic bixbyite M_2O_3 oxides [24](open blue triangles) with increasing atomic number.

Although Y is not a lanthanide, the lattice constant of Y_2O_3 can be sorted in between Dy and Er. This effect persists in reactively sputtered films as well. Remarkably, the MO_xH_y lattice constants follow the trend of the lanthanide contraction of the bixbyite-M_2O_3 compounds (open blue triangles).[24] Hence, cation substitution allows for the tuning of the unit cell dimensions of rare-earth based MO_xH_y and could thereby enable the tailoring of optical and electrical properties. In addition, for each cation M, the absolute lattice constant of the MO_xH_y is even larger than that of the corresponding structural unit of the bixbyite-M_2O_3 unit cell. While this effect is puzzling at first, it can be explained by a large concentration of H^- ions present in the fcc-MO_xH_y structure.

Considering charge neutrality and attributing formal valencies of M^{3+} and O^{2-}, the valence of H in MO_xH_y can be estimated from the chemical composition data obtained by ion beam analysis (not shown). In fact, we find that charge neutrality is obeyed (within measurement accuracy) only if we assign a valence of –1 to H, whereas assuming H in the form of H^+ or OH^- would result in a violation of the charge neutrality. Interestingly, Miniotas et al. arrived at the same conclusion about the role of H in GdO_xH_y thin films.[31] Hence, in a simplified picture, we can regard the expanded fcc-MO_xH_y structure as a bixbyite-M_2O_3 structure where O^{2-} is substituted by $2H^-$ where the additional H^- may occupy both the structural O vacancies of the bixbyite lattice and the octahedral positions in the fcc lattice. This may result in a smaller Madelung interaction and hence a large lattice volume. Further experiments are required to directly confirm the presence of H^- ions in MO_xH_y materials.

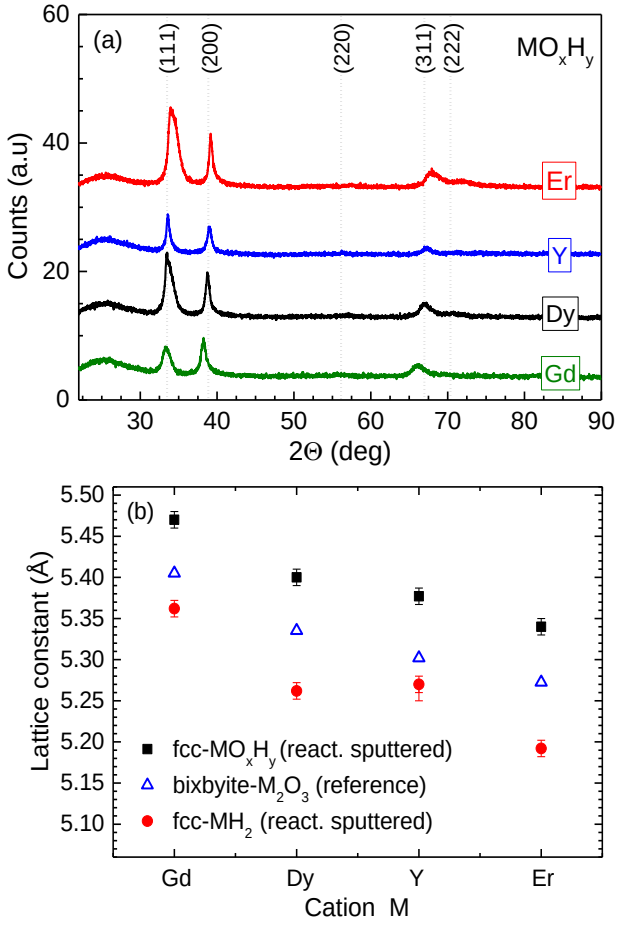

Figure 4.7. (a) XRD patterns of rare-earth oxyhydride thin films with different cations M. The vertical lines are peak positions corresponding to fcc-YH_2 ICDD-PDF pattern #04-06-6935 with a 3.3% expanded lattice constant of 5.38 °A to match the experimental data. The lanthanide contraction effect due to decreasing cation radius with an increasing number of 4f electrons is visible in the systematic shift of the (200) and (311) peaks towards higher scattering angles. (b) Lattice constants of Yttrium and lanthanide-based dihydride MH_2 (full red circles), oxide M_2O_3 (open blue triangle), and photochromic MO_xH_y oxyhydride (full black squares) thin films. Experimental XRD results of the present work (full symbols) are compared to reference data taken from the ICDD-PDF database (open triangles). Note that due to the structural similarity to the fcc unit cell only $\frac{1}{2}$ of the bixbyite M_2O_3 lattice constant is shown here.

4.4. Photochromic effect and change of absorption coefficient

We estimated the optical band gap of the films using a Tauc plot. The absorption coefficient, $\alpha(\lambda)$, is calculated from the transmittance and reflectance spectra shown in Figure 4.8 using the following expression $T(\lambda) = [1 - R(\lambda)] \exp[-\alpha(\lambda)d]$, where d is the thickness of film and $R(\lambda)$ and $T(\lambda)$ are the measured reflectance and transmittance.[32] The optical band gap can be estimated by linear extrapolation of a plot of $(\alpha h\nu)^{1/m}$ as a function of the photon energy to zero absorption. The band gap is found at the x-intercept.[33] m is a coefficient that denotes the nature of the band gap. For direct band gap material m = 1/2 and for an indirect band gap m = 2.[33] The best Tauc fits are obtained with an exponent of m = 2 indicating that the bandgaps of all oxyhydrides are indirect. This also confirmed by our experimental findings where the minimum energy required to create photo-darkening matches the band gap defined in this way.

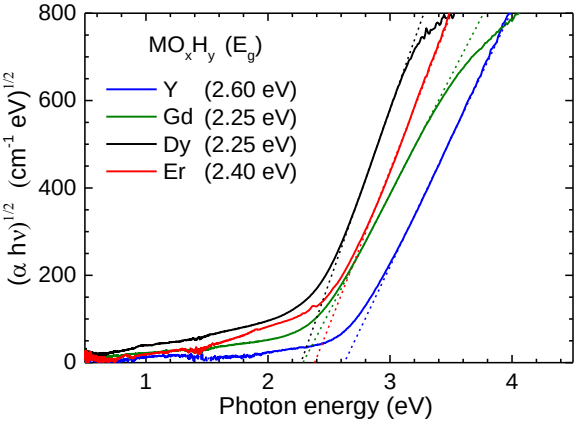

Figure 4.8. Tauc plot for determination of the indirect optical band gap, Eg, of MOxHy thin films for various cations M. The dashed lines are linear fits of the absorption edge extrapolated to zero absorption. The film thicknesses are in the range of 270 to 350 nm. Taking into account the uncertainties of the measured absorption coefficient and linear fitting, we estimate an experimental uncertainty of about ΔE_g=0.05 eV.

Using m = 1/2 as the exponent in the Tauc plot (assuming a direct bandgap) would result in band-gap values approximately 1 eV larger than given above. Perhaps the only comparison available is a report by Miniotas et al. stating E_g =(3.260.2) eV for a $GdO_{0.6}H_{1.53}$ (19 at. % O) thin film.[32] Since the oxygen content is very close to our GdO_xH_y material and not all analysis details were disclosed, they very likely overestimated the bandgap value by assuming a direct transition. Employing the Tauc plot method, we find that YO_xH_y has a bandgap of E_g =(2.60 ± 0.05) eV consistent

with earlier reports.[8,9] The lanthanide oxyhydrides have lower bandgaps of 2.40 eV (ErO_xH_y) and 2.25eV (GdO_xH_y and DyO_xH_y). This confirms the general notion that the bandgap of the MO_xH_y oxyhydrides is substantially lower than that of the corresponding bixbyite-M_2O_3 oxides (4.9–5.4 eV).[24,34] Just below the band edge in the absorption spectra of each material we observe the so-called Urbach tail. The data shows a long absorption tail for higher wavelengths, which extends to the visible part of the spectrum.

All the oxyhydrides we have investigated show photochromic behavior as displayed in Figure 4.9a. UV illumination causes a decrease of transmittance for all MO_xH_y films, in a wide spectral range from E_g to 2500nm and beyond. We did not observe any change of E_g due to photo-darkening. The corresponding wavelength-dependent optical absorption coefficient changes are shown in Figure 4.9b. The change of absorption coefficient between the two states is not homogenous across all wavelengths and a broad maximum of the photochromic response is observed in each material. While for M=(Y, Dy, and Er) the photochromic behavior is similar in magnitude ($\Delta\alpha_{max} \simeq 20\ 000\ cm^{-1}$) with a strong decrease towards the NIR, GdO_xH_y shows an unusually strong photochromic response extending far into the NIR. In general, for each material, the optical contrast is a function of film thickness and illumination conditions. Thus, in order to compare the photochromic performance of the different oxyhydride materials, another set of samples of the same thickness (300 nm) was illuminated under the same conditions followed by bleaching in dark conditions at room temperature. To study the kinetics of the photochromic effect, we plot the average transmittance over the wavelength of 450-1000 nm as a function of time.

We define the (absolute) photochromic contrast $\Delta T(\lambda,t)$ as the change of transmittance with respect to the initial value, T_0, in the bleached state before UV-illumination, i.e., $\Delta T(\lambda,t) = T_0((\lambda,0) - T(\lambda,t)$. A comparison of the time-dependent and spectral averaged contrast, $\langle\Delta T\rangle$, is shown in Figure 4.10. YO_xH_y is the most transparent material in the bleached state ($\langle\Delta T_0\rangle$ = 79.8%) while the lanthanide oxyhydrides are initially less transparent ($\langle\Delta T\rangle$ = 67.9–71.3%). These differences are mainly due to the lower bandgap and higher sub-bandgap absorption (Urbach's tail)[37] present in the lanthanide oxyhydrides (see Figure 4.8).

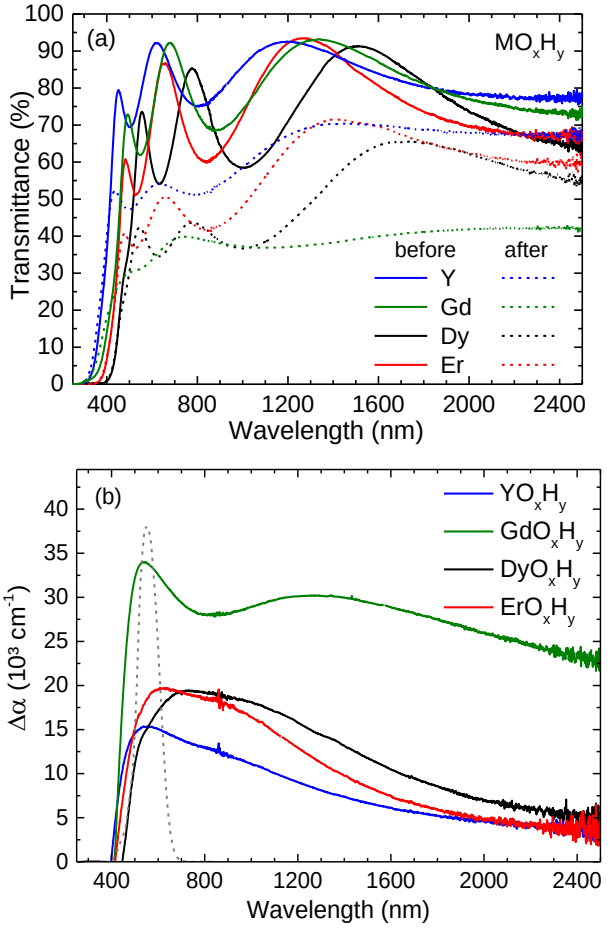

Figure 4.9. Photochromic response of Y and lanthanide oxyhydride thin films (thickness between 270 and 350 nm) after 5 h of UV illumination at 5070 μWcm^{-2}. (a) Transmittance before (solid lines) and after photo-darkening (dotted lines). (b) Corresponding change of the absorption coefficient. Note that the absorption coefficients are calculated taking into account the reflectance R(λ) (not shown) using the expression T(λ)=[1 - R(λ)] exp[–α(λ)d].[32] The normalized human eye luminosity function according to Sharpe et al.[35] is shown as a dashed curve in (b).

During photo-darkening, all materials initially show a fast (nearly exponential) increase of contrast followed by a slow change with nearly linear behavior until the light source is switched off after about 8 hours. In particular, GdO_xH_y and YO_xH_y show a fast photochromic response and reach large optical contrast values of ⟨ΔT⟩ = (25–33)% already after 15 min of illumination. While the maximum optical contrast values of Y, Dy, and Er are comparable ⟨ΔT⟩ = (33–37)%, a significantly higher maximum

contrast of ⟨ΔT⟩ = 45.5% is observed for Gd. According to Figure 4.9b, this enhanced photochromic contrast is a result of the large absorption coefficient change of GdO_xH_y, especially in the NIR range. The kinetics of ⟨ΔT(t)⟩ during bleaching are well described by an exponential decay function ⟨ΔT(t)⟩ ∝ exp $(-t/\tau_B)$ using the (thermal) bleaching time constant, τ_B, as a fitting parameter. We find that DyO_xH_y bleaches the fastest (τ_B = 215 ± 15 min), followed by Y and Gd, while ErO_xH_y shows the slowest bleaching rate of all materials (τ_B = 1260 ± 80min). Our ongoing studies indicate that the bleaching kinetics not only depend on the cation but also on sputter deposition parameters and illumination conditions. Therefore, additional experimentation is required for a more quantitative comparison.

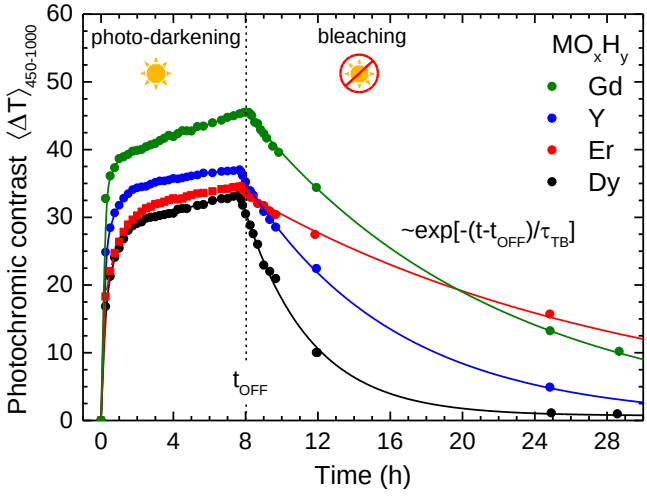

Figure 4.10. Wavelength average optical contrast of Y and lanthanide oxyhydride films (d=300 nm) during UV illumination at 5860 μW cm^{-2} followed by (thermal) bleaching in the dark. The spectral averaging between 450 and 1000 nm effectively reduces the influence of optical interference patterns on ΔT(t).

4.5. Absence of photochromic effect in YH_3 thin films

The photochromic effect at ambient conditions is observed in reactive magnetron sputtered REO_xH_y thin films. When YO_xH_y was first reported, initially it was speculated that its properties could be explained in analogy to the transparent γ-YH_3 phase which may stabilize in the fcc instead of hcp structure because of the incorporation of oxygen into the lattice.[9] They reported atomic ratios of up to H/Y ≈ 3 in their elastic recoil detection (ERD) and nuclear reaction analysis (NRA) measurements.[37] However, the low H_2 partial pressures during reactive sputtering make the formation of YH_3 film improbable. Earlier in this chapter, we showed that REO_xH_y (where RE = Y, Gd, Dy, Er) is in fact formed by air oxidation of as-deposited metallic β-REH_2 (where RE = Y, Gd, Dy, Er) films.

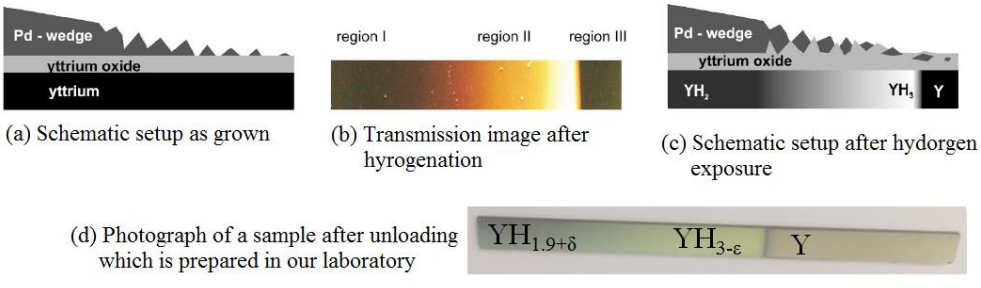

(a) Schematic setup as grown

(b) Transmission image after hyrogenation

(c) Schematic setup after hydorgen exposure

(d) Photograph of a sample after unloading which is prepared in our laboratory

Figure 4.11. Schematic representation of a thin film of Y with a Pd capping layer of different thicknesses.[38] (a) As grown film (b) after hydrogenation (c) after unloading. Here the authors exposed the as-grown Y layer to air before growing the Pd capping layer. The results are similar if the Pd capping layer is grown directly on Y film. The nature of the underlying yttrium surface determines the Pd critical thickness at which $YH_{3-\varepsilon}$ is observed during unloading. Larger Pd thickness is required if Pd is grown on yttrium surface immediately. (d) Photograph of 150 nm Y cap film with Pd gradient capping layer after unloading. A pressure cell at 1 bar of H_2 was used in our laboratory. Here Pd capping layer is grown directly after Y deposition.

In order to show whether or not YH_3 exhibit photochromic properties, a thin film of metallic Y is grown by DC sputtering technique, followed by growing Pd capping layer with gradient thickness ranging from zero to few nanometers. The Pd layer acts as a catalyst for hydrogen dissociation and absorption. Depending on the Pd capping layer thickness, the film has divided into three regions (Figure 4.11a).[38] Upon exposure to hydrogen, Pd allows hydrogen to diffuse into the metallic yttrium layer to form a face-centered-cubic metallic $YH_{1.9+\delta}$ phase and upon a further increase of the hydrogen concentration the hexagonal $YH_{3-\varepsilon}$ phase is formed [38]. The metal-insulator

transition can be verified in the transmission image in Figure 4.11b. The optical transmission of a YH_x film provides a direct indication of the amount of hydrogen in the yttrium film. The dihydride-trihydride phase transitions are reversible at room temperature by changing the surrounding hydrogen gas pressure. During unloading, In region I with thicker Pd capping layer, $YH_{3-\varepsilon}$ reverse back to dihydride phase. This is due to full coverage of this region with Pd.[38] In region II, the film is covered by nonconnected Pd clusters instead of continuous film.[38] In this region, the Pd will be covered by YO_x and as a result the film stays in the trihydride phase after unloading.[38] Figure 4.11d shows the hydrogenated Y film with Pd capping layer in our laboratory. The same three regions are observed.

Transmittance spectra of these regions are presented in Figure 4.12a together with their XRD diffraction patterns. Region III shows that it is metallic yttrium with a hcp crystal structure. Region I shows a transmittance window in the range of 1.5–2.0 eV characteristic of metallic β-$YH_{1.9+\delta}$ dihydride and its XRD pattern confirms a fcc structure is formed. In region II, the opening of an indirect optical band gap of 2.4 ± 0.2 eV is observed with hcp crystal structure corresponding to $YH_{3-\varepsilon}$ phase. Notably, exposure of such a film to 4 hours of UV light results in no photochromic effect (Figure 4.12c&d) This illustrates the importance of composition and how crucial the presence of both oxide and hydride ions are in observing the photochromic effect in REO_xH_y thin films.[23]

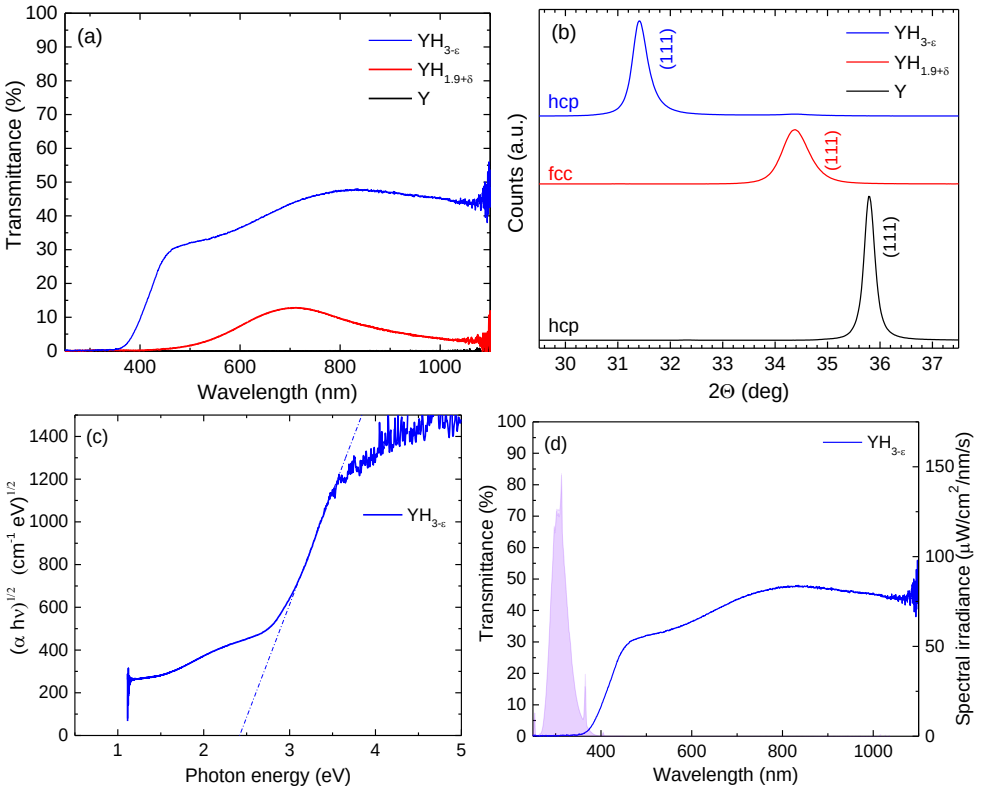

Figure 4.12. (a) Transmittance spectra and (b) XRD patterns (b) of Y thin film with Pd gradient capping layer corresponding to region III (metallic phase), I ($YH_{1.9+\delta}$ phase) and II ($YH_{3-\varepsilon}$ phase). (c) Tauc plot of the sample corresponding to region II ($YH_{3-\varepsilon}$ phase) indicating a band gap of 2.4 ± 0.05 eV (using only transmittance data). (d) Photochromism was not observed in the sample corresponding to region II ($YH_{3-\varepsilon}$ phase), illuminated for four hours using UV light with emission lines centered around λ = 310 nm and 5151 μW/cm² total irradiance.

4.6. Energy threshold: minimum photon energy required to obtain photochromic effect in rare-earth oxyhydride

At present, the nature of the photochromic mechanism in rare-earth oxyhydride is under debate. In general, the type of inorganic solids that shows the photochromic effect has a large band gap where negligible optical absorption is observed in the material's un-activated state in the visible region of the spectrum.[39] A characteristic color of a photochromic material arises from the formation of metastable color centers by trapping of free carriers that absorb light in the visible region.[39] These metastable centers form as a result of electron-hole pair formation due to absorption of photons with energies corresponding to the band gap of the material.[39,40] This causes the optical excitation of electrons from the valence band or an impurity level close to valance band to the conduction band.[39,40] At present, there is still little known about the photochromic mechanism in YO_xH_y thin films. In the following experiments, we demonstrate that photon energies larger than the band gap of rare-earth oxyhydride are required to create a photochromic effect. Electronic transitions induced by absorption of photons and the minimum energy for this transition is determined from the spectral responsivity of the films to different photon energies. We found that the photochromic effect strongly depends on the wavelength of the light and there is a minimum energy required to trigger photochromism. Figure 4.13 shows the spectral irradiance produced by a quartz tungsten halogen lamp in combination with an IR filter (to minimize heating during illumination) and different long pass filters. The filters are named after their cut on wavelength, which is defined as the wavelength after which the transmittance increases to 50% throughput (Figure 4.14). However, this means these filters transmit light at a shorter wavelength than their cut on wavelength. In order to accurately find the minimum energy required to observe the photochromic effect, we determined the stop-band limit value for each filter. Stop-band limit corresponds to a wavelength after which the transmittance goes to zero. The determined values are within the error of the noise produced by the detector (Figure 4.14).

Figure 4.15a&b shows the optical response of 300 nm films of YO_xH_y and GdO_xH_y as a function of exposure to radiation of different wavelengths over time. Before every exposure, the sample was fully bleached to its original state (T_0) before illumination. Each subsequent light exposure was done with a filter with a lower cut on wavelength. Each illumination step was carried on until saturation contrast was observed, indicated by reaching a plateau in average transmittance curve. From Figures 4.15a&b, it is clear that as the energy of the photons increases, the curves follow an exponential decay trend.

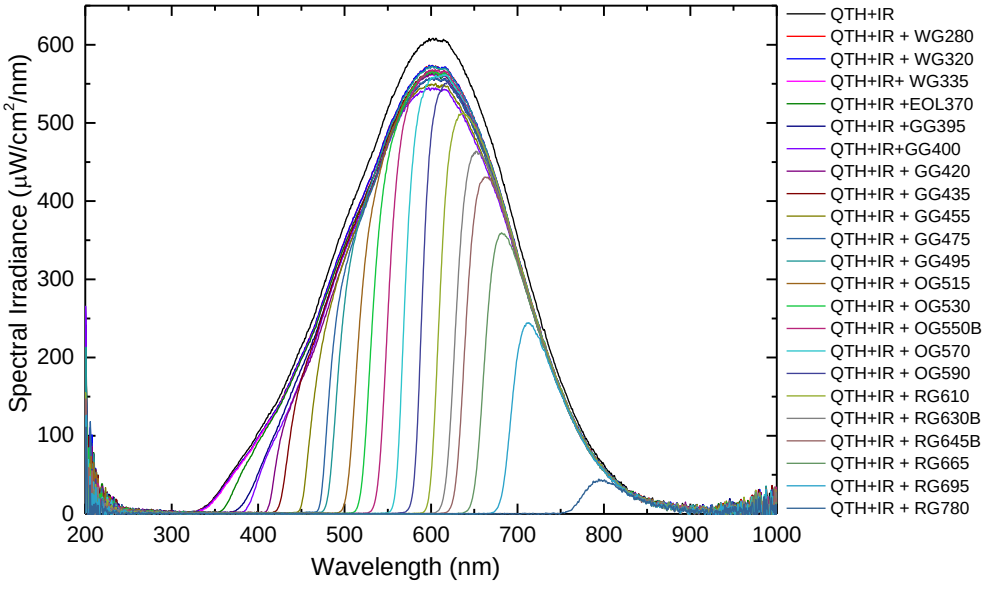

Figure 4.13. Spectral irradiance of the QTH lamp in combination with IR and long-pass filters (values shown on the legend indicate the cut on the wavelength of the long pass filters).

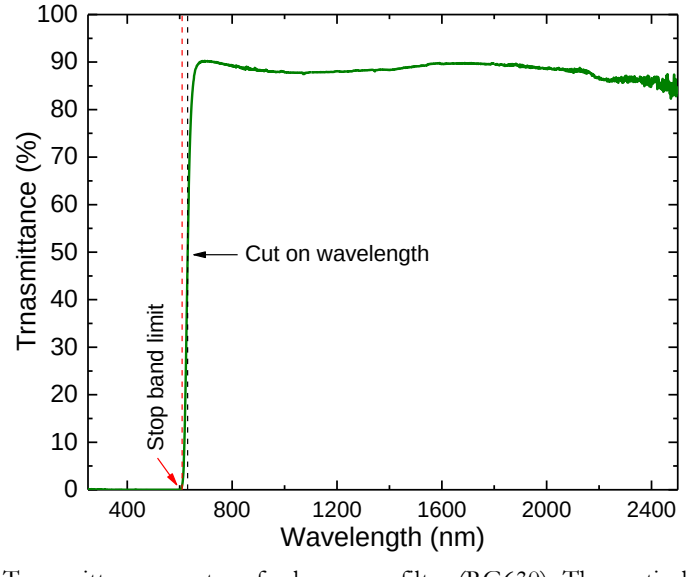

Figure 4.14. Transmittance spectra of a long pass filter (RG630). The vertical lines are the cut on wavelength (back dashed line) and stop band limit (red dashed line)

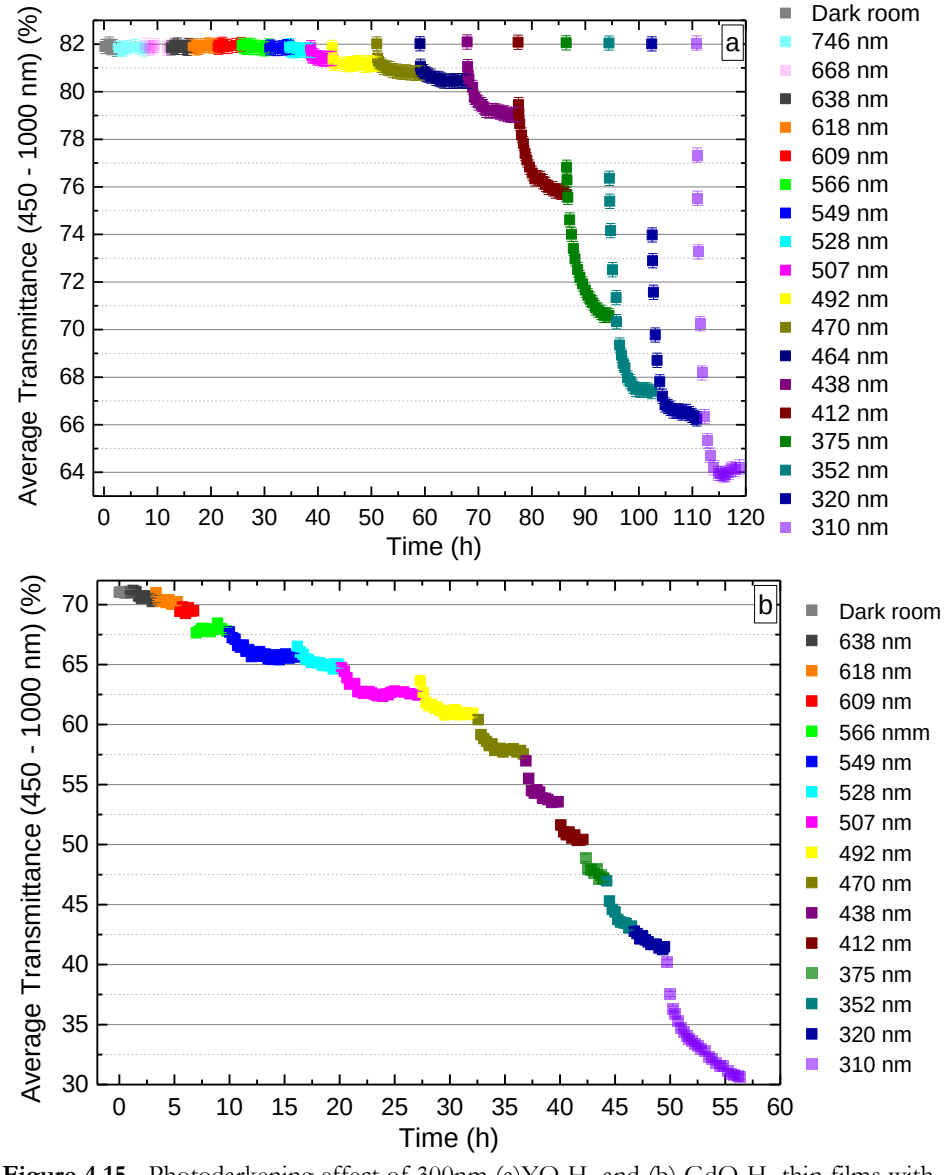

Figure 4.15. Photodarkening effect of 300nm (a)YO_xH_y and (b) GdO_xH_y thin films with QTH lamp in combination with IR and long pass filters (the wavelength values shown here are the stop band limit, corresponding to wavelength after which light is transmitted). The samples are subjected to multiple illuminations starting from exposure to longer wavelengths. After each illumination, the sample is allowed to relax (bleach) back to its initial state characterized by the maximum transmittance. In GdO_xH_y the time between each illumination experiment varied depending on how long it took for a sample to bleach and was not always the same. Therefore the initial values are taken out from the graph and each subsequent illumination is shown in continuation of the previous darkening experiment. .

Next, the (absolute) photochromic contrasts were calculated and plotted vs the stop band limit of each filter (see Figure 4.16). Here the darkening of the MO_xH_y (M=Y, Gd) can be directly related to their optical absorption edge of the material. It appears that the darkening follows the absorption curve suggesting its relation to the excitation of electrons to the conduction band. The analysis of data indicates that the photochromic effect requires a band gap excitation. The activation energies for YO_xH_y (E_g = 2.60 ± 0.05 eV) and GdO_xH_y (E_g = 2.25 ± 0.05 eV) were found to start below the corresponding band gap of these materials - starting with the optical contrast values of (⟨ΔT⟩ = 0.5%) at a stop band limit of 507 nm for YO_xH_y, slightly below its band gap.

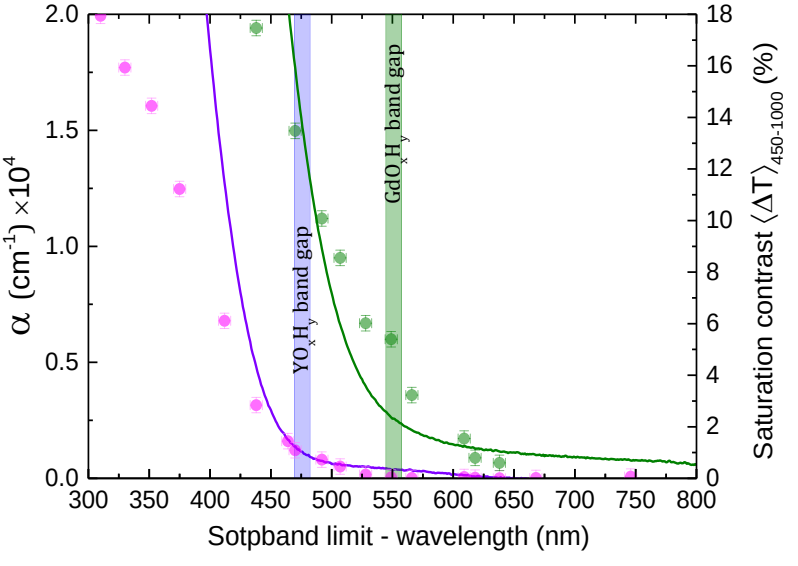

Figure 4.16. Saturation contrast vs stop band limit (long pass filter) for (a)YO_xH_y thin film with a band gap of E_g =(2.60 ± 0.05) eV and (b) GdO_xH_y thin film with a band gap of E_g =(2.25 ± 0.05) eV films. The saturation contrast values were obtained from darkening curves in Figure 4.15a&b. The optical band gap values are determined using the Tauc plot method.

An optical contrast value of (⟨ΔT⟩ = 0.5%) was observed at stop band limit of 638 nm for GdO_xH_y which is way below the band gap of this material. One possible explanation is the longer absorption tail GdO_xH_y sample. Long absorption tail suggests structural disorder, indicating the presence of defects and vacancies.[41] This implies that the amount of such structural defects is substantially higher in Gd as compared to the Y-based film, suggesting a different level of defects present. Distribution of defect states within the forbidden gap and excitation from defect

levels within the gap in GdO_xH_y could be a possible explanation for the start of activation energy at values much lower than the band gap of GdO_xH_y film in comparison to YO_xH_y film. The difference in defect density between the samples will, therefore, be useful in the further analysis of the nature of the photochromic effect.

4.7. Reproducibility of the photochromic effect and the so-called memory effect

In order to investigate the reproducibility of the photochromic effect, the samples are subjected to multiple illumination cycles. The reproducibility of the photochromic effect indicates that the history of a sample is not important. In our experiment after each illumination cycle, the sample is allowed to relax (bleach) back to its initial state characterized by the maximum initial transmittance. The cyclic illumination experiments so far indicate the presence of a memory effect. This means the previously irradiated area shows faster darkening when illuminated the second time. This can be observed as a change of contrast, i.e. the difference in transmittance between initial and illuminated state. Figure 4.17 shows the contrast $\langle \Delta T \rangle$ increases after every cycle. The photochromic behavior clearly is different from the first cycle to the following cycles in terms of contrast and bleaching speed. The photochromic contrast increases by 5% from the first cycle to the second. This indicated that the sample somehow remembers its darkened state and occupies it easier in the following cycle. The contrast only changed slightly from the second to the fourth cycle. We also observed that the bleaching constant, τ_B, is increased from $\tau_B = 57 \pm 5$ min for the first cycle to $\tau_B = 179 \pm 10$ min for the 2nd cycle, 295 ± 30 for the 3rd cycle and to 578 ± 37 min and 552 ± 45 min for the 4th and 5th cycles. The results indicate that a reproducible behavior is observed after multiple cycles. Therefore, what is important is the cumulative illumination time and it is expected that after a sufficient number of illumination cycles the sample stabilizes. Longer illumination time would be an alternative in establishing stabilized samples. It is important to note that the presence of the memory effect does not disappear even if the sample is kept in the bleached state for a longer period of time. This indicates some structural changes are occurring that affects the photochromic dynamics. The XRD data did not reveal any difference between the cycles.

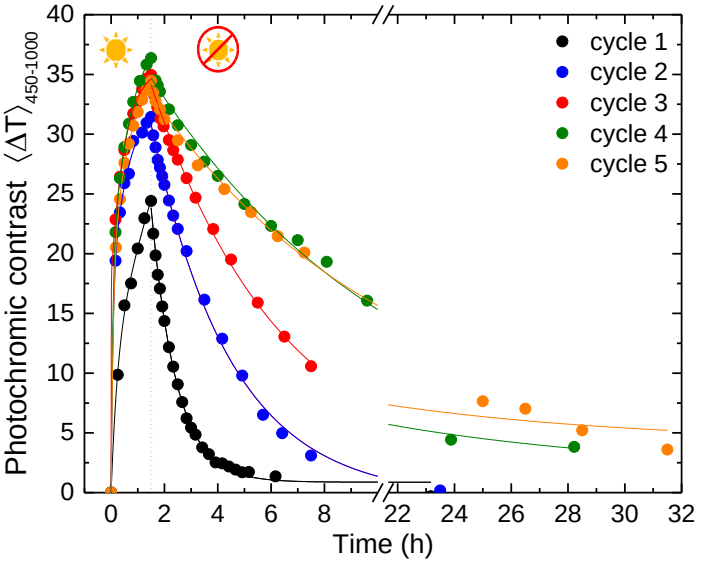

Figure 4.17. Multiple illumination cycles of 350 nm YO_xH_y thin film. Using a UV lamp at 5860 μW cm^{-2} total irradiances for 90 min followed by thermal bleaching in the dark.

4.8. Optical bleaching

As discussed earlier the photochromic process is a reversible reaction as shown upon removal of the exciting light source. The bleaching process may occur by exposing the material to longer wavelengths (optical bleaching) or thermally (thermal bleaching) or both.[6] In the photochromic section, we showed thermal bleaching at room temperature for all our samples, where the fastest time constant was around 200 min. Bleaching in the dark and at room temperature is typically very slow because of the presence of the energy barrier for the backward reaction which can be overcome by increasing the temperature or optical bleaching. Optical bleaching corresponds to photons with smaller energies than excitation energy which can considerably reduce the bleaching time constant. This optical phenomenon has been observed in silver halide doped glasses which has been discussed in chapter 3. We suspect some similarities in our photochromic materials to a well-known example of inorganic photochromic materials, silver halide doped glasses. In these glasses, the photochromic behavior involves the interaction of light with delocalized defects.[42] Here we investigate if optical bleaching accelerates the reverse reaction in YO_xH_y and GdO_xH_y by illumination with photons with energies below their band gap. Previously we demonstrated that photons with energies above the band gap lead to photo-darkening.

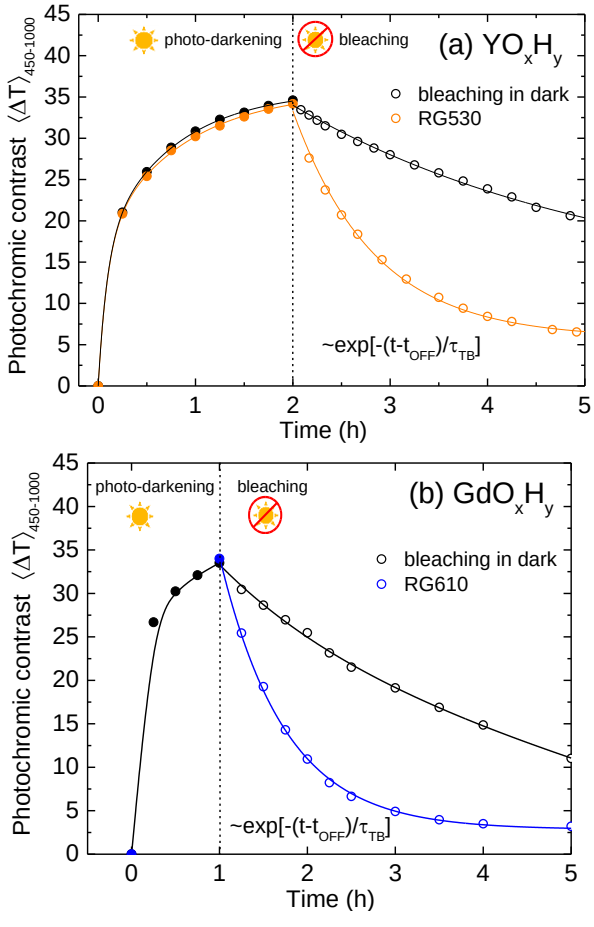

Figure 4.18. Analysis of optical bleaching kinetics on YO_xH_y and GdO_xH_y thin films (350 and 309 nm respectively grown above their critical pressure).

The photo-darkening leads to optical changes occurring in a wide spectral range starting from E_g of the material to 2500 nm and beyond. The difference in absorption coefficient in darkened state and bleached state suggest a wide spectral region available for optical bleaching. Maximum energy for optical bleaching corresponds to photons with lower energies below the band gap of the material. In order to show the effect of optical bleaching, two sets of YO_xH_y and GdO_xH_y were selected and illuminated with UV light under the same conditions (Figure 4.18a & b). After films reached a similar absolute contrast ($\langle\Delta T\rangle \approx 35\%$), the illumination was stopped. In each material, one sample was let to bleach in dark conditions at room temperature while the other samples are exposed to longer wavelengths of light above their band gap. Quartz tungsten halogen lamp was used as a light source coupled with the IR filter to prevent

samples from heating up. A 610 nm filter was used for YO_xH_y film and a 530 nm filter for GdO_xH_y film. A blowing fan was used to minimize any temperature effect.

The kinetics of $\langle \Delta T(t) \rangle$ during bleaching are described by an exponential decay function where, τ_B, is bleaching time constant. We find that films bleach the slowest (τ_B = 204 ± 19 min for GdO_xH_y and τ_B = 220 ± 19 min for YO_xH_y) in the dark. Bleaching process becomes faster when the films are exposed to the light of longer wavelengths. The bleaching time constant reduces to 44 ± 5 for GdO_xH_y and 50 ± 10 for YO_xH_y. These experiments indicate the possible existence of optical bleaching in our materials. The thermal bleaching rate is very slow and the bleaching process can be accelerated by illumination with long wavelength light. However, the effect of heat cannot completely be ruled out. Although the IR filter cut off wavelength is longer than 900 nm and a blowing fan was used, the surroundings of the sample warmed up due to the lamp heating up. The photon energies associated with optical bleaching still need clarification. Radiation at a different wavelength with the use of laser or LED as a light source can help us confirm the presence or absence of optical bleaching. Furthermore, we yet have to find out if optical bleaching threshold exists.

4.9. Applicability of these materials

Smart window technology is developed in order to improve the energy efficiency of residential and office buildings. These windows are developed to regulate solar heating and day light illumination in buildings. A possible way to realize such windows is the use of photochromic materials. Photochromism of rare-earth metal oxyhydrides is promising for application in energy saving smart windows due to their long term stability and the fact that the photo-induced darkening does not depend on UV light only. This is a promising feature, enabling us to design a material that also darkens at the inner glass surface of a double glazed window pane. This allows us to have a photochromic coating between two window glass panes which can protect the coating material from environmental conditions and provide long term durability. Figure 4.19 shows 1 sun irradiance, the sensitivity of the human eye, the optical transmittance of 1 mm borosilicate glass (typical window glass material) and the band gap of different rare-earth oxyhydrides. We demonstrated in the previous section that the photodarkening is triggered by photon energies around the band gap of the material. we also showed that the optical band gap, photochromic contrast and wavelength range of photochromic response depend on the type of cation used. As some part of UV light is blocked by the window pane, there is a limited energy range from sunlight for photo-darkening to take place. Window glass blocks most of UV radiation while

allowing transmission of visible light into the interior.[43] Figure 4.19 shows that light with wavelengths above 300 nm is transmitted through 1 mm borosilicate window glass, while below 300 nm is blocked. Depending on rare-earth material used, the wavelength region between 300 nm until the band gap can contribute to the darkening of the film behind the glass that can photo-darken a film. Tailoring of the bandgap of the material (band gap larger than 2.6 eV is favorable) allows us to have a colorless photochromic window which remains active behind a glass pane. The optical band gap of these materials can be tuned and adjusted by growing these films at higher deposition pressures, which leads to the higher porosity of films and films that are more oxygen-rich. Alternatively, oxygen can be added during deposition to increase the band gap. This enables one to tailor the photochromic response for energy saving smart windows. In case a coloration of the window is allowed, the use of different cations or combination of them allows us to obtain such a tuning.

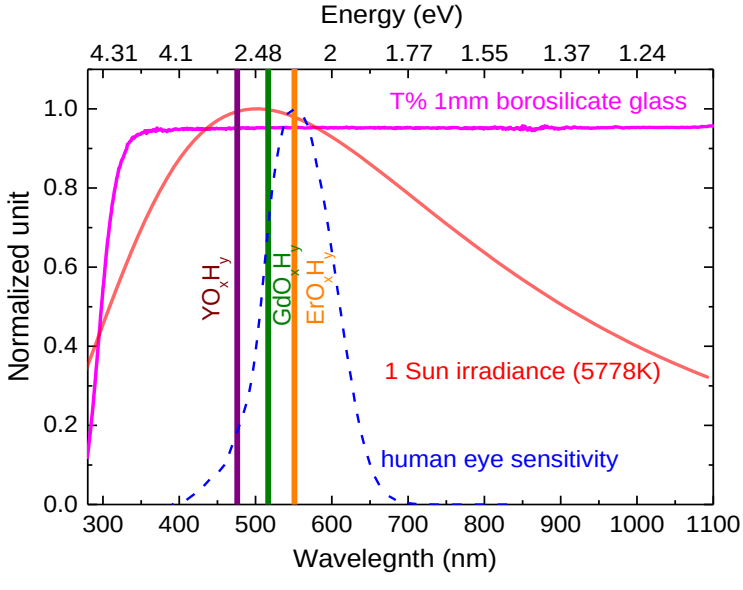

Figure 4.19. The pink line on top shows the transmittance of 1 mm borosilicate window glass. The blue dashed curve indicates the normalized human eye luminosity function according to Sharpe et al.[35] The red line is 1 sun irradiance. The region available from sunlight behind the window at which can darken the film depends on the material that is used. The vertical lines indicate the band gap of different rare-earth oxyhydrides.

What makes these materials interesting is that the darkening is color neutral; and covers the sensitivity of the human eye. The photochromic contrast starts from E_g and extends up to the Mid-IR region, especially in case of GdO_xH_y. GdO_xH_y thin

films show the strongest photochromic contrast (up to 45% at only 300nm film thickness) in a very wide spectral range. These materials are suitable for the light-modulation in the visible as well as a barrier for heat irradiated by the sun at longer wavelengths. Such properties make the rare-earth oxyhydrides ideal for application such as smart windows for energy efficient buildings.

4.10. Conclusion

In conclusion, our work demonstrates that stable lanthanide dihydride thin films can be grown directly by reactive magnetron sputtering. Rare-earth metal oxyhydride MO_xH_y (M=Gd, Dy, Er) thin films exhibit a photochromic effect similar to YO_xH_y suggesting a common physical mechanism, (iii) initial transmittance, photochromic contrast values, and photo-darkening speed are promising for applications such as smart windows. Cation alloying is a viable approach to tailor the photochromic properties of MO_xH_y because they share the same fcc-structure while the optical bandgap, photochromic contrast, and bleaching rate vary substantially between different cations. The photon energy required to obtain a photochromic effect is given by the optical band gap of the material, as shown in the energy threshold measurements. Photon energies larger than the band gap are require to photo-darken the rare-earth oxyhydrides. The photochromic process is reversible and bleaching occurs through thermal bleaching or interaction with the light of longer wavelengths (optical bleaching). The latter needs to be confirmed with further experiments. We have shown that YH_3 does not exhibit photochromic properties, revealing the importance of the presence of both oxide and hydride ions for the photochromic effect in rare-earth oxyhydrides. We noticed a memory effect in contrast and bleaching time constant upon illumination cycling. A stabilized photochromic behavior is observed after multiple illumination cycles or longer illumination time. We suggested a permanent change from the initial cycle and the following cycles that cannot be reversed. Photochromism in rare-earth oxyhydride has the benefit that photo-darkening is induced by UV as well as visible light. This is a promissing feature for the use of these materials in double glazed windows.

References

[1] J. N. Huiberts, R. Griessen, M. Kremers, A. T. M. van Gogh, N. J. Koeman, J. P. Dekker*, et al.*, "Yttrium and lanthanum hydride films with switchable optical properties," *Journal of Alloys and Compounds,* vol. 253-254, pp. 44-50, 1997.

[2] J. N. Huiberts, J. H. Rector, R. J. Wijngaarden, S. Jetten, D. de Groot, B. Dam*, et al.*, "Synthesis of yttriumtrihydride films for ex-situ measurements," *Journal of Alloys and Compounds,* vol. 239, pp. 158-171, 1996.

[3] Y. Pivak, H. Schreuders, and B. Dam, "Effect of the structure transformation on the (de-)hydrogenation hysteresis of La1−zYzHx films as studied by hydrogenography," *Journal of Materials Chemistry,* vol. 22, p. 24453, 2012.

[4] E. S. Kooij, A. T. M. van Gogh, D. G. Nagengast, N. J. Koeman, and R. Griessen, "Hysteresis and the single-phase metal-insulator transition in switchable YHx films," *Physical review B: Condensed matter and materials physics,* vol. 62, pp. 10088-10100, 2000.

[5] A. T. M. van Gogh, D. G. Nagengast, E. S. Kooij, N. J. Koeman, J. H. Rector, R. Griessen*, et al.*, "Structural, electrical, and optical properties of $La_{1-z}Y_zH_x$ switchable mirrors," *Physical Review B,* vol. 63, p. 195105, 04/20/ 2001.

[6] G. H. Brown, "Introduction " in *Photochromism: Techniques of chemistry, vol. III*, G. H. Brown, Ed., ed New York Wiley-Interscience, 1971.

[7] M. Irie, "Photochromism: Memories and Switches Introduction," *Chemical Reviews,* vol. 100, pp. 1683-1684, 2000/05/01 2000.

[8] T. Mongstad, C. Platzer-Björkman, J. P. Maehlen, L. P. A. Mooij, Y. Pivak, B. Dam*, et al.*, "A new thin film photochromic material: oxygen-containing yttrium hydride," *Solar Energy Materials and Solar Cells,* vol. 95, pp. 3596-3599, 2011.

[9] T. Mongstad, S. Z. Karazhanov, A. Holt, J. P. Maehlen, B. C. Hauback, and C. Platzer-Bjorkman, "Transparent yttrium hydride thin films prepared by reactive sputtering," *Journal of Alloys and Compounds,* vol. 509, pp. S812-S816, 2011.

[10] J. Montero, F. A. Martinsen, S. Z. Karazhanov, B. Hauback, E. S. Marstein, M. Garcia-Tecedor*, et al.*, "Photochromic mechanism in oxygen-containing yttrium hydride thin films: an optical perspective," *Physical Review B,* vol. 95, 2017.

[11] T. Mongstad, C. Platzer-Bjorkman, J. P. Maehlen, L. P. A. Mooij, Y. Pivak, B. Dam*, et al.*, "A new thin film photochromic material: oxygen-containing yttrium hydride," *Solar Energy Materials and Solar Cells,* vol. 95, pp. 3596-3599, Dec 2011.

[12] R. Pardo, M. Zayat, and D. Levy, "Photochromic organic-inorganic hybrid materials," *Chemical Society Reviews,* vol. 40, pp. 672-687, 2011.

[13] K. Sasaki and T. Nagamura, "Ultrafast all-optical switch using complex refractive index changes of thin films containing photochromic dye," *Applied Physics Letters,* vol. 71, pp. 434-436, 1997.

[14] H. Tian and S. Yang, "Recent progresses on diarylethene based photochromic switches," *Chemical Society Reviews,* vol. 33, pp. 85-97, 2004.

[15] R. J. Araujo, "Photochromism in glasses containing silver halides," *Contemporary Physics,* vol. 21, pp. 77-84, 1980/01/01 1980.

[16] G. P. Smith, "Photochromic glasses: properties and applications," *Journal of Materials Science,* vol. 2, pp. 139-152, March 01 1967.

[17] T. Mongstadt, "Thin-film metal hydrides for solar energy applications," Ph.D. thesis University of Oslo, Norway, 2012.

[18] American Society for Testing and Materials (ASTM), Terrestrial Reference Spectra for Photovoltaic Performance Evaluation, ASTM G173-03, global tilt , http://rredc.nrel.gov/solar/spectra/am1.5/.

[19] M. Sakai, T. Kontani, O. Nakamura, K. Takeyama, Y. Uwatoko, Y. Obi*, et al.*, "Electrical Transport and Optical Properties of Hydrogen-Deficient YH_2 Films," *Japanes journal of Applied Physics Part 1* vol. 43, pp. 681-687, 2004.

[20] A. T. M. van Gogh, "Probing the meal-insulator transition in rare-earth based switchable mirrors," Ph.D. thesis Vrije Universiteit Amsterdam, The Netherlands, 2001.

[21] R. D. Shannon, "Revised Effective Ionic-Radii and Systematic Studies of Interatomic Distances in Halides and Chalcogenides," *Acta Crystallographica Section A,* vol. 32, pp. 751-767, 1976.

[22] W. Cai and V. Shalaev, "Electric metamaterials," in *Optical Metamaterials: Fundamentals and Applications*, ed New York, NY: Springer New York, 2010, pp. 59-75.

[23] S. Cornelius, G. Colombi, F. Nafezarefi, H. Schreuders, R. Heller, F. Munnik*, et al.*, "Oxyhydride nature of rare-earth-based photochromic thin films," *The Journal of Physical Chemistry Letters,* vol. 10, pp. 1342-1348, 2019.

[24] G. Adachi and N. Imanaka, "The binary rare earth oxides," *Chemical reviews,* vol. 98, pp. 1479-1514, 1998.

[25] Y. Fukai, "The metal-hydrogen system : basic bulk properties," 2nd rev. and updated ed. ed. Berlin ;: Springer, 2005.

[26] L. N. Yannopoulos, R. K. Edwards, and P. G. Wahlbeck, "The thermodynamics of the yttrium-hydrogen system," *Journal of Physical Chemistry C,* vol. 69, pp. 2510-2515, 1965.

[27] J. A. Thornton, "The microstructure of sputter-deposited coatings," *Journal of Vacuum Science & Technology A: Vacuum, Surfaces, and Films,* vol. 4, pp. 3059-3065, 1986.

[28] A. Anders, "A structure zone diagram including plasma-based deposition and ion etching," *Thin Solid Films,* vol. 518, pp. 4087-4090, May 31 2010.

[29] T. Drüsedau, T. Bock, T. John, F. Klabunde, and W. Eckstein, "Energy transfer into the growing film during sputter deposition: an investigation by calorimetric measurements and Monte Carlo simulations," *Journal of Vacuum Science & Technology,* vol. 17, pp. 2896-2905, 1999.

[30] W. Eckstein and J. P. Biersack, "Reflection of heavy ions," *Zeitschrift für Physik B Condensed Matter,* vol. 63, pp. 471-478, 1986.

[31] A. Miniotas, B. Hjörvarsson, L. Douysset, and P. Nostell, "Gigantic resistivity and band gap changes in GdOyHx thin films," *Applied Physics Letters* vol. 76, pp. 2056-2058, 2000.

[32] M. Cesaria, A. P. Caricato, and M. Martino, "Realistic absorption coefficient of ultrathin films," *Journal of Optics,* vol. 14, 2012.

[33] J. Tauc, R. Grigorovici, and A. Vancu, "Optical properties and electronic structure of amorphous germanium," *Physica Status Solidi (b),* vol. 15, pp. 627-637, 1966.

[34] A. V. Prokofiev, A. I. Shelykh, and B. T. Melekh, "Periodicity in the band gap variation of Ln_2X_3 (X = O, S, Se) in the lanthanide series," *Journal of Alloys and Compounds,* vol. 242, pp. 41-44, 1996.

[35] L. T. Sharpe, A. Stockman, W. Jagla, and H. Jagle, "A luminous efficiency function, V*(λ), for daylight adaptation," *J Vis,* vol. 5, pp. 948-68, 2005.

[36] E. A. Davis and N. F. Mott, "Conduction in non-crystalline systems V. Conductivity, optical absorption and photoconductivity in amorphous semiconductors," *Philosophical Magazine,* vol. 22, pp. 0903-0922, 1970.

[37] C. C. You, D. Moldarev, T. Mongstad, D. Primetzhofer, M. Wolff, E. S. Marstein*, et al.*, "Enhanced photochromic response in oxygen-containing yttrium hydride thin films transformed by an oxidation process," *Solar Energy Materials and Solar Cells,* vol. 166, pp. 185-189, 2017.

[38] A. Borgschulte, R. J. Westerwaal, J. H. Rector, B. Dam, R. Griessen, and J. Schoenes, "Effect of the strong metal-support interaction on hydrogen sorption kinetics of Pd-capped switchable mirrors," *Physical Review B,* vol. 70, 2004.

[39] M. Sharon, "An introduction to the physics and electrochemistry of semiconductors : fundamentals and applications," ed. Newark, United States John Wiley & Sons, Incorporated, 2016.

[40] A. V. Dotsenko, L. B. Glebov, and V. A. Tsekhomsky, *Physics and Chemistry of Photochromic Glasses*. Boca Raton: CRC Press, 1998.

[41] S. Knief and W. von Niessen, "Disorder, defects, and optical absorption in a-Si and a Si:H," *Physical Review B,* vol. 59, pp. 12940-12946, 05/15/ 1999.

[42] N. F. Borrelli, *Photosensitive Glass and Glass-Ceramics*: CRC press, 2016.

[43] I. Duarte, A. Rotter, A. Malvestiti, and M. Silva, "The role of glass as a barrier against the transmission of ultraviolet radiation: an experimental study," *Photodermatology, Photoimmunology & Photomedicine,* vol. 25, pp. 181-184, 2009.

5

Effect of the addition of zirconium on the photochromic properties of yttrium oxyhydride

Thin films of yttrium oxyhydride have interesting, reversible photochromic properties, the origin of which is poorly understood. To investigate the role of point defect mobility, we probed the effect of lattice contraction as induced by the addition of zirconium. Interestingly, we find no loss of photochromic contrast for $Y_{1-z}Zr_zO_xH_y$ films with a small Zr cationic fractions ($z < 0.15$). At larger fractions the photochromic contrast is reduced. Zirconium is found to slow down the bleaching process, which suggests that the mobility of point defects may play a role in the thermal bleaching process. However, we cannot rule out substitution of zirconium in the YO_xH_y lattice which may also affect the photochromic properties.

This chapter is partially based on:
F. Nafezarefi, S. Cornelius, J. Nijskens, H. Schreuders and B. Dam. "Effect of the addition of zirconium on the photochromic properties of ytrrium oxy-hydride". *Solar Energy Materials and Solar Cells*, Volume 200, 2019.

5.1. Introduction

Photochromism is defined as a light-induced reversible transformation between two states of a material that has different optical absorption spectra.[1,2] Oxyhydride films based on yttrium or rare-earth cations exhibit photochromic properties when exciting them with photon energies larger than the band gap (typically between 2.25 and 2.6 eV).[3] The films are prepared by reactive magnetron sputtering of metallic Y in an Ar/H_2 gas mixture. On deposition, a black metallic YH_2 phase is formed which is stable in air. When the deposition pressure is raised above a certain critical value, the film takes up oxygen upon exposure to air and transforms into a photochromic, semiconducting oxyhydride.

By a combination of Rutherford backscattering and elastic recoil detection, we recently found that the photochromic nature is maintained over a wide composition range described by the formula REO_xH_{3-2x} where $0.5 \leq x \leq 1.5$.[4] This implies that the RE cation maintains the 3^+ valence for all photochromic compositions, with a variable occupation of oxygen and hydrogen in the tetrahedral and octahedral sites of the fcc lattice. Thus, the photochromic phase can be clearly distinguished from the non-photochromic hydroxides.[4]

At present, little is known about the nature of the photochromic effect in yttrium oxyhydrides (YO_xH_y). We suspect some similarities with silver halide doped silicate glass.[5] The photochromic behavior in the latter system involves the optical excitation of electron-hole pairs in silver halide nano-particles. The free electrons get trapped at interstitial silver ions, which thereby become neutralized and mobile.[6,7] This eventually leads to the formation of small specks of metallic silver, which are light absorbing.[5,6] A similar mechanism may be involved in YO_xH_y films, where metallic Y or YH_2 nano-clusters might form in the YO_xH_y matrix.[8] The formation and dissolution of those clusters would then involve the mobility of certain point defect species.

To investigate whether the mobility of point defects is involved in the photochromism of YO_xH_y, we investigated the effect of a change of lattice spacing on the kinetics of the photochromic effect. Ngene et al. reported on the lattice contraction of yttrium and its hydrides upon addition of zirconium (Zr).[9] In that work, metallic Y-Zr alloy films were prepared by magnetron co-sputtering and capped with Pd to allow for ex-situ hydrogenation. This resulted in a compression of the yttrium lattice proportional to Zr concentration. Remarkably, the compression effect persisted during

hydrogenation to the YH_2 and YH_3 phase.[9] X-ray absorption spectroscopy indicates the formation of ZrH_x nano-clusters that are coherently coupled to the yttrium hydride matrix. Although photochromic YO_xH_y films are prepared differently (reactively sputtered in the dihydride state and subsequently oxygenated by air-exposure) a similar compression effect may occur. Both Y and Zr are expected to form an fcc dihydride [10], while the lattice constant of ZrH_2 (4.823 Å)[11] is much less than that of YH_2 (5.27 Å).[3]

Indeed, we find that a lattice contraction takes place in YO_xH_y when adding Zr to the reactive sputter process. We observe an increase in the bleaching time constant for all Zr concentrations, which indicates that mobile species may be involved in the photochromic process. Interestingly, we find no loss of photochromic contrast for films with small (< 0.15) Zr cationic fractions.

5.2. Experimental

Thin films of $Y_{1-z}Zr_zO_xH_y$ were prepared on unheated UV-grade fused silica (f-SiO_2) substrates by DC reactive magnetron sputtering of 2-inch metallic yttrium and zirconium targets (both 99.9% purity) in an Ar/H_2 gas mixture (5N purity) with 12.5 vol. % of H_2 at a total pressure of 0.5 Pa in a UHV chamber operating at a base pressure of ~10^{-6} Pa. The target discharge powers were varied in the range of 112-56 W for yttrium and 0-81 W for zirconium, to maintain a constant total flux of metal atoms while changing the Zr content in the films from z=0 to 0.5. The Zr/(Y+Zr) fraction, z, was calculated based on the calibrated Zr and Y metal fluxes as a function of discharge power, which was determined by separate measurements of the deposition rate of dense singe-element metallic films. After deposition, the films were oxidized in air at ambient conditions. As the optical contrast is a function of film thickness, the deposition time was adjusted to obtain a film thickness of 230 nm (~ 10% uncertainty) for all $Y_{1-z}Zr_zO_xH_y$ compositions as determined by surface profilometry.

The effects of the Zr fraction (up to z = 0.5) on the structural and optical properties of $Y_{1-z}Zr_zO_xH_y$ were investigated by means of X-ray diffraction (XRD) and optical spectroscopy. XRD patterns were collected in Bragg-Brentano geometry using a Bruker D8 Advance diffractometer equipped with a Co X-ray tube and a LynxEye 1D Si-strip detector. The UV/VIS/NIR transmittance and reflectance of the films were measured with a Perkin Elmer Lambda 900 spectrophotometer covering the spectral range of 200-2500 nm. Since the collection time of this device is several minutes per

spectrum due to the moving monochromator, it was mainly used for static measurements. For a fast measurement of the dynamic transmittance changes during photo-darkening and bleaching, a customized optical fibre based spectrometer is used. The main components are a deuterium and quartz tungsten halogen white light source (DH2000-BAL, Ocean Optics B.V.) and a Si array wavelength-dispersive spectrometer (HR4000, Ocean Optics B.V.). This set up allows acquiring transmittance spectra in the range of 230-1100 nm within a few seconds.
Photo-darkening of $Y_{1-z}Zr_zO_xH_y$ films was performed by illumination with a low pressure mercury lamp (HeroLab GmbH) with emission lines centered around λ = 310 nm and 6873 $\mu W/cm^2$ total irradiance. All measurements were performed at room temperature.

5.3. Results

5.3.1. The nature of zirconium in yttrium oxyhydride

Structural properties

The main goal of this chapter is to analyze the effect of the addition of Zr to the YO_xH_y lattice and its effect on photochromic properties. But first, we need to know which phase of Zr is formed in YO_xH_y matrix. At present, it is not clear whether a ZrO_xH_y phase exists and whether it is photochromic. We have previously shown the synthesis of YH_2 thin films using magnetron sputtering at room temperature. The formation enthalpy for YH_2 is about -225 kJ/mole which is of the same order as ZrH_2 (-165 kJ/mole).[12] Therefore, it is likely that under similar conditions we will form ZrH_2. Both Y and Zr are expected to form an fcc dihydride [10], while the lattice constant of ZrH_2 (4.823 Å)[11] is much less than that of YH_2 (5.27 Å).[3] To investigate this further, Zr-based films are grown in a reactive Ar/H_2 atmosphere at various pressures. In addition, a pure metal film was grown at 0.5 Pa in a pure Ar atmosphere for the sake of comparison.

For phase identification, we rely on XRD data. Figure 5.1 demonstrates the XRD patterns of a pressure series of Zr-based films. We compare the diffraction pattern of the films to the reference patterns of Zr metal, Zr hydride and ZrO_2 in order to determine the phases present. The orange pattern on the top shows the Zr film grown at 0.5 Pa in an Ar atmosphere which matches well with the peaks originating from the Zr α-phase (hexagonal close-packed structure). Upon introducing hydrogen into the sputtering process at the same pressure, the film diffraction pattern changes. These diffractions do not correspond to crystalline Zr but may correspond to the formation of Zr hydride. The Zr-H system is complex.[14,15] Phases reported in the Zr-H system include ξ-ZrH_x phase with a trigonal crystal structure with hydrogen concentration

interval 0.25≤ x ≤0.5;[14] the stoichiometric face-centered tetragonal γ-phase with 1:1 Zr to H ratio (ZrH-type structure); understoichiometric face-centered cubic (fcc) δ-ZrH_x phase with CaF_2-type structure where x = ~1.6−2 and a face centered tetragonal (fct) ε-ZrH_x phase where x = ~1.7−2 (ThH_2-type structure).[14]
The understoichiometric δ-ZrH_{2-x} phase has been found in bulk and thin films.[14] However, the tetragonal ε-ZrH_x phase has not been reported in thin films so far.[14] Upon introduction of hydrogen in our sputtering system, it is most likely to form tetragonal ε-ZrH_x and/or δ-ZrH_x phase.

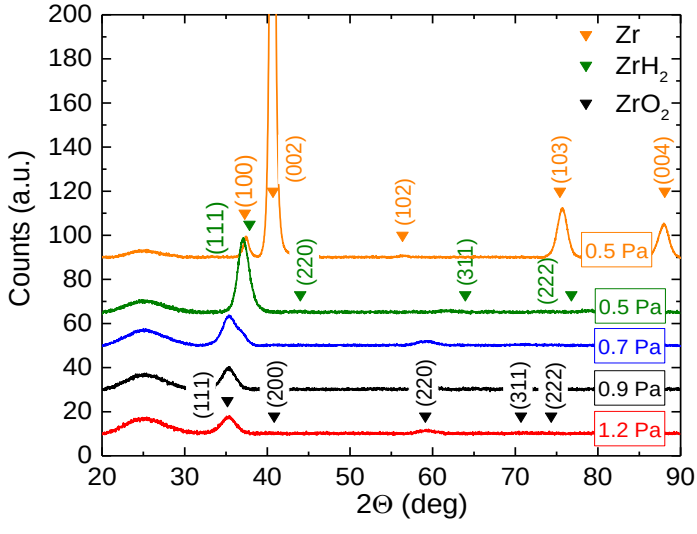

Figure 5.1. Background subtracted XRD patterns of Zr-based films prepared at various deposition pressures. The pure Zr film (orange patern) is prepared in Ar atmosphere, all other films deposited in Ar/H_2 atmosphere. The triangle marks represent the HKL peak positions of labeled phases. Fcc-ZrO_2 (ICDD-PDF #00-04901642), fcc δ-ZrH_{2-x} (ICDD-PDF #01-071-4972) and hcp-Zr (ICDD PDF #04-003-4129). The XRD pattern of Zr metal film is shown for comparison.

The diffraction pattern of Zr-based films deposited at 0.5 Pa in Ar/H_2 atmosphere is shown in Figure 5.1 in green. This diffraction pattern can be largely fit with the fcc δ-ZrH_x phase. The (111) diffraction peak shows the highest intensity, suggesting (111) preferred orientation. Perhaps the deviation of other diffraction peaks from the ideal cubic structure can be caused by compression or distortion of some crystallites with that orientation due to strain in the film. As the deposition pressure is increased to 0.7 Pa, the structure of a face-centered cubic ZrO_2 (space group Fm-3m) appears.[16] A broad (111) diffraction peak appears with a small shoulder on its right side indicating the presence of fcc δ-ZrH_x phase as it coincides with the (111) diffraction peak of the

film prepared at 0.5 Pa. Optical analysis of this film shows a lower over-all transmittance in comparison to films prepared at higher pressures (see Figure 5.4). This suggests an incomplete transformation to ZrO_2 on exposure to air and hence the presence of some remaining δ-ZrH_x in the matrix. Films prepared at even higher pressures show only a face-centered cubic ZrO_2 (space group Fm-3m) with a unit cell of 5.128 Å.[16] Optical analysis of these films reveals the formation of large band gap material (see Figure 5.4).

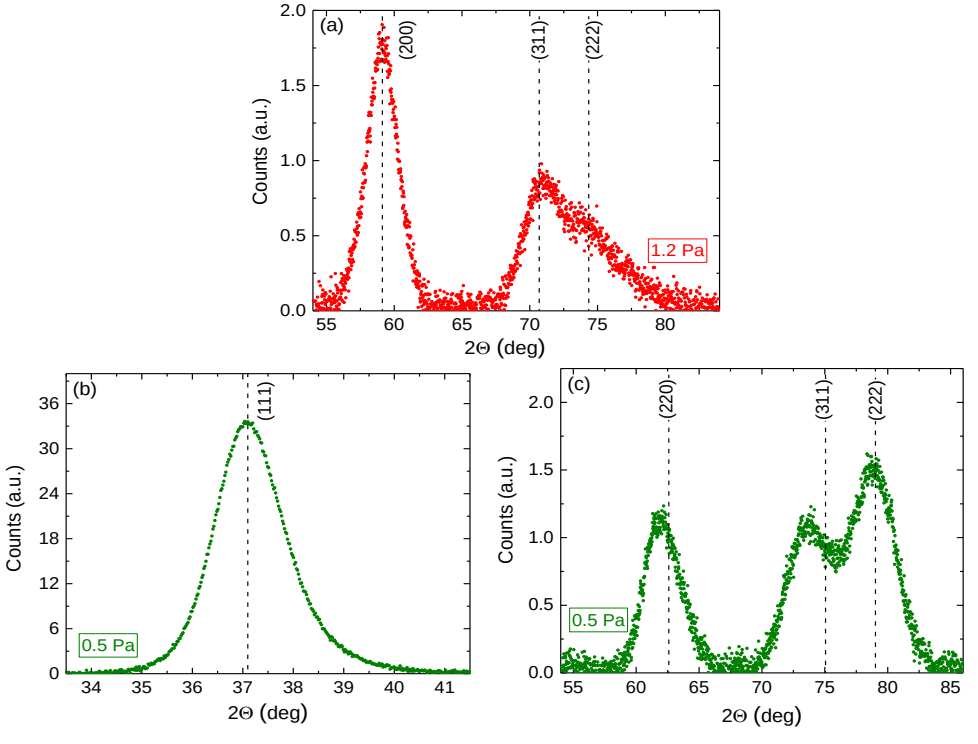

Figure 5.2. (a) narrow range XRD pattern of Zr-based films deposited at 1.2 Pa. The vertical dashed lines are peak positions corresponding to fcc- ZrO_2 ICDD PDF pattern #00-049-1642. (b&c) Narrow range diffraction pattern of the film prepared at 0.5 Pa. The vertical dashed lines are peak positions corresponding to fcc δ-ZrH_{2-x} (ICDD-PDF pattern #01-071-4972) with a 1.7% expanded lattice constant of 4.87 Å to match (111) diffraction peak position.

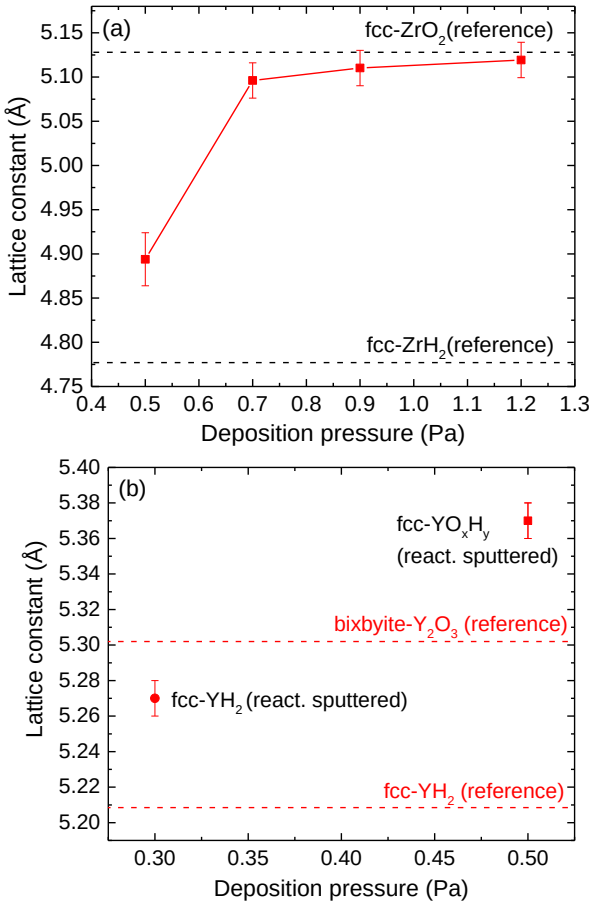

Figure 5.3. (a) Lattice constants versus deposition pressure for Zr-based films. The reference values of fcc-ZrO_2 ICDD-PDF pattern #00-04901642 and fcc-ZrH_2 ICDD-PDF pattern #01-071-4972 are added for comparison. Lattice constants were determined from the fcc (111) diffraction peak positions obtained by fitting a constrained double Pseudo-Voigt peak function [17] to the experimental data. (b) Lattice constants versus deposition pressure for Y-based films. The reference values of fcc-YH_2 ICDD-PDF pattern #04-06-6935 and bixbyite Y_2O_3 ICDD-PDF pattern #00-041-1105 are added for comparison. Note that because of the structural similarity to the fcc unit cell only $\frac{1}{2}$ of the bixbyite Y_2O_3 lattice constant is shown here.

Figure 5.3a shows the lattice constant of Zr-based films calculated for the various deposition pressures. For comparison, the lattice parameter of Y-based films is depicted in Figure 5.3b from our previous work.[3] The lattice parameter of yttrium films prepared at 0.3 Pa in Ar/H_2 atmosphere, is close to that of the β-YH_2 phase [3], with a 1.18% lattice expansion in comparison to the reference. We attributed this

expansion of directly sputtered film to a certain amount of disorder of the H sub-lattice due to the non-equilibrium nature of reactive sputtering.[3] This film appeared black with characteristic YH_2 transmittance window. This film did not show any photochromic properties. As the pressure is increased, above certain critical deposition pressure (p*), the film air-oxidize at room temperature to form a stable semiconducting transparent photochromic film. The lattice constant of this film is larger than that of bixbyite-Y_2O_3.[3] We refer to these films as YO_xH_y.[3]

In the case of Zr-based films, the lattice constant of the film prepared at 0.5 Pa in Ar/H_2 atmosphere shows a 1.7% lattice expansion in comparison to fcc Zr-hydride. For the film fabricated at 0.7 Pa, a cubic oxide pattern becomes visible with some remaining δ-ZrH_x clusters (supported by optical analysis). At higher pressures, upon exposure to air the films transform from metallic δ-ZrH_x to a pure ZrO_2 phase with a lattice constant very close to fcc-ZrO_2. Although there is a critical deposition pressure where upon exposure to air oxygen atoms are incorporated into the matrix, we observe no indication for the formation of a ZrO_xH_y phase.

Optical properties

The optical transmittance spectra of the films grown at various pressures in an Ar/H_2 atmosphere are shown in figure 3a. It appears that the average transmittance increases with the deposition pressure. We obtain a film with zero transmittance at 0.5 Pa, while a semi-transparent film is obtained when increasing the deposition pressure to 0.7 Pa. Upon further increase of deposition pressure highly transparent films are obtained.

The absorption coefficient of the films, $\alpha(\lambda)$, is calculated using the expression $T(\lambda) = [1 - R(\lambda)] \exp[-\alpha(\lambda)d]$, where α is the absorption coefficient of the material and d is the film thickness.[17] By applying the Tauc model, the optical band gap of a material can be determined from the linear extrapolation of the curve $(\alpha h\nu)^{1/m}$ vs. photon energy to $h\nu = 0$. The exponent m characterizes the nature of the band transition where m = 1/2 corresponds to direct transition and m = 2 to indirect transition.[18] A plot of $(\alpha h\nu)^2$ versus $h\nu$ was established to estimate the value of the optical band gap of the Zr-based films. The $(\alpha h\nu)^{1/2}$ versus $h\nu$ plot did not show a meaningful linear region and therefore we concluded that the transition is direct. A linear fit was made and the band gap values were obtained from the intercept and displayed in figure 3b. Zr hydride films deposited at pressures > 0.7 Pa oxidize in air. The film grown at 1.2 Pa shows the highest transmittance and some optical absorption below the band gap. In comparison to the mixed Y-based oxyhydrides, the optical band gap of these oxidized

Zr-based films is large (≥ 5 eV). This value strongly suggests the formation of ZrO_2 (E_g in the range 5 – 6 eV).[13]
The lower transmittance of the film prepared at 0.7 Pa could be an indication of some remaining δ-ZrH_x in ZrO_2 matrix. For a Zr oxyhydride to be present, we would expect a smaller bandgap similar to what we observe in yttrium-oxyhydride.

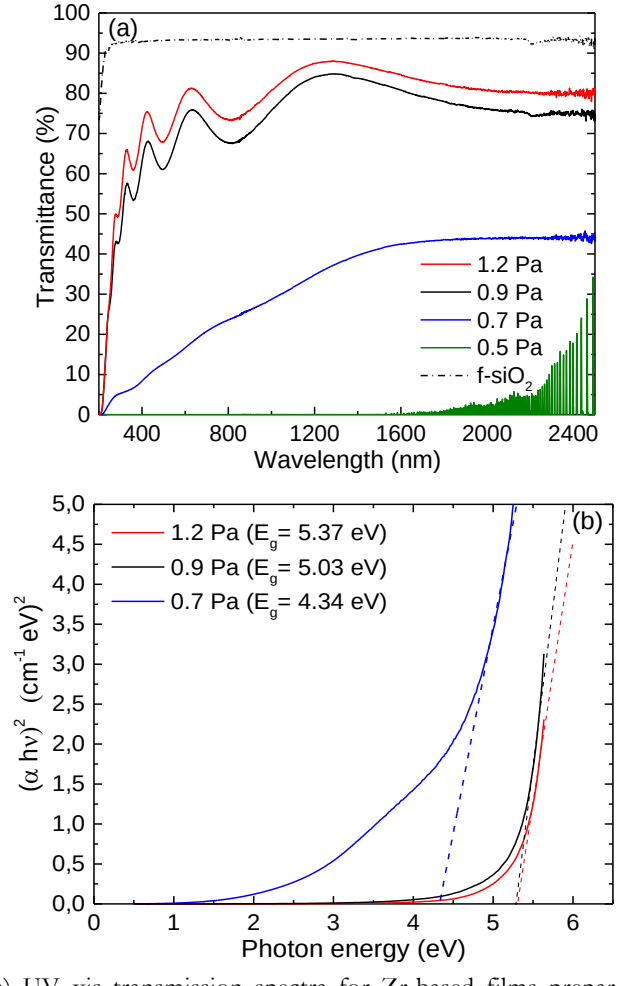

Figure 5.4. (a) UV–vis transmission spectra for Zr-based films prepared at different deposition conditions in Ar/H_2 atmosphere with thicknesses between 271 and 351 nm (b) calculated band gaps using Tauc plot for all samples

Photo-darkening

Here we set to investigate if the Zr-based films show any sign of photochromism. Figure 5.5 shows the spectral transmittance of the Zr-based films deposited at 0.7, 0.9 and 1.2 Pa in Ar/H_2 atmosphere, before and after UV illumination. The as-deposited film sputtered at 0.5 Pa in Ar/H_2 is metallic δ-ZrH_x and not photochromic. It is clear from Figure 5.5 that the transmittance of all films increases due to illumination. This increase occurs together with a blue shift in the absorption edge. This behavior suggests UV induced oxidation. Note, that the photochromic effect observed in YO_xH_y films involves excitations with photon energies higher than the band gap. The energy maximum of the light source used is in the range of 4.96-4.84 eV which is a little below the band gap values of Zr-based films (~ around 5 eV). Nevertheless, the film prepared at 0.7 Pa did not show any sign of photochromism even though the excitation energy exceeded the optical band gap suggested by the Tauc analysis.

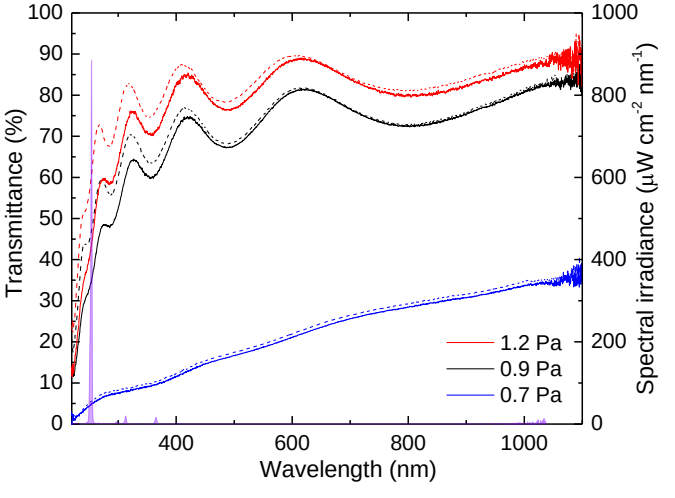

Figure 5.5. Illumination response of Zr-based films (with thickness between 271 and 351 nm). The transmittance of films are shown before (solid line) and after (dotted line) photo-darkening. low-pressure mercury lamp (HeroLab GmbH) was used with emission lines centered around λ = 250 nm and 2578 μW/cm² total irradiance.

Based on the optical and structural analysis we conclude that within the range of the sputtering conditions used, the formation of ZrO_xH_y is not possible. At 0.5 Pa, a δ-ZrH_x phase is formed, which is stable in air. At 0.7 Pa, upon air exposure a mixture of fcc ZrO_2 and metallic δ-ZrH_x is formed. This suggest presence of some remaining δ-ZrH_x in the ZrO_2 matrix. A further increase of deposition pressure, air exposure leads to the formation of films resembling ZrO_2 which is supported by transmittance data, band gap calculation and cubic oxide pattern. The illumination of all the above films

shows no indication of photochromism. From this, we conclude that if Zr addition affects the photochromic properties of YO_yH_x it will only do so indirectly through modification of YO_xH_y.

5.3.2. Influence of the addition of zirconium to yttrium oxy hydride thin films on the optical, structural and photochromic properties

Structural properties

Figure 5.6a shows the X-ray diffraction patterns of $Y_{1-z}Zr_zO_xH_y$ films. All compositions can be indexed to a fcc structure with predominant diffraction peaks corresponding to the (111) and (200) lattice planes. We find that the cubic structure of YO_xH_y is retained upon Zr addition up to z = 0.5 and no additional diffraction peaks are observed. This suggests that if any secondary phases such as Zr, ZrH_2 or ZrO_2 are formed, they are either X-ray amorphous or their diffraction peaks overlap. Since hcp-Zr has a distinct diffraction pattern we can rule out the presence of this phase. On the other hand, δ-ZrH_x and ZrO_2 exhibit an fcc structure. In particular, the lattice constant of ZrO_2 is close to that of YO_xH_y, which may hamper its detection. Taking into account the optical behavior (see Figure 5.8a), is seems likely that low concentrations of light absorbing δ-ZrH_x clusters are formed at high Zr contents, which cannot be detected by XRD. This hypothesis is supported, by an earlier report of ZrH_x nano-particle formation in $(Y,Zr)H_2$ thin films probed by EXAFS.[9]

The increasing relative intensity of the (111) reflection as compared to the (200) reflection may be related to a change in orientation of crystallites or to a change in oxygen/hydrogen ratio. On Zr addition, we observe a shift to higher diffraction angles for all reflections. To evaluate the effect of Zr addition in more detail we use the (200) diffraction peak to determine the change in the lattice parameter. The peaks are fitted as a linear combination of two Pseudo-Voigt functions describing the Co $K_{\alpha 1,2}$ doublet [17] as shown in Figure 5.6b. The peak position of the $K\alpha_1$ component is used to calculate the lattice spacing d_{200} and the fcc lattice parameter via Bragg's law (Figure 5.7a).

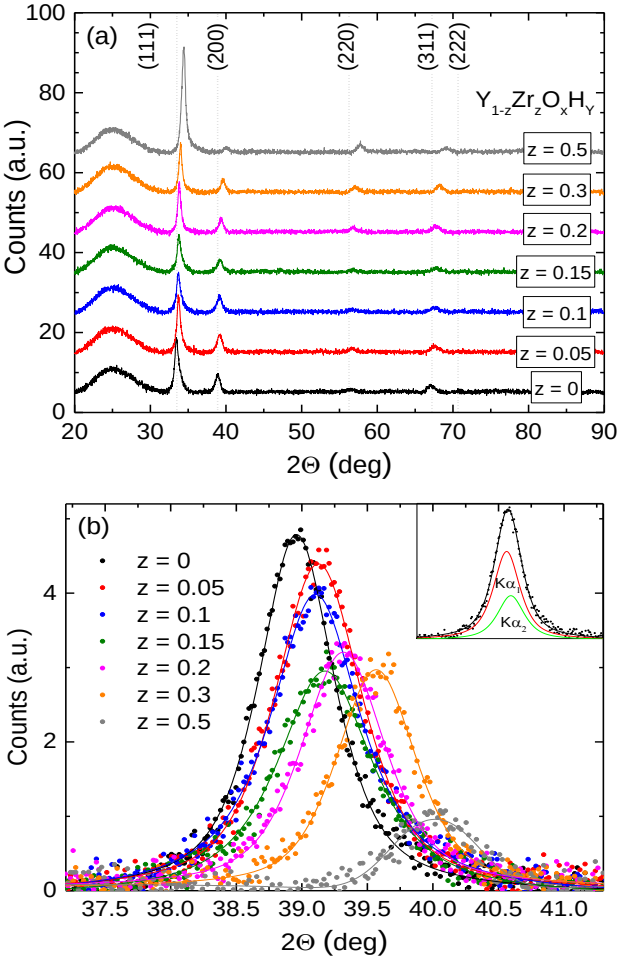

Figure 5.6. (a) Background subtracted XRD patterns of $Y_{1-z}Zr_zO_xH_y$ films with a Zr content of up to z = 0.5. The vertical lines are peak positions corresponding to fcc-YH_2 ICDD-PDF pattern #04-06-6935 with a 3.1% expanded lattice constant of 5.37 Å to match the experimental data where z = 0. (b) Detail showing the shift of the (200) diffraction peak to higher diffraction angles as the Zr fraction is increased. Lines are double Pseudo-Voigt fits to the data. The inset illustrates the two components of the Co-$K\alpha_{1,2}$ doublet used for peak fitting in case of z=0.

We observe a continuous decrease of the fcc lattice constant with increasing Zr content which suggests a compression of the YO_xH_y lattice. This result is similar to the contraction observed by Ngene et al.[9] in fcc-$Y_{1-z}Zr_zH_2$ up to a Zr fraction z = 0.12 (Figure 5.7b). Our results demonstrate a similar effect in $Y_{1-z}Zr_zO_xH_y$ which remains present up to z = 0.5. The lattice contraction in the Zr-doped YH_2 system is

somewhat stronger (~ 1% contraction at z = 0.1) than in YO_xH_y (~ 0.3 % contraction at z = 0.1).

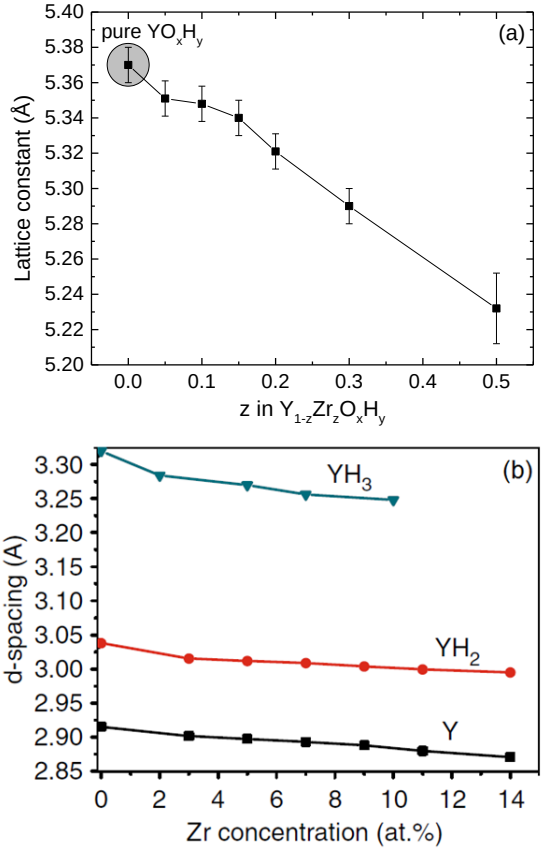

Figure 5.7 (a) The lattice constant of the fcc $Y_{1-z}Zr_zO_xH_y$ films as a function of the Zr - fraction, as calculated from the fit of the (200) reflection shown in figure 5b. (b) Change of d-spacing as function of the Zr in Y, YH_2 (dehydrogenated) and YH_3 (hydrogenated) films. (reused from reference [9])

Optical properties

As shown in Figure 5.8a the $Y_{1-z}Zr_zO_xH_y$ films are semiconductors. Pure YO_xH_y shows the highest transmittance and only weak optical absorption below the band-gap. With increasing Zr content, we observe a continuous decrease of transmittance in a wide spectral range from UV to NIR. This reduced transmittance can be explained by light absorption due to the presence of metallic clusters, probably incompletely oxidized δ-ZrH_x. Moreover, Zr addition appears to affect the fundamental absorption edge of the $Y_{1-z}Zr_zO_xH_y$ films. The absorption coefficient, α(λ), is calculated from the

transmittance and reflectance spectra shown in Figure 5.8 using the expression T = (1-R) exp (–αd), where d is the film thickness.[17] This allows us to determine the optical band gap of the films by a linear extrapolation of a plot of $(\alpha h\upsilon)^{1/m}$ vs. photon energy to zero absorption (Tauc plot) as shown in Figure 5.9a. For all samples the best Tauc fits are obtained with an exponent of m = 2 indicating an indirect transition.[17]

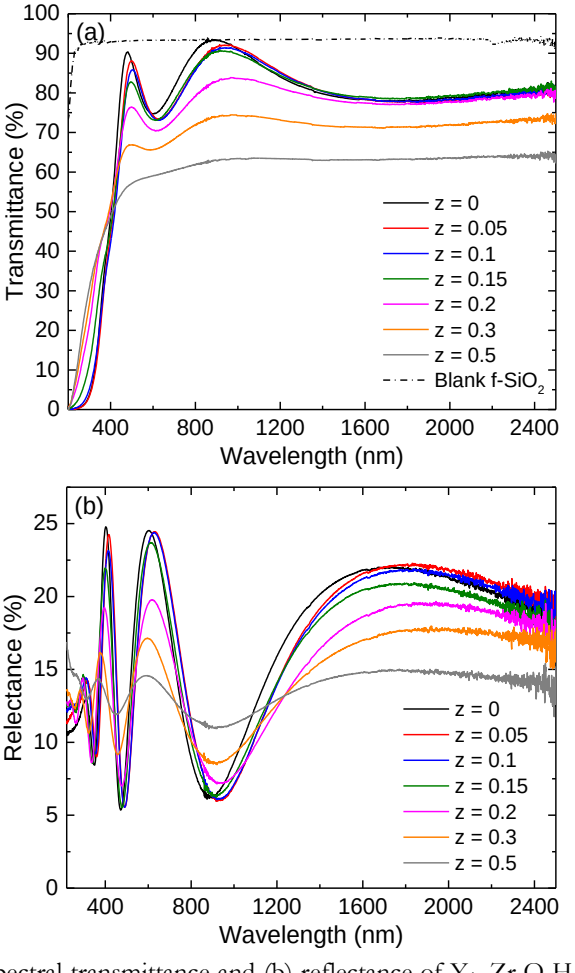

Figure 5.8. (a) Spectral transmittance and (b) reflectance of $Y_{1-z}Zr_zO_xH_y$ films (d ≈ 230 nm) before illumination.

The optical band gap values deduced using the Tauc plot method shown in Figure 5.9b as a function of the Zr content, reveal a minimum value at z = 0.15. The shape of the Tauc plots for Zr contents z > 0.15 suggests the formation of a broad

distribution of defect states within the forbidden gap probably due to an increasing amount of disorder and defects in the films induced by Zr addition.

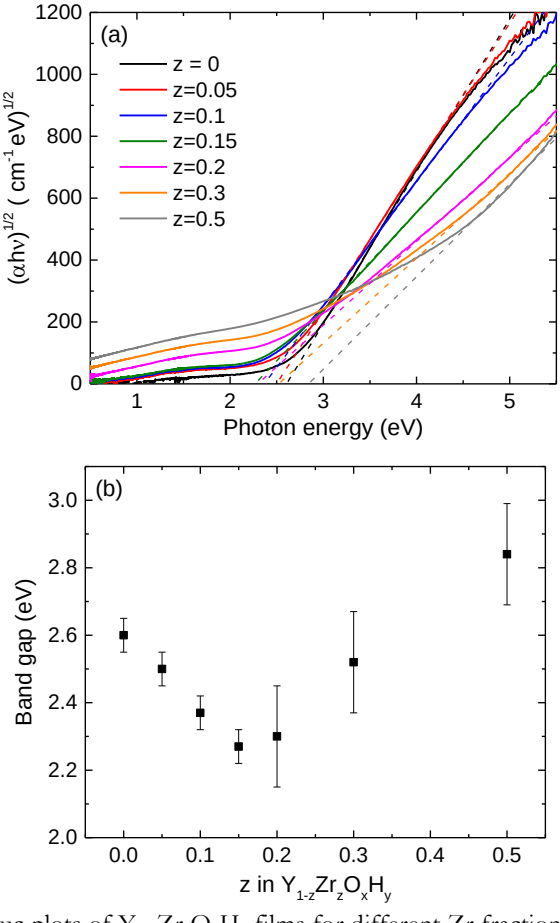

Figure 5.9. (a) Tauc plots of $Y_{1-z}Zr_zO_xH_y$ films for different Zr fractions. An absorption tail at lower photon energies is observed and increases to higher absorption values as Zr is added to the system. (b) Optical band gap of $Y_{1-z}Zr_zO_xH_y$ versus the Zr fraction.

Our recent work indicates that the electronic structure of YO_yH_x is related to that of YH_3.[4] Therefore, we expect a comparable impact of compression on the bandgap. Unfortunately, in the hydride experiments the effect of Zr on the bandgap of $Y_{1-z}Zr_zH_3$ was not investigated.[9] Hence, we refer to the high pressure experiments on YH_3 by Wijngaarden et al.[19] They observed that a lattice compression of ~ 2% at 7 GPa results in a 6% reduction of the bandgap. Limiting our analysis to z = 0.15, the reduction of the band gap by 15% is quite strong in comparison, given the small

(0.6%) lattice contraction. This suggests that the reduction in bandgap is not solely due to lattice compression. Chemical substitution might also contribute.

Photochromic properties

All $Y_{1-z}Zr_zO_xH_y$ films in this study are found be photochromic. While the as-deposited films are transparent, their transmittance drops as soon as they are exposed to UV illumination (Figure 5.10). Upon removal of UV light, the films bleach at room temperature and return to their initial transparent (bleached) state.

We define the relative (spectral) photochromic contrast $\Delta T(\lambda,t)$ as the change of the transmittance normalized to its initial value before UV illumination $T_0 = T(\lambda,0)$, i.e. $\Delta T(\lambda,t) = [T_0 - T(\lambda,t)]/T_0$. In order to reduce the effect of the thin film optical interference patterns, it is reasonable to discuss only the spectral averaged values of transmittance $\langle T \rangle$ and contrast $\langle \Delta T \rangle$ in the 450 - 1000 nm range. The initial transmittance of the $Y_{1-z}Zr_zO_xH_y$ films decreases from $\langle T_0 \rangle$ = 86.2 % for YO_xH_y to $\langle T_0 \rangle$ = 61.7% for z = 0.5. Under continuous illumination for several hours the transmittance decreases until a dynamic equilibrium between photo-darkening and thermal bleaching is established which results in the maximum (saturation) photochromic contrast (Figure 5.11a). With increasing Zr content the maximum contrast increases slightly from 36.6% for pure YO_xH_y to 39.5% for $Y_{0.9}Zr_{0.1}O_xH_y$. However, a further increase of the Zr fraction leads to a strong reduction in the relative contrast to 11.1% at z = 0.5 (Figure 5.11b).

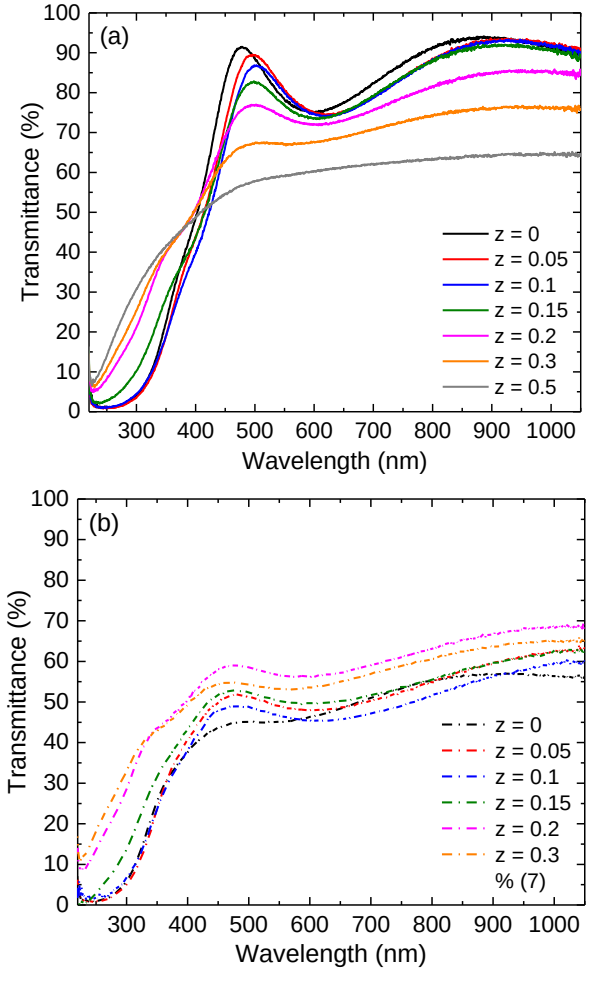

Figure 5.10. Spectral transmittance of $Y_{1-z}Zr_zO_xH_y$ films (d ≈ 230 nm): (a) before illumination and (b) after UV illumination. The photo-darkening does not induce any change in the band gap.

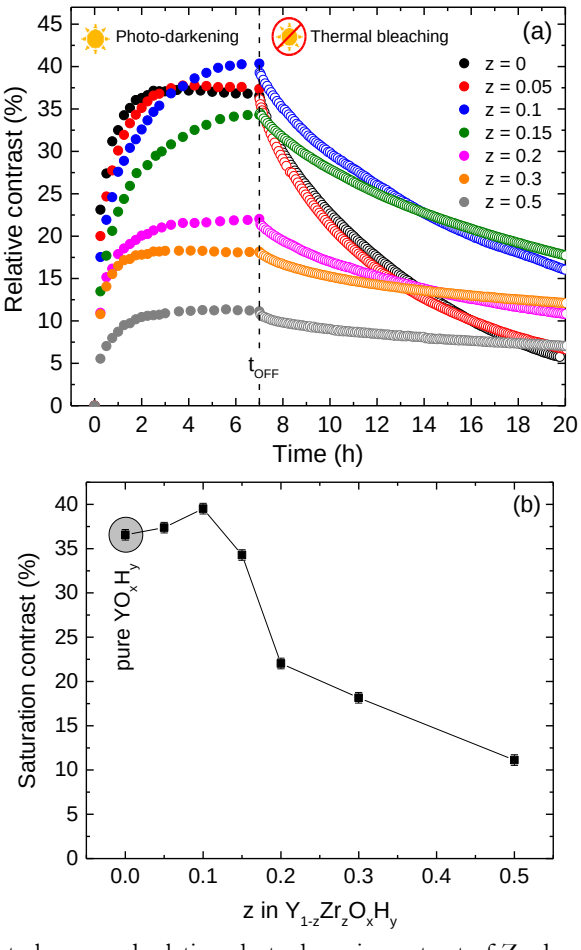

Figure 5.11. Spectral averaged relative photochromic contrast of Zr-doped YO_xH_y films: (a) during UV illumination at 6873 μWcm^{-2} followed by (thermal) bleaching in the dark and (b) maximum value (after 7 hours) as a function of Zr content.

To investigate the effect of Zr on the mobility of point defect species involved in the bleaching process, we analyze the kinetics of thermal bleaching after the UV illumination is switched off. Absorption in many dilute material systems satisfies the Lambert-Beer law:

$$T(\lambda, t) = \exp(-\alpha(\lambda, t) \cdot d) \tag{5-1}$$

where d is the layer thickness and α equals the absorption coefficient. Normalizing the transmittance to its initial value before UV illumination yields:

$$\frac{T}{T_0} = \exp(-(\alpha - \alpha_0) \cdot d) = \exp(-\Delta\alpha \cdot d) \tag{5-2}$$

$$\ln\left(\frac{T}{T_0}\right) = -\Delta\alpha \cdot d \tag{5-3}$$

Where the change in absorption coefficient is given by the product of the time dependent concentration of the absorbing species, c(t), and its absorption cross-section:

$$\Delta\alpha(\lambda, t) = c(t) \cdot \sigma(\lambda) \tag{5-4}$$

Assuming thermal bleaching obeys first order kinetics, we introduce the bleaching time constant, τ_B (s), to describe the change of the concentration as follows:

$$\frac{dc}{dt} = -\frac{1}{\tau_B} c \tag{5-5}$$

This yields as solution an exponential decrease of the concentration starting from its initial value $c_0 = c(t_{off})$ at the time when the UV illumination is stopped (See Figure 5.10a):

$$c(t) = c_0 \exp\left(-\frac{1}{\tau_B} t\right) \tag{5-6}$$

Combining equations 5-3, 5-4 and 5-6 yields the expression:

$$\ln\left(-\ln\left(\frac{T}{T_0}\right)\right) = -\frac{1}{\tau_B} t + \ln(c_0 \sigma d) \tag{5-7}$$

which shows that the bleaching time constant can be determined from the linear slope of the left hand side of the equation (which depends only on experimental quantities) as a function of time. The corresponding plot of the spectral averaged transmittance data (Figure 5.10a) in the bleaching region is shown in Figure 5.11a. We find that the time dependence is indeed nearly linear for all sample compositions (variation in the ambient temperature may be the cause of not perfectly linear behavior), which is a strong indication that thermal bleaching in $Y_{1-z}Zr_zO_xH_y$ follows first order kinetics. From a linear fit we obtain the bleaching time constants as displayed in Figure 5.11b. A substantial increase of bleaching time constant, i.e. slower thermal bleaching, with increasing Zr content is observed.

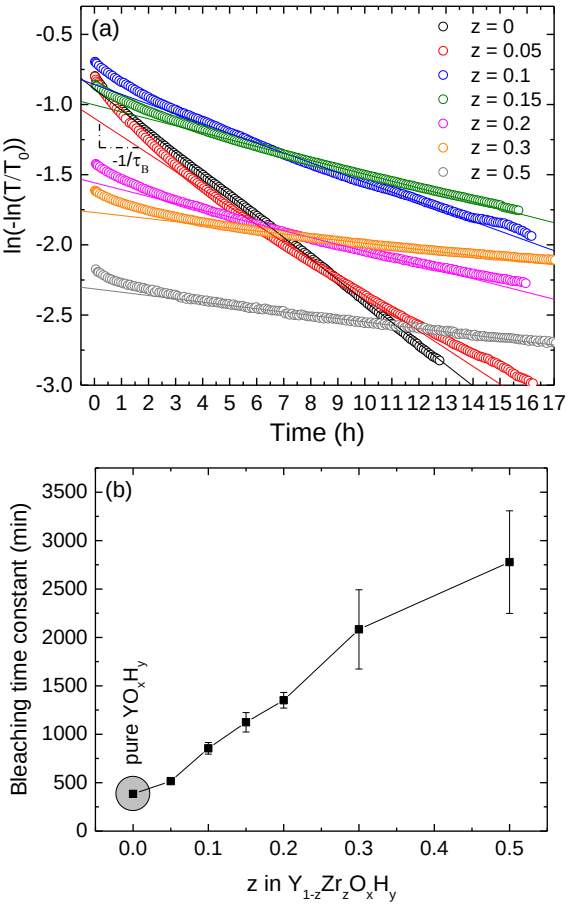

Figure 5.12. (a) Determination of bleaching time constant based on equation (7) from the slope of linear region which quantifies the rate at which bleaching take place (b) Dependence of bleaching time constant on Zr content of photochromic $Y_{1-z}Zr_zO_xH_y$ films. The bleaching speed is decreasing with increasing Zr fraction.

5.4. Discussion

Photochromic properties are determined by the kinetics of the involved darkening and bleaching processes. During UV illumination both photo-darkening and thermal bleaching are active simultaneously and an equilibrium of both processes is established at a certain concentration of absorbing species resulting in a saturation of the optical contrast. When the UV light source is turned off, only the bleaching process remains active causing a return to the initial transparent state.[2]

It is reasonable to assume that the mobility of point defect species is involved in the darkening and bleaching processes. This concept is based on the analogy to silver halide doped glasses where photochromism is due to the diffusion of point defects and reversible nucleation/dissolution of light absorbing Ag metal nano-particles.[6] It is expected that the mobility of such point defects could be affected by a compression of the lattice, which would lead to a change in kinetics.

From the lattice compression and the optical behaviour we conclude that Zr partly substitutes in the YO_xH_y lattice and partly forms metallic δ-ZrH_x clusters, which may both contribute to the observed lattice compression. The correlation between the lattice compression and thermal bleaching time constant suggests that the mobility of the species involved in the bleaching process is reduced by the decrease of the lattice volume.

However, we cannot rule out other effects due to the substitution of zirconium in the YO_xH_y lattice. Considering photochromic glasses as a model system, Zr in $Y_{1-z}Zr_zO_xH_y$ might play a similar role as Cu in silver halide doped glasses, where Cu is added to enhance the photochromic contrast of the glass. The Cu^+ ions act as hole traps, slowing down the recombination process of the photo-excited carriers, while simultaneously preventing the formation of Cl_2 which would make the process irreversible.[5] The substitution of Y by Zr may have a similar effect. In YO_xH_y films Y is in 3+ state while Zr is likely to be in the 2+ state which means that Zr^{4+} could be formed by trapping holes generated during UV illumination and thus effectively reducing the rate of recombination. This would increase the rate constant of the photo-darkening process and slow down the bleaching process. However, the data obtained so far do not allow us to verify the presence of this mechanism.

Since the photochromic saturation contrast is the result of the equilibrium between photo-darkening and bleaching, slower bleaching would imply a larger saturation contrast with increasing Zr content. For low Zr concentrations up to $z = 0.1$ there is indeed a weak increase of saturation contrast. However, above $z = 0.1$ the saturation contrast decreases rapidly, while bleaching speed continuously decreases. Hence, large Zr concentrations probably lead to a dilution of active photochromic species, which counteracts the slower bleaching. To analyse such countervailing trends we would need a detailed analysis of the photo-darkening kinetics. Unfortunately, so far we could not extract reliable kinetic parameters for photo-darkening from the time dependent transmittance during UV-illumination to separate photo-bleaching and darkening contributions.

5.5. Conclusion

To explore the effect of lattice compression on the photochromic properties of YO_xH_y thin films, we investigated Zr doping of this material. Firstly, we find that sputtering Zr in Ar/H_2 atmosphere under similar conditions as in fabricating YO_xH_y does not lead to the formation of ZrO_xH_y. Instead, depending on the sputtering conditions, we form δ-ZrH_x, δ-ZrH_x in ZrO_2 matrix or ZrO_2, as determined on the basis of optical and structural analysis. None of the Zr-based films show photochromic properties. Therefore we conclude that if Zr addition affects the photochromic properties of YO_yH_x it will only do so indirectly through modification of YO_xH_y. We find that adding Zr to YO_xH_y causes: 1) a compression of the fcc lattice, 2) slower thermal bleaching, 3) changes in photochromic contrast, 4) a reduction of the optical transmission in the bleached state, and 5) a narrowing of the bandgap. The compression of the fcc YO_xH_y lattice is probably due to both the presence of δ-ZrH_x nano-clusters and/or the substitution of Zr in the YO_xH_y lattice. The latter is consistent with the large effect of Zr on the bandgap, while the reduction of the optical transmission in the bleached state points to the presence of δ-ZrH_x nanoclusters.

We find that the thermal bleaching time constant of the $Y_{1-z}Zr_zO_xH_y$ films increases substantially as the Zr content is increased. At the same time, the relative photochromic contrast improves up to z = 0.1. Upon a further increase of the Zr fraction, the photochromic contrast drops significantly but remains present, indicating a decreasing amount of photochromic active material. Since we did not observe any photochromism in films where Zr is the only cation, we conclude that the change in the photochromic kinetics is due to a change in the properties of the YO_xH_y matrix.

The strong correlation between lattice compression and slower bleaching kinetics suggests that the mobility of point defect species involved in the photochromic process may be impeded by the lattice compression. However, we cannot exclude that (substitutional) Zr^{2+} may act as a hole trap preventing recombination of the excited electron-hole pairs and thus slowing down the bleaching process. An investigation of the local structure using X-ray absorption spectroscopy (XAS) is needed to establish the nature of Zr in $Y_{1-z}Zr_zO_xH_y$, which is required to fully understand its effect on the photochromic properties.

References

[1] M. Irie, "Photochromism: memories and switches introduction," *Chemical Review,* vol. 100, pp. 1683-1684, 2000.

[2] G. H. Brown, "Introduction," in *Photochromism: Techniques of chemistry, vol. III*, G. H. Brown, Ed.: New York Wiley-Interscience, 1971.

[3] F. Nafezarefi, H. Schreuders, B. Dam, and S. Cornelius, "Photochromism of rare-earth metal-oxy-hydrides," *Applied Physics Letters,* vol. 111, no. 10, 2017.

[4] S. Cornelius *et al.*, "Oxyhydride nature of rare-earth-based photochromic thin films," *The Journal of Physical Chemistry Letters,* vol. 10, pp. 1342-1348, 2019.

[5] H. J. Hoffmann, "Photochromic glasses," in *The Properties of Optical Glass*, H. B. a. N. Neuroth, Ed. Berlin: Springer, 1995.

[6] R. J. D. Tilley, *Defects in Solids* Wiley & Sons, Inc., 2008.

[7] A. V. Dotsenko, L. B. Glebov, and V. A. Tsekhomsky, *Physics and chemistry of photochromic glasses* (CRC Press laser and optical science and technology series). Boca Raton: CRC Press, 1998.

[8] J. Montero *et al.*, "Photochromic mechanism in oxygen-containing yttrium hydride thin films: An optical perspective," *Physical Review B,* vol. 95, no. 20, 2017.

[9] P. Ngene, A. Longo, L. Mooij, W. Bras, and B. Dam, "Metal-hydrogen systems with an exceptionally large and tunable thermodynamic destabilization," *Nature Communications*, vol. 8, no. 1, pp. 1-8. doi: 10.1038/s41467-017-02043-9

[10] Y. Fukai, The metal-hydrogen system : basic bulk properties, 2nd rev. and updated ed. ed. Berlin ;: Springer, 2005.

[11] P. Zhang, B.-T. Wang, C.-H. He, and P. Zhang, "First-principles study of ground state properties of ZrH_2," *Computational Materials Science,* vol. 50, no. 12, pp. 3297-3302, 2011.

[12] S. Banerjee and A. K. Tyagi, Functional materials : preparation, processing and applications, London: Elsevier, 2012.

[13] H. Jiang, R. I. Gomez-Abal, P. Rinke, and M. Scheffler, "Electronic band structure of zirconia and hafnia polymorphs from the," *Physical Review B,* vol. 81, no. 8, 2010.

[14] M. Magnuson, F. Eriksson, L. Hultman, and H. Hogberg, "Bonding structures of ZrH_x thin films by X-ray spectroscopy," *Journal of Physical Chemistry C,* vol. 121, no. 46, pp. 25750-25758, 2017.

[15] T. Maimaitiyili *et al.*, "Observation of the δ to ε Zr-hydride transition by in-situ synchrotron X-ray diffraction," *Crystal Research and Technology,* vol. 51, no. 11, pp. 663-670, 2016.

[16] R. Chintaparty, B. Palagiri, R. R. Nagireddy, and V. s. R. I. Reddy, "Effect of phase transformation on optical and dielectric properties of zirconium oxide nanoparticles," *Phase Transitions,* vol. 88, no. 9, pp. 929-938, 2015.

[18] A. J. Illig, C. T. Chantler, and A. T. Payne, "Voigt profile characterization of copper Kα," *Journal of Physics B: Atomic, Molecular and Optical Physics,* vol. 46, no. 23, 2013.

[17] J. Tauc, R. Grigorovici, and A. Vancu, "Optical Properties and Electronic Structure of Amorphous Germanium," *physica status solidi (b),* vol. 15, no. 2, pp. 627-637, 1966.

[19] R. J. Wijngaarden *et al.*, "Towards a metallic YH3 phase at high pressure," *Journal of Alloys and Compounds,* vol. 308, no. 1-2, pp. 44-48, 2000.

6

Photochromic neodymium oxyhydride thin films

Here, we report on the photochromic properties of NdO_xH_y thin films. This material belongs to the recently discovered family of rare-earth (Y, Dy, Er, Gd) oxyhydrides which all show photochromic behaviour. Neodymium stands out for its very large ionic radius in comparison to Y and the other rare-earth tested so far. While the overall switching kinetics appears to be similar to the other rare earths, we find that the band gap of NdO_xH_y is much smaller compared to the other rare-earth oxyhydrides. To protect NdO_xH_y from decomposition in air, we found that atomic layer deposition of a Al_2O_3 capping layer, shows promising protective properties.

6.1 Introduction

Photochromic yttrium oxyhydrides (YO_xH_y) have gained attention over the past decade because of the fact that the critical wavelength for photo-darkening in these materials extends to the visible wavelength. Moreover, these materials darken over a wide range of wavelengths well into the near infrared.[1] While such switchable optical properties are attractive for smart window applications, the switching speed is prohibitive.[2]
The YO_yH_x structure is closely related to semiconducting YH_3, however, the presence of oxygen is essential to obtain a photochromic effect.[3] Thus far, all REO_xH_y films are prepared in the metallic dihydride state by reactive magnetron sputtering and transform into a semiconducting photochromic oxyhydride when exposed to air.[4] Only if the films are prepared at low enough reactive deposition pressure, the films remain in the dihydride state. Apparently the higher thin film density obtained in this way prevents a thorough oxidation of the film.[4]
You et al[2] found that the composition of sputtered films influence the optical properties of the film as reflected in the photochromic behavior. The deposition of a YHO thin film with a lateral composition gradient allowed them to prepare a black to yellow transparent film, depending on the oxygen content. They find the smallest band gap and the largest photo-darkening performance at the boundary between the black and transparent region.

We found that thin films of Dy, Er and Gd oxyhydride exhibit a photochromic effect similar to YO_xH_y.[4] These rare earth oxyhydrides can be described by the general formula REO_xH_{3-2x} and form over a large part of the compositional range $0.5 \leq x \leq 1.5$.[5] We proposed that all rare-earths oxyhydrides (incl. Sc) share a common physical mechanism inducing the photochromic effect [4,5] The recent discovery of hydride ion (H^-) conductivity in the LaOH, shows that this class of materials might have a wider range of application in the field of energy storage and conversion.[6]

Given certain similarities with silver chloride based photochromic glasses where interstitial silver forms clusters [7,8], we propose that the mobility of point defects is responsible of the photochromism in REO_xH_y. In this context, the formation of REH_2 has been proposed to be responsible for the darkening and the mobility of H^- or O^{2-} would then play a role in the kinetics of the effect. Therefore, we recently investigated the effect of lattice compression by doping YO_xH_y with large amounts of Zr. Since the structural nature of this mixture was hard to asses, the observed

reduction of the optical bleaching time constant could not unequivocally be contributed to the lattice compression achieved.[9]

Here, we explore the effect of RE size on the photochromic properties of rare earth oxyhydride. Figure 6.1 shows the ionic radius as a function of atomic number for a selection of rare earth elements. The difference in ionic radius between the rare earth cations studied so far was rather small (Gd, Dy, Y and Er). Preliminary experiments revealed that cerium or praseodymium oxyhydrides films are unstable in air and rapidly peel from the substrate. Hence, as one of the large RE cations we choose to investigate neodymium oxyhydride. NdO_xH_y films prove to be relatively stable over a couple days. Using an Al_2O_3 protective coating, the stability was improved further. Remarkably, the photochromic switching kinetics is similar to that of the other rare-earth oxyhydrides, suggesting that point defect mobility plays a minor role in the kinetics of the photochromic effect. However, the bandgap is much smaller than in other RE's allowing for a much larger fraction of solar light to be used to darken the film.

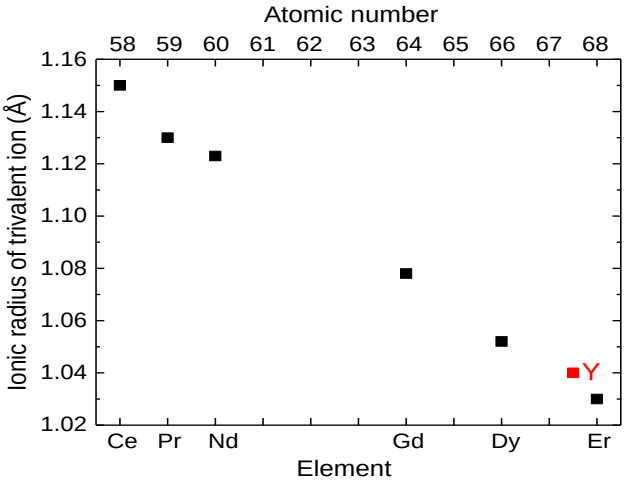

Figure 6.1. Ionic radius of the rare earth elements versus atomic number. In terms of ionic radius, yttrium falls under the group of heavy rare earth elements.[10]

6.2 Experimental methods

Thin films of NdH_2 and NdO_xH_y were fabricated by direct current reactive magnetron sputtering of a neodymium target (purity 99.9%, MaTeck) at 100 W in an Ar/H_2 gas mixture (5N purity) with 12.5 vol.% of H_2. The vacuum system operated at a base pressure of 10^{-6} Pa. The films were grown at various deposition pressures using fused silica (f-SiO_2) as substrate material. After deposition, the films were oxidized in air at

ambient conditions. The thickness of the films was measured by surface profilometry (~ 10% uncertainty). As neodymium is one of the more reactive lanthanide rare-earth metals, these films rapidly oxidize and degrade in air. Therefore, some films were covered by an amorphous Al_2O_3 protection layer prepared in a stand-alone Veeco® Fiji G Atomic Layer Deposition (ALD) system. The Al_2O_3 films were deposited at 87 °C using TMA (Trimethylaluminum) as a precursor and oxygen as the reactant. The TMA pulse time was set to 0.06 s, followed by a wait time of 4 sec and the application of an oxygen plasma for 6 sec at 300 Watt. The base pressure during this process varied from 0.1 – 0.2 mbar. To obtain a 25 nm thick film 300 cycles were needed.

The Optical properties of the films were studied by means of optical spectroscopy. Transmittance and reflectance of the films for static measurements were measured with a Perkin Elmer Lambda 900 spectrophotometer covering the spectral range of 200-2500 nm. From these measurements the change of absorption coefficient due to illumination was calculated. A customized optical fiber-based spectrometer was used for dynamic measurements. The light source is an ocean optics DH-2000 BAL deuterium-halogen lamp covering the spectral range of 230-1100 nm. The temporal change in transmittance was monitored during the photo-darkening and bleaching process. This set up is equipped with a LED light source collimated by Kohler optics with a narrow emission spectrum centered around λ = 385 nm and a 75140 $\mu W/cm^2$ maximum total irradiance at 500 mA. Structural properties of the films were analyzed by X-ray diffraction (XRD) using a Bruker D8 Advance diffractometer equipped with a Co X-ray tube and a LynxEye 1D Si-strip detector in Bragg-Brentano geometry. Because of the complexity of the analysis of the XRD patterns, the structural properties are discussed in the appendix.

6.3 Results

6.3.1 As-deposited neodymium based thin films

Optical properties

Figure 6.2a shows the optical transmittance spectra of as-deposited Nd-based films prepared at various deposition pressures. Films prepared at 0.3 and 0.5 Pa show a low overall transmittance and a weak transmittance window cantered around 900 nm, which is a characteristic of rare earth dihydride films.[11] The transmittance spectrum of the film prepared at 0.6 Pa, reveals the appearance of an absorption edge and a transmittance increase at longer wavelengths extending into the NIR. The overall transmittance is substantially lower than films prepared at higher pressures. We

assume that the film fabricated at this pressure is partially transformed from dihydride to oxyhydride upon exposure to air. Below this critical deposition pressure of p*= 0.6 Pa the films remain metallic dihydrides, whereas films deposited above p* transform into semiconducting oxy-hydrides after air exposure. Above p* the transmittance of the air exposed films increases drastically and the sharp fundamental absorption edge becomes more apparent. The resulting change of the average average transmittance as a function of the deposition pressure is presented in Figure 6.2b.

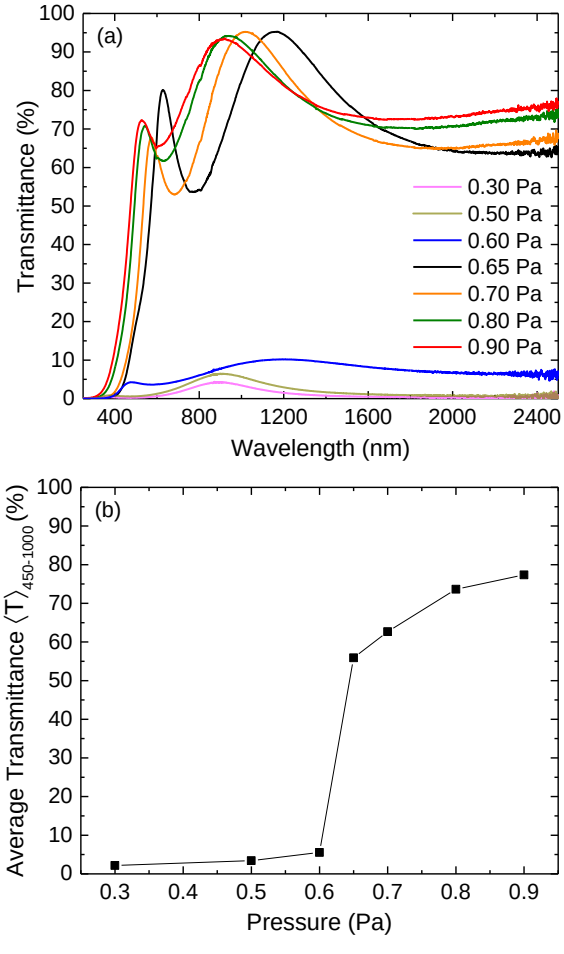

Figure 6.2. (a) Optical transmittance spectra of neodymium (oxy)hydride thin films sputtered at various deposition pressures (thickness between 200 and 230 nm). (b) Average transmittance of the films as a function of deposition pressure.

From the transmission and reflection spectra we calculate the values of the absorption coefficient $\alpha(\lambda)$ using the expression: $T(\lambda) = [1 - R(\lambda)] \exp[-\alpha(\lambda)d]$.[12]

By applying the Tauc model, the optical band gap of a material is determined from the linear extrapolation of the curve $(\alpha h\nu)^{1/m}$ vs. photon energy to zero absorption.[13] The exponent m depends on whether the transition is direct (m = 1/2) or indirect (m = 2). We find that m = 2 gives the best fit. The deviation from a straight line is possibly due to impurities and internal stress in the films. Figure 6.3a shows the plots of $(\alpha h\nu)^{1/2}$ vs. photon energy of neodymium hydride films as a function of deposition pressure. The optical band gap values are depicted in Figure 6.3b. Clearly, the size of the optical band gap increases with increasing deposition pressure from 1.65 to 2.11 eV. This is the smallest band gap value range we observed among the investigated rare earth oxyhydrides so far.

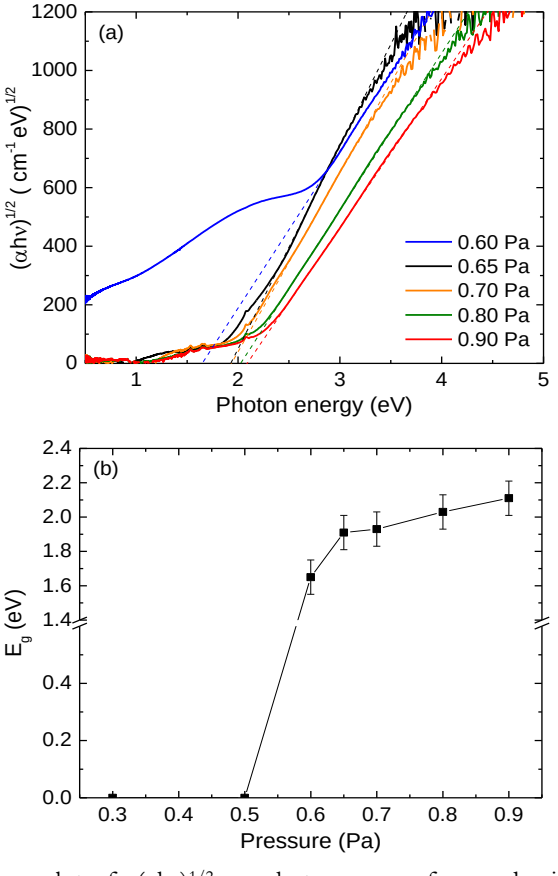

Figure 6.3. (a) Tauc plot of $(\alpha h\nu)^{1/2}$ vs. photon energy for neodymium hydride thin films prepared at different pressure. (b) The indirect optical band gap of the neodymium hydride thin films as a function of deposition pressure. (films prepared in a pressure range of 0.6-0.9 Pa showed a meaningful linear region in their Tauc plot for band gap determination).

Rutherford backscattering and elastic recoil detection data reveal an increase of (O^{2-}/H^{-}) anion ratio along with an increase in deposition pressure.[5] Hence, the relation between the pressure and the bandgap can be explained assuming a mixed hydrogen/oxygen valence band which shifts to lower energy levels with increasing oxygen content. The NdO_xH_y band gap is the smallest observed among the rare earth oxyhydrides investigated so far. It shows that the optical band gap of rare earth oxyhydrides may be tailored not only by changing the deposition pressure, but also by replacing the cation with another rare earth.

According to the relation between the bandgap and the hydrogen concentration of a MO_xH_y (M = Y, Gd, Dy, Er) film described by Cornelius et al. [5], the band gap decreases with increasing concentration of hydrogen. Given the chemical similarity of the RE, we expect a similar trend in NdO_xH_y. Nevertheless, the absolute bandgap value may change due to nature of the RE. In Nd_2O_3, the filled 4f-orbitals are situated above the 2p O levels which make up the valence band. These 4f levels may interact with the occupied H 1s levels in NdO_xH_y and hence lead to a valence band shift resulting in the observed small band gap values.

Photochromic properties

Photochromism is the reversible transformation of a material between two states that have different optical absorption spectra. Such a change is induced by the absorption of electromagnetic radiation of sufficient energy.[14] When a photochromic material is illuminated, its absorption generally increases due to the formation of light-absorbing species – a process referred to as photo-darkening. [14] Upon removal of activating light, the concentration of absorbing species decreases and the material reverts back to the original state, which is referred to as thermal bleaching.[14] There are several parameters that are used to quantify the photochromic effect. To eliminate the effect of the differences in initial transmittance between films, we define the relative transmittance as the transmittance at a given time normalized to its initial value $T_{relative} = T(\lambda,t)/T(\lambda,0)$. The relative contrast is described by $\Delta T(\lambda,t)=[T(\lambda,0) - T(\lambda,t)]/ T(\lambda,0)$. In these equations, the average transmittance in the range of 450-1000 nm, $\langle T \rangle$, is used to reduce optical interference effects.

All Nd oxyhydride films prepared above 0.6 Pa, showed photochromic properties. The transmittance of all films in VIS-NIR region decreases as soon as the films are illuminated (by a collimated LED light source). Figure 6.4a shows the photochromic performance of sputtered films as a function of deposition pressure. The relative contrast after 30 min of illumination is depicted in Figure 6.4b. The strongest contrast

is observed in the film prepared just above p* at 0.65 Pa and decreases with increasing deposition pressure.

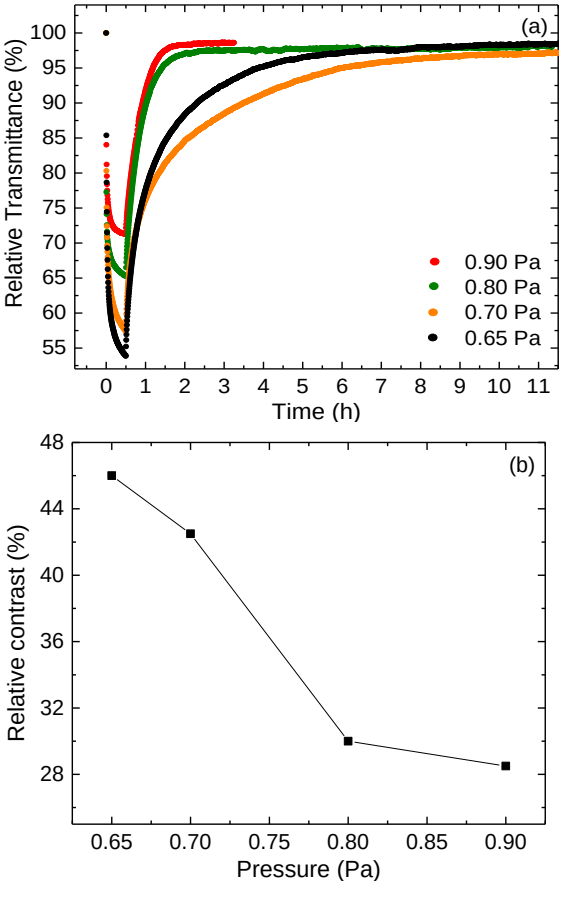

Figure 6.4. The photochromic response of the NdO_xH_y films prepared above the critical pressure. Films were illuminated using a collimated LED light source with a narrow emission spectrum centered around λ = 385 nm and 75140 μW/cm² maximum total irradiance at 500 mA. Followed by (thermal) bleaching in the dark at ambient conditions.

As soon as irradiation ceases, thermal bleaching starts. This process can be described with the help of the Lambert-Beer law. The absorption coefficient of the material is a function of concentration of absorbing species, c(t), and its absorption cross-section σ.

$$\Delta\alpha(\lambda, t) = c(t) \cdot \sigma(\lambda) \tag{6-1}$$

According to the Lambert–Beer law, the transmittance of light in dilute systems decreases exponentially with the film thickness, d, and absorption coefficient, α.

$$T(\lambda, t) = \exp(-\alpha(\lambda, t) \cdot d) \tag{6-2}$$

The change in transmittance contributing to darkening effect can be expressed as follows:

$$\frac{T}{T_0} = \exp(-(\alpha - \alpha_0) \cdot d) = \exp(-\Delta\alpha \cdot d) \tag{6-3}$$

Where T_0 is the initial transmittance and α_0 is the initial absorption coefficient before darkening starts and $\Delta\alpha$ corresponds to the difference in absorption coefficient between darkened and bleached state. Rewriting an exponential equation in logarithmic form, yields:

$$\ln\left(\frac{T}{T_0}\right) = -\Delta\alpha \cdot d \tag{6-4}$$

Assuming the kinetics is first order for thermal bleaching process, the transformation process is directly related to following equation which describes the change of concentration of darkened state:

$$\frac{dc}{dt} = -\frac{1}{\tau_B} c \tag{6-5}$$

Where τ_B (s) is the characteristic bleaching time constant. Solving this equation taking c_0 as the initial concentration when the illumination is switched off gives (see Figure 6.4a):

$$c(t) = c_0 \exp\left(-\frac{1}{\tau_B} t\right) \tag{6-6}$$

Combining equations 1-1, 6-4 and 6-6 yields the expression:

$$\ln\left(-\ln\left(\frac{T}{T_0}\right)\right) = -\frac{1}{\tau_B} t + \ln(c_0 \sigma d) \tag{6-7}$$

Hence, when taking the double natural logarithm of the normalised transmittance a linear relation with time is obtained. Provided that the assumption of first order kinetics is valid bleaching time constant τ_B can be determined from the linear slope in Figure 6.5a, The curves indeed indicate first order kinetics for the first stages of the thermal bleaching in NdO_xH_y films. From the linear fit, we obtain the bleaching time constants as a function of deposition pressure displayed in Figure 6.5b. We observe a

strong decrease in the bleaching time constant, i. e., faster thermal bleaching when increasing deposition pressure above p = 0.7 Pa.

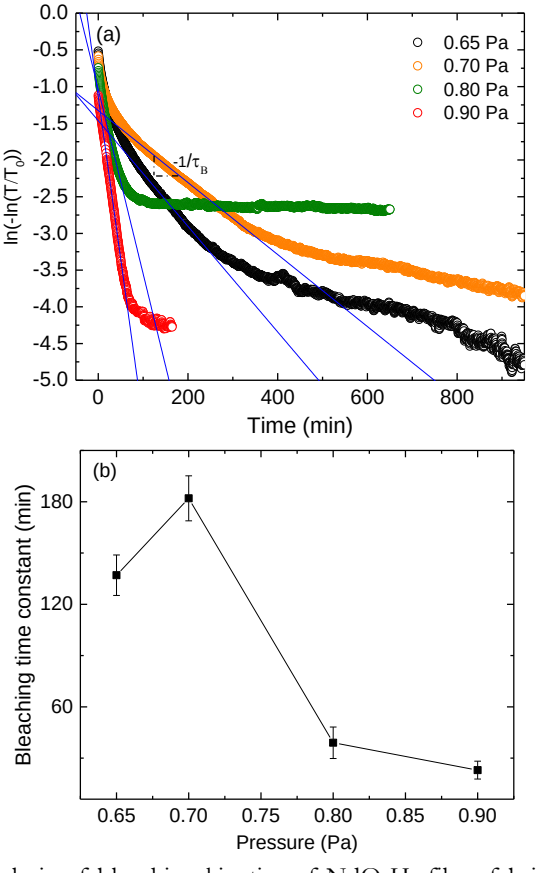

Figure 6.5. (a) Analysis of bleaching kinetics of NdO_xH_y films fabricated at different pressures. b) bleaching time constants versus deposition pressure.

Apparently, a high contrast correlates with a slow bleaching speed. Indeed, the photochromic saturation contrast is the result of an equilibrium between photo-darkening and bleaching. During illumination photo-darkening and thermal bleaching processes are simultaneously active. The absorbing species formed due to irradiation are at the same time affected by thermally induced relaxation. Slower bleaching implies therefore that a larger contrast can be obtained. It is unclear, however, how the thermal bleaching process relates to the higher O^{2-} to H^- ratio which is obtained at higher deposition pressures.

Effect of oxidation of NdO_xH_y on its optical

The optical and structural analysis shown so far is obtained directly after deposition of the films. Due its reactive nature, Nd containing hydride and oxyhydride films oxidize in air. In order to gain insight into the oxidation process after air exposure, the oxidation of the films was tracked in terms of optical and structural properties. The effect of air oxidation on transmittance is demonstrated in Figure 6.6 for two samples prepared at 0.5 Pa and 0.8 Pa, respectively.

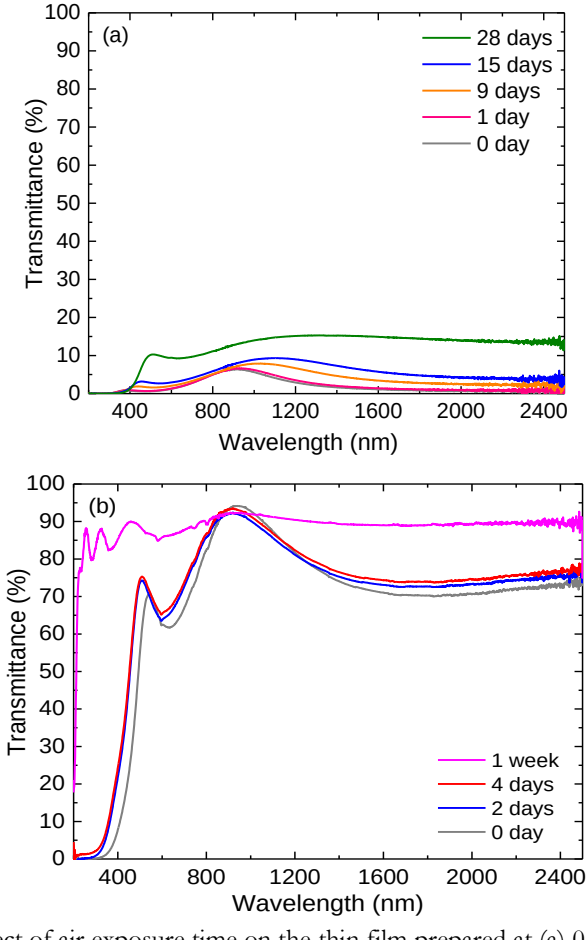

Figure 6.6. Effect of air exposure time on the thin film prepared at (a) 0.5 Pa and (b) 0.8 Pa.

For the film prepared at 0.5 Pa (Figure 6.6a), the initial transmittance window centered around 900 nm expands to longer wavelengths and an absorption edge starts to appear at around 400nm together with an overall increased transmittance. This indicates the transformation of metallic dihydride to semiconducting neodymium

oxyhydride. The oxidation rate of the films prepared above critical pressure is much faster, as exemplified for the case of 0.8Pa (Figure 6.6b). This film immediately transforms into an semiconductor on exposure to air. Further exposure of these films initially leads to a blue shift of the optical absorption edge, indicating an increase of the band gap. After one week, these films have oxidized completely showing band gaps around 5eV similar to that of Nd oxide [15] and peeled off from the substrate after around one week.

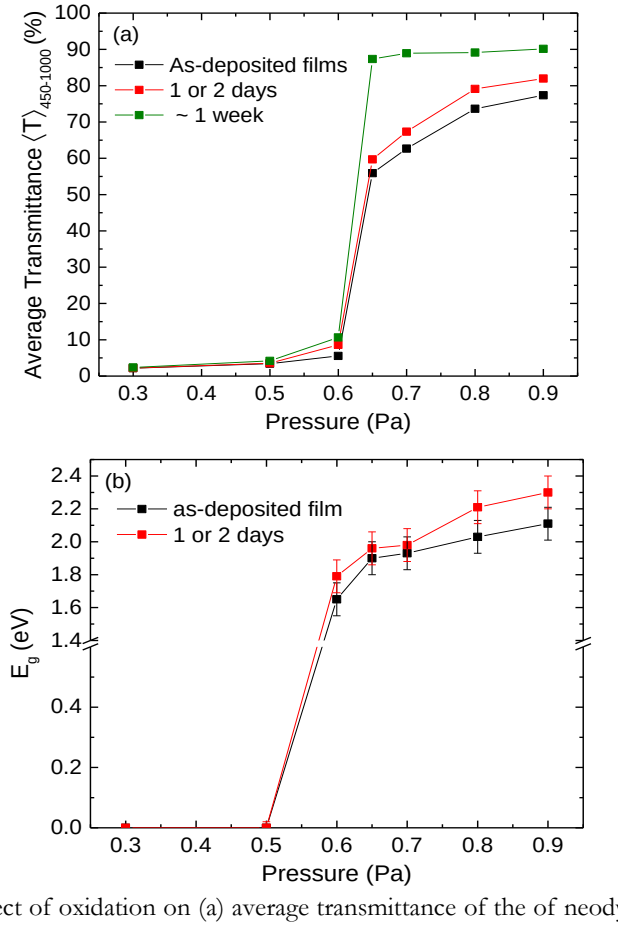

Figure 6.7. Effect of oxidation on (a) average transmittance of the of neodymium based films as a function of deposition pressure. (b) the band gap of the films as a function of deposition pressure which is obtained from Tauc plot.

Figure 6.7 shows a summary of oxidation effects on average transmittance and optical band gap of the films as a function of deposition pressure. This shows that the Nd-based films are much more prone to oxidation than the YO_yH_x films, which are

generally stable in air. For a fair comparison of the photochromic properties we therefore developed a method to protect the Nd-based films against oxidation.

6.3.2 Effect of the protection layer (ALD)

Optical properties

Atomic layer deposition (ALD) of metal oxide layers enables precise and reproducible metal oxide layer growth with complete surface coverage which is pinhole free.[16] In this work, we used Al_2O_3 as a protection layer for NdO_xH_y thin film. This cap layer appears to provide a good protection preventing the degradation of NdO_xH_y films in air under ambient conditions.

Figure 6.8 shows the change of average transmittance and band gap of the films before and after addition of a protection layer for various deposition pressures. Comparison of the average transmittance and band gap before and after ALD coating suggests that a certain amount of oxidation occurs during ALD fabrication of Al_2O_3 - probably due to the introduction of oxygen plasma. According to Figure 6.8a this oxidation is similar to the effect of 1 or 2 days of air exposure. However, the photochromic NdO_xH_y becomes more stable against air-oxidation after ALD capping with Al_2O_3. While uncapped films prepared at pressures above 0.6 Pa oxidize and delaminate after only one-week exposure to air, the ALD coated samples are stable for more than 2 weeks. This demonstrates that ALD coating is an effective method to prepare stable photochromic NdO_xH_y films for further studies and applications.

The transmittance of as-deposited and ALD coated NdO_xH_y films is displayed in Figure 6.9 as for overview. Using transmittance and reflectance (not shown) data, the optical band gap values deduced using the Tauc plot method are shown in Figure 6.10. After ALD coating the average transmittance of the samples has increased (Figure 6.8a) and the absorption edge (Figure 6.8 and 6.10) is shifted towards shorter wavelengths. This shift is samller for films fabricated at 0.65 Pa and 0.7 Pa.

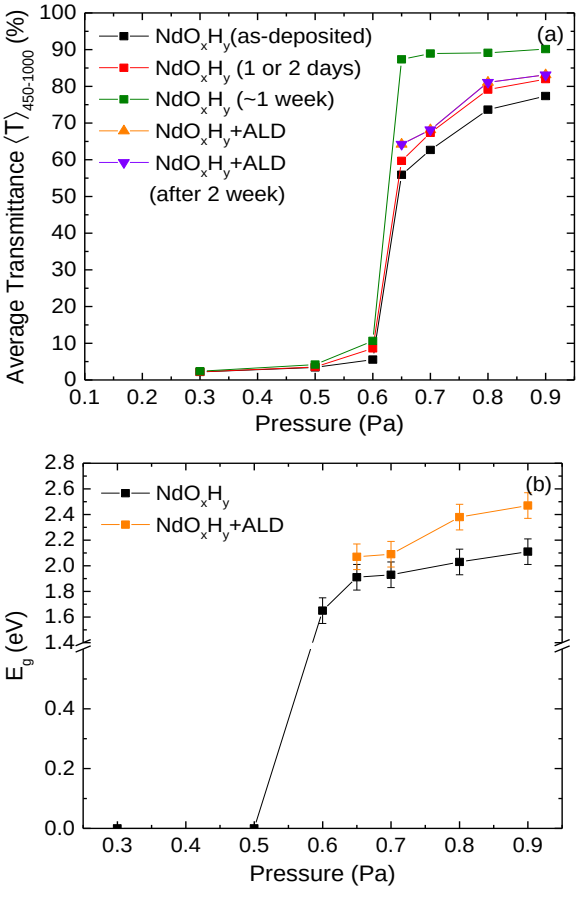

Figure 6.8. (a) Average transmittance; (b) indirect band gap of as-deposited and ALD coated NdO_xH_y film.

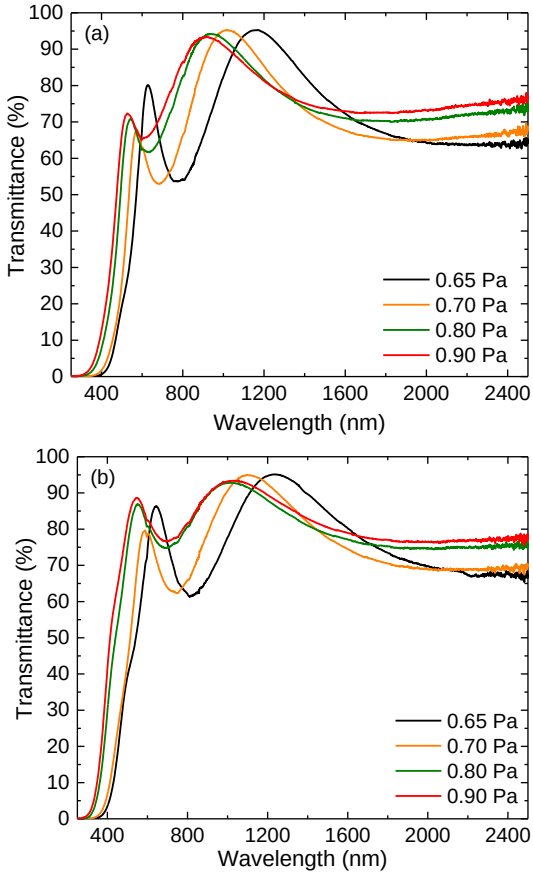

Figure 6.9. Optical transmittance spectra of (a) as-deposited and (b) ALD coated NdO_xH_y films grown at different deposition pressures.

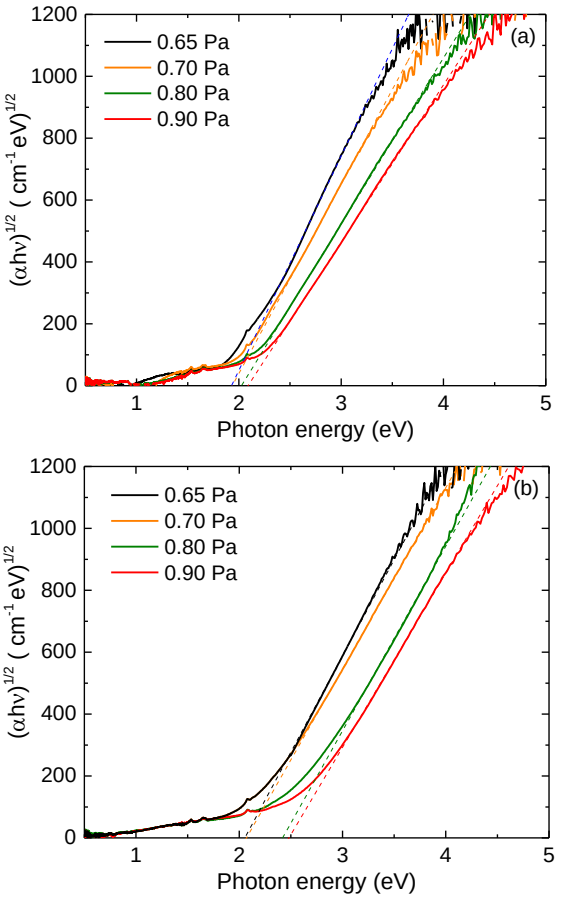

Figure 6.10. (a) Tauc plot for determination of band gap of (a) as-deposited and (b) ALD coated NdO_xH_y films prepared at various deposition pressure. The dashed lines are the linear fits of the absorption edges.

Photochromic properties, the effect of capping layer

Now that we tackled the problem of oxidation and degradation of NdO_xH_y thin films with a protection layer, it is important to assess the photochromic properties of these films. Here, we investigate the kinetics of photo-darkening and bleaching process after exposing the films to 30 min of LED illumination followed by bleaching in the dark at ambient conditions. Figure 6.11 shows the change of the average relative transmittance acquired during and after the illumination is ceased for as-deposited and ALD coated Nd-based films prepared at various deposition pressures. Remarkably, at all deposition pressures the maximum photo-darkening is reduced by the ALD coating process (see also Figure 6.12).

The relative contrast is strongest in the film sputtered at the lowest pressure close to critical pressure (0.65 Pa) while it decreases as the deposition pressure is increased. Although the dependency of contrast on deposition pressure follows a similar trend for both types of films, the photo-darkening is weaker in all ALD coated films (Figure 6.11a). This can be related to the fact that the ALD process induces a certain amount of oxidation. Note, that all films were illuminated within 1 hour after deposition. In the case of ALD coated films, they were illuminated after addition of protection layer which was done immediately after films deposition. All ALD coated films showed higher average transmittance and band gap value in comparison to as-deposited films at the start of the illumination process. Therefore, based on transmittance spectra of the films in the bleached state, we assumed that the ALD coated films contained more oxygen.

As mentioned earlier, the linear regime in the plot of the quantity $\ln(-\ln(T/T_0))$ versus the time yields the bleaching rate, τ_B. The bleaching time constants corresponding to the transmittance data in Fig 6.11 are determined using equation 7 and summarized in Fig 6.12b.

A substantial decrease of the bleaching time constant, i.e. faster thermal bleaching, is observed with increasing deposition pressure for both as-deposited and ALD coated films. For all deposition pressures, the bleaching time constant τ_B was found to be larger in case of ALD coated films, especially for films prepared close to the critical pressure. This is surprising as we expect these films to bleach faster given their poor photochromic contrast. This suggests that the exposure of the film to air is in part responsible for the photochromic contrast, as is the case for WO_3.[17] This would indicate that the surrounding ambient atmosphere plays a role during thermal bleaching of the photochromic films.

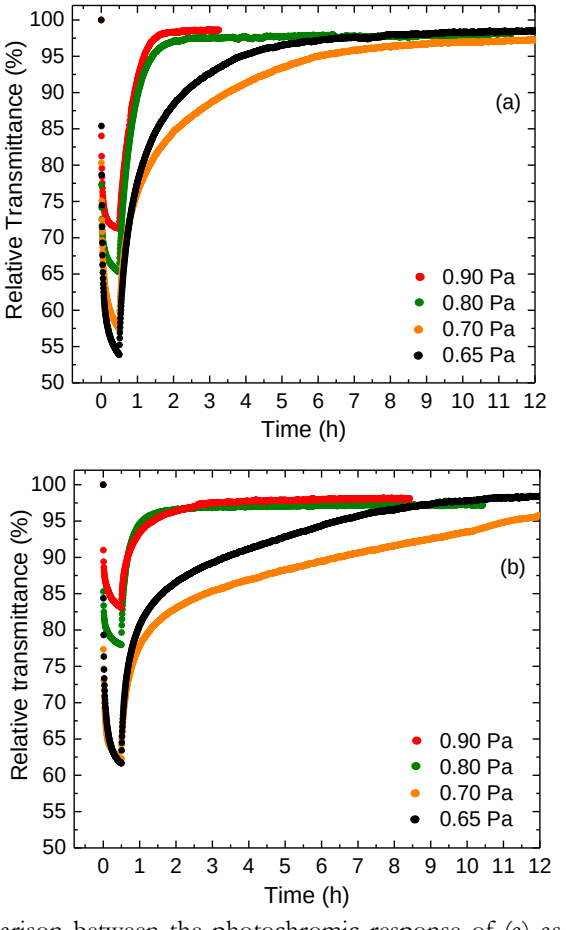

Figure 6.11. Comparison between the photochromic response of (a) as-deposited and (b) ALD coated films for various deposition pressures. Films were illuminated using a collimated LED light source with a narrow emission spectrum centered around λ = 385 nm and 75140 μW/cm² maximum total irradiance at 500 mA followed by (thermal) bleaching in the dark at ambient conditions.

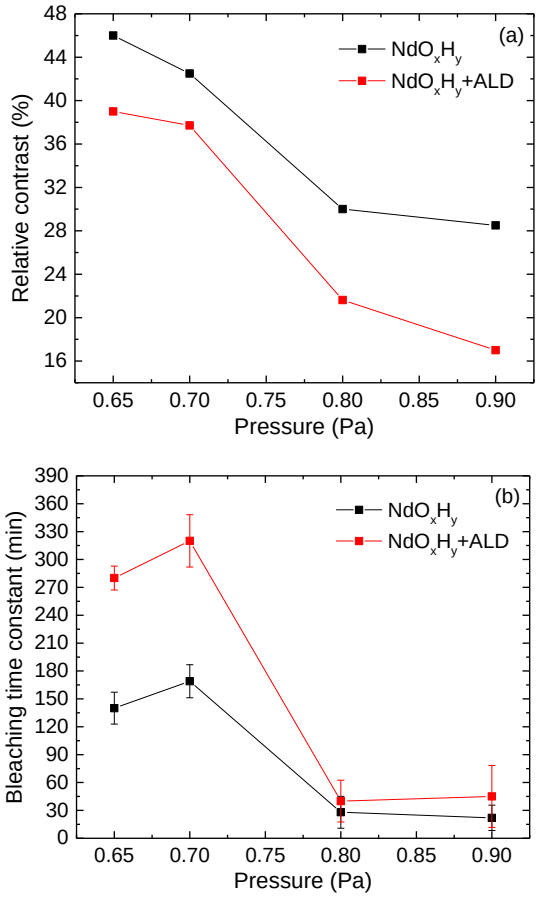

Figure 6.12. (a) The relative contrast and (b) bleaching time for as-deposited and ALD coated films as a function of deposition pressure obtained from the analysis of data shown in Figure 6.11.

6.3.3 Comparison of photochromic properties of NdO_xH_y and YO_xH_y thin films

So far we have shown the photochromic properties of neodymium oxyhydride and its dependence on deposition pressure. A question raised earlier in introduction, if the photochromic effect in rare earth oxyhydride is affected by the cation size. Since the Nd^{3+} cations are larger than other rare earth metals, it is expected that the bigger lattice provides more space for the mobility of the species involved in the photochromic process. Here, we want to compare the optical properties of NdO_xH_y to its well-known yttrium based counterpart. Since the photochromic properties depend on the deposition pressure we compare the darkening and bleaching behavior of as-deposited films of these two materials as a function of deposition pressure.
A similar trend is observed in the plot of the relative contrast versus deposition pressure for NdO_xH_y and YO_xH_y (Figure 6.13a). Both materials are not photochromic when deposited below their critical pressure (p*), since (stable) metallic dihydride films are formed in this regime. When the deposition pressure is increased above p*=0.35 Pa (Y) and p*=0.6 Pa (Nd) photochromic oxyhydrides are formed after air-exposure. We found a similar material dependent difference in case of the heavier lanthanides (Gd, Er).[4] At deposition pressures far above p* we find a decrease of photochromic contrast in both materials. Films prepared under these conditions generally tend to oxidize more rapidly and take up a larger amount of oxygen, which is believed to reduce photochromic contrast. As a result, a maximum in contrast is observed at pressures slightly above p* for both Nd and Y based oxyhydrides. Note that the maximum relative contrast of NdO_xH_y (~46%) is somewhat larger than that of Y (35%). However, direct comparison of contrast is complicated because it also depends on film thickness and absorption coefficients, which is discussed below.

The general trend of bleaching time constant in both rare earth oxyhydrides also shows a similar trend with a shift to higher pressures in case of Nd (Figure 6.13b). Both materials show a (nearly) monotic decrease of bleaching time constant (i.e. faster thermal bleaching) with increasing deposition pressure. The largest bleaching time constants are observed in the vicinity of p*. Apparently, the maximum time constant of YO_xH_y (~300 min) is larger than that of NdO_xH_y. This indicates that the cation size may have an effect on bleaching kinetics. Assuming that bleaching is related to point defect mobility, the latter may be facilitated by the larger Nd^{3+} cations and the resulting expanded crystal lattice. However, given the substantial effect of the deposition conditions and the resulting film microstructure and chemical composition on contrast and kinetics, a quantification of the cation size effect remains challenging.

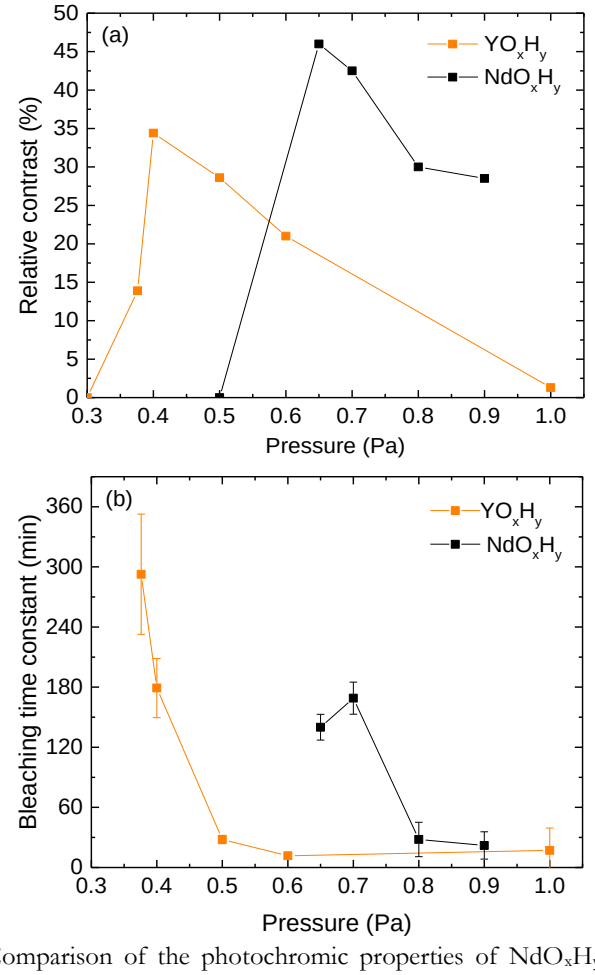

Figure 6.13. Comparison of the photochromic properties of NdO_xH_y (230 nm) and YO_xH_y (150 nm) as a function of deposition pressures. (a) Relative contrast (b) bleaching time. The films were illuminated for 30 min at 75140 μW/cm² followed by (thermal) bleaching in the dark at ambient conditions.

6.3.4 Stability of ALD coated NdO_xH_y films

In order to further investigate the influence of the Al_2O_3 capping layer on the stability of the NdO_xH_y films, the surface characteristics of the films were evaluated after a period of three months by optical microscopy (Figure 6.14 a&b). We observed pinholes throughout the surface of the films. Probably, this is due to dust particles. Since the films were exposed to air when they were transferred to the ALD chamber, we suspect that the films were not fully clean at the start of the ALD process. These dust particles allow oxygen to pass through pinholes and diffuse into the film where bubbles form. Through the bubbles, oxygen is transported leading to expansion and burst which give rise to additional entry ports for oxygen and water vapor. Since the surrounding of the pinhole looks very stable, the stability of ALD-coated NdO_xH_y films is probably significantly improved by the transportation of the films to the ALD chamber in Ar bag.

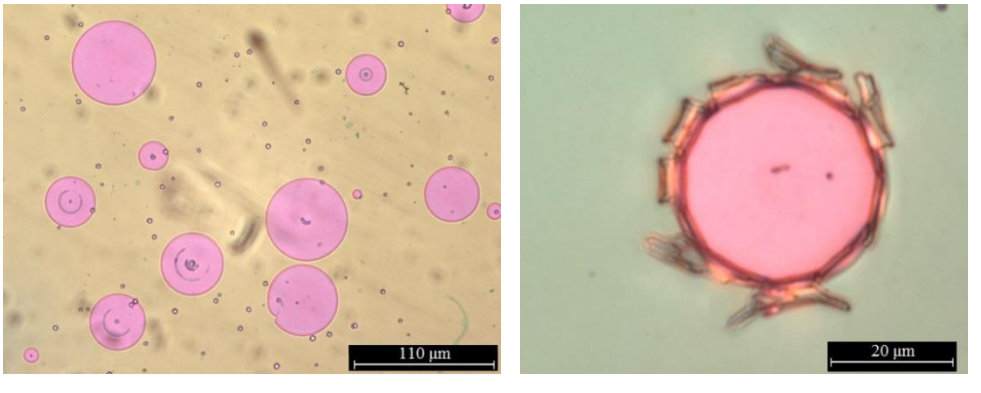

Figure 6.14. Images of ALD coated NdO_xH_y thin film after a period of three months with a use of differential interference contrast microscopy for optimizing image contrast. An overview of the film (left). A detail image of the pinhole on the surface of the film (right).

6.4 Application

Figure 6.15 shows a comparison of the absorption coefficient change due to photo-darkening of all RE oxyhydrides studied in this work. Since the absorption coefficient is purely a material property, this graph allows us to discuss the application potential of the different materials. Apart from GdO_xH_y ($\Delta\alpha_{max}$ ~ 32000 cm^{-1}), the photochromic effect in other rare-earth oxyhydride appears to be similar in magnitude ($\Delta\alpha_{max}$ ~ 15000-20000 cm^{-1}) in the VIS spectral range. While the photochromic contrast of Y, Dy and Er oxyhydrides is relatively low ($\Delta\alpha_{max}$ ~ 5000 cm^{-1}) in the NIR,

this is not true in case of Gd and Nd. In these materials, the photochromic effect extends into NIR spectral range with magnitudes of $\Delta\alpha > 20000$ cm^{-1} at $\lambda = 2400$ nm. Here, NdO_xH_y shows a unique interesting property where the photochromic response has a similar magnitude from the VIS to NIR. This would be a an advantage for smart windows because it allows for regulation of room brightness as well as heat management.

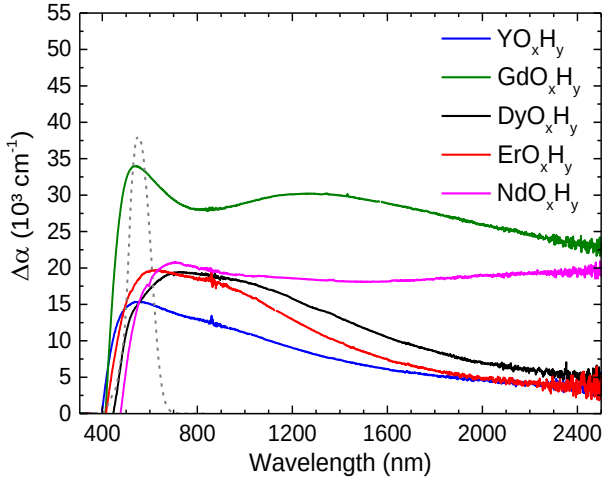

Figure 6.15. Comparison of the change in absorption coefficient of various rare-earth oxyhydride prepared just above their critical pressures (thickness between 230 and 350 nm) after 5 h of UV illumination at 5070 μWcm^{-2}. The absorption coefficients are calculated using the expression $T(\lambda)=[1 - R(\lambda)] \exp[-\alpha(\lambda)d]$.[12] The normalized human eye luminosity function is shown as a dashed curve according to Sharpe et al.[18] The onset and maximum are red-shifted for materials with lower band gap like NdO_xH_y. The NdO_xH_y film is coated with a 40 nm Al_2O_3 protection layer.

6.5 Discussion

Our experimental findings show that structural, optical and photochromic properties of the neodymium oxyhydrides can be tailored by the deposition pressure. Upon exposure to air, the metal-to-insulator transition from NdH_2 to NdO_xH_x starts at a critical deposition pressure of 0.6 Pa by the opening of a bandgap. The bandgap seems to slowly evolve towards the bandgap of Nd_2O_3 (4 – 4.9 eV [15]), with increasing deposition pressure and thus increasing O^{2-} to H^- ratio. The determined bandgaps of the NdO_xH_y films range from 1.65 eV to 2.11 eV which is the smallest band gap among reported rare earth oxyhydrides so far. According to the relation between the bandgap and the hydrogen concentration of a MO_xH_y (M=Y, Gd, Dy, Er) film described by Cornelius et al. [5], the band gap decreases with increasing concentration

of hydrogen. Given the chemical similarity of the RE, we expect a similar trend in NdO_xH_y. Nevertheless, the absolute bandgap value may change due to nature of Nd. In Nd_2O_3, the filled 4f-orbitals are situated above the 2p O levels which make up the valence band. These 4f levels may interact with the occupied H 1s levels in NdO_xH_y and hence lead to a valence band shift resulting in the observed small band gap values.

We find that the saturation contrast is highest close to the critical pressure and decreases as the deposition pressure increases. We expect that this is related to the composition and microstructure of the films. Films fabricated close to critical pressure, with a lower O^{-2}/H^- ratio and a more dense packing show the highest contrast and slowest bleaching. In comparison, films fabricated at higher pressure are expected to have more porosity and higher O^{-2}/H^- ratio show a smaller contrast and faster bleaching. This somehow affects the photochromic reaction that takes place, probably by a higher mobility of photochromic species. The photochromic saturation contrast is the result of the equilibrium between photo-darkening and bleaching, which is reached after a certain amount of time as these two processes occur simultaneously upon illumination. A lower bleaching rate, therefore, allows faster darkening and that is what we observed for films prepare close to critical pressure.

The difference in absorption coefficients and thickness of the films prevents any direct conclusion regarding the rare-earth dependence of the contrast. We find that the thermal bleaching time constant is only weakly affected by the type of rare earth metals that is used and mostly affected by microstructure and composition of the film. There is a factor of 10 difference in bleaching speed if you change the deposition pressure.
Our results show a fundamental step towards understanding and engineering of photochromic rare earth oxyhydrides. The results presented here might be of interest for certain applications, for example, if NdO_xH_y is used, one can block visible and infrared light with the same strength.

6.6 Conclusion

In conclusion, our work demonstrates that 1) NdO_xH_y can be added to the family of lanthanide oxyhydride thin films which exhibit photochromic properties, 2) structural, optical and photochromic properties are very much influenced by the deposition pressure which affects the microstructure and composition of the films. When increasing the deposition pressure and thus increasing the O^{2-} to H^- ratio the bandgap slowly evolves towards the bandgap of Nd_2O_3. We find the bandgap of NdO_xH_y is the smallest reported among rare earth oxyhydrides studied so far.) 3) NdO_xH_y shows

a uniquely flat photochromic response from the VIS to NIR. This would be an advantage for smart window design because it allows for regulation of room brightness as well as heat management. However, the typical photochromic switching time are of a similar magnitude as the other REO_xH_y, which suggests that point defect mobility is not the determining factor for the kinetics of the photochromic effect. 4) The addition of an ALD protection layer right after deposition improves the stability of NdO_xH_y thin films as it protects against further air-oxidation. The ALD process has an unexpected effect on the crystal symmetry of the film, which may be related to the oxygen plasma involved in the deposition process. In addition, we observe that the capped films have a reduced photochromic contrast, which warrants further study.

References

[1] T. Mongstad, C. Platzer-Bjorkman, S. Z. Karazhanov, A. Holt, J. P. Maehlen, and B. C. Hauback, "Transparent yttrium hydride thin films prepared by reactive sputtering," *Journal of Alloys and Compounds,* vol. 509, pp. S812-S816, Sep 2011.

[2] C. C. You, D. Moldarev, T. Mongstad, D. Primetzhofer, M. Wolff, E. S. Marstein*, et al.*, "Enhanced photochromic response in oxygen-containing yttrium hydride thin films transformed by an oxidation process," *Solar Energy Materials and Solar Cells,* vol. 166, pp. 185-189, 2017.

[3] J. Montero, F. A. Martinsen, S. Z. Karazhanov, B. Hauback, E. S. Marstein, M. Garcia-Tecedor*, et al.*, "Photochromic mechanism in oxygen-containing yttrium hydride thin films: An optical perspective," *Physical Review B,* vol. 95, 2017.

[4] F. Nafezarefi, H. Schreuders, B. Dam, and S. Cornelius, "Photochromism of rare-earth metal-oxy-hydrides," *Applied Physics Letters,* vol. 111, p. 103903, 2017.

[5] S. Cornelius, G. Colombi, F. Nafezarefi, H. Schreuders, R. Heller, F. Munnik*, et al.*, "Oxyhydride Nature of Rare-Earth-Based Photochromic Thin Films," *The journal of physical chemistry letters,* vol. 10, pp. 1342-1348, 2019.

[6] G. Kobayashi, Y. Hinuma, S. Matsuoka, A. Watanabe, M. Iqbal, M. Hirayama*, et al.*, "Pure H^- conduction in oxyhydrides," *Science (New York, N.Y.),* vol. 351, pp. 1314-7, 2016.

[7] A. V. Dotsenko, L. B. Glebov, and V. A. Tsekhomsky, *Physics and Chemistry of Photochromic Glasses*. Boca Raton: CRC Press, 1998.

[8] R. J. D. Tilley, *Defects in Solids* Wiley & Sons, Inc. , 2008.

[9] F. Nafezarefi, S. Cornelius, J. Nijskens, H. Schreuders, and B. Dam, "Effect of the addition of zirconium on the photochromic properties of yttrium oxy-hydride," *Solar Energy Materials and Solar Cells,* vol. 200, 2019.

[10] R. D. Shannon, "Revised Effective Ionic-Radii and Systematic Studies of Interatomic Distances in Halides and Chalcogenides," *Acta Crystallographica Section A,* vol. 32, pp. 751-767, 1976.

[11] A. T. M. van Gogh, D. G. Nagengast, E. S. Kooij, N. J. Koeman, J. H. Rector, R. Griessen*, et al.*, "Structural, electrical, and optical properties of $La_{1-z}Y_zH_x$ switchable mirrors," *Physical Review B,* vol. 63, p. 195105, 04/20/ 2001.

[12] M. Cesaria, A. P. Caricato, and M. Martino, "Realistic absorption coefficient of ultrathin films," *Journal of Optics,* vol. 14, 2012.

[13] J. Tauc, R. Grigorovici, and A. Vancu, "Optical Properties and Electronic Structure of Amorphous Germanium," *physica status solidi (b),* vol. 15, pp. 627-637, 1966.

[14] G. H. Brown, "Introduction," in *Photochromism: Techniques of chemistry, vol. III*, G. H. Brown, Ed., ed New York Wiley-Interscience, 1971.

[15] A. V. Prokofiev, A. I. Shelykh, and B. T. Melekh, "Periodicity in the band gap variation of Ln_2X_3 (X = O, S, Se) in the lanthanide series," *Journal of Alloys and Compounds,* vol. 242, pp. 41-44, 1996.

[16] W. He, "ALD: Atomic Layer Deposition – Precise and Conformal Coating for Better Performance," in *Handbook of Manufacturing Engineering and Technology*, A. Y. C. Nee, Ed., ed London: Springer London, 2015, pp. 2959-2996.

[17] S. Wang, W. Fan, Z. Liu, A. Yu, and X. Jiang, "Advances on tungsten oxide based photochromic materials: strategies to improve their photochromic properties," *Journal of Materials Chemistry C,* vol. 6, pp. 191-212, 2018.

[18] L. T. Sharpe, A. Stockman, W. Jagla, and H. Jagle, "A luminous efficiency function, V*(λ), for daylight adaptation," *J Vis,* vol. 5, pp. 948-68, 2005.
[19] B. D. Cullity and S. R. Stock, Elements of x-ray diffraction, 3rd ed. ed. Upper Saddle River, NJ: Prentice Hall, 2001.
[20] H. Yamashita, T. Broux, Y. Kobayashi, F. Takeiri, H. Ubukata, T. Zhu*, et al.*, "Chemical Pressure-Induced Anion Order-Disorder Transition in LnHO Enabled by Hydride Size Flexibility," *Journal of the American Chemical Society,* vol. 140, pp. 11170-11173, 2018.
[21] M. Widerøe, H. Fjellvåg, T. Norby, F. Willy Poulsen, and R. Willestofte Berg, "NdHO, a novel oxyhydride," *Journal of Solid State Chemistry,* vol. 184, pp. 1890-1894, 2011.
[22] A. J. Illig, C. T. Chantler, and A. T. Payne, "Voigt profile characterization of copper Kα," *Journal of Physics B: Atomic, Molecular and Optical Physics,* vol. 46, no. 23, 2013.

Appendix

Structural properties of NdO_xH_y

XRD patterns of neodymium hydride films reactively deposited at 0.3, 0.5 and 0.6 Pa are shown in Figure A6.16. These films appear to have an fcc structure corresponding to NdH_2, showing a preferred out of plane orientation along the fcc (111) direction. A detailed plot of the (111) diffraction peak is presented in Figure A6.16. This diffraction peak appears to shift to larger angles when the deposition pressure is increased from 0.3 Pa to 0.6 Pa. Possibly this shift is associated with the presence of a small amount of oxygen.

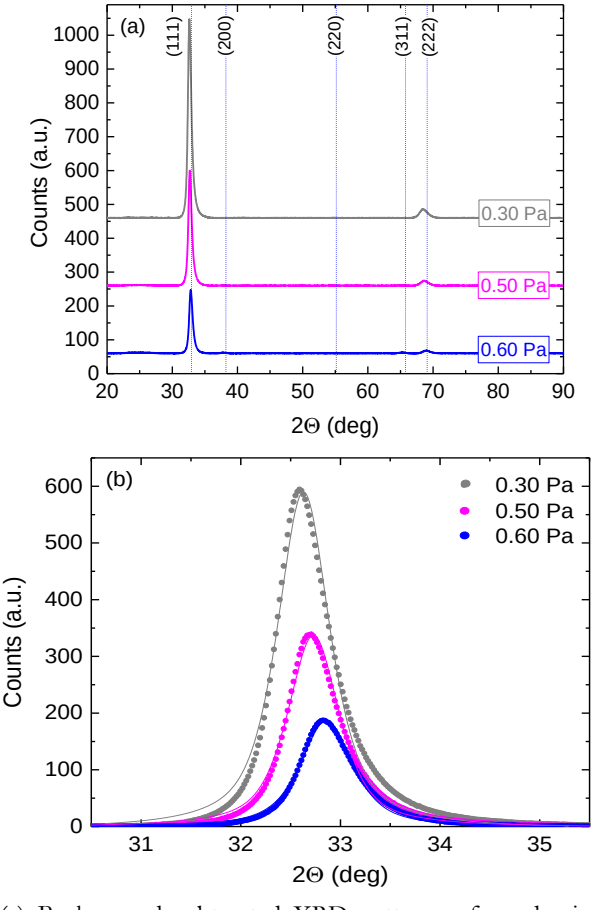

Figure A6.16. (a) Background subtracted XRD patterns of neodymium hydride thin films, prepared below the critical pressure. Vertical dashed lines correspond to ICDD-PDF pattern fcc-NH_2 #04-003-4756. (b) Detailed view of (111) for films fabricated below critical pressure.

Additional diffraction peaks appear when the deposition pressure is further increased. The X-ray diffraction patterns of the films prepared at 0.65, 0.7, 0.8 and 0.9 Pa are shown in Figure A6.17. In this case, additional lattice reflections turn up.

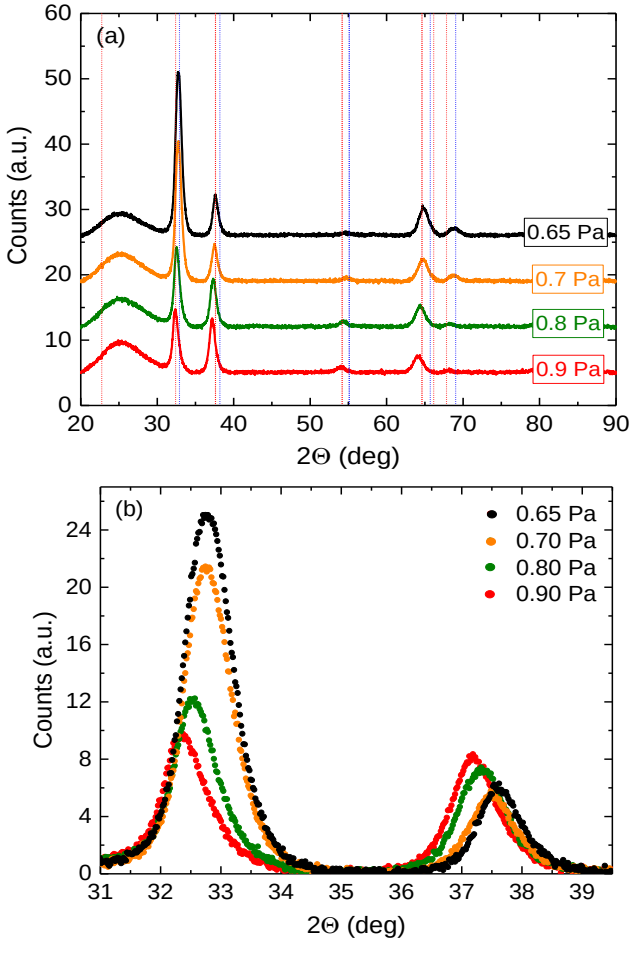

Figure A6.17. (a) Background subtracted XRD patterns of neodymium hydride thin films, prepared below the critical pressure. Vertical dashed lines correspond to ICDD-PDF pattern of fcc-NH_2 #04-003-4756 (blue) and tetragonal NdOH #04-017-9415 (red) (b) Detailed view showing the first two diffraction peaks of as-deposited films fabricated above the critical pressure.

In order to find out whether a cubic or tetragonal structure is formed, for each peak a double Pseudo-Voigt peak function (to account for the Cu-$K_{\alpha\,1/2}$ doublet)[22] was fitted to the experimental data. We considered instrumental error and error from fitting of

the peaks [$2\theta_{corr}= 2\theta_{(111)} - 2\theta_{offset}$]. From this value of θ, the lattice spacing d can be determined from Bragg's law:[19]

$$n\lambda=2d\sin\theta \quad (2)$$

Where d is the corresponding lattice spacing and n is an integer. The lattice spacing in cubic unit cell is related to hkl values and can be expressed as:[19]

$$d_{hkl} = \frac{a}{\sqrt{h^2+k^2+l^2}} \quad (3)$$

We assume that an fcc structure is formed and assign the (hkl) indices to the peaks. Four Bragg reflection peaks corresponding to (111), (200), (311) and (222) crystal orientations were identified (Figure A6.17b). The lattice constant values were obtained from each indexed peak. Figure A6.18 shows the lattice constant values calculated from each hkl-peak for films as a function of deposition pressure. Regardless of the deposition pressure, we observe that the calculated lattice constant shows a strong deviation from the cubic structure. Figure A6.19 shows an overview of trend of change of lattice constant calculated from different diffraction peaks as function deposition pressure. It appears that the lattice constant first decreases with increasing pressure, until it reaches a minimum value at a deposition pressure of 0.6 Pa and then it continuously increases with pressure. The reason for this minimum is not known. All films show a lattice expansion relative to the reference value of 5.464 Å corresponding neodymium dihydride even films prepared below critical pressure. This could be possibly understood by realizing that reactive sputtering is a non-equilibrium process that does not yield a highly ordered hydride structure, while the reference value refers to an annealed hydrogenated bulk specimen (ICDD-PDF fcc-NH_2 #04-003-4756). We observe a mismatch of lattice constant calculated from different reflection peaks assuming a cubic structure for films prepared above the critical pressure. This suggests distortion of cubic structure. Possibly, oxygen incorporation into the film plays a role in such a formation after air exposure.

Stoichiometric LnOH powders are reported to crystallize in the anion-disordered face-centered cubic (fcc) fluorite type structure ($Fm\bar{3}m$) (Ln = Sm, Gd, Tb, Dy, Ho, and Er) or in an anion-ordered superstructure with tetragonal (P4/nmm) symmetry.[20] In general, large Ln^{3+} ions (Ln = La−Nd) favour the formation of the ordered fluorite structure (P4/nmm).[20] As shown by Widerøe et al.[21] *stoichiometric* neodymium oxyhydride (NdOH) crystalizes in an anion-ordered superstructure with tetragonal (P4/nmm) symmetry, where the anion ordering takes place along the c-axis.[21] Indeed, our oxyhydride films appear to have a tetragonal symmetry (Figure A6.20), although the a/c ratio differs from that of Widoroe. This could be related to the fact that the

O/H ratio may deviate from 1. However, increasing the deposition pressure, which generally increases the O/H ratio, leads to an increase of both a and c. This suggests a subtle difference between the powder and the thin film structure possibly related to a higher amount of vacancies or a different O/H ratio in the thin films.

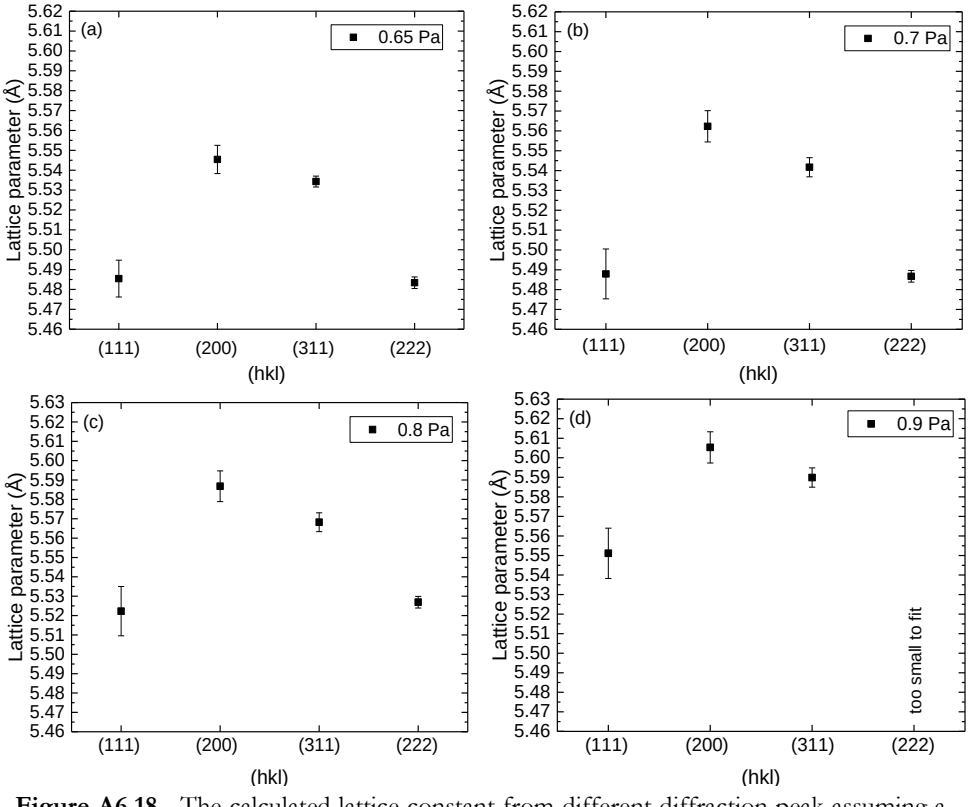

Figure A6.18. The calculated lattice constant from different diffraction peak assuming a fcc structure. The as-deposited NdO_xH_y films prepared at (a) 0.65 pa (b) 0.7 pa (c) 0.8 pa (d) 0.9 pa. The 2θ values were obtained by fitting Pseudo-Voigt peak function to experimental data (the peak positions were corrected for instrumental error and error from fitting).

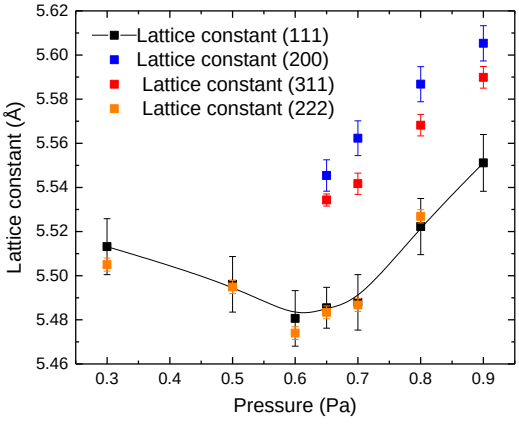

Figure A6.19. NdO_xH_y lattice constants as a function of deposition pressure, determined from the (111) and (200) diffraction peaks, respectively. The peaks are fitted as a linear combination of two Pseudo-Voigt functions (to account for the Co-$K_{\alpha 1,2}$ doublet[22]) to the experimental data.

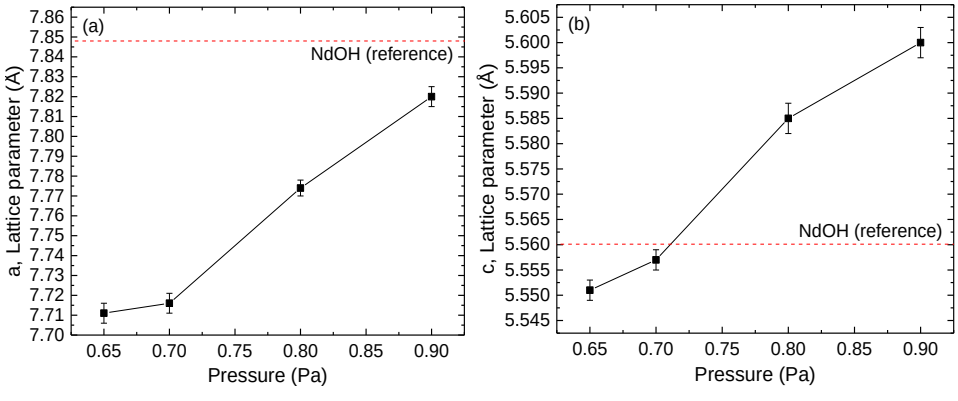

Figure A6.20. NdO_xH_y lattice parameters as a function of deposition pressure. The reference values of tetragonal NdOH #04-017-9415 are added for comparison.

Effect of oxidation of NdO_xH_y on its structural properties

The degradation Nd based films over time is evident from the changes in the optical properties. The effect of oxidation on the lattice constant as a function of deposition pressure is shown in Figure A6.21. For the films prepared below critical pressure (0.3 and 0.5 Pa), one can see that upon oxidation the lattice constant first decreases towards the minimum value that we observed for the film prepared at 0.6 Pa. On the other hand, the lattice constant of the film prepared at 0.6 Pa increases upon oxidation.

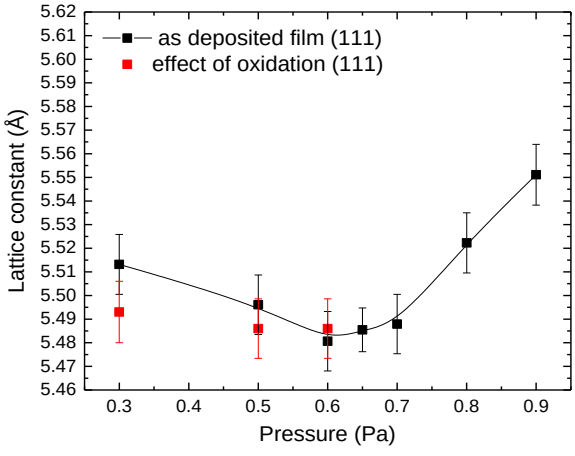

Figure A6.21. Influence of oxidation on the lattice constant calculated from (111) diffraction peak for the films as a function of deposition pressure.

For films prepared above the critical pressure, Figure A6.22 shows the effect of oxidation on the first two diffraction peaks (assuming films above critical pressure have a tetragonal structure) of the NdO_xH_y film prepared at 0.9 Pa. While the first diffraction peaks is found to reduce in intensity and shifts to lower diffraction angles slightly, the second peak decreases in intensity and shifts more rapidly to lower diffraction angles over time. The reason for this observation is unknown.

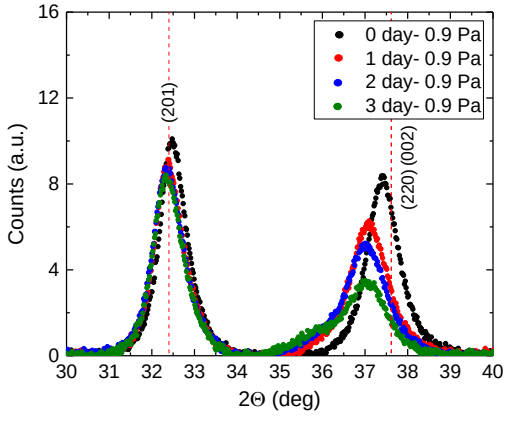

Figure A6.22. (a) Background subtracted XRD pattern of the NdO_xH_y film prepared at 0.9 Pa over the period of three days. Vertical dashed lines correspond to ICDD-PDF pattern of tetragonal NdOH #04-017-9415.

Effect of protection layer (ALD) on structural properties of NdO_xH_y

To counter this effect a set of NdO_xH_y films was prepared above critical pressure and capped with Al_2O_3 within 2-3 min after deposition by atomic layer deposition (ALD). ALD of metal oxide layers enables the precise and reproducible metal oxide layer growth with a complete surface coverage which is pinhole free.[20]

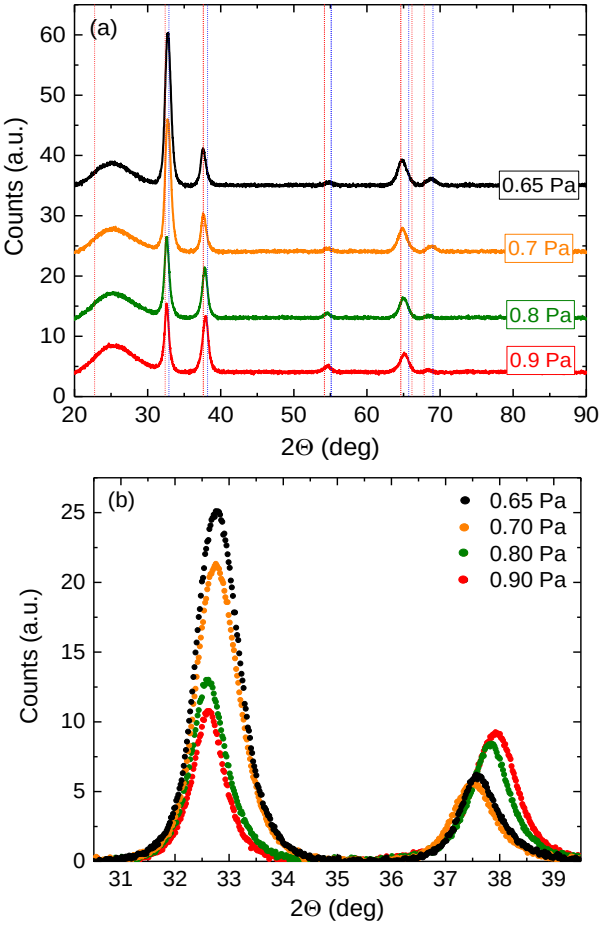

Figure A6.23. (a) Background subtracted XRD pattern of the ALD coated NdO_xH_y films prepared at different deposition pressures. (b) Detailed view showing the first two diffraction peaks of ALD coated films fabricated above the critical pressure.

Figure A6.23a shows the diffraction pattern of the as-deposited and ALD coated NdO_xH_y films as a function of deposition pressure. Similar to as-deposited films, we tried to verify if a cubic or tetragonal structure is formed. A sum of two Pseudo-Voigt function (to account for the Cu-$K_{\alpha\ 1/2}$ doublet) was used to determine the diffraction

peak positions. First we assumed a cubic structure might have formed and assigned the (hkl) indices to the peaks. Four Bragg reflection peaks corresponding to (111), (200), (311) and (222) crystal orientations were found. The lattice constant values were determined from each diffraction peak and depicted in Figure A6.24. For films prepared at 0.65 Pa and 0.7 Pa, a strong deviation from the cubic structure is also observed for ALD coated films. However, for films prepared at 0.8 and 0.9 Pa, similar values for the lattice constant are obtained from different indexed peaks. This suggests that the tetragonality depends also on the O/H ratio.

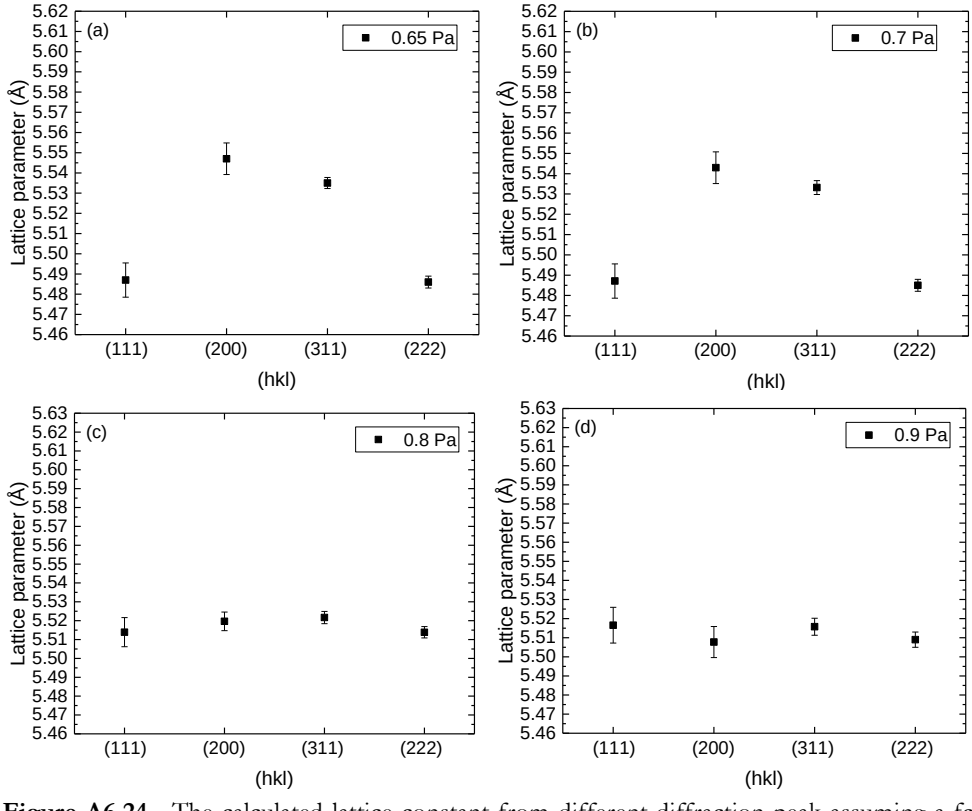

Figure A6.24. The calculated lattice constant from different diffraction peak assuming a fcc structure. The ALD coated NdO_xH_y films were prepared at (a) 0.65 Pa (b) 0.7 Pa (c) 0.8 Pa (d) 0.9 Pa. The 2θ values were obtained by fitting Pseudo-Voigt peak function to experimental data (the peak positions were corrected for instrumental error and error from fitting).

Comparing the average transmittance and band gap before and after ALD coating (Figure 6.8), we find that the coating process leads to increase in bandgap especially for the samples sputtered at 0.8 and 0.9 Pa. The plasma treatment apparently increases the oxygen content strongly. In that case the amount of hydrogen might become too

small to lead to an ordering effect, which might be the reason that these films reveal a cubic symmetry again.

Next, we investigated whether the ALD coated films prepared 0.65 Pa and 0.7 Pa have a tetragonal structure. The lattice parameters a and c from Wideroe's work were taken to calculate the theoretical 2θ values for the different (hkl) planes. The lattice parameters a & c were changed to obtain the best match to experimental fitted 2θ values (within 2θ error). Figure A6.25 shows the obtained lattice parameters a & c for as-deposited and ALD coated films as a function of deposition pressure.

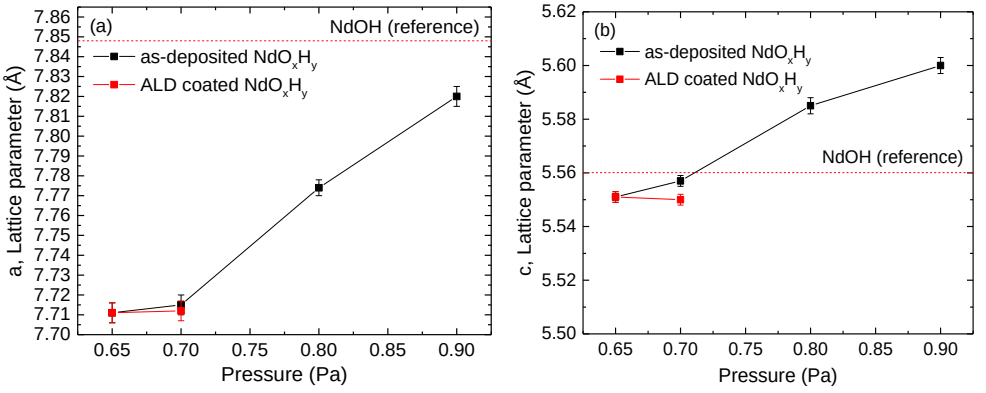

Figure A6.25. The calculated lattice parameters a & c for as-deposited and ALD coated NdO_xH_y films as a function of deposition pressure. The reference values of tetragonal NdOH #04-017-9415 are added for comparison.

7

Electronic nature of yttrium hydride, yttrium oxyhydride and yttrium oxide thin films

The photochromic yttrium oxyhydride has attracted attention for the past decades because of its peculiar optical properties such as a sensitivity to visible light and a resulting strong darkening over a wide range of wavelengths. We showed in chapter 4 that metallic dihydride thin films can be made by reactive sputtering of yttrium metal targets in an argon and hydrogen atmosphere. Above a certain critical deposition pressure, the metallic dihydride film turn to transparent semiconductor upon exposure to air. Thus a yttrium oxyhydride thin film is produced.[1] Here we investigate the electronic structure differences between yttrium hydride, yttrium oxyhydride and yttrium oxide thin films in relation to their photochromic nature using XPS depth profiling.

7.1 Introduction

We showed in chapter 4 that LnO_xH_y thin films with Ln = Gd, Dy, Er exhibit reversible photochromic properties when exposed to illumination at ambient conditions.[1] This switchable optical property enables their utilization in many technological applications, such as smart windows. We recently established a ternary RE−O−H composition-phase diagram based on chemical composition analysis by a combination of Rutherford backscattering and elastic recoil detection.[2] We reported that these oxyhydride films are photochromic over a large part of their entire composition range ($0.5 \leq x \leq 1.5$) as described by the formula REO_xH_{3-2x}.[2] This implies that the RE cation maintains the 3+ valence for all photochromic compositions and that the presence of both oxide and hydride ions are crucial for the photochromic effect at ambient conditions.[2] The exact mechanism involved in the photochromic effect of rare earth oxyhydrides is not yet exactly clear, although a series of studies point to the development of structural [1,3,4] and electronic modifications[5] upon illumination.

In this work, we study the electronic nature of yttrium hydride and oxyhydride thin films by means of X-ray photoelectron spectroscopy (XPS). XPS is a powerful tool to gain information about the chemical composition and chemical binding behavior of atoms within the thin films. Therefore, we set to investigate the nature of the various yttrium compounds. Furthermore, we try to establish whether the XPS signal changes in yttrium oxyhydride upon photo-darkening.

7.2 Experimental methods

Thin films of yttrium oxide, yttrium oxyhydride and yttrium hydride were fabricated using reactive magnetron sputtering of a yttrium target (with 99.99% purity) with a sputtering power of 200 W. The 100 nm yttrium oxyhydride and dihydride thin films were prepared at 0.5 Pa and 0.3 Pa respectively by DC reactive magnetron sputtering in an Ar/H_2 atmosphere. The 100 nm yttrium oxide film is prepared at 0.3 Pa by Pulsed DC plasma excitation (50 kHz, 90% duty cycle) in Ar/O_2 atmosphere. All samples were grown on a silicon (Si) (100) wafer substrate for XPS analysis.

To investigate the chemical composition and chemical bonding of atoms within the films, X-ray photoelectron spectroscopy (XPS) measurements were carried out. This analysis was performed using the Thermo Scientific K-alpha apparatus equipped with a Al K-α ($h\nu$ = 1486.6 eV) X-ray source, a flood gun and an ion gun. The binding energy

scale of the spectrometer is calibrated using Au $4f_{7/2}$ at 84.0 eV and Cu $2p_{3/2}$ at 932.7 eV in reference to the Fermi level. A 400-μm diameter X-ray spot was used in the analysis. A flood gun was used to minimize possible sample charging. The survey spectrum was recorded at the analyzer pass energy (E_p) of 50 eV and the core level spectra are recorded with E_p = 20 eV for the detailed scans of Y 3d , O 1s and Si 2p excitations, with an energy step size of 0.1 eV, a dwell time of 50 ms, and averaging 15 scans. The valence band spectra were recorded with E_p = 35 eV because of low intensity. Ar 2p and C 1s were performed in snapshot mode for the purpose of calibration correction. In this mode the pass energy of the analyser is increased and the electron signal from the entire range is recorded rather than selected energy range. This gives and advantage of fast data acquisition at the cost of energy resolution.

The pass energy is the energy of the electrons that pass through the analyzer. The selected pass energy influences the transmission and resolution of the analyser.[6] Ensuring that all the electrons that enter the spectrometer have the same energy resolution. The lower pass energy usually results in a better energy resolution but at the cost of a lower signal to noise ratio.[6]

Argon ion sputtering is used in order to remove atoms from the surface under study. The films are etched along their depth. The energy of Ar^+ ions for depth profiling is 500 eV. The films were sputtered (etched) along the depth of the film to obtain the surface and interface chemistry information from the surface to the bulk of the film. The CasaXPS program is used for deconvolution of the peaks. A Shirley baseline was employed for background modeling together with the best proportion of Gaussian to Lorenzian ratio for each peak in CasaXPS for peak decomposition.

Optical transmittance measurements were carried out using a Perkin Elmer Lambda 900 spectrophotometer with a wavelength range of 200-2500nm. XRD patterns were collected in Bragg-Brentano geometry using a Bruker D8 Advance diffractometer equipped with a Co X-ray tube and a LynxEye 1D Si-strip detector. For photo-darkening experiments of the yttrium oxyhydride film, a HeroLab low-pressure mercury lamp with emission lines centered around λ = 310 nm and 6873 μW/cm² total irradiance. The absolute UV irradiance was determined using a calibrated USB-2000+ spectrometer (Ocean Optics) with a relative uncertainty of about 10%.

7.2.1. Correction for charging effects

Many metals and semiconductors spontaneously form an insulating oxide layer on their surfaces when they come to contact with air. As a consequence of their insulating nature, they are easily prone to charging.[7] In XPS experiments charging effects are identified by a photoelectron peak shift and peak broadening.[8] The correct identification of chemical bonding environments using XPS relies on accurately determining small shifts in core-level binding energies. The coexistence of multiple similar or related phases makes XPS chemical-state analysis complex if charging is involved. The Y 3d core levels associated with the metal, the oxide and the hydride lie within few eV of each other. Therefore, charge referencing and charge control are very critical for producing reliable XPS data that can be compared to data by other researchers. Elemental Y $3d_{5/2}$ is reported at 155.56 eV while Y $3d_{5/2}$ for β-$YH_{1.9+\delta}$ phase is found at 156 eV.[9] The Y $3d_{5/2}$ for YH_3 appears at 158 eV.[9] In the hydrides the exact kinetic energy of the Y$3d_{5/2}$ photoelectrons depends on the H concentration.[9] For Y_2O_3 thin films deposited at substrate temperatures above $\approx$ 800K a chemical shift of 2.5 eV is reported. These films showed a very intense O 1s singlet.[10] On the other hand, the yttrium oxide film deposited at room temperature showed the Y $3d_{5/2}$ component at 156.6 eV. The oxygen emission line in this film showed a week intensity.[10]

The C1s core level peak in the range of 284.6 and 285 eV is commonly used as an easy-to-use internal energy reference element for the calibration of XPS data.[11] In our case 284.6 eV is selected.[12] Nevertheless, there are many fundamental reasons why the carbon photoelectron peak is not always an ideal reference. The binding energy for the C1s core level depends on the nature of the carbon contamination on the specimen. It has been reported that the calibration procedure based on the C 1s peak of adventitious carbon can be highly arbitrary, which results in incorrect spectral interpretation.[11] Literature study shows the binding energy values for the C 1s level of adventitious carbon range from 284.6 to 285.2 eV.[13]

In our work, after few minutes of Ar-ion etching, C 1s signal disappears (therefore the C 1s peak of adventitious carbon could not be used as an internal reference for the depth profiling data) and the Y 3d and O 1s peaks shift which indicates that the local electronic environment of the corresponding atoms is affected by the etching and changes from surface to deeper inside the film.

Another attempt to solve the binding energy referencing is based on using core-level lines of implanted Ar atoms.[11] What makes this approach interesting is that the

incident energy is in the range of 1-5 keV, making the implantation depth largely overlap with the XPS probing depth. The Ar $2p_{3/2}$ photoelectron line may encounter pronounced chemical shifts depending on the implantation matrix.[14, 15] In their study on yttrium oxide, oxyhydride and dihydride Mongstad et al.[16] report taking Ar 2p peak value of 243.9 to calibrate the spectra in yttrium hydride and yttrium oxide thin films. It is not clear if this is the Ar $2p_{3/2}$ or Ar $2p_{1/2}$ photoelectron line. Unfortunately, the Ar photoelectron line was not shown and they do not report on any shift due to the matrix.

In general, because of the uncertainty of the Fermi level and the presence of charging, it is difficult to determine the binding energy of the Ar photoelectron levels in insulating materials.[12] Kohiki et. at. suggested correcting this by using the difference in extra atomic relaxation between implanted Ar into conducting and insulating materials. They found a value of 241.5 ± 0.2 eV in metals and 242.3 ± 0.4 eV for insulating materials of Ar $2p_{3/2}$ photoelectron line.[12] Hughes et. al. confirmed the value of 242.3 eV in case of Y_2O_3.[17] According to Kihiki et al. the charge shift and corrected binding energy (BE) of the system can be calculated by[12]

$$\Delta E = BE_{Ar_{2p\,3/2}}(\text{observed}) - 242.3\ eV \tag{7-1}$$

$$BE_{(\text{Corrected})} = \text{observed binding energy} - \Delta E \tag{7-2}$$

Note that Kihiki et al. questioned the use of carbon 1s binding energy as a means to calculate a binding energy correction. Nevertheless, they tentatively used C 1s to correct the Ar $2p_{3/2}$. They observed a lower C 1s value in comparison to conductive materials (0.8 eV difference). They corrected the C 1s and relative to that the Ar $2p_{3/2}$ peak.

In order to test this method, we attempted to use implanted argon atoms as a referencing method in our experiments. Initially, argon is not visible in the XPS spectrum. It only appears when etching starts to progress. The Ar $2p_{3/2}$ peak signal slightly changes in position during the etching process. The Ar $2p_{3/2}$ photoelectron line is situated at a binding energy of 241.56 ± 0.2 eV in yttrium oxide films (17 min of etching). In yttrium dihydride and oxyhydride films, however, Ar $2p_{3/2}$ is situated at a remarkably higher binding energy of 243.68 ± 0.2 eV and 243.26 ± 0.2 eV respectively (16 min of etching). Taking a binding energy of 242.3 eV for the Ar $2p_{3/2}$ peak for the normalization of binding energies in oxyhydride and dihydride film would artificially transfer all binding energies to lower values, up to 1.4 eV. In case of yttrium dihydride f 6 min of etching would place the Y $3d_{5/2}$ at 154.13 ± 0.2 eV which is even lower than

reported values for Y metal. Pelisson-Schecker et al. found that the Ar $2p_{3/2}$ peak for implanted argon in Al-Si-N samples shift with varying Si content by as much as 1 eV due to the increase of concentration of implanted argon atoms.[18] This type of effect does not qualify as chemical shifts as the noble gases rarely have chemical reactivity and there is no new bond formation involving inert gas atoms.[11] Nevertheless, the shortcoming in this technique is that the noble character of implanted Ar atoms does not guarantee constant binding energy, hence they do not serve as a reliable binding energy reference.[11]

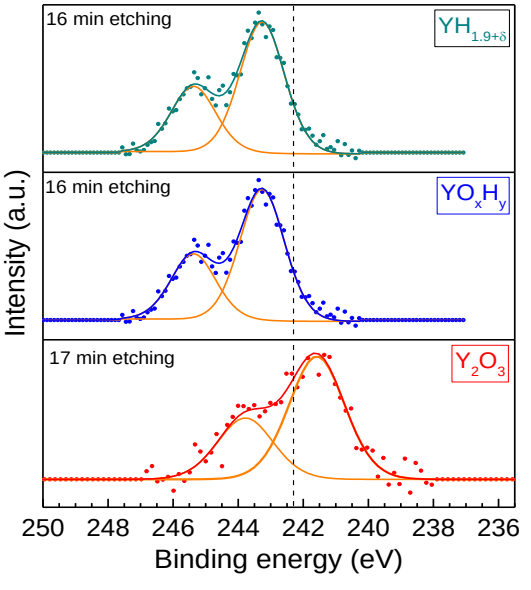

Figure 7.1. XPS Ar 2p core level lines of argon trapped within the yttrium dihydride, yttrium oxyhydride and yttrium oxide thin films. The vertical line is the recommended binding energy of Ar $2p_{3/2}$ for Y_2O_3.[12,17] The doublet lines of Ar 2p is fitted using two components of identical line shape with the constraint of equal FWHM. the value of doublet separation between the Ar $2p_{3/2}$ and Ar $2p_{1/2}$ was fixed to 2.1 eV.[19] Snapshot Ar 2p spectra are used for rapid data acquisition during depth profiling. Note that, the YH_2 thin film was transferred to XPS load lock after 4 hours of air exposure.

An alternative approach was considered using a gold referencing procedure where half of the sample was sputtered with gold and the depth profile was performed on the area covered half with gold while probing with XPS. Although the Au $4f_{7/2}$ line was found on 84 eV, the Y $3d_{5/2}$ line for our oxide film was lower than mostly reported literature values.[20-22] In view of these difficulties, no reliable internal referencing element was found for calibration and in this work we present as received fitted data.

7.3 Results

We showed in chapter 4 that by reactive sputtering of an yttrium metal target in an Ar/H_2 mixture below a critical pressure, a thin film resembling metallic β-$YH_{1.9+\delta}$ can be prepared.[1] This film shows low overall transmittance and a transmittance window characteristic of yttrium dihydride [23] (figure 7.2a). The diffraction pattern of this film reveals the face-centered cubic (fcc) structure of the CaF_2 prototype (space group Fm-3m) with a predominant diffraction peak corresponding to the (111) lattice plane (figure 7.2b). We find a lattice constant of 5.27 ± 0.01 Å for this as-deposited dihydride film. When the deposition pressure is increased, the metallic dihydride film -upon exposure to air- turns into a semiconducting film with average transmittance of $\langle T \rangle$ = 74 % in the 450 - 1000 nm range and an optical band gap of E_g = (2.5 ± 0.05) eV.

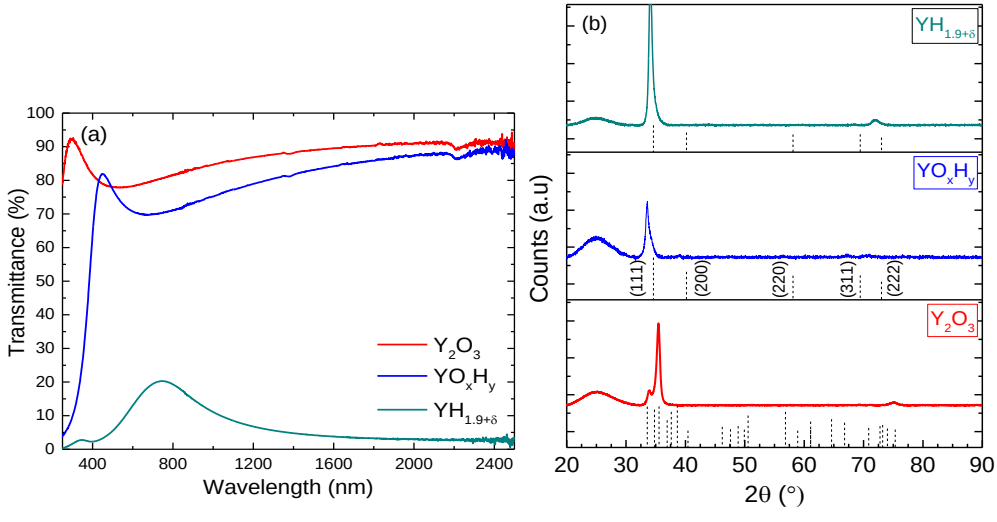

Figure 7.2. (a) Optical transmittance spectra and (b) Background subtracted XRD patterns of yttrium oxide, dihydride and oxyhydride thin films (thickness of ~100 nm). The hkl peak positions of a monoclinic yttrium oxide based on ICDD-PDF 00-044-0399 and fcc-YH_2 ICDD-PDF pattern 04-06-6935 are added as vertical dashed lines.

The fcc structure in this film is retained and the oxygen incorporation leads to a lattice expansion (5.37 ± 0.01 Å). Reactive sputtering of yttrium metal target in an Ar/O_2 mixture leads to the formation of an oxide film with an average transmittance of $\langle T \rangle$ = 82 % in the 450 - 1000 nm range and optical band gap of E_g = (5.5 ± 0.05) eV, which is in the range of literature values reported for yttrium oxide.[20] The XRD pattern of this film approximately coincides with that of monoclinic pattern from the database (which

sputter deposition conditions exactly determine the formation of the monoclinic or bixbyite variety is not known yet).

An XPS survey spectrum was first recorded to identify all elements present on the surface of films followed by high-resolution spectra of the Y 3d, O 1s, Si 2p (not shown here). Depth profiling was performed by alternating a combination of Ar^+ ion sputtering/bombardment followed by XPS data acquisition and sputtering. Thus, the core level peaks were measured along the depth of the films.

Figure 7.3 shows the Y 3d and O 1s photoemission peaks of an yttrium oxide film as a function of depth. The bottom picture corresponds to the as-deposited film top surface, the XPS spectra on top of that represent the consecutive stages obtained upon etching. The Y 3d XPS spectrum consists of two distinct peaks corresponding to different electronic spin states called Y $3d_{5/2}$ and Y $3d_{3/2}$ with spin-orbit splitting of 2.05 eV between Y $3d_{5/2}$ and Y $3d_{3/2}$ components where an intensity ratio between $I_{3/2}/I_{5/2}$ of 0.7 is assumed.[24, 25] In our peak simulation the full width at half maximum of the doublet components is permitted to change but set equal for the Y $3d_{5/2}$ and Y $3d_{3/2}$ component.[20] The first Y $3d_{5/2}$ and $3d_{3/2}$ pair with binding energy at 155.7 ± 0.2 eV and 157.75 ± 0.2 eV are assigned to Y_2O_3. As these values are within the reported literature values for Y_2O_3.[26] We represented these peaks as blue lines in all XPS curves. Please note, that in the Y-based spectra we indicate the valence associated with the peaks. It has been reported that Y_2O_3 exhibits a high reactivity towards water and reacts with ambient moisture on its surface to form hydroxylated sites (Y-OH)[22] which is known to produce positive chemical shifts in the Y binding energy.[20,27] Therefore, the second doublet which appears at 156.4 ± 0.2 eV and 158.45 ± 0.2 eV is attributed to hydroxylated sites. Note, that these simulate hydroxide spectra are represented by orange lines. The presence of hydroxyl groups is corroborated by the O 1s spectra. The O 1s is de-convoluted into three sub-peaks located at 528.26 ± 0.2 eV, 530.42 ± 0.2 eV and 531.18 ± 0.2 eV respectively. We expect the first peak at lowest binding energy to correspond to lattice oxygen in yttrium oxide.[28] The peak at highest binding energy probably originated from carbon-containing impurities.[20] The peak in the middle is associated with hydroxyl group (–OH) on the surface (physisorbed oxygen).[29] The C 1s binding energy (not shown) was found at 284.04 ± 0.2 eV and 288.50 ± 0.2 eV, which correspond to adventitious carbon and carbonates, respectively.[30]

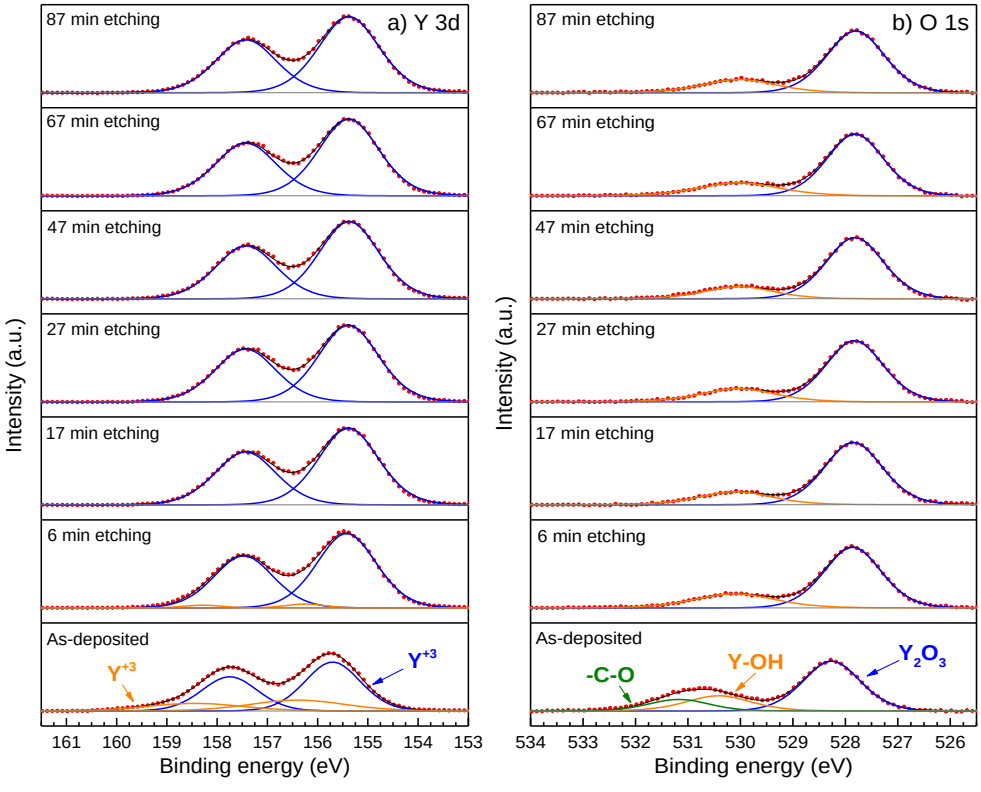

Figure 7.3. Background corrected XPS spectra (a) Y 3d and (b) O 1s core level spectra of yttrium oxide thin film, before and after etching. This film was transferred to the XPS load lock after 4 hours of air exposure. The data are presented in their raw form. Through this etching time we did not observe Si 2p peak.

The reported binding energy of Y_2O_3 oxide in the literature reveals a scattering of values (Y $3d_{5/2}$ between 156.2 and 157.4 eV).[26, 31] Therefore the use of binding energy difference between Y $3d_{5/2}$ and O 1s lines in Y_2O_3 [ΔBE_Y = BE (O 1s) – BE (Y $3d_{5/2}$) where $372.8 \leq \Delta BE_Y \leq 372.1$] has been suggested to indicate the correct energy scale calibration of the XPS system.[26] The binding energy difference is insensitive to the effect of surface charging and suitable for the comparative analysis of XPS results determined by different spectrometers. The ΔBE_Y values obtained for yttrium oxide film in our study is shown in table 7.1. They are within the acceptable range reported for Y_2O_3 and characterize the yttrium ions in their highest oxidation state (Y^{3+}).[26] The minimum ratio of O/Y in this thin film was 1.38 (This has been calculated by the area under the curve of the Y 3d and O 1s core level).

We find that, after few minutes of Ar-ion etching, the C 1s signal disappears. As seen in the Y 3d spectra, the peak associated to yttrium hydroxide is found to decrease in intensity and disappears upon on further etching. As a result, the peaks corresponding to the Y_2O_3 become the only visible component in Y 3d spectra. Similarly, the O1s core level spectra shows that the peak associated with the hydroxyl group (–OH) reduces in intensity after few mins of etching but remains present throughout the film. Such a peak is reported to exist inevitably in Y_2O_3 films prepared by reactive sputtering.[21] The peaks corresponding to lattice oxygen in Y_2O_3 stays dominant throughout the film.

Figure 7.4 shows the high-resolution XPS Y 3d and O 1s spectra of the yttrium dihydride film as a function of etching time. Three chemical environments are found for yttrium atoms at the surface of the as-deposited film. The doublet (Y $3d_{5/2}$ and Y $3d_{3/2}$) occurring 156.24 ± 0.2 eV and 158.29 ± 0.2 eV. The location of these peaks is associated with the presence of Y_2O_3 (within the range reported in literature) suggesting that the dominant oxidation state present at the surface is Y^{3+}. The doublet at higher binding energy (158.8 ± 0.2 eV and 160.81 ± 0.2 eV) demonstrates again a reaction with atmospheric moisture resulting in the formation of hydroxylated sites. The third doublet is found at lower binding energies of 156.24 ± 0.2 eV and 158.29 ± 0.2 eV. Since this film shows characteristic optical and structural properties of yttrium dihydride, we expect this peak reflects the presence of YH_2 corresponding to a Y^{2+} state (pink line). The location of these peaks are 0.5 eV lower than values reported by Hayoz et. al. for yttrium dihydride.[9] Note that, they did not specify their calibration method and therefore is hard to compare absolute values. Although the value of these peaks in our work is close to elemental yttrium[9,32], we do not expect formation yttrium metal in our film based on optical and structural analysis.

Three different oxygen species can be distinguished on deconvolution of O1s spectra of the as-deposited film in Figure 7.4b. The peak at the highest bonding energy at 530.17 ± 0.2 eV is assigned to lattice oxygen originating from Y_2O_3. The peak observed at a lower binding energy of 532.48 ± 0.2 eV is expected to be originating from hydroxyl groups. The peak at 533.27 ± 0.2 eV corresponds to carbon-containing impurities. This peak disappears after few mins of etching. The peaks corresponding to -OH bond reduces in intensity after 6 minutes of Ar^+ beam etching and disappears eventually.

As seen in the Y 3d spectra, with increasing the etching time, the intensity of the peaks associated with Y^{2+} increases and becomes the dominant feature, while the intensity of the Y^{3+} peaks decreases. The minimum ratio of O/Y in this film was 0.12. This suggests

that some oxygen is able to penetrate the dihydride film on air exposure although optically we do not see any indication for this. The binding energy difference (ΔBE_Y) between Y $3d_{5/2}$ (corresponding to Y^{3+}) and O 1s lines through the depth profile is shown in table 7.1. The presented values are within the acceptable range reported for Y_2O_3.

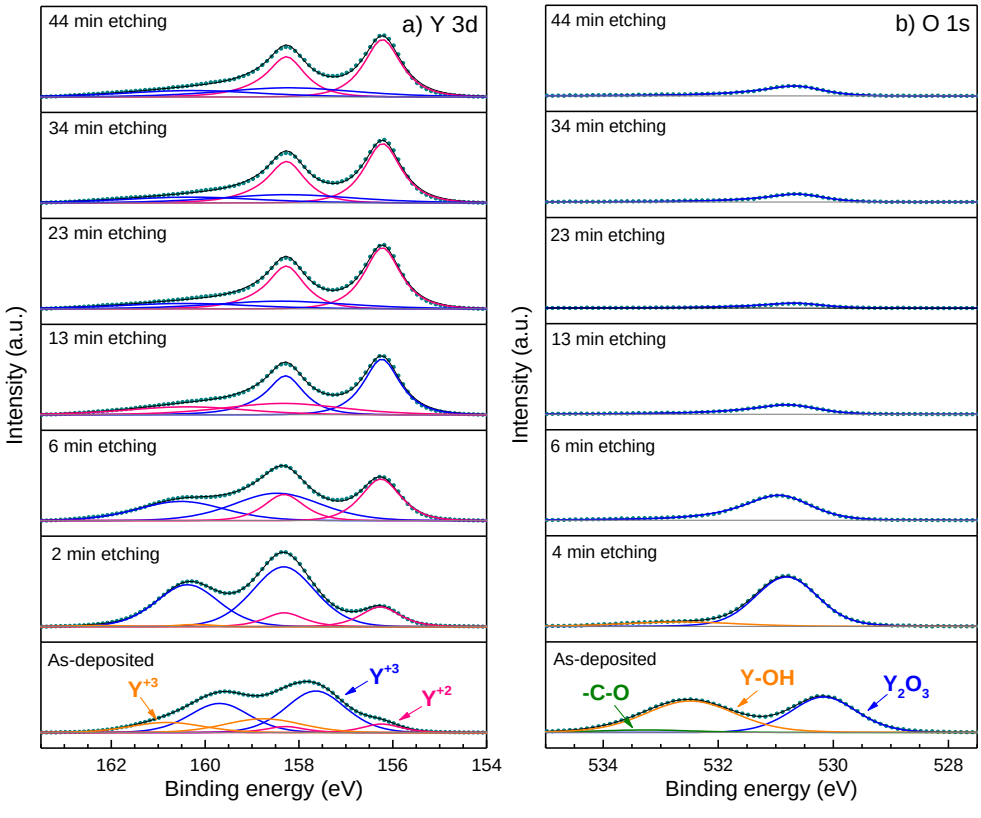

Figure 7.4. Background corrected XPS spectra (a) Y 3d and (b) O 1s core level spectra of yttrium dihydride thin film, before and after etching. This film was immediately transferred to XPS load lock with only a few minutes of air exposure. The data are presented as the raw data.

So far we thought that yttrium dihydride thin films are stable in air due to an amorphous self-limiting oxide layer formed at the surface. However, given the presence of oxygen deep into the film, we decided to expose the yttrium dihydride film to air for a period of 4 hours before being introduced to the XPS chamber. Figure 7.5 presents the O 1s and Y 3d high-resolution XPS scan for such a film. The fitted Y 3d spectra of the surface is de-convoluted into four peaks. The peak pair at highest binding energy (158.1 ± 0.2 eV and 160.15 ± 0.2 eV) is attributed to hydroxylated sites (Y-OH)[22],

while the peak pair at lower binding energy (157.00 ± 0.2 eV and 159.05 ± 0.2) corresponds to Y_2O_3. The doublet at the lowest binding energy (155.48 eV ± 0.2 and 157.54 ± 0.2 eV) corresponds to YH_2 and thus indicates the presence of Y^{+2}. The O 1s spectra shows three components. The peak at 529.25 ± 0.2 eV, 531.40 ± 0.2 eV and 532.19 ± 0.2 eV. The peak at lowest binding energy is originated from lattice oxygen in Y_2O_3. The peak at higher binding energy is stronger and broader, implying mixture of various contributions from O-C (due to contamination) and O-H (hydroxylation due to water absorption)[30] as a result of air exposure before the film is introduced in the XPS system.

After few minutes of Ar-ion etching, C 1s signal disappears indicating that carbon-containing impurities are limited to the surface of the film. The high-resolution spectra of O 1 s (Figure 7.5b), shows that the peak corresponding to the lattice oxygen and surface −OH groups remain present throughout the film.

In the Y 3d spectra the peak associated to hydroxylated sites decreases in intensity and disappears upon on further etching. The peaks associated with presence of Y^{2+} increase in intensity on etching. However, the peaks associated with Y_2O_3 (presence of Y^{3+} ions) remain present throughout the film albeit reduced in intensity. Note, that Y^{2+} appears to be no longer the dominant oxidation state, although optically we still see the characteristic transmittance window of a dihydride film. While reminding ourselves that XPS is a surface sensitive technique, these depth profile measurements indicate that oxygen does penetrate the dihydride films. The XPS data can only be reconciled with the optical data by assuming that the oxidation takes place along the whole growth pillars without fully converting them. The minimum ratio of O/Y in this film was 0.98.

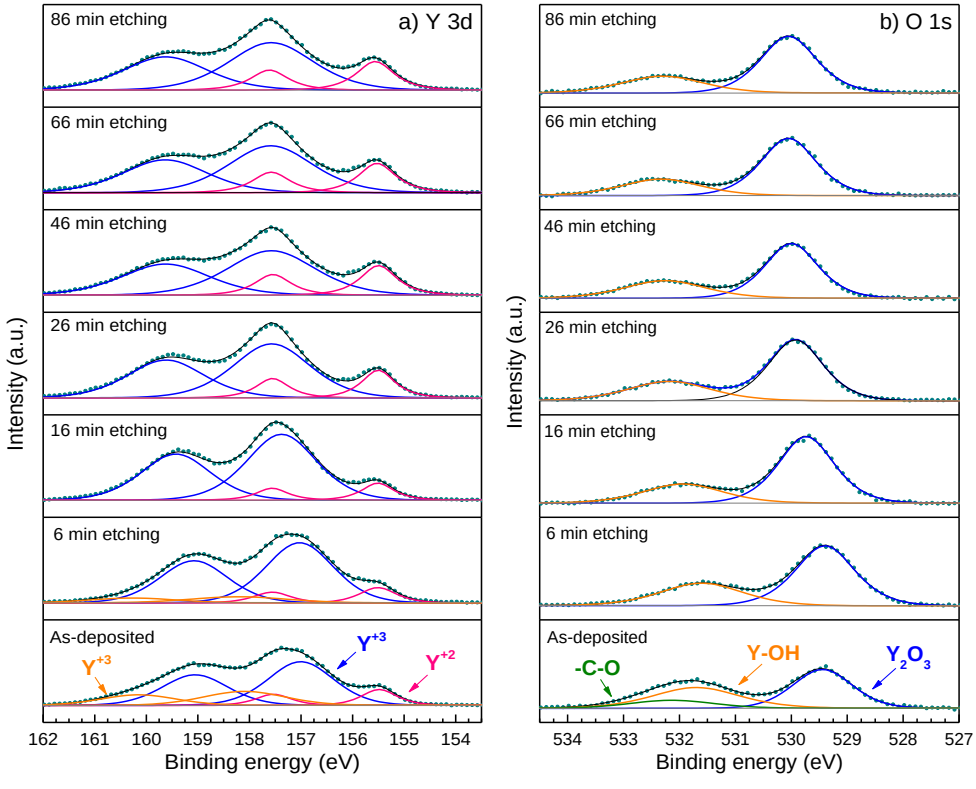

Figure 7.5. Background corrected XPS spectra of yttrium dihydride thin film prepared at 0.3 Pa in a Ar/H_2 atmosphere (a) Y 3d doublet (b) O 1s. This film was transferred to XPS load lock after 4 hours of air exposure. The data are presented as the raw data.

Figure 7.6 shows the high-resolution XPS spectra for Y 3d and O 1s of the yttrium oxyhydride film as a function of etching time. At the thin film surface, the Y 3d core level peak shows two main contributions. Note, that there is no clear distinction between YH_3 and Y_2O_3 other than presence of O 1s. This is due to the scattering in values of the binding energy in the literature for yttrium oxide [26] while only limited data is available in literature for binding energy of yttrium tri-hydride.[9, 32] Therefore, we assigned the double at lower binding energies to the presence of Y^{+3}. We also looked if the ΔBE_Y values are within the acceptable range [ΔBE_Y = BE (O 1s) – BE (Y $3d_{5/2}$) = 372 ± 0.7]. Hence, the ΔBE_Y value obtained in this film are within the acceptable range reported for Y_2O_3 and describes the yttrium ions in their highest oxidation state (Y^{3+}).

The Y 3d doublet that appears at the highest binding energies 158.07 ± 0.2 eV and 160.12 ± 0.2 eV indicates that yttrium is combined with atmospheric moisture to give

hydroxylated sites. This double peak together with the doublet at 157.03 ± 0.2 eV and 159.08 ± 0.2 eV are assigned to Y^{3+}. In Figure 7.6b, three types of surface oxygen species can be distinguished in the deconvoluted O 1s spectra. The binding energies of 529.25 ± 0.2 and 531.40 ± 0.2 eV are ascribed to the lattice oxygen associated with Y_2O_3,and the hydroxyl groups respectively. The weak peak at 532.19 ± 0.2 eV probably originates from carbon-containing species. After few minutes of Ar-ion etching, C 1s signal disappears from theO 1s spectrum. The two main peaks associated with lattice oxygen in Y_2O_3 and hydroxyl group remain visible throughout the film.

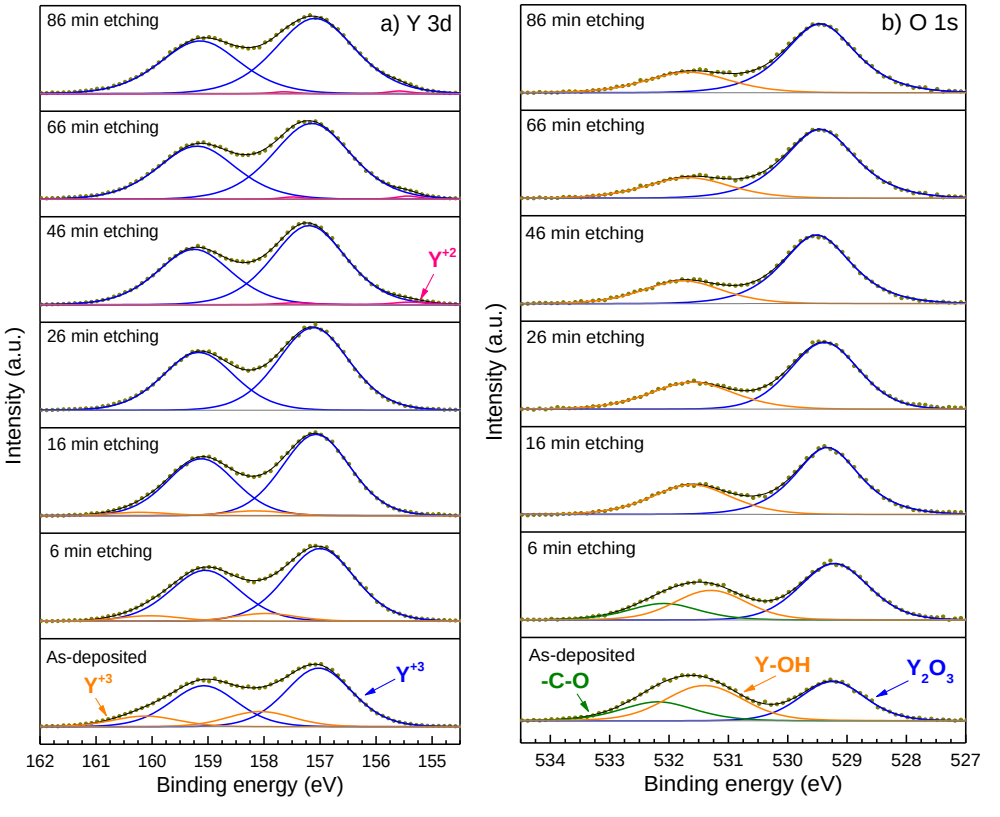

Figure 7.6. Background corrected XPS spectra for yttrium oxyhydride thin film prepared at 0.5 Pa in Ar/H_2 atmosphere (a) Y 3d doublet (b) O 1s. This film was transferred to XPS load lock after 8 hours of air exposure. The data are presented as the raw data. Through this etching time we did not observe Si 2p peak.

In the Y 3d spectra, the doublet associated with hydroxylated sites disappears after a few minutes of etching, leaving only the Y_2O_3 related peaks. After sputtering the surface for more 46 minutes, the Y 3d spectra shows the appearance of new weak

components. The Y $3d_{5/2}$ and Y $3d_{3/2}$ peaks are observed at 155.4 ± 0.2 eV and 157.45 eV ± 0.2. The location of these peaks is close to what has been found for the films prepared at lower pressure of 0.3 Pa, corresponding to the presence of YH_2 which were assigned to the Y^{+2} ion. Nevertheless, Y^{3+} is the dominant oxidation state present in the bulk of the film with a minor percentage of Y^{+2} ions. This confirms our earlier analysis that the photochromic YO_xH_y films contain predominantly Y^{3+} states.[2] The minimum ratio of O/ Y in this film was 1.32.

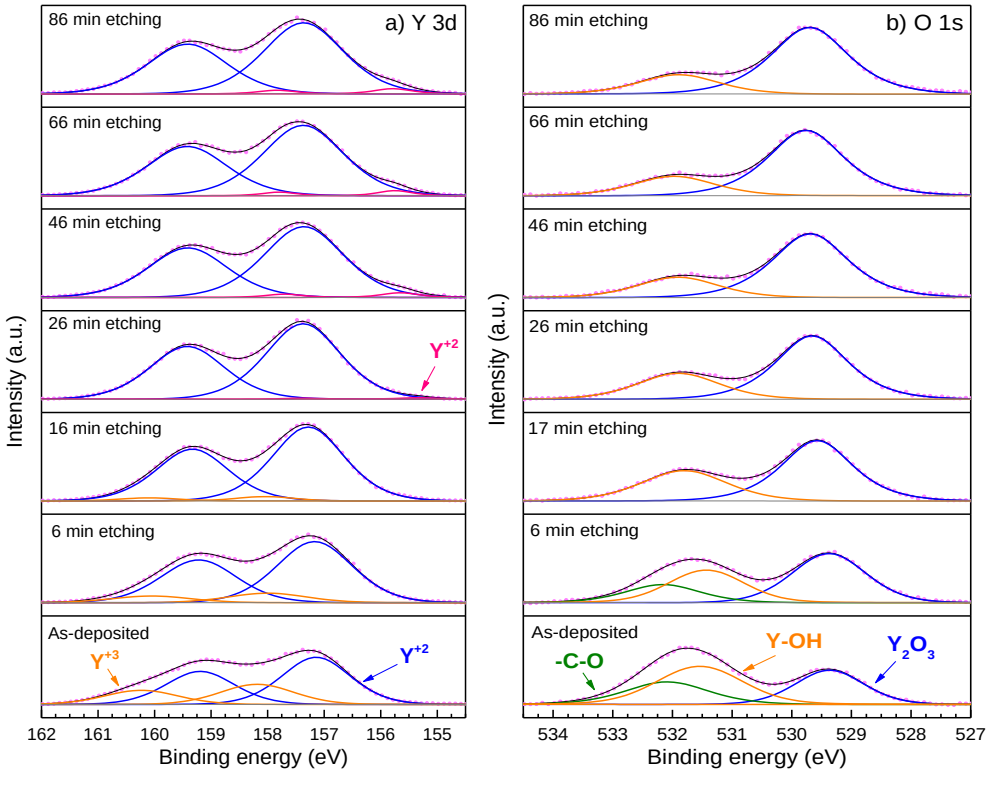

Figure 7.7. Background corrected XPS spectra for illuminated yttrium oxyhydride thin film prepared at 0.5 Pa in Ar/H_2 atmosphere (a) Y 3d doublet (b) O 1s. This film was transferred to XPS load lock after 8 hours of air exposure. The data are presented as the raw data. Through this etching time we did not observe Si 2p peak.

Figure 7.7 shows the Y 3d and O 1s XPS core level spectra obtained from an yttrium oxyhydride film after 5 hours of illumination. The Y3d and O 1s, show similar components in the illuminated and unilluminated film on the top surface layers. Interestingly, we observe an increase in intensity associated with the presence of Y^{+2} ,

suggesting an increase of this component due to illumination. The average ratio of Y/O in this film was 1.25.

Table 7.1. Binding energy difference between Y $3d_{5/2}$ and O 1s lines at different etching time for yttium dihydride, yttrium oxyhydride and yttrium oxide thin films.

Yttrium Oxide		**Yttrium oxyhydride**		**Yttrium dihydride+air**	**Yttrium dihydride**	
Etching time (min)	ΔBE_Y	Etching time (min)	ΔBE_Y	ΔBE_Y	Etching time (min)	ΔBE_Y
0	372.56 ± 0.1	0	372.22 ± 0.1	372.44 ± 0.1	0	372.53 ± 0.1
6	372.44 ± 0.1	6	372.21 ± 0.1	372.37 ± 0.1	2	372.49 ± 0.1
17	372.45 ± 0.1	16	372.29 ± 0.1	372.35 ± 0.1	6	372.49 ± 0.1
27	372.43 ± 0.1	26	372.27 ± 0.1	372.35 ± 0.1	13	372.48 ± 0.1
47	372.45 ± 0.1	46	372.31 ± 0.1	372.43 ± 0.1	23	372.35 ± 0.1
67	372.43 ± 0.1	66	372.31 ± 0.1	372.47 ± 0.1	34	372.38 ± 0.1
87	372.42 ± 0.1	86	372.31 ± 0.1	372.47 ± 0.1	44	372.46 ± 0.1

7.4 Discussion

The XPS spectra of the yttrium dihydride film suggests the presence of a small amount of oxygen throughout the film, depending on the amount of air exposure. Since, the optical properties are that of the dihydride and XPS is a surface technique, the most likely explanation is that air oxidation has taken place along the growth columns of the film. The presence of oxygen is not strange as yttrium has an exceptionally high affinity for oxygen, with a free energy of formation for the oxide of 1817 kJ/mol.[33] However, at this stage, we cannot exclude some oxidation may have taken place in the XPS chamber during sputter etching. The background pressure during the sputter etching was $5\text{-}6\times10^{-7}$ mbar which may indicate an air leakage.

After etching of the yttrium oxyhydride film, a weak doublet is observed at lower binding energy. This peak is consistent with the signature peak of Y^{+2} in yttrium dihydride film, indicating small presence of Y^{+2} ions. The intensity of this peak increases in an illuminated film.[34, 35] This may be related to photochromic mechanism such as in silver halide photochromic glasses. The illumination of yttrium oxyhydride film possibly leads to the growth of YH_2 nano-clusters. Formation of such metallic

domains upon illumination of YO_xH_y films has been proposed previously.[36,37] However, more theoretical and experimental work is required to prove such a mechanism for the photochromism in YO_yH_x.

7.5 Conclusion

Photoemission spectroscopy is a well-established method to investigate the electronic states in the matter. In this chapter, the O 1s and Y 3d XPS spectra for yttrium dihydride, yttrium oxyhydride and yttrium oxide thin films are investigated. The C1s spectra is commonly used as an easy-to-use internal energy reference element for the calibration of XPS data. Since C 1s disappears after few minutes of etching, implanted Ar was believed to be a reliable alternative. However, using implanted Argon for calibration of our XPS data was not possible as a large chemical shift of up to 1.4 eV was observed in the Ar $2p_{3/2}$ photoelectron line after sputter etching. Since no internal referencing could be used in our films for calibration, the spectra were presented as raw data.

All films showed adsorbed moisture on its surface. The O1s and C1s spectra confirm the presence of hydroxide and carbonate groups on the surface of all films. The Y 3d spectra of yttrium oxide film showed one-component in the bulk of the film which indicates that a single, equivalent chemical environment occurs around the Y^{3+} ion. The convolution of Y 3d spectra of yttrium dihydride film indicates the presence of both Y^{+2} and Y^{+3} components in the bulk of the film. The latter is due to oxidation. We find that when the yttrium dihydride is exposed to air for longer period of time, it absorbs more oxygen while it still shows yttrium dihydride characteristics in optical experiments.

The Y 3d spectra of yttrium oxyhydride film showed one main component which is assigned to Y^{+3}. A weak component at lower binding energy was found indicating the small presence of YH_2. The formation of Y^{+2} appeared to increase with illumination. This hints towards formation of YH_2 clusters in the YO_xH_y matrix.

References

[1] F. Nafezarefi, H. Schreuders, B. Dam, and S. Cornelius, "Photochromism of rare-earth metal-oxy-hydrides," *Applied Physics Letters,* vol. 111, p. 103903, 2017.

[2] S. Cornelius, G. Colombi, F. Nafezarefi, H. Schreuders, R. Heller, F. Munnik*, et al.*, "Oxyhydride Nature of Rare-Earth-Based Photochromic Thin Films," *The journal of physical chemistry letters,* vol. 10, pp. 1342-1348, 2019.

[3] C. V. Chandran, H. Schreuders, B. Dam, J. W. G. Janssen, J. Bart, A. P. M. Kentgens*, et al.*, "Solid-State NMR Studies of the Photochromic Effects of Thin Films of Oxygen-Containing Yttrium Hydride," *Journal of Physical Chemistry C,* vol. 118, pp. 22935-22942, Oct 9 2014.

[4] J. P. Maehlen, T. T. Mongstad, C. C. You, and S. Karazhanov, "Lattice contraction in photochromic yttrium hydride," *Journal of Alloys and Compounds,* vol. 580, pp. 119-121, 2013.

[5] M. P. Plokker, S. W. H. Eijt, F. Naziris, H. Schut, F. Nafezarefi, H. Schreuders*, et al.*, "Electronic structure and vacancy formation in photochromic yttrium oxy-hydride thin films studied by positron annihilation," *Solar Energy Materials & Solar Cells,* vol. 177, 2018.

[6] G. W. Ewing, *Analytical instrumentation handbook*, 2nd ed., rev. and expanded. ed. New York: M. Dekker, 1997.

[7] J. Cazaux, "Mechanisms of charging in electron spectroscopy," *Journal of Electron Spectroscopy and Related Phenomena,* vol. 105, pp. 155-185, 1999.

[8] J. Cazaux, "Secondary electron emission and fundamentals of charging mechanisms in XPS," *Journal of Electron Spectroscopy and Related Phenomena,* vol. 178-179, pp. 357-372, 2010.

[9] J. Hayoz, T. Pillo, M. Bovet, A. Zuttel, S. Guthrie, G. Pastore*, et al.*, "Preparation and characterization of clean, single-crystalline YH_x films ($0 \leq x \leq 2.9$)onW(110)," *Journal of Vacuum Science & Technology A Vacuum Surfaces and Film,* vol. 18, pp. 2417-2431, 2000.

[10] J. Hayoz, M. Bovet, T. Pillo, L. Schlapbach, and P. Aebi, "Oxygen-segregation-controlled epitaxy of Y2O3 films on Nb(110)," *Applied Physics A : Materials Science and Processing,* vol. 71, pp. 615-618, 2000.

[11] G. Greczynski and L. Hultman, "X-ray photoelectron spectroscopy: towards reliable binding energy referencing," *Progress in Materials Science,* p. 100591, 2019.

[12] S. Kohiki, T. Ohmura, and K. Kusao, "A new charge-correction method in X-ray photoelectron spectroscopy," *Journal of Electron Spectroscopy and Related Phenomena,* vol. 28, pp. 229-237, 1983.

[13] P. Swift, "Adventitious carbon—the panacea for energy referencing?," *Surface and Interface Analysis,* vol. 4, pp. 47-51, 1982.

[14] P. H. Citrin and D. R. Hamann, "Measurement and calculation of polarization and potential-energy effects on core-electron binding energies in solids: X-ray photoemission of rare gases implanted in noble metals," *Physical Review B,* vol. 10, pp. 4948-4963, 12/15/ 1974.

[15] G. Moretti, "Auger parameter and Wagner plot in the characterization of chemical states by X-ray photoelectron spectroscopy: a review," *Journal of Electron Spectroscopy and Related Phenomena,* vol. 95, pp. 95-144, 1998.

[16] T. Mongstad, A. Thogersen, A. Subrahmanyam, and S. Karazhanov, "The electronic state of thin films of yttrium, yttrium hydrides and yttrium oxide," *Solar Energy Materials and Solar Cells,* vol. 128, pp. 270-274, Sep 2014.

[17] A. E. Hughes and B. A. Sexton, "Comments on the use of implanted Ar as a binding energy reference," *Journal of Electron Spectroscopy and Related Phenomena,* vol. 50, pp. C15-C18, 1990.

[18] A. Pélisson-Schecker, H. J. Hug, and J. Patscheider, "Charge referencing issues in XPS of insulators as evidenced in the case of Al-Si-N thin films," *Surface and Interface Analysis,* vol. 44, pp. 29-36, 2012.

[19] M. Prenzel, T. de los Arcos, A. Kortmann, J. Winter, and A. von Keudell, "Embedded argon as a tool for sampling local structure in thin plasma deposited aluminum oxide films (4 pages)," *Journal Of Applied Physics,* vol. 112, p. 103306, 2012.

[20] T. Gougousi and Z. Chen, "Deposition of yttrium oxide thin films in supercritical carbon dioxide," *Thin Solid Films,* vol. 516, pp. 6197-6204, 2008.

[21] P. Lei, J. Zhu, Y. Zhu, C. Jiang, and X. Yin, "Yttrium oxide thin films prepared under different oxygen-content atmospheres: microstructure and optical properties," *Applied Physics A : Materials Science & Processing,* vol. 108, pp. 621-628, 2012.

[22] R. Xu, S. K. Selvaraj, N. Azimi, and C. G. Takoudis, "Growth Characteristics and Properties of Yttrium Oxide Thin Films by Atomic Layer Deposition from Novel Y(iPrCp)3 Precursor and O3," *ECS Transactions,* vol. 50, pp. 107-116, 2013.

[23] A. T. M. van Gogh, D. G. Nagengast, E. S. Kooij, N. J. Koeman, J. H. Rector, R. Griessen*, et al.*, "Structural, electrical, and optical properties of $La_{1-z}Y_zH_x$ switchable mirrors," *Physical Review B,* vol. 63, p. 195105, 04/20/ 2001.

[24] S. A. Barve, B. S. A. Jagannath, N. Mithal, M. N. Deo, N. Chand, B. M. Bhanage*, et al.*, "Microwave ECR plasma CVD of cubic Y 2O 3 coatings and their characterization," *Surface & Coatings Technology,* vol. 204, pp. 3167-3172, 2010.

[25] L. Mai, N. Boysen, E. Subas1, T. d. l. Arcos, D. Rogalla, G. Grundmeier*, et al.*, "Water assisted atomic layer deposition of yttrium oxide using tris(N , N '-diisopropyl-2-dimethylamido-guanidinato) yttrium," *RSC Advances,* vol. 8, pp. 4987-4994, 2018.

[26] R. E. J., A. V. V., K. V. N., P. L. D., P. I. P., and R. C. V., "Electronic Structure and Optical Quality of Nanocrystalline Y2O3 Film Surfaces and Interfaces on Silicon," *Journal of Physical Chemistry C,* vol. 118, pp. 13644-13651, 2014.

[27] L. Lin, S. A. Starostin, X. Ma, S. Li, S. A. Khan, and H. V., "Facile synthesis of lanthanide doped yttria nanophosphors by a simple microplasma-assisted process," *Reaction Chemistry & Engineering,* vol. 4, pp. 891-898, 2019.

[28] D. Barreca, G. A. Battiston, D. Berto, R. Gerbasi, and E. Tondello, "Y_2O_3 Thin Films Characterized by XPS," *Surface Science Spectra,* vol. 8, pp. 234-239, 2001.

[29] P. de Rouffignac, J. S. Park, and R. G. Gordon, "Atomic Layer Deposition of Y2O3 Thin Films from Yttrium Tris(N,N'-diisopropylacetamidinate) and Water," *Chemistry of materials : a publication of the American Chemical Society.,* vol. 17, p. 4808, 2005.

[30] I.-S. Park , Y. Chan Jung , S. Seong, J. Ahn , J. Kang , W. Noh*, et al.*, "Atomic layer deposition of Y_2O_3 films using heteroleptic liquid $(iPrCp)_2Y$(iPr-amd) precursor," *Journal of Materials Chemistry C,* vol. 2, pp. 9240-9247, 2014.

[31] Y.-D. Chung, D.-H. Cho, S.-B. Kim, and W. S. Han, "Comment on 'Enhancement in hardness and transmittance of ZnS via SiO_2/Y_2O_3 multilayer'," *Journal of Alloys and Compounds,* vol. 664, pp. 648-649, 2016.

[32] A. Fujimori, F. Minami, and N. Tsuda, "Electronic-Structure of Cerium Hydrides - Augmented-Plane-Wave Linear-Combination-of-Atomic-Orbitals Energy-Bands," *Physical Review B,* vol. 22, pp. 3573-3582, 10/15/ 1980.

[33] H. J. Hoffmann, "Photochromic glasses," in *The Properties of Optical Glass*, H. Bach and N. Neuroth, Eds., ed Berlin: Springer, 1995, pp. 275-290.

[34] G. Adachi and N. Imanaka, "The Binary Rare Earth Oxides," *Chemical Reviews,* vol. 98, pp. 1479-1514, 1998.
[35] R. J. D. Tilley, *Defects in Solids* Wiley & Sons, Inc. , 2008.
[36] J. Montero and S. Z. Karazhanov, "Spectroscopic Ellipsometry and Microstructure Characterization of Photochromic Oxygen-Containing Yttrium Hydride Thin Films," *physica status solidi (a),* vol. 215, 2018.
[37] J. Montero, F. A. Martinsen, S. Z. Karazhanov, B. Hauback, E. S. Marstein, M. Garcia-Tecedor*, et al.*, "Photochromic mechanism in oxygen-containing yttrium hydride thin films: An optical perspective," *Physical Review B,* vol. 95, 2017.

Summary

The experiments presented in this thesis have provided new insights regarding the photochromic properties of rare earth oxyhydrides (REO_xH_y). We discovered that thin films of rare-earth (Y, Dy, Er, Gd, Nd) oxyhydrides show unique photochromic properties under ambient conditions. We showed that by direct current reactive magnetron sputtering of rare earth metal targets in an Ar and H_2 atmosphere a metallic dihydride thin films can be made. However, above a certain critical deposition pressure, a semiconductor REO_xH_y thin film is formed upon exposing the films to air. These films show photochromic properties. Compared to YO_xH_y, the optical bandgaps of the lanthanide-based oxyhydrides are smaller, while photochromic contrast and kinetics show large variation among different cations. The photon energy required to obtain a photochromic effect is given by the optical band gap of the material, as shown in the energy threshold measurements. Photon energies larger than the band gap are required to photo-darken the rare-earth oxyhydrides. The photochromic process is reversible and bleaching occurs through thermal bleaching and possibly through interaction with the light of longer wavelengths (optical bleaching). However, the latter needs to be confirmed with further experiments. We have shown for the first time also that semiconducting YH_3 does not exhibit photochromic properties, revealing the importance of the presence of both oxide and hydride ions for the photochromic effect in rare-earth oxyhydrides.

The photochromic response starts from the band gap and extends up to the Mid-IR region, especially in the case of GdO_xH_y. The largest contrast change matches the sensitivity of the human eye. GdO_xH_y thin films show the strongest photochromic contrast (45% at film thickness of 300 nm) over a very wide spectral range. These materials are suitable for modulation of the visible light as well as the thermal part of the solar spectrum. The photo- darkening in the rare-earth oxyhydride does not depend on UV light only. This is a promising feature, enabling us to design a material that also darkens at the inner glass surface of a double glazed window pane. Such properties make the rare-earth oxyhydrides ideal for application such as smart windows for energy-efficient buildings.

A well-known example of an inorganic photochromic material is glass containing silver halide crystals doped with copper. Light of sufficiently high energy (UV or blue) to overcome the band gap of the silver chloride generates electron-hole pairs. The electrons are trapped by interstitial silver ions to form mobile silver atoms which coagulate to form a silver speck at the interface of the silver halide/glass matrix. The plasmonic resonances in these metallic particles are responsible for the induced optical absorption. On the other hand, holes are trapped by Cu^{+} ions to form Cu^{2+} ions and slow down the recombination process. We suspected some similarities between photochromism in rare-earth oxyhydrides with that in silver halide doped silicate glass and speculate that metallic Y or YH_2 nano-clusters form in the YO_xH_y matrix upon illumination. This means that the formation and dissolution of these clusters would involve the mobility of certain point defect species. To investigate whether the photochromic effect in YO_xH_y involves the mobility of such point defects, we explored the effect of a change of lattice spacing on the kinetics of the photochromic effect by addition of zirconium.

We find that upon adding Zr to YO_xH_y 1) the fcc lattice is compressed, 2) the bleaching speed is decreased, 3) the photochromic contrast changes, 4) the optical transmission in the bleached state reduces, and 5) narrowing of the bandgap is observed. We conclude these changes are due to change in the properties of the YO_xH_y matrix as we did not detect any photochromism in films where Zr is the only cation.

Considering photochromic glasses as a model system, Zr in $Y_{1-z}Zr_zO_xH_y$ might play a similar role as Cu in silver halide doped glasses, where Cu is added to enhance the photochromic contrast of the glass. The incorporated Zr into the matrix might occupy an Y site, thus forming a substitution similar to copper in AgCl. In YO_xH_y films Y is in 3+ state while Zr is likely to be in the 2+ state. Upon illumination Zr^{4+} could be formed by trapping holes thus reducing the rate of recombination. This implies an increase in the rate constant of the photo-darkening process and which would slow down the bleaching process. However, the data obtained so far do not allow us to verify the presence of this mechanism. Up to a Zr concentration of $z = 0.1$, the saturation contrast increases while the bleaching speed decrease. However, above $z = 0.1$ the saturation contrast decreases rapidly, while the bleaching speed continuously decreases. Dilution of active photochromic species at large Zr contration probably counterbalances the slower bleaching. Detailed analysis of the photo-darkening kinetics is required to analyse such countervailing trends to separate the photo-bleaching and darkening contributions.

In the first part of this thesis, we showed that we did not find a correlation between the ionic radius of the rare-earth metal and the photochromic properties of the oxyhydride films. However, the difference in ionic radius between the rare-earth cations studied was rather small (Gd, Dy, Y and Er). Hence, as one of the large RE cations we choose to investigate neodymium oxyhydride. The bandgap is much smaller than in other RE's allowing for a much larger fraction of solar light to be used to darken the film. Remarkably, the photochromic switching kinetics is similar to that of the other rare-earth oxyhydrides, suggesting that point defect mobility plays a minor role in the kinetics of the photochromic effect.

Our experimental findings show that structural, optical and photochromic properties of the neodymium oxyhydrides can be tailored by the deposition pressure. Direct comparison of observed contrast between YO_xH_y and NdO_xH_y is complicated because it also depends on film thickness and absorption coefficients. We find that the thermal bleaching time constant is not strongly affected by the type of rare-earth metals that is used and mostly affected by microstructure and composition of the film. We find that the thermal bleaching time constant is only weakly affected by the type of rare-earth metals that is used and mostly affected by microstructure and composition of the film. There is a factor of 10 difference in bleaching speed if you change the deposition pressure. The addition of an ALD protection layer right after deposition is a possible solution to assure the stability of NdO_xH_y thin films against air-oxidation.

Next, we study the electronic structure differences between yttrium oxide, hydride and oxyhydride by means of XPS technique. The Y 3d spectra of yttrium oxide film reveals that a single, equivalent chemical environment occurs around the Y^{3+} ion. The convolution of Y 3d spectra of yttrium dihydride film indicates the presence of both Y^{3+} (minority) and Y^{2+} (majority) component in the bulk of the film. We find that when the yttrium dihydride is exposed to air for a longer period of time, it absorbs a more oxygen while it still shows yttrium dihydride characteristics in optical experiments. The Y 3d spectra of yttrium oxyhydride film showed one main component which is assigned to Y^{3+}. A weak component at lower binding energy was found indicating the presence of a small amount of YH_2. The formation of Y^{2+} appeared to increase with illumination. This hints towards the formation of YH_2 clusters in the YO_xH_y matrix which may help us to understand the underlying mechanism of the photochromic effect in YO_xH_y.

Samenvatting

De experimenten die in deze scriptie worden gepresenteerd bieden nieuwe inzichten in het fotochrome eigenschappen van zeldzame aardmetaal oxyhydriden (REO_xH_y). Wij hebben ontdekt dat een zeer dunne laag, ook wel film, van zeldzame aardmetaal (Y, Dy, Er, Gd, Nd) oxyhydriden unieke fotochrome eigenschappen vertoont bij kamercondities. Door middel van gelijkstroom reactieve magnetron sputteren van zeldzame aardmetalen in een Ar en H_2 atmosfeer hebben wij laten zien dat zo'n film van metallische dihydride kan worden geproduceerd. Echter, boven een bepaalde kritische depositie druk, woudt bij blootstelling aan lucht een halfgeleider REO_xH_y gevormd. Deze film vertoont fotochrome eigenschappen. Vergeleken met YO_xH_y zijn de optische bandgaps van op-lantanide-gebaseerde oxyhydriden kleiner, terwijl het fotochrome contrast en de kinetiek grote variatie vertonen bij verschillende kationen. De fotonenergie die nodig is om een fotochroom effect te bereiken wordt gegeven door de optische bandgap van het materiaal, zoals vertoont in de energiedrempelmetingen. Fotonenergieën groter dan de bandgap zijn nodig om de zeldzame aardmetaal oxyhydriden te foto-verduisteren. Het fotochrome proces is reversibel en de verbleking gebeurt via thermische verbleking en mogelijk ook door middel van interactie met licht van langere golflengten (optische verbleking). De laatste optie moet echter nog worden geverifieerd in verdere experimenten. De halfgeleider YH_3 vertoont geen fotochromische eigenschappen, wat het belang outhult van de aanwezigheid van beide oxide- en hydride-ionen voor het fotochrome effect in zeldzame aardmetaal oxyhydriden.

De fotochrome respons begint bij de bandgap en gaat door tot aan de midden-IR regio, voornamelijk in het geval van GdO_xH_y. De grootste contrastverandering en het maximum corresponderen met de sensitiviteit van het menselijk oog. Een film GdO_xH_y vertoont het sterkste fotochrome contrast (45% bij een filmdikte van 300 nm) over een breed spectraal bereik. Deze materialen das zijn bruikbaar voor de modulering van zowel zichtbaar licht als het thermische deel van het zonnespectrum. De foto-verduistering in de zeldzame aardmetaal oxyhydriden is niet afhankelijk van UV licht. Dit is een veelbelovend kenmerk waardoor materialen kunnen worden ontworpen die ook verduisteren aan de binnenkant van dubbelzijdig glas. Dit soort

eigenschappen maken zeldzame aardmetaal oxyhydriden ideaal voor toepassingen zoals slimme-ramen voor energie-efficiënte gebouwen.

Een welbekend voorbeeld van een anorganisch fotochroom materiaal is glass waar koper-gedoopte zilver halide kristallen in zitten. Licht met een energie hoog genoeg (UV of blauw) om de bandgap van zilverchloride te overbruggen produceert in dit materiaal elektron-gat paren. De vrijgekomen elektronen worden gevangen door interstitiële zilver ionen waardoor mobiele zilveratomen worden gevormd. Deze atomen klompen samen tot zilverdeeltjes die zich tussen de zilverhalide en de glaslaag in positioneren. De plasmon resonanties in deze metallische deeltjes zijn de oorzaak van de geïnduceerde optische absorptie. Aan de andere kant worden de gevormde gaten gevangen door Cu^{+} ionen waardoor Cu^{2+} ionen worden gevormd die het recombinatieproces vertragen. We verwachten overeenkomsten tussen het fotochromisme in zeldzame aardmetaal oxyhydriden en het zilver-halide gedoopt silica glas en speculeren dat metallische Y of YH_2 nano-clusters worden gevormd in de YO_xH_y matrix bij berlichting. Dit zou betekenen dat de vorming en oplossing van deze clusters gepaard gaat met de mobiliteit van bepaalde punt-defecten. Om te onderzoeken of de fotochrome effecten in YO_xH_y gepaard gaan met de mobiliteit van zulke puntdefecten is gekeken naar de effecten van een verandering in roosterafstand d.m.v. toevoeging van zirkonium op de kinetiek van het fotochrome effect.

We hebben ontdekt dat de toevoeging van Zr bij YO_xH_y gepaard gaat met 1) een samendrukking van het fcc rooster, 2) een vertraging van de verblekingstijd, 3) het fotochrome contrast verandert, 4) de optische transmissie in de verbleekte staat reduceert is en 5) de grootte van de bandgap verkleint. We concluderen dat deze veranderingen het gevolg zijn van een verandering in de eigenschappen van de YO_xH_y matrix, aangezien geen fotochromisme was gedetecteerd in lagen waar Zr het enige aanwezige kation is.

Aangezien fotochroom glas als een model systeem kan worden beschouwd, zou het kunnen dat Zr in $Y_{1-z}Zr_zO_xH_y$ een gelijkende rol speelt als Cu in zilver halide gedoopt glas, waarbij Cu is toegevoegd als versterker van het fotochromisch contrast. De opname van Zr in de matrix kan de positie van een Y plek innemen, gelijkend aan de vervanging die koper doet in AgCl. In een film YO_xH_y is Y in de 3+ staat, terwijl Zr waarschijnlijk zich in de 2+ staat bevindt. Bij illuminatie zou Zr^{4+} kunnen vormen wegens het vangen van gaten en daarmee de recombinatiesnelheid vertragen. Dit impliceert een toename in de reactiesnelheid van het foto-verduisteringsproces, waardoor de verbleking vertraagt. Echter is de tot nu toe verkregen data niet sterk

genoeg om de aanwezigheid van dit mechanisme te verifiëren. Tot aan een Zr concentratie van z = 0,1 neemt het saturatiecontrast toe, gepaard gaand met een vertraagd verblekingsproces, maar boven z = 0,1 neemt het saturatiecontrast juist sterk af, terwijl een afname van de verblekingssnelheid zichtbaar is. Verdunning van het actieve fotochrome materiaal met hoge concentraties Zr werken waarschijnlijk als tegenwicht van de vertraagde verbleking. Gedetailleerde analyse van de foto-verduisterende kinetiek is nodig om te analyseren of deze compenserende trends kloppen en om onderscheid te maken tussen foto-verbleking en -verduisterende contributies.

In het eerste deel van dit proefschrift laten we zien dat er geen correlatie gevonden is tussen de ion straal van zeldzame aardmetalen en de fotochromische eigenschappen van oxyhydride films. Echter zijn de verschillen in ionische radii van de bestudeerde zeldzame aardmetaal kationen nogal klein (voor Gd, Dy, Y en Er), daarom is er gekeken naar neodymium (Nd), een RE element met een veel grotere ion straal, om het effect van kation straal op het fotochrome effect van REO_xH_y te bestuderen. Onze experimentele bevindingen tonen dat structurele, optische en fotochromische eigenschappen van neodymium oxyhydriden kunnen worden aangepast door middel van de depositiedruk. Directe vergelijking van het geobserveerde contrast tussen YO_xH_y en NdO_xH_y is lastig, omdat dit contrast ook afhankelijk is van de filmdikte en de absorptie coëfficiënten. We vonden dat de tijdsconstante van thermische verbleking niet sterk afhankelijk is van het gebruikte type zeldzaam aardmetaal, maar dat de microstructuur en de compositie hier voornamelijk een rol bij spelen. De verblekingssnelheid van het materiaal kan een factor 10 worden veranderd met variërende depositiedruk. De toevoeging van een ALD bescherming direct na de depositie is een optie om de stabiliteit van NdO_xH_y te verzekeren tegen in lucht oxidatie.

Vervolgens zijn de electronische structuurverschillen tussen yttrium oxide, hydride en oxyhydride bestudeerd met behulp van XPS. De Y 3d spectra van yttrium oxide films onthullen dat er een enkele equivalente omgeving aanwezig is rondom het Y^{3+} ion. De niet-eenduidige Y 3d spectra van yttrium dihydride films tonen aan dat niet alleen Y^{3+} (minderheid) maar ook Y^{2+} (meerderheid) componenten in de bulk aanwezig zijn. Wanneer yttrium dihydride voor een langere tijd is blootgesteld aan lucht vinden we dat meer zuurstof wordt geabsorbeerd, terwijl de optische eigenschappen nog steeds het karakter van yttrium dihydride vertonen. De Y 3d spectra van yttrium oxyhydride films vertonen voornamelijk de aanwezigheid van het Y^{3+} component. Een zwak signaal bij een lagere bindingsenergie is ook aanwezig en duidt op de aanwezigheid van

YH_2. De formatie van Y^{2+} lijkt toe te nemen na langere illuminatie. Dit hint naar de formatie van YH_2 clusters in de YO_xH_y matrix, wat kan helpen bij het verder begrijpen van het onderliggende mechanisme van het fotochrome effect in YO_xH_y.

Acknowledgments

Writing this section is bitter-sweet. The PhD journey coming to an end makes me feel nostalgic and happy. I want to take this opportunity to express my deepest gratitude to all those who have joined me along the way. First of all, I would to express my deepest appreciation towards my promoter Prof. Bernard Dam for all his guidance, support, invigorating discussions and inspiring suggestions. For giving me the opportunity and resources to work at his group, to grow scientifically and personally. Your patience, pragmatic leadership, authenticity and integrity have always been sources of admiration and inspiration for me.

I am thankful to all the committee members who have accepted to read my thesis and attend my PhD defense. I want to express my gratitude to Dr. Steffen Cornelius. It was a great pleasure working with you. Thank you for patiently and comprehensively answering all my questions and our in-depth scientific discussions. Your critical attitude and high standards of perfection is inspiring.

Special thanks to Bart Boshuizen, for developing LabVIEW software for the photochromic project and all your guidance and technical support for XPS measurements. You are always a great help. Ben Norder, thank you for all your help regarding XRD. Marcel Bus, thank you for the AFM training. Most importantly I would like to thank you three for bringing humor to workplace. With an upbeat atmosphere in the department, there is a higher probability students will brainstorm innovative ideas and think further outside the box.

Warmhearted thanks to all MSc and BSc students for their hard work and continues enthusiasm in their respective projects. Eline (your endless amount of energy is remarkable), Martijn, Hayati, Marina (I don't think I had ever seen you without a smile), Lijie (you use sense of humor in a sophisticated and creative way), Joost and Jelle (I admire your kindness and positivism).

It was a great privilege to be a part of a group with so many great minds; Andreas, Wilson, Hans, Andreas, Fokko, thank you for all the inspiring discussion during group meetings and Borrel. My gratitude goes to Herman and Joost for not only for their technical support but making life in the group very *gezellig*. All the great conversation

and laughter that you guys brought during coffee breaks and group activities. Thank you for being always supportive and making MECS such an awesome place to work every day. Special thanks to Heleen for helping me with all administrative affairs on the first two years of my PhD. I always say you have superpowers. Another thanks to Rajshree for all the help and support. You are very kind.

Without a doubt the contribution of all current and former group members, spending time in MECS was a fruitful professional and personal experience. In this context, I want to acknowledge, Christian, Sarmila, Sneha, Lucas (Thank you for all the laughs and funny memories), Nienke, Moreno, Bartek, Digda, Ming, Jicheng, Anirudth, Davide, Divya (conversations with you are never boring and I always learn something new), Kai, Kailun (a colleague like you is more than just a colleague, you are like a magic pill), Mark (thank you for your infectious laughter and for making my memories from MECS brighter), Nathan (thank you for all the great and inspiring conversations), Robin, Sanjana (you are just double awesome), Martin (thank you for all the hilarious conversations), Recep (thank you for being so kind and sympathetic), Bernhard, Audrey, Giorgio (I always appreciate your great energy), Diana (thank you for being kind hearted) and Marijn (thank you for bringing laughter and positive energy to the office, you are always helpful). I would also like to thank great people from OM group that I had a pleasure to get to know; Damla, Kevin (I truly appreciate your understanding and support), Cansel, Aditya. I would also like to thank Elena, Ali and Robert from ISE group for all the great conversations. Not to forget Tom, Lars and Marten from the Reactor institute. I would also like to thank Matija, Serhii and Angie from ASM group.

I believe that many of the connections and relationships we make on our journey through life exist simply to help us learn and grow. Completion of this PhD research would not be possible without the love and support of all my dearest friends. My lovely girls Laura and Yildiz, I am so happy we all met thanks to Maria putting us in contact with each other. I am thankful for all the delightful time and for heart-fully supporting me through difficult times. Supack, darling, I am so grateful to have met you in the graduate school. Thanks for all the laughter and most importantly thanks for introducing me to Gratzia. I love hanging out with you girls in Rotterdam and I would never forget our fun trip to Berlin. Gratzia, honey, you are simply the best. Thank you for being so incredibly compassionate. Sharhzad, my gracious friend, I am thankful to Mercedes for taking me to play tennis and introducing us. Thanks for all the happy memories and great times we spend together. Specially the trip to Interlaken in Switzerland. I feel blessed to have you as my friend. Your thoughtfulness is a gift I will always treasure. Anahid, it was an honor to be your and Mohammad's paranymph.

I am truly grateful for your friendship. Someone as strong and kind as you are is hard to find. Tomaz, thanks for all board game nights, you always made the games more fun. Thanks for taking me to bouldering where I met Remco. It was great getting to know you. Dear Maryam, I am very happy to have gotten to know you in Delft and visit you in Utrecht. Now, I am happy you came to work in Delft. I admire your determination. Mahnaz, darling, thanks for sharing the time off from PhD with me. Going to Greece with you is simply unforgettable. Nazila, honey, I think the greatest part of giving the presentation and attending 4TU Dutch materials, was meeting you. I feel so lucky to have you as my friend. You make my heart smile. Another great occasion in which I met a dear friend, was attending a NWO meeting in Amersfoort. It was such a delightful day and I am so happy to have met you, Melisa. Marianitzel & Simon, I always say one of the great thing about Graduate School is meeting other great PhDs. I am glad to have met you guys at the beginning of my PhD. Elmira, darling, I feel very fortunate to have met you. You are a ray of sunshine to me and everyone else around you. I'm so happy to have you as my friend and I am really touched by your kindness. I also would like to thank my neighbors, Sotia, Afshin, Bianca, Stefan, Wenjuan for the wonderful brunches we had together. Asal, darling, thank you for bringing laughter and life whenever I meet you. You are high spirited and beautiful inside-out. Mladen, thank you for giving me so many beautiful memories and all the amazing trips we had together. Thank you for introducing me to Tsegay. It was great getting to know him.

Learning to dance Salsa was a great part of my PhD life and I would like to thank the Sosalsa society for arranging all the amazing events. I am also grateful for having the opportunity to go to a variety of courses at the sport center at the university. Climbing classes helped me a lot during stressful times.

I would like to express my deepest appreciation to my Mom and Dad. I am very thankful for your love, support and encouragement throughout my life. Mom, your fight with cancer gives me strength and inspiration when I am down, to believe and never give up when life gets hard. Thank you both for teaching me that a single act of kindness goes a long way. My dear brothers, Ali and Mojtaba, I think you never know the true value of a moment until it becomes a memory. I am overwhelmingly grateful to have you all in my life. Thank you for stepping in and helping me when help was and is necessary.

Curriculum Vitae

Fahimeh Nafezarefi was born on 19th August 1985 in Tehran, Iran. In 2008 she graduated from Queen Mary University of London, UK with a bachelor degree in Polymer technology. In 2010 she recieved her Master degree in Advanced materials Science from Technical University of Munich, University of Augsburg, Ludwig Maximilian University of Munich (joint Master's degree), Germany. From 2010 to 2012, she worked in Swiss Federal Laboratories for Materials Science and Technology (EMPA) as an intern and later as Research Associate. In 2015, she pursued a Ph.D. research in Materials for Energy Conversion and Storage group at Delft University of Technology (TUDelft), under the supervision of prof. dr. Bernard Dam. During this period, she was working on rare-earth oxhydrides thin films, researching all the key aspects concerning their structure and optical properties. The results of her research project are described in this thesis.

List of

Publications

F. Nafezarefi, S. Cornelius, H. Schreuders and B. Dam. "A new photochromic thin film: Neodymium oxyhydride,". Manuscript in preparation, 2020.

F. Nafezarefi, S. Cornelius, J. Nijskens, H. Schreuders and B. Dam. "Effect of the addition of zirconium on the photochromic properties of ytrrium oxy-hydride,". *Solar Energy Materials and Solar Cells*, Volume 200, 2019.

S. Cornelius, G. Colombi, F. Nafezarefi, H. Schreuders, R. Heller, F. Munnik and B. Dam, "Oxyhydride nature of rare-earth-based photochromic thin films," *The Journal of Physical Chemistry Letters,* vol. 10, pp. 1342-1348, 2019.

M. P. Plokker, S. W. H. Eijt, F. Naziris, H. Schut, F. Nafezarefi, H. Schreuders, S. Cornelius and B. Dam, "Electronic structure and vacancy formation in photochromic yttrium oxy-hydride," *Solar Energy Materials and Solar Cells*, Volume 177, 2018.

F. Nafezarefi, H. Schreuders, B. Dam, and S. Cornelius, "Photochromism of rare-earth metal oxy-hydrides," *Applied Physics Letters,* vol. 111, no. 10, 2017.